Graded Cellular Structures: A Strategy to Tune the Structural Performance of Cellular Materials

Hamed Niknam Jahromi

Department of Bioreseource Engineering
McGill University, Montreal

May 2020

A thesis submitted to McGill University in partial fulfillment of the requirements of the degree of Doctor of Philosophy

Abstract

Desire to reduce the weight of structures without sacrificing specific functionalities persists for a long time. In the last few decades, cellular materials have opened new avenues for the lightweighting of structural elements. A variety of approaches has been proposed to engineer the base materials and topologies of cellular materials to decrease the weight and improve the performance of structures. Most of these approaches involve sophisticated designs or cumbersome manufacturing technologies. In the current study, we present a straightforward strategy to rationally design lattice structures and improve their specific characteristics without increasing the total weight. In this method, we vary the relative density and topology of cells across the structure to tune the mechanical response of cellular structures. Both numerical and experimental analyses are utilized to examine the response of graded cellular structures in different analyses, including bending, buckling, compression, and tension. Experimental studies are conducted on additively manufactured graded cellular samples. Depending on the topological features of a graded cellular structure, we select an appropriate additive manufacturing technology to fabricate the samples. The numerical methods for analyzing cellular structures are established by two different approaches, including detailed finite element modeling and hybrid homogenized modeling. In the detailed modeling, we import the as-designed structures in commercial FE software and set the proper analysis parameters to evaluate their response. The hybrid model, which is substantially faster but less accurate than detailed modeling, is grounded on the standard mechanics homogenization techniques and equivalent properties.

The results of analyzing different graded structures reveal exciting potentials in controlling their structural performance. In bending, we can increase the flexural rigidity about three times by

optimum variation of relative density across the structure. Such optimal variation with simple 2D topology can even outperform uniform cellular beams, whose cells' stiffness is at the theoretical limit (Voigt bond). Interestingly, our results show that we can even change the direction of thermal deformation by specific variations of relative density. In buckling analysis, we initially draw the curtains from two different buckling responses in cellular materials and distinguish between local and global bucklings. Next, we analyze the effect of different variations of relative density and show that by changing the variation, we may transform the buckling behavior of a cellular plate from in-plane buckling to out-of-plane buckling or vice versa. This property grading strategy can also substantially improve the energy absorption capabilities of a cellular structure under compression. As shown in the results, specific gradients can simultaneously increase the stiffness and energy absorption of a cellular structure no matter what the base cell topology is.

Altogether, the proposed design approach promises a strategy to reduce the weight of a cellular structure without sacrificing its structural performance. Consequently, rationally graded cellular structures can replace the uniform cellular structures in many applications such as sandwich panels and shock absorbers. Future research can shed more light on other potentials of these structures, which can further fill the gaps in material selection charts.

Résumé

Le désir de réduire le poids des structures sans sacrifier des fonctionnalités spécifiques persiste depuis longtemps. Au cours des dernières décennies, les matériaux cellulaires ont ouvert de nouvelles voies pour alléger les éléments structurels. Diverses approches ont été proposée**s** pour concevoir les matériaux de base et les topologies des structures cellulaires afin de réduire le poids et d'améliorer les performances. La plupart de ces approches impliquent des conceptions sophistiquées ou des technologies de fabrication complexes. Dans cette étude, nous présentons une stratégie simple pour concevoir des structures en treillis et ainsi améliorer les caractéristiques spécifiques sans toutefois augmenter le poids total d'une structure. Cette méthode a pour objectif de varier les densités relatives des cellules à travers la structure afin de régler la réponse mécanique des structure cellulaires. Des analyses numériques et expérimentales sont utilisées pour observer la réaction des structures cellulaires dans différent situation incluant la flexion, le flambage, la compression et la tension. De plus, des études expérimentales sont menées sur une variété d'échantillons. Selon les caractéristiques topologiques d'une structure cellulaire graduée, nous sélectionnons une technologie de fabrication additive appropriée et fabriquons les échantillons. Les méthodes numériques d'analyse des structures cellulaires sont basées sur deux approches différentes : la modélisation détaillée par éléments finis et la modélisation hybride homogénéisée. Dans la modélisation détaillée, nous importons les structures telles que conçues dans un logiciel FE commercial et définissons le paramètre d'analyse approprié pour évaluer leur réponse. Le modèle hybride est basé sur les techniques d'homogénéisation mécanique standard et les propriétés équivalentes. Bien qu'il soit moins précis, il est toutefois substantiellement plus rapide que la modélisation détaillée.

Les résultats de l’analyse de différentes structures révèlent des potentiels excitants dans leurs performances. En flexion, nous pouvons augmenter la rigidité en flexion environ trois fois par variation optimale de la densité relative à travers la structure. Une telle variation optimale avec une topologie 2D simple peut surpasser un faisceau cellulaire uniforme dont la rigidité des cellules est à la limite théorique (liaison Voigt). Aussi, nos résultats démontrent que nous pouvons même changer la direction de la déformation thermique par des variations spécifiques de densité relative. Dans l’analyse de flambement, nous dessinons initialement les rideaux de deux comportements de flambement différents dans les matériaux cellulaires et distinguons les flambements locaux et globaux. Ensuite, nous analysons l’effet de différentes variations de densité relative et démontrons qu’en changeant la variation, nous pouvons transformer le comportement de flambage d'une plaque cellulaire de flambage dans le plan au flambage hors du plan ou vice versa. Cette stratégie de gradation peut également améliorer considérablement les capacités d’absorption d’énergie d’une structure cellulaire en compression. Comme le démontrent les résultats, des gradients spécifiques peuvent augmenter la rigidité et l’absorption d’énergie d’une structure cellulaire, quelle que soit la topologie des cellules de base. Globalement, l’approche proposée promet une stratégie pour réduire le poids d’une structure cellulaire sans sacrifier les performances. Par conséquent, des structures cellulaires à gradation rationnelle peuvent remplacer les structures cellulaires uniformes dans de nombreuses applications telles que les panneaux sandwich et les amortisseurs. Les recherches futures peuvent révéler d’autres potentiels de ces structures, ce qui peut encore combler les lacunes des tableaux de sélection des matériaux.

Table of Contents

Acknowledgments

I would like to thank Prof. Hamid Akbarzadeh, my supervisor, for his supports, dedication, and insight during my Ph.D. He has been directly involved in all my research activities, and I greatly appreciate the time he spent reviewing my works and providing constructive comments on my reports.

I also thankful for the financial support I received from McGill Graduate Dean's Award, McGill Graduate Excellence Award, Schulich Graduate Fellowship, Fonds de recherche du Québec – Nature et technologies (FRQNT) Doctoral Award and Doctoral Internship Program. I am also grateful to Compute Canada and Calcul Québec for the access to the supercomputers Graham and Beluga.

I would like to express my gratitude to my past and present friends and peers at Advanced Multifunctional and Multiphysics Metamaterials Lab (AM^3L): Armin Mirabolghasemi, Hamidreza Yazdani Sarvestani, Alireza SeyedKanani, Jiahao Shi, Liang He, Shahin Eskandari, Ehsan Estakhrian, Mehdi Eynbeygui, Newsha Mazaheri, Hossein Mofatteh, Jun Cai, Youjian Li, Nicholas D'Ambrosio, and Minghan Xu.

Last but most importantly, I would like to appreciate two women without whom I would not be able to take a single step in my life: My mother, Zahra, for all the efforts she has been putting throughout my life, and the love of my life, Farnaz, for love, happiness, meaning, hope, courage, passion, emotion and enjoyment she has brought to my every moment.

Contribution to Original Knowledge

Chapters 2 to **7** present the main contributions of the current thesis. These contributions are summarized as follows:

Chapter 2:

- Employing homogenization for structural analysis of a cellular material
- Proposing the idea of multi-direction *Functionally Graded Cellular Materials* to tune the mechanical performance of cellular plates
- Presenting specific gradients that enable a significant increase in buckling load and flexural stiffness of graded cellular plates

Chapter 3:

- Distinguishing between local and global buckling in cellular plates
- Investigating the effect of parameters that can transform the buckling response of cellular plates, including, geometry, slenderness ratio, relative density, number of cells
- Presenting specific gradients that increase both local and global buckling load of cellular plates

Chapter 4:

- Employing homogenization for structural analysis of a cellular material subjected to thermal and mechanical loading
- Introducing the most efficient gradients in tuning the bending behavior of a graded cellular beam

- Presenting specific gradients that can change the direction of deformation of a beam subjected to thermal loading

Chapter 5:

- Evaluating the idea of the functionally graded cellular beam through systematic experimentation on 3D printed samples
- Utilizing an optimization method to find the most efficient gradient for increasing flexural stiffness of a cellular beam

Chapter 6:

- Evaluating the response of graded cellular materials in large deformation
- Presenting specific gradients that can enhance the stiffness and energy absorption of cellular structures at the same time
- Investigating the difference between stress-strain curves of different 3D cellular topologies in large deformation

Chapter 7:

- Proposing a design route which can substantially increase the stretchability of cellular structures
- Enabling elastomeric-level stretchability in brittle polymers without modifying their base materials

Contribution of Authors

This dissertation is organized as a Manuscript-based thesis, according to the McGill University guidelines. Six peer-reviewed scientific articles comprise this thesis in **Chapters 2** to **7** as follows:

- **Niknam, H.**, Akbarzadeh, A.H., Rodrigue, D., Therriault, D.; Architected Multi-Directional Functionally Graded Cellular Plates; *Materials & Design*, 148 (2018) 188-202
    - **Contributions**: HN programmed FE analysis for homogenization-based analysis, obtained the results, and wrote the paper. AHA planned the framework, provided supervision, and wrote and edited the paper. DR and DT provided advisory comments, and wrote and edited the paper.
- **Niknam, H.**, Akbarzadeh, A.H.; In-Plane and Out-of-Plane Buckling of Architected Cellular Plates: Numerical and Experimental Study; *Composite Structures*, 206 (2018) 739-749
    - **Contributions:** HN conducted detailed FE analysis and experimentation on molded elastomeric cellular samples, and wrote and edited the paper. AHA planned the framework, provided supervision, and wrote and edited the paper.
- **Niknam, H.**, Akbarzadeh, A.H.; Thermo-Mechanical Bending of Architected Functionally Graded Cellular Beams; *Composite Part B: Engineering*, 174 (2019) 107060
    - **Contributions:** HN wrote the code for the hybrid homogenized modelling, conducted detailed FE analysis, and wrote and edited the paper. AHA planned the framework, provided supervision, and wrote and edited the paper.
- **Niknam, H.**, Yazdani Sarvestani, H., Jakubinek M., B., Ashrafi, B., Akbarzadeh, A., H.; 3D Printed Accordion-like Materials: A Design Route to Achieve Ultrastretchability; *Additive Manufacturing*. 34 (2020) 101215

- **Contributions:** HN proposed the design, and fabricated part of samples by 3D printing, and wrote and edited the paper. HYS conducted FE analysis, analyzed data, and wrote and edited the paper. MBJ fabricated part of samples and wrote and edited the paper. BA provided supervision, and wrote and edited the paper. AHA conceived the research framework, provided supervision, and wrote and edited the paper.

- Seyedkanani, A., **Niknam, H.**, Akbarzadeh, A.H.; Bending Behavior of Optimally Graded 3D Printed Cellular Beams; *Additive Manufacturing*, 35 (2020) 101327
    - **Contributions:** AS wrote the program for optimization, 3D printed samples, and conducted the experiments, and wrote and edited the paper. HN wrote a code for hybrid-homogenized modeling, 3D printed samples, conducted experiments, and wrote and edited the paper. AHA planned the framework, provided supervision, and wrote and edited the paper. (This paper is co-first authored by AS and HN, and will appear only in the current thesis)
- **Niknam, H.**, Akbarzadeh; Graded Lattice Structures: Simultaneous Enhancement in Stiffness and Energy Absorption, (2020), (Submitted to journal)
    - **Contributions:** HN fabricated samples, conducted detailed FE analysis and experimental tests, and wrote and edited the paper. AHA planned the framework, provided supervision, and wrote and edited the paper.

1 Chapter One: Background and Introduction

Stone age, Copper age, Bronze age, and Iron age are the different stages of development through human history after the materials demonstrated their importance in human life. During the last century, material scientists proposed different materials with unprecedented properties. Among them, we can name composites [1], polymers [2], ceramics [3], carbon nanotubes[4], and superalloys [5]. Each of these materials has contributed to the advance of materials selection charts on different aspects, including, but not limited to, stiffness, flexibility, toughness, strength, stretchability, and thermal conductivity. This progression has enabled the design and fabrication of structures for novel applications in an extreme environment whether it is the celestial space [6], ultrahigh-temperature combustion chambers [7] or the human body [8]. Two principal strategies achieve these unique properties: manipulating the molecular structures at micro/nanoscale (e.g., semiconductors, biomaterials) [9] or special treatment of the base materials at macro-scale (e.g., heat treatment of metals and polymers) [10]. Both strategies are often expensive and demand individual facilities.

As an alternative to these costly methods of developing new materials to fill the gaps of material selection charts, “Cellular Materials” received more and more attention since the middle of the 1970s [11]. A Cellular Material is defined as “an interconnected network of solid struts or plates that form the edges and faces of cells” [11]. In other words, cellular materials are composites of solid and air and can be built by embedding voids or porosities in fully dense base materials. As a result, no matter what the base material is, different properties can be achieved when used as a cellular solid. **Figure 1-1** demonstrates how using base material along with the cellular design can

expand the material selection chart. We can make a metallic cellular solid whose conductivity and density are as low as polymers or a cellular polymer whose stiffness is the same as elastomers.

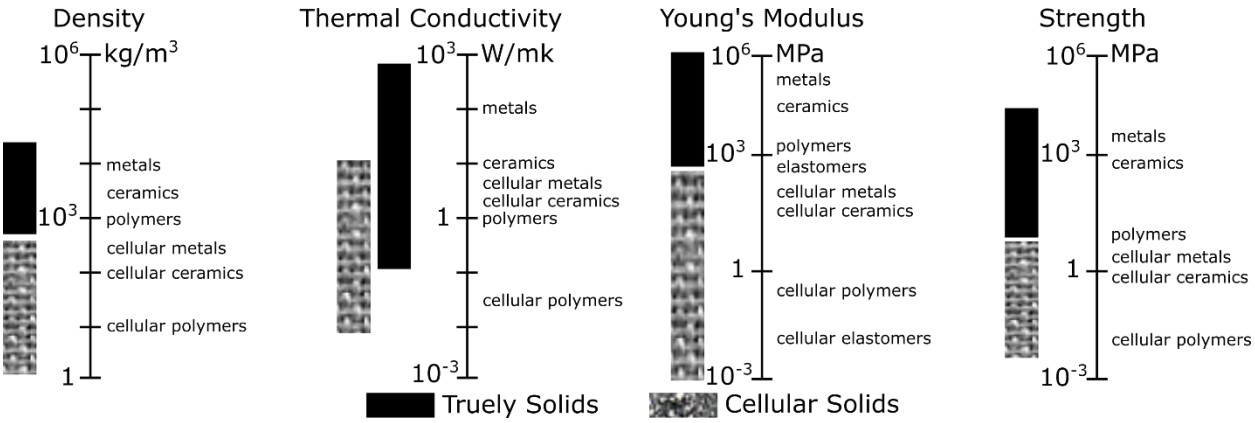

Figure 1-1- *Density, thermal conductivity, Young's modulus, and strength of cellular solids and truly solids [11].*

Cellular materials are divided into two main groups, based on the distribution pattern of porous unit cells, which are *foams* and *lattices.* Pores or voids are distributed stochastically in the *foams* without following a specific pattern, e.g., sponge and wood. Foams are often fabricated by injecting gas into a melted solid. If the gas forms discrete pockets that are surrounded by solids, the foam is known as *closed-cell* (**Fig. 1-2a**); if the gas pockets are connected, foam is named *open-cell* (**Fig. 1-2b**) [12]. On the contrary, the arrangement of voids in the *lattices*, e.g., hexagonal honeycombs and re-entrant cells showing auxetic behavior, follows a specific order, and cells are tessellated in a periodic pattern. While foams are always distributed in space, lattices can be two- or three-dimensional. In the former one, a two-dimensional (2D) geometry is extruded in one direction (**Fig. 1-2c**) while in the latter, a three-dimensional (3D) topology is patterned over the space (**Fig. 1-2d**).

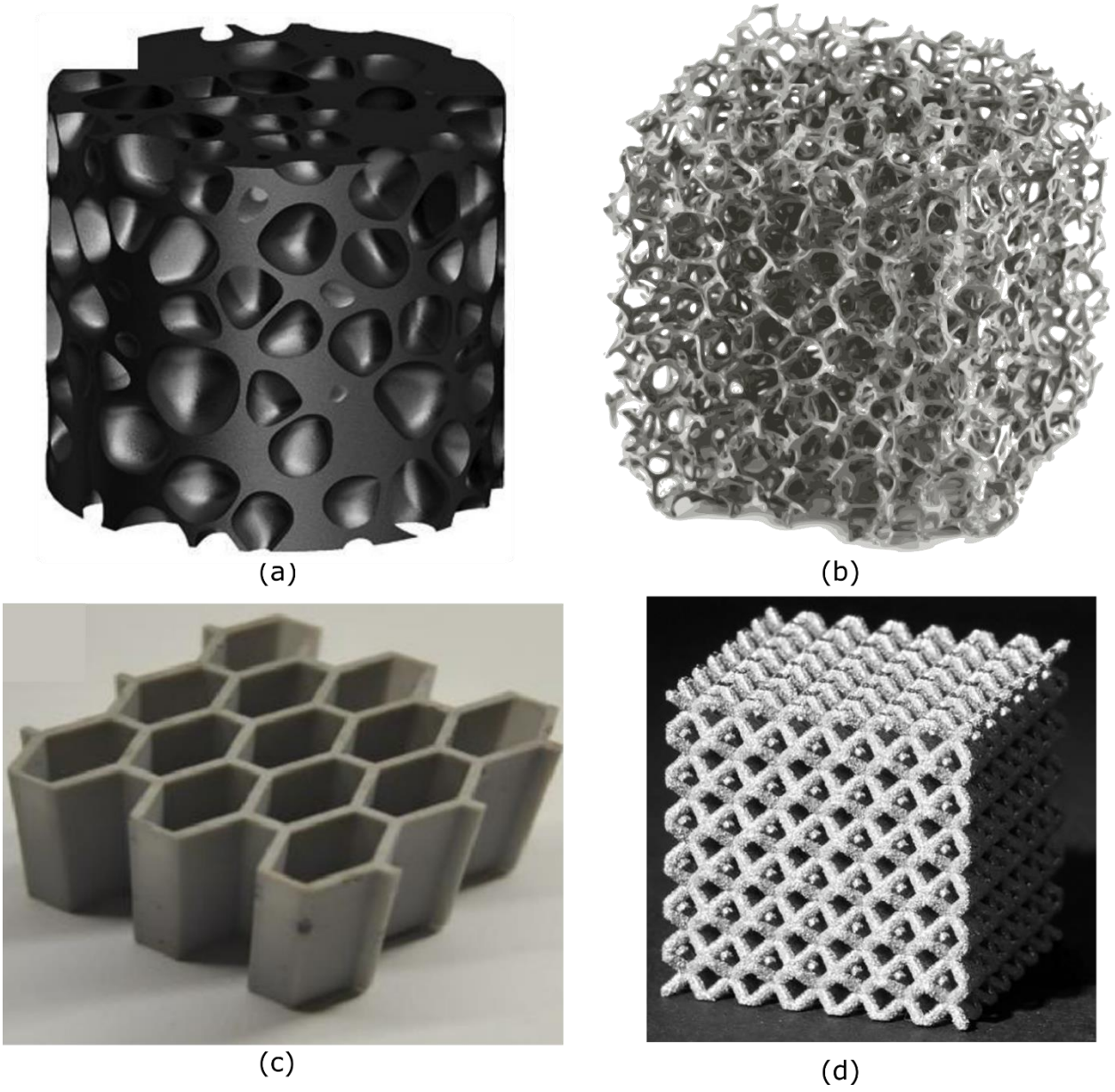

Figure 1-2- *Different types of cellular solids: (a) Closed-cell foam [13], (b) Open-cell foam [14], (c) 2D extruded lattice [15], and (d) 3D lattice [16].*

Three main factors that define the properties of cellular materials are *Base material*, *Relative Density*, and *Topology* [11].

Base material: The material that constitutes the solid sections of cellular material is its base material. Although we can achieve unique material properties with the concept of cellular materials, we are limited to definite bounds dictated by the base material.

Relative Density: The relative density of a cellular solid is defined as the ratio of the volume of the solid constituent to the total volume of cellular material. Relative density is the most important structural characteristic that defines cellular material properties. Relative density, the same as the base material, imposes an upper and lower bounds for different properties of cellular structures.

Topology: Difference in topology is what brings about the possibility of gaining controllable properties while the base material and the total weight remain unchanged. Topology can refer to either the geometrical features of a representative volume in lattices or the variation of geometry across a structure.

1.1 Applications of Cellular Materials

As discussed, cellular materials have made possible achieving extraordinary properties which cannot be found in any other group of materials; therefore, variety of industries have taken advantage of them including aeronautics [17], automotive [18], energy production [19], and construction industries [20]. These applications have been developed in the past few decades because cellular materials can extend the capability of conventional materials. Next, we will provide examples of how cellular materials can make differences in specific applications where *Thermal*, *Mechanical*, *Filtering*, and *Electro-magnetic* functionalities are required.

1.1.1 Mechanical

Including void in a solid can effectively reduce the weight of a structure while certain mechanical functionalities are not profoundly affected. Nature has taken advantage of this fact in different materials to reduce the weight while maintaining the biological materials strong and structurally durable; bone and wood are two examples of natural cellular material with a high load-carrying capacity. The most well-known mechanical elements that have exploited cellular material design are sandwich structures. Sandwich structures are three-layer structure with two thin skin-layer at each side and a low-density core in the middle [21]. The skin material usually has high stiffness, whereas the core typically has high compressive and shear strength. When these are bonded together, this combination gives the sandwich structure a high flexural modulus.

Another particular mechanical functionality of cellular structures is their high energy absorption capabilities. An intervening medium is required for protection against the overloading, which reduces the stress to a level below a damage threshold. Cellular materials are examples of such medium where the presence of void enables significant volume decrease at constant pressure [22]. As a result, cellular solids are being used in an application where energy must be dissipated or absorbed to avoid damage to human or more valuable products, for example, in car bumpers, elevator shock absorbers, and packaging industry.

1.1.2 Thermal

Polymeric, ceramic, and glass cellular materials are being employed as a thermal insulator for a wide variety of applications [11]. The thermal conductivity of polymer and glass is low, and it can be further reduced by the introduction of another low-conductivity phase that is air. Furthermore, the thermal mass of cellular materials (defined as the amount of refrigerant needed to cool down

the insulation itself) is significantly less than the solid constituent materials [11]. Therefore, lattice and foam have formed insulators that are used in every day and high-technology applications, such as disposable coffee cup, modern buildings [23], turbine insulation blanket [19] and refrigerated trucks [24].

1.1.3 Filtration

Foams and lattices can be used as filters at different levels. The obvious application of foams for filtration is in noise cancellation as in headphone cushions. However, they have also been used in more complicated structures. For example, cellular membranes are designed and fabricated for filtering fluids in refinery plants [25]. Porous ceramic solids enable high-quality metal casting; impurities will be filtered out by passing the melted metal through a cellular ceramic [26].

1.1.4 Electrical

Cellular materials are often not being utilized for their electrical properties, but their capabilities to attenuate electromagnetic waves come as a secondary functionality. For example, the low density of polymeric foams drastically reduces their dielectric loss factor, which is desirable for generators enclosures [27].

Different examples for applications of cellular solids are shown in **Fig. 1-3**.

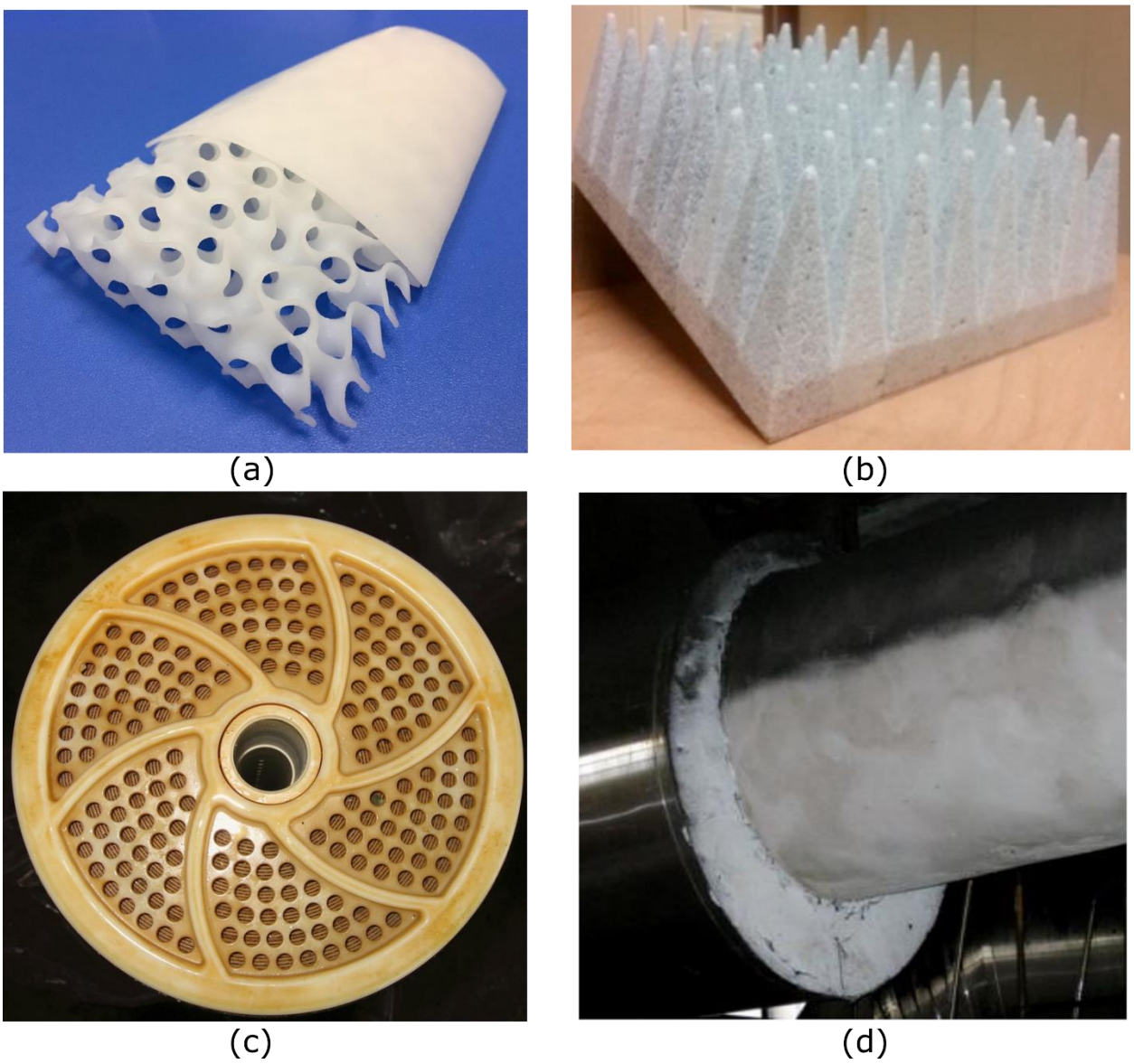

Figure 1-3 *- Cellular solids in different application: (a) Aircraft wing model made out of a sandwich structure with cellular core [28], (b) Composite structure for insulation against electromagnetic waves [29], (c) Cellular membrane for water filtration, and (d) Solid foam for the thermal insulation of piping [30].*

1.2 Fabrication methods of Cellular Solids

Although cellular materials have opened new avenues in design and expanded the functionality of lightweight structures, challenges related to manufacturing their complex microarchitectures have

curtailed the progress in research and application of these materials. These limitations hinder the production of complex geometries with variable shapes, and, as a result, experimental evaluation of different cellular solids have advanced at a slow pace. Appropriate manufacturing methods of cellular solids depend on the base material, geometry, and whether the cellular solid is foam or lattice. In this section, a brief overview of several most conventional fabrication methods of cellular solids is presented.

Powder metallurgy, *hollow spheres,* and *lotus-type* are the three major foam fabrication technologies [31]. *Powder metallurgy* is a relatively novel technology that was initially developed for fabricating aluminum foams [31]. In this method, metal powder is first combined with a foaming agent and then compacted under appropriate pressure. The mixture is then brought to the metal melting point and subjected to heat treatment to optimize the crystal structure. Pores will appear in the foams after consolidation [32]. In the *Hollow sphere* process, pre-manufactured hollow spheres are consolidated with an adhesive matrix and cast in a metal matrix. Unlike powder metallurgy, hollow sphere processes can be used to manufacture both open- and closed-cell foams [33]. The *lotus-type* method involves diffusing a gas, either hydrogen or hydrogen-helium mixture, into liquid metal. As the steel solidifies, the gas leaves the metal and create porosities within the body of solid [34].

Honeycomb, as the first-known lattice structure, has been traditionally fabricated with three different methods: *expansion*, *corrugation,* and *molding* [35]. In the *expansion* method, a sheet is cut into specified dimensions, and strips of adhesive are printed on it. The adhesive is applied in such a way that adhesive prints on adjacent sheets are shifted by half of the distance between adjacent points on the same sheet. After solidification and curing of the adhesive, the cut block is

sliced into the required thickness of the core, and then the block slice is expanded to form honeycombs [36]. In the *corrugation* method, the substrate comes in sheet form and passes through corrugated rollers to pre-form the core walls. The adhesive is applied to the surfaces, and the sheets are stacked. The stacks are then placed in an oven to cure the adhesive [37]. Finally, in the *molding* method, a rigid frame called a matrix or mold is built, and liquid material is cast into this mold. The cellular solids are fabricated by exposing it to prescribed environmental conditions. All these methods have been initially used for fabricating periodic metallic honeycombs.

New manufacturing technologies have been introduced in the last few decades, which have enabled the fabrication of cellular materials out of alternative base materials and arbitrary complex topologies [38]. A three-dimensional spatial periodic cellular structure can be made by press forming technology in which a sheet is perforated to create a pattern and then bending at the nodes [38]. Stiffer and harder metals such as Inconel were also used to fabricate lattice structures by metal wire approaches [39].

However, the most significant leap toward manufacturing three-dimensional complex topology cellular solids was the inception of additive manufacturing (AM) technology. Additive manufacturing, so-called 3D Printing, has facilitated the fabrication of engineered topologies that are not manufacturable with other processes [40-44]. Stereolithography (SLA) and Fused Deposition Molding (FDM), as the most conventional additive manufacturing technologies, have been employed in the fabrication of 2D and 3D cellular structures [45]. Direct laser writing was customized and used for fabricating 3D plate-lattices as a class of low-density materials with a near-optimal stiffness [46]. Metallic smooth-shell structures with complex gyroid and shell-like lattice architectures have been manufactured with selective laser melting (SLM), and the effect of

different AM parameters on their compressive behavior has already been investigated [41, 47, 48]. Examples of three-dimensional topologies manufactured with AM are presented in **Fig. 1-4**.

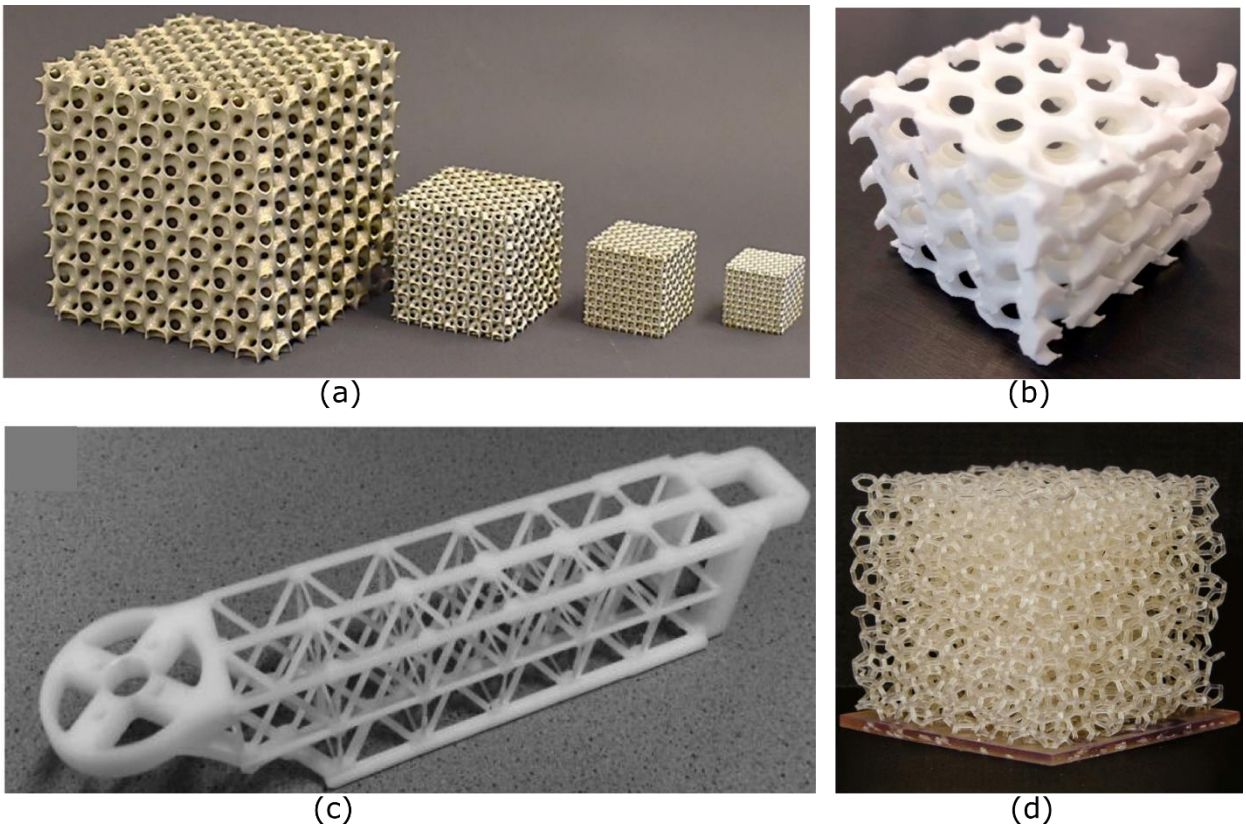

Figure 1-4 - *Cellular solids manufactured by different 3D printing technologies: (a) Selective Laser Melting (SLM) [48], (b) Selective Laser Sintering (SLS) [49], (c) Fused Deposition molding (FDM) [50], and (d) Stereolithography (SLA) [51].*

1.3 Modeling response of cellular solids

The objective of modeling cellular solids is predicting their response when subjected to specific loading or environmental conditions without conducting experimental tests. The endeavors to model the responses of cellular solids can be categorized into three groups: *analytical*, *numerical*,

and *homogenization* models. In this section, we will have a brief review of the pros and cons of these modeling approaches.

Analytical modeling: As discussed earlier, cell topology plays a significant role in the response of cellular structures. This fact has impeded the possibility of presenting an analytical model to predict the response of cellular solids for complex architectures. In the case of mechanical response, presenting the analytical model is limited to simple few geometries. For example, Gibson and Ashby [11] applied one-dimensional beam theories to predict the buckling load, yield stress, stiffness, and flexural rigidity of honeycomb structures. Similar formulations have also been presented for other 2D geometries, such as triangular, rectangular, and Kagome cells [52, 53]. However, all these models have limited applicability and cannot be generalized for complex three-dimensional architectures.

Numerical modeling: Finite element (FE) analysis has enabled to study the behavior of cellular solids with any geometry and subjected to different loadings. FE simulation has been utilized to analyze both two-dimensional [52, 54-56] and three-dimensional [42, 57-60] lattices as well as foams [61-63]. Different types of analyses, such as compaction [42, 56, 62, 64-67], tension [68-71], bending [72-74], and thermal conductivity [75-77] have been performed by commercial and non-commercial software. In most cases, experiments have verified the reliability of the results. Detailed software modeling is often an acceptable alternative to experiments; however, it is sometimes computationally expensive. In particular, if the number of cells constructing the cellular structure increases or if the topology is complex, the number of elements required for discretization for finite element modeling increases substantially. Subsequently, the analysis will be computationally cumbersome.

Homogenization modeling: Homogenization modeling involves replacing a representative volume element (RVE) of a cellular structure with an equivalent homogenous solid. In this method, we first utilize FE or other numerical techniques to evaluate the effective properties of the cellular solid and then will solve the equivalent simplified model with either analytical or numerical techniques [78-80]. This method drastically decreases the computational time of detailed numerical modeling of cellular materials and structures. It has been utilized for a variety of different analyses, including stiffness [81, 82], flexural rigidity [83-85], impact [86, 87] etc. The main drawback of the homogenization modeling is its incapability to capture local phenomena. Consequently, this modeling is often not applicable for analyses that involves large deformation or failure [81, 82]. Nevertheless, recent studies have proposed novel homogenization techniques that can capture plasticity [88] or nonlinear behaviors [89, 90].

1.4 Research objectives

In the current study, we introduce strategies to improve mechanical functionalities of cellular lattice structures by putting forward the idea of varying cell properties across the structure. Thus far, researchers have generally focused on architecting the geometry of cells for improving the cellular structure responses while the weight remains unchanged. However, an engineered design of cellular architecture in which cells with different properties are distributed rationally can also achieve a major enhancement in the mechanical performance of cellular structures.

The idea of varying architectural design parameters across the structure to improve the performance of mechanical elements have been exploited in different humanmade materials like *Composite Laminates* [91, 92] and *Functionally Graded Materials* (FGMs) [93-97] for a few decades. Nevertheless, a limited number of studies have explored a similar strategy to enhance the

mechanical [98-112] and thermal [113-120] functionalities of cellular solids. In the current research, we explore the effect of relative density variation in different cellular structures, including beams, plates, and blocks, and on different structural behaviors, including bending, buckling, free vibration, tension, and compression. We have employed both theoretical (beam and plate theory) and computational (homogenization and finite element analysis) methods to analyze the response of these cellular structures. We have also fabricated multiple specimens utilizing different AM technologies and conducted experiments on the samples to realize graded cellular structures and to validate our theoretical and computational predictions. A brief overview of the next chapters of this thesis is presented below to outline a comprehensive perspective of the conducted research.

Chapter 2 presents a homogenization-based study on multi-directional functionally graded cellular (FGC) plates. The buckling load, bending deformation, and natural frequency of various FG cellular plates are obtained based on Third-order Shear Deformation Theory (TSDT). It is shown that the mechanical behavior of FGC plates can be tuned by choosing appropriate variation functions to optimize their mechanical performance. The results are compared with FE detailed modeling in a few cases to ensure the accuracy of using homogenization for these non-periodic cellular structures. Different grading functions enable substantial improvement in the mechanical responses of FGC plates, e.g., a 56% increase in the flexural rigidity.

Chapter 3 focuses on the buckling of FGC plates through detailed FE modeling. As discussed earlier, the homogenization-based models are incapable of capturing local deformation in cellular solids; therefore, the results presented in **Chapter 2** are valid only if no local deformation occurs during the deformation. In the next step of this research, we move forward and consider the local

deformation by FE modeling and verify the results with experimental analyses. The results reveal that the relative density variation strategy works for improving both local and global buckling load of cellular plates.

In **Chapter 4**, we continue the investigation on graded cellular solids by studying the effect of thermal and mechanical loads on the flexural response of cellular beams. We employ homogenization-based TSDT and FE to model the thermo-mechanical response for different loading conditions. Results show that specific gradients along the length can even change the deformation mode of cellular beams.

Chapter 5 includes further studies in the behavior of graded cellular beam by conducting experimental tests. Bending tests performed on 3D printed samples confirm the detailed FE modeling results. We also conduct a TLBO optimization study to find the optimum distribution of cells across a cellular beam. We show that gradients across the thickness of a beam are more effective in improving the flexural rigidity compared to gradients along the length. Results also reveal that optimally graded cellular beams have the potential to outperform uniform cellular beams made of ideal unit cells (Voigt bound for elastic properties).

Chapter 6 presents the energy absorption capacity of graded cellular solids. Several graded samples with different geometries are additively manufactured with SLA 3D printers and experimentally tested under compression. We also utilize ANSYS AUODYN solver to obtain the same result computationally. The experimental and computational results reveal the possibility of increasing energy absorption, structural stiffness, and strength of cellular structures.

Chapter 7 includes a study on improving the stretchability of cellular solids through a novel design of their underlying microarchitecture. In this chapter, we propose an accordion-like design that can

increase the stretchability of brittle polymers up to twenty times. The numerical and experimental results suggest a brittle polymer can behave like flexible silicone elastomers by rational design of their underlying microarchitecture.

Finally, **Chapter 8** draws some general conclusions from this dissertation and proposes potential ideas for future studies.

1.5 References

[1] I.M. Daniel, O. Ishai, I.M. Daniel, I. Daniel, Engineering mechanics of composite materials, Oxford university press New York1994.

[2] R.F. Landel, L.E. Nielsen, Mechanical properties of polymers and composites, CRC press1993.

[3] C.B. Carter, M.G. Norton, Ceramic materials: science and engineering, Springer2007.

[4] A. Loiseau, P. Launois-Bernede, P. Petit, S. Roche, J.-P. Salvetat, Understanding Carbon Nanotubes: From Basics to Applications, Springer2006.

[5] R.C. Reed, The superalloys: fundamentals and applications, Cambridge university press2008.

[6] J. Meseguer, I. Pérez-Grande, A. Sanz-Andrés, Spacecraft thermal control, Elsevier2012.

[7] K. Upadhya, J.M. Yang, W. Hoffman, Advanced Materials for Ultrahigh Temperature Structural Applications Above 2000 Deg C, American Ceramic Society Bulletin 76(12) (1997) 51-56.

[8] L. Ricotti, A. Menciassi, Nanotechnology in biorobotics: opportunities and challenges, Nanoparticle Research 17(2) (2015) 84.

[9] S.I. Stupp, P.V. Braun, Molecular manipulation of microstructures: biomaterials, ceramics, and semiconductors, Science 277(5330) (1997) 1242-1248.

[10] A.A. Aly, Heat treatment of polymers: a review, International Journal of Materials Chemistry and Physics 1(2) (2015) 132-140.

[11] L.J. Gibson, M.F. Ashby, Cellular Solids: Structure and Properties, Cambridge University Press1999.

[12] N.A. Fleck, V.S. Deshpande, M.F. Ashby, Micro-architectured materials: past, present and future, Proceedings of the Royal Society A: Mathematical, Physical and Engineering Sciences 466(2121) (2010) 2495-2516.

[13] M. Dabo, T. Roland, G. Dalongeville, C. Gauthier, P. Kékicheff, Ad-hoc modeling of closed-cell foam microstructures for structure-properties relationships, European Journal of Mechanics - A/Solids 75 (2019) 128-141.

[14] M. Borovinšek, M. Vesenjak, J. Matela, Z. Ren, Computational reconstruction of scanned aluminum foams for virtual testing, Serbian Society of Computational Mechanics 2 (2008) 16-28.

[15] J.J. Andrew, J. Ubaid, F. Hafeez, A. Schiffer, S. Kumar, Impact performance enhancement of honeycombs through additive manufacturing-enabled geometrical tailoring, International Journal of Impact Engineering 134 (2019) 103360.

[16] T. Tancogne-Dejean, D. Mohr, Stiffness and specific energy absorption of additively-manufactured metallic BCC metamaterials composed of tapered beams, International Journal of Mechanical Sciences 141 (2018) 101-116.

[17] V. Vasiliev, A. Razin, Anisogrid composite lattice structures for spacecraft and aircraft applications, Composite Structures 76(1-2) (2006) 182-189.

[18] D.-H. Kim, H.-G. Kim, H.-S. Kim, Design optimization and manufacture of hybrid glass/carbon fiber reinforced composite bumper beam for automobile vehicle, Composite Structures 131 (2015) 742-752.

[19] N.P. Padture, M. Gell, E.H. Jordan, Thermal barrier coatings for gas-turbine engine applications, Science 296(5566) (2002) 280-284.

[20] A.V. Tsantilis, T.C. Triantafillou, Innovative seismic isolation of masonry infills using cellular materials at the interface with the surrounding RC frames, Engineering Structures 155 (2018) 279-297.

[21] J.R. Vinson, Sandwich structures: past, present, and future, Sandwich structures 7: advancing with sandwich structures and materials, Springer2005, pp. 3-12.

[22] A.G. Evans, M. He, V.S. Deshpande, J.W. Hutchinson, A.J. Jacobsen, W.B. Carter, Concepts for enhanced energy absorption using hollow micro-lattices, International Journal of Impact Engineering 37(9) (2010) 947-959.

[23] Z. Zhang, J.L. Provis, A. Reid, H. Wang, Mechanical, thermal insulation, thermal resistance and acoustic absorption properties of geopolymer foam concrete, Cement and Concrete Composites 62 (2015) 97-105.

[24] M. Ahmed, O. Meade, M.A. Medina, Reducing heat transfer across the insulated walls of refrigerated truck trailers by the application of phase change materials, Energy Conversion and Management 51(3) (2010) 383-392.

[25] M. Urgun-Demirtas, P.L. Benda, P.S. Gillenwater, M.C. Negri, H. Xiong, S.W. Snyder, Achieving very low mercury levels in refinery wastewater by membrane filtration, Journal of Hazardous Materials 215-216 (2012) 98-107.

[26] K. Araki, J.W.J.J.o.t.A.C.S. Halloran, Porous ceramic bodies with interconnected pore channels by a novel freeze casting technique, 88(5) (2005) 1108-1114.

[27] R. Kuku, N. Raji, T. Bello, Development and performance evaluation of sound proof enclosure for portable generators, Research Journal of Applied Sciences 4 (2012) 2600-2603.

[28] J. Feng, J. Fu, C. Shang, Z. Lin, B. Li, Sandwich panel design and performance optimization based on triply periodic minimal surfaces, Computer-Aided Design 115 (2019) 307-322.

[29] L. Pometcu, C. Méjean, R. Benzerga, A. Sharaiha, P. Pouliguen, C.L. Paven, On the choice of the dielectric characterization method for foam composite absorber material, Materials Research Bulletin 96 (2017) 107-114.

[30] S. Xu, L. Chen, M. Gong, X. Hu, X. Zhang, Z. Zhou, Characterization and engineering application of a novel ceramic composite insulation material, Composites Part B: Engineering 111 (2017) 143-147.

[31] B.H. Smith, S. Szyniszewski, J.F. Hajjar, B.W. Schafer, S.R. Arwade, Steel foam for structures: A review of applications, manufacturing and material properties, Journal of Constructional Steel Research 71 (2012) 1-10.

[32] C. Park, S.J.M.S. Nutt, E. A, PM synthesis and properties of steel foams, 288(1) (2000) 111-118.

[33] O. Friedl, C. Motz, H. Peterlik, S. Puchegger, N. Reger, R.J.M. Pippan, M.T. B, Experimental investigation of mechanical properties of metallic hollow sphere structures, 39(1) (2008) 135-146.

[34] T. Ikeda, H. Nakajima, T.J.M. Aoki, M.T. A, Fabrication of lotus-type porous stainless steel by continuous zone melting technique and mechanical property, 36(1) (2005) 77-86.

[35] T. Bitzer, Honeycomb core, in: T. Bitzer (Ed.), Honeycomb Technology: Materials, Design, Manufacturing, Applications and Testing, Springer Netherlands, Dordrecht, 1997, pp. 10-42.

[36] S.V. Rupani, G. Acharya, S.S. Jani, Design, Modelling and Manufacturing aspects of Honeycomb Sandwich Structures: A Review, (2017).

[37] M.M. Gauthier, Engineered materials handbook, ASM International1995.

[38] H.J.C.M. Wadley, M.F. Technology, Cellular metals and metal foaming technology, (2001) 381-386.

[39] H.N.G. Wadley, N.A. Fleck, A.G. Evans, Fabrication and structural performance of periodic cellular metal sandwich structures, Composites Science and Technology 63(16) (2003) 2331-2343.

[40] F. Mezzadri, V. Bouriakov, X. Qian, Topology optimization of self-supporting support structures for additive manufacturing, Additive Manufacturing 21 (2018) 666-682.

[41] I. Maskery, N.T. Aboulkhair, A.O. Aremu, C.J. Tuck, I.A. Ashcroft, Compressive failure modes and energy absorption in additively manufactured double gyroid lattices, Additive Manufacturing 16 (2017) 24-29.

[42] L. Zhang, S. Feih, S. Daynes, S. Chang, M.Y. Wang, J. Wei, W.F. Lu, Energy absorption characteristics of metallic triply periodic minimal surface sheet structures under compressive loading, Additive Manufacturing 23 (2018) 505-515.

[43] H. Yazdani Sarvestani, A.H. Akbarzadeh, A. Mirbolghasemi, K. Hermenean, 3D printed meta-sandwich structures: Failure mechanism, energy absorption and multi-hit capability, Materials & Design 160 (2018) 179-193.

[44] A. Gross, P. Pantidis, K. Bertoldi, S. Gerasimidis, Correlation between topology and elastic properties of imperfect truss-lattice materials, Journal of the Mechanics and Physics of Solids 124 (2019) 577-598.

[45] T.D. Ngo, A. Kashani, G. Imbalzano, K.T.Q. Nguyen, D. Hui, Additive manufacturing (3D printing): A review of materials, methods, applications and challenges, Composites Part B: Engineering 143 (2018) 172-196.

[46] T. Tancogne-Dejean, M. Diamantopoulou, M.B. Gorji, C. Bonatti, D. Mohr, 3D Plate-Lattices: An Emerging Class of Low-Density Metamaterial Exhibiting Optimal Isotropic Stiffness, Advanced Materials 30(45) (2018) 1803334.

[47] C. Bonatti, D. Mohr, Smooth-shell metamaterials of cubic symmetry: Anisotropic elasticity, yield strength and specific energy absorption, Acta Materialia 164 (2019) 301-321.

[48] C. Bonatti, D. Mohr, Mechanical performance of additively-manufactured anisotropic and isotropic smooth shell-lattice materials: Simulations & experiments, Journal of the Mechanics and Physics of Solids 122 (2019) 1-26.

[49] I. Maskery, L. Sturm, A.O. Aremu, A. Panesar, C.B. Williams, C.J. Tuck, R.D. Wildman, I.A. Ashcroft, R.J.M. Hague, Insights into the mechanical properties of several triply periodic minimal surface lattice structures made by polymer additive manufacturing, Polymer 152 (2018) 62-71.

[50] Y. Tang, G. Dong, Q. Zhou, Y.F. Zhao, Lattice Structure Design and Optimization With Additive Manufacturing Constraints, IEEE Transactions on Automation Science and Engineering 15(4) (2018) 1546-1562.

[51] S. Bi, E. Chen, S. Gaitanaros, Additive manufacturing and characterization of brittle foams, Mechanics of Materials 145 (2020) 103368.

[52] X. Zhang, H. Zhang, Theoretical and numerical investigation on the crush resistance of rhombic and kagome honeycombs, Composite Structures 96 (2013) 143-152.

[53] R.S. Kumar, D.L. McDowell, Generalized continuum modeling of 2-D periodic cellular solids, International Journal of Solids and Structures 41(26) (2004) 7399-7422.

[54] K.P. Dharmasena, H.N.G. Wadley, Z. Xue, J.W. Hutchinson, Mechanical response of metallic honeycomb sandwich panel structures to high-intensity dynamic loading, International Journal of Impact Engineering 35(9) (2008) 1063-1074.

[55] D. Ruan, G. Lu, B. Wang, T.X. Yu, In-plane dynamic crushing of honeycombs—a finite element study, International Journal of Impact Engineering 28(2) (2003) 161-182.

[56] X.M. Qiu, J. Zhang, T.X. Yu, Collapse of periodic planar lattices under uniaxial compression, part II: Dynamic crushing based on finite element simulation, International Journal of Impact Engineering 36(10) (2009) 1231-1241.

[57] M. Smith, Z. Guan, W.J. Cantwell, Finite element modelling of the compressive response of lattice structures manufactured using the selective laser melting technique, International Journal of Mechanical Sciences 67 (2013) 28-41.

[58] H.E. Burton, N.M. Eisenstein, B.M. Lawless, P. Jamshidi, M.A. Segarra, O. Addison, D.E.T. Shepherd, M.M. Attallah, L.M. Grover, S.C. Cox, The design of additively manufactured lattices to increase the functionality of medical implants, Materials Science and Engineering: C 94 (2019) 901-908.

[59] D.-W. Lee, K.A. Khan, R.K. Abu Al-Rub, Stiffness and yield strength of architectured foams based on the Schwarz Primitive triply periodic minimal surface, International Journal of Plasticity 95 (2017) 1-20.

[60] V.S. Deshpande, N.A. Fleck, M.F. Ashby, Effective properties of the octet-truss lattice material, Journal of the Mechanics and Physics of Solids 49(8) (2001) 1747-1769.

[61] R. Jhaver, H. Tippur, Processing, compression response and finite element modeling of syntactic foam based interpenetrating phase composite (IPC), Materials Science and Engineering: A 499(1) (2009) 507-517.

[62] N.J. Mills, R. Stämpfli, F. Marone, P.A. Brühwiler, Finite element micromechanics model of impact compression of closed-cell polymer foams, International Journal of Solids and Structures 46(3) (2009) 677-697.

[63] S. Youssef, E. Maire, R. Gaertner, Finite element modelling of the actual structure of cellular materials determined by X-ray tomography, Acta Materialia 53(3) (2005) 719-730.

[64] L. Aktay, A.F. Johnson, B.-H. Kröplin, Numerical modelling of honeycomb core crush behaviour, Engineering Fracture Mechanics 75(9) (2008) 2616-2630.

[65] D. Xiao, Z. Dong, Y. Li, W. Wu, D. Fang, Compression behavior of the graded metallic auxetic reentrant honeycomb: Experiment and finite element analysis, Materials Science and Engineering: A 758 (2019) 163-171.

[66] K. Bertoldi, P.M. Reis, S. Willshaw, T. Mullin, Negative Poisson's Ratio Behavior Induced by an Elastic Instability, Advanced Materials 22(3) (2010) 361-366.

[67] S. Babaee, J. Shim, J.C. Weaver, E.R. Chen, N. Patel, K. Bertoldi, 3D Soft Metamaterials with Negative Poisson's Ratio, Advanced Materials 25(36) (2013) 5044-5049.

[68] J. Zhang, G. Lu, D. Ruan, Z. Wang, Tensile behavior of an auxetic structure: Analytical modeling and finite element analysis, International Journal of Mechanical Sciences 136 (2018) 143-154.

[69] M.R. Hassan, F. Scarpa, N.A. Mohamed, In-plane Tensile Behavior of Shape Memory Alloy Honeycombs with Positive and Negative Poisson's Ratio, Journal of Intelligent Material Systems and Structures 20(8) (2009) 897-905.

[70] A. Rafsanjani, A. Akbarzadeh, D. Pasini, Snapping Mechanical Metamaterials under Tension, Advanced Materials 27(39) (2015) 5931-5935.

[71] H. Mae, M. Omiya, K. Kishimoto, Effects of strain rate and density on tensile behavior of polypropylene syntactic foam with polymer microballoons, Materials Science and Engineering: A 477(1) (2008) 168-178.

[72] H. Takabatake, N. Yanagisawa, T. Kawano, A simplified analysis of rectangular cellular plates, International Journal of Solids and Structures 33(14) (1996) 2055-2074.

[73] G. Sun, X. Huo, D. Chen, Q. Li, Experimental and numerical study on honeycomb sandwich panels under bending and in-panel compression, Materials & Design 133 (2017) 154-168.

[74] J. Xiong, L. Ma, A. Stocchi, J. Yang, L. Wu, S. Pan, Bending response of carbon fiber composite sandwich beams with three dimensional honeycomb cores, Composite Structures 108 (2014) 234-242.

[75] C.Y. Zhao, Review on thermal transport in high porosity cellular metal foams with open cells, International Journal of Heat and Mass Transfer 55(13) (2012) 3618-3632.

[76] P. Innocenti, F. Scarpa, Thermal conductivity properties and heat transfer analysis of Multi-re-entrant auxetic honeycomb structures, Journal of Composite Materials 43(21) (2009) 2419-2439.

[77] R.S. Kumar, D.L. McDowell, Rapid Preliminary Design of Rectangular Linear Cellular Alloys for Maximum Heat Transfer, AIAA Journal 42(8) (2004) 1652-1661.

[78] B. Hassani, E. Hinton, A review of homogenization and topology optimization I—homogenization theory for media with periodic structure, Computers & Structures 69(6) (1998) 707-717.

[79] B. Hassani, E. Hinton, A review of homogenization and topology opimization II—analytical and numerical solution of homogenization equations, Computers & Structures 69(6) (1998) 719-738.

[80] B. Hassani, E. Hinton, A review of homogenization and topology optimization III—topology optimization using optimality criteria, Computers & Structures 69(6) (1998) 739-756.

[81] S. Arabnejad, D. Pasini, Mechanical properties of lattice materials via asymptotic homogenization and comparison with alternative homogenization methods, International Journal of Mechanical Sciences 77 (2013) 249-262.

[82] S.J. Hollister, D.P. Fyhrie, K.J. Jepsen, S.A. Goldstein, Application of homogenization theory to the study of trabecular bone mechanics, Journal of Biomechanics 24(9) (1991) 825-839.

[83] G. Dai, W. Zhang, Cell size effects for vibration analysis and design of sandwich beams, Acta Mechanica Sinica 25(3) (2009) 353-365.

[84] N. Buannic, P. Cartraud, Higher-order effective modeling of periodic heterogeneous beams. I. Asymptotic expansion method, International Journal of Solids and Structures 38(40) (2001) 7139-7161.

[85] G.M. Dai, W.H. Zhang, Size effects of basic cell in static analysis of sandwich beams, International Journal of Solids and Structures 45(9) (2008) 2512-2533.

[86] C. Wang, K.R. Ramakrishnan, K. Shankar, E. Morozov, H. Wang, A. Fien, Homogenized shell element-based modeling of low-velocity impact response of stainless-steel wire mesh, Mechanics of Advanced Materials and Structures (2020) 1-16.

[87] J.M. Hundley, E.C. Clough, A.J. Jacobsen, The low velocity impact response of sandwich panels with lattice core reinforcement, International Journal of Impact Engineering 84 (2015) 64-77.

[88] S. Nemat-Nasser, Experimentally-based Micromechanical Modeling of Metal Plasticity with Homogenization from Micro-to Macro-scale Properties, in: O.T. Bruhns, E. Stein (Eds.) IUTAM Symposium on Micro- and Macrostructural Aspects of Thermoplasticity, Springer Netherlands, Dordrecht, 2002, pp. 101-113.

[89] K. El Nady, F. Dos Reis, J.F. Ganghoffer, Computation of the homogenized nonlinear elastic response of 2D and 3D auxetic structures based on micropolar continuum models, Composite Structures 170 (2017) 271-290.

[90] F. Dell'Isola, I. Giorgio, M. Pawlikowski, N.L. Rizzi, Large deformations of planar extensible beams and pantographic lattices: heuristic homogenization, experimental and numerical examples of equilibrium, Proceedings of the Royal Society A: Mathematical, Physical and Engineering Sciences 472(2185) (2016) 20150790.

[91] A.S. Sayyad, Y.M. Ghugal, Bending, buckling and free vibration of laminated composite and sandwich beams: A critical review of literature, Composite Structures 171 (2017) 486-504.

[92] K. Draiche, A.A. Bousahla, A. Tounsi, A.S. Alwabli, A. Tounsi, S. Mahmoud, Static analysis of laminated reinforced composite plates using a simple first-order shear deformation theory, Computers and Concrete 24(4) (2019) 369-378.

[93] G.N. Praveen, J.N. Reddy, Nonlinear transient thermoelastic analysis of functionally graded ceramic-metal plates, International Journal of Solids and Structures 35(33) (1998) 4457-4476.

[94] R.C. Batra, Higher-order shear and normal deformable theory for functionally graded incompressible linear elastic plates, Thin-Walled Structures 45(12) (2007) 974-982.

[95] D.K. Jha, T. Kant, R.K. Singh, A critical review of recent research on functionally graded plates, Composite Structures 96 (2013) 833-849.

[96] J. Reddy, Z.-Q. Cheng, Three-dimensional thermomechanical deformations of functionally graded rectangular plates, European Journal of Mechanics-A/Solids 20(5) (2001) 841-855.

[97] B. Karami, M. Janghorban, A. Tounsi, Galerkin's approach for buckling analysis of functionally graded anisotropic nanoplates/different boundary conditions, Engineering with Computers 35(4) (2019) 1297-1316.

[98] T.C. Lim, Functionally graded beam for attaining Poisson-curving, Journal of Materials Science Letters 21(24) (2002) 1899-1901.

[99] S.-J. Lee, J. Wang, B.V. Sankar, A micromechanical model for predicting the fracture toughness of functionally graded foams, International Journal of Solids and Structures 44(11) (2007) 4053-4067.

[100] A. Ajdari, P. Canavan, H. Nayeb-Hashemi, G. Warner, Mechanical properties of functionally graded 2-D cellular structures: A finite element simulation, Materials Science and Engineering: A 499(1) (2009) 434-439.

[101] A. Ajdari, H. Nayeb-Hashemi, A. Vaziri, Dynamic crushing and energy absorption of regular, irregular and functionally graded cellular structures, International Journal of Solids and Structures 48(3) (2011) 506-516.

[102] L. Cui, S. Kiernan, M.D. Gilchrist, Designing the energy absorption capacity of functionally graded foam materials, Materials Science and Engineering: A 507(1) (2009) 215-225.

[103] D. Chen, J. Yang, S. Kitipornchai, Elastic buckling and static bending of shear deformable functionally graded porous beam, Composite Structures 133 (2015) 54-61.

[104] C. Lira, F. Scarpa, Transverse shear stiffness of thickness gradient honeycombs, Composites Science and Technology 70(6) (2010) 930-936.

[105] Y. Hou, Y.H. Tai, C. Lira, F. Scarpa, J.R. Yates, B. Gu, The bending and failure of sandwich structures with auxetic gradient cellular cores, Composites Part A: Applied Science and Manufacturing 49 (2013) 119-131.

[106] L. Boldrin, S. Hummel, F. Scarpa, D. Di Maio, C. Lira, M. Ruzzene, C.D.L. Remillat, T.C. Lim, R. Rajasekaran, S. Patsias, Dynamic behaviour of auxetic gradient composite hexagonal honeycombs, Composite Structures 149 (2016) 114-124.

[107] S. Arabnejad Khanoki, D. Pasini, Multiscale Design and Multiobjective Optimization of Orthopedic Hip Implants with Functionally Graded Cellular Material, Journal of Biomechanical Engineering 134(3) (2012) 031004-031004-10.

[108] C. Lira, F. Scarpa, R. Rajasekaran, A Gradient Cellular Core for Aeroengine Fan Blades Based on Auxetic Configurations, Journal of Intelligent Material Systems and Structures 22(9) (2011) 907-917.

[109] L. Francesconi, A. Baldi, X. Liang, F. Aymerich, M. Taylor, Variable Poisson's ratio materials for globally stable static and dynamic compression resistance, Extreme Mechanics Letters 26 (2019) 1-7.

[110] J. Zhang, Z. Wang, L. Zhao, Dynamic response of functionally graded cellular materials based on the Voronoi model, Composites Part B: Engineering 85 (2016) 176-187.

[111] A. Panesar, M. Abdi, D. Hickman, I. Ashcroft, Strategies for functionally graded lattice structures derived using topology optimisation for Additive Manufacturing, Additive Manufacturing 19 (2018) 81-94.

[112] F. Xu, X. Zhang, H. Zhang, A review on functionally graded structures and materials for energy absorption, Engineering Structures 171 (2018) 309-325.

[113] G. Park, S. Kang, H. Lee, W. Choi, Tunable multifunctional thermal metamaterials: Manipulation of local heat flux via assembly of unit-cell thermal shifters, Scientific Reports 7(January) (2017) 1-15.

[114] T. Yang, K.P. Vemuri, P.R. Bandaru, Experimental evidence for the bending of heat flux in a thermal metamaterial, Applied Physics Letters 105(8) (2014) 103-106.

[115] F. Chen, D.Y. Lei, Experimental realization of extreme heat flux concentration with easy-to-make thermal metamaterials, Scientific reports 5 (2015) 11552.

[116] G. Park, S. Kang, H. Lee, W. Choi, Tunable Multifunctional Thermal Metamaterials: Manipulation of Local Heat Flux via Assembly of Unit-Cell Thermal Shifters, Scientific Reports 7 (2017) 41000.

[117] G. Xu, H. Zhang, M. Xie, Y. Jin, Geometrical effects on the concentrated behavior of heat flux in metamaterials thermal harvesting devices, AIP Advances 7(10) (2017) 105322.

[118] Y. Wang, L. Zhang, S. Daynes, H. Zhang, S. Feih, M.Y. Wang, Design of graded lattice structure with optimized mesostructures for additive manufacturing, Materials & Design 142 (2018) 114-123.

[119] A. Takezawa, X. Zhang, M. Kato, M. Kitamura, Method to optimize an additively-manufactured functionally-graded lattice structure for effective liquid cooling, Additive Manufacturing 28 (2019) 285-298.

[120] R.H. Tarkhanyan, D.G. Niarchos, Reduction in lattice thermal conductivity of porous materials due to inhomogeneous porosity, International Journal of Thermal Sciences 67 (2013) 107-112.

2 Chapter Two: Architected Multi-Directional Functionally Graded Cellular Plates[1]

2.1 Preface

The earliest study in this research focuses on the response of Functionally Graded Cellular (FGC) plates from three aspects of structural responses, including bending, free vibration, and buckling. In this initial research, we evaluate several basic concepts that form the foundation of our subsequent studies. First, we ensure the capabilities of homogenization techniques in handling the structural response of graded cellular structures. Second, we examine various two-dimensional topologies so that we can narrow down to the most efficient ones for the next investigations. Third, we consider a general power-law function and different variations of relative density and cell architecture, and, in the end, we find out the most effective gradient function.

[1] Reproduced with permission from Niknam, H., Akbarzadeh, A.H., Rodrigue, D., Therriault, D.; Architected Multi-Directional Functionally Graded Cellular Plates; *Materials & Design*, 148 (2018) 188-202.

2.2 Abstract

Inspired by bamboo, the concept of architected multi-directional functionally graded cellular materials (FGCMs) is introduced. These architected porous materials are made by assembling porous unit cells of dissimilar densities and cell topologies. The mechanical properties of functionally graded cellular (FGC) plates are analyzed to indicate the potential of multi-directional FGCMs for improving the performance of lightweight structural elements. Standard mechanics homogenization is used to predict the mechanical properties of cells with arbitrary superellipse voids. The homogenized effective properties, along with the finite element method and shear deformation theory are exploited to predict the mechanical responses of FGC plates. Numerical results reveal substantial improvement in structural responses when FGCMs are appropriately used; e.g., 56% improvement in bending stiffness is found in an FGC rectangular plate compared to a cellular plate with the same weight and with uniform distribution of constitutive cells. Numerical results show that cell variation through the thickness of FGC plates is more effective on the structural responses than variations through the length or width. Finally, multi-objective optimization is implemented to show the maximum improvement achievable via architecture variations within FGC structures.

2.3 Introduction

Since the 1960s, several investigations revealed that cellular materials may exhibit outstanding properties and can be used as an alternative to fully dense solids [1, 2]. These materials are mainly classified into two groups as foams and lattices based on pore's periodicity. Unlike foams, in which the pores of dissimilar topologies are distributed stochastically, lattices are periodically designed by tessellating porous cells. Architected cellular solids gain their extraordinary multifunctional

properties, mainly from their underlying architecture [3]. Architecting the pore shape in lattices enables engineers to design lightweight materials with unprecedented mechanical properties, e.g., high energy absorption capability [4], high stiffness to density ratio [5, 6], and controllability of their elastic wave propagation and vibration insulation characteristics [7, 8]. These specific characteristics of cellular materials can be used in many applications, from lightweight sandwich panels [9-12] and thermal shields [13] to porous biomaterials and implants [14, 15].

Several investigations have been performed to study the mechanical behavior of cellular materials. The majority of these early investigations on the mechanical properties of advanced porous materials were summarized by Gibson and Ashby in their textbook on "Cellular Solids, Structures, and Properties" [1]. Application of cellular materials as mechanical elements was first introduced in the design of structural sandwich panels in 1969, where periodic honeycomb sheets were used as the core of sandwich panels [16]. Afterward, several attempts have been made to understand the structural characteristics of honeycombs with a hexagonal cellular core. For instance, a constitutive elastic model was developed to predict the elastic properties of honeycombs [17, 18] and different structural analyses, from flexural bending to impact tests, were performed on these sandwich panels with periodic cellular cores [19, 20]. It was shown that negative Poisson's ratio could be obtained by modifying the geometrical features of the constitutive honeycombs as the core of sandwich panels [2, 21]. The studies above, along with several other investigations [22-26], have strived to better understand the deformation mechanism of architected lattices and their potential engineering applications.

In all the studies mentioned above, the characteristic properties of the representative cell, i.e., relative density and void (pore) topology, were uniform across the lightweight structure. However,

recent technical developments in advanced manufacturing techniques, like additive manufacturing [27] and powder metallurgy [28], opened exciting new opportunities to design and manufacture graded cellular structures. Nature is the first engineer who designed graded solids and porous materials. Three examples of graded materials in nature are bamboos, the beak of the Humboldt squid, and dentin-enamel junction (**Fig. 2-1**). For example, the microstructure of bamboos presents a functionally graded distribution of fibers in the longitudinal and radial directions leading to an exceptional combination of strength- and the stiffness-to-weight ratio [29]. The beak of the Humboldt squid *Dosidicus Gigas* also presents one of the hardest and stiffest completely organic materials [30]. The hydrated beak exhibits a large stiffness gradient of two orders of magnitudes, from the tip to the base of the beak. The dentin-enamel junction of the tooth also represents a functionally graded zone where the enamel and dentin close to the interface show a graded microstructure to reduce the stress concentration [31, 32]. Inspired by these natural and biological materials, architected functionally graded cellular materials (FGCMs) were introduced via the concept of bio-inspiration, so the cell architecture is made to vary continuously in arbitrary directions. Cellular structures in which the cells' relative density and topology vary across the lightweight structures with a pre-defined distribution function are called "Functionally Graded Cellular (FGC)" structures. Despite enormous potentials of FGCMs for optimizing lightweight advanced structures, these novel materials and structures are yet to be fully explored in terms of multiscale modeling and fabrication.

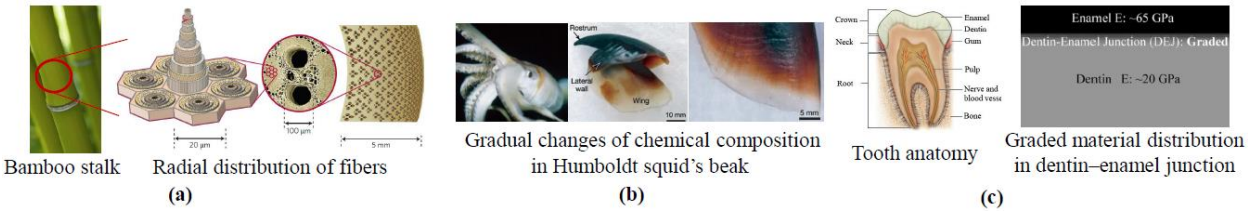

Figure 2-1- *Examples of functionally graded materials in nature: (a) Moso culm bamboo [29, 33], (b) Humboldt squid's beak [30] and (c) Dentin-enamel junction of tooth [31, 32].*

Nevertheless, a few studies are available in the literature implementing the idea of graded cellular properties in the structural, mechanical design. One of the earliest research in the field of FGC structures was performed to apply the idea of the graded honeycomb structure to obtain a Poisson-curving structure. This structure experiences a significant change in its thickness as a result of a prescribed curvature [34]. Afterward, a finite element based micromechanical model was proposed to predict the fracture toughness of FGC foams [35]. Through several other studies, it was reported that FGCMs can improve the mechanical response of cellular structures. For instance, it was revealed that the density gradient could enhance the yield strength and elastic modulus of cellular FGC structures [36] and the dynamic crushing energy absorption capacity of functionally graded foams could be improved compared to conventional foams [37, 38]. More recently, it was found that a symmetric distribution of relative density can lead to higher buckling capacity and improved bending resistance [39]. Other studies revealed that the variation of honeycomb's wall thickness across a cellular structure might lead to an increase in the transverse shear stiffness [40]. Later on, the effect of other honeycomb's geometrical parameters on the bending, failure, and dynamic behavior of lightweight honeycomb structures [41, 42] was explored to further improve the mechanical behavior of FGC structures by tuning the density and aspect ratio gradient. Moreover,

FGC structures were shown to be suitable for practical applications such as orthopedic hip implants [15] and cores of aero-engine fan blades [43].

It is worth mentioning that topology optimization has also been implemented recently to find the optimized shape for mechanical elements [44]. Gradient-based topology optimization techniques, such as solid isotropic material with penalization (SIMP) [45], evolutionary structural optimization (ESO) [46], and level set [47], have been used to find the optimized distribution of porosity within the design elements [48]. Multiscale approaches have also been proposed to optimize the void geometry of cells as well as cell distribution across the structure. In other words, multiscale topology optimization approaches try to couple macroscale and microscale topology optimization without a significant increase in computational cost [49, 50]. However, the topology optimization is computationally expensive. It does not provide a clear insight into the effect of directional property variation and cell topology architecture on the structural response of cellular media. As a result, we aim at developing an efficient methodology for the optimized design of structural members made of multi-directional FGCMs. We will utilize the higher-order structural theories along with homogenization technique and multi-objective optimization.

To the best of author's knowledge, no study in the literature has reported the effect of multi-directional variation of cell relative density and pore (void) topology across a lightweight cellular plate. From a structural perspective, most of the papers in the field of graded cellular materials focus on a single functionality of graded cellular materials, e.g., transverse shear stiffness of one-dimensional graded honeycomb [40], dynamic impact of one-dimensional graded Voronoi foams [51], and dynamic crushing of one-directional graded honeycombs [37]. The current study aims at providing a computationally efficient methodology for designing optimized lightweight cellular

structures by introducing the concept of "*multidirectional functionally graded cellular materials*." Therefore, a higher-order structural theory and standard mechanics homogenization are employed to develop a computational framework for optimizing the overall structural performance of advanced cellular structures. In specific, this paper makes an effort to provide a clear understanding of the effect of density and cell architecture variations in different directions on the structural response of thin to moderately-thick cellular plates. This understanding can guide and train topology optimization algorithms to reduce their computational cost for achieving the optimum topology and relative density distribution within advanced cellular-based metamaterials. The cell topology is modeled by a superellipse function [52], and the effective properties are obtained by standard mechanics homogenization [53] (**Section 2.4**). A generalized power-law function is proposed to model the variation of cell characteristics in multiple directions (**Section 2**.4). The governing equations for the structural analysis of FGC plates are obtained by using Reddy's third-order shear deformation theory [54] and discretized and solved by a finite element model (FEM) (**Section 2.5**). The results are compared and validated with a commercial finite element software analysis (**Section 2.7.1**).

Furthermore, the advantages of FGC structures over regular cellular structures are illustrated through various examples, and the effect of different distribution functions are investigated. It is shown that the variation of cell properties across the thickness of the FGC structure has a more dominant effect on tuning the structural responses than the other directions (**Sections 2.7.2** and **2.7.3**). Finally, a multi-objective optimization algorithm is implemented to obtain the maximum mechanical performance of FGC plates by tailoring the distribution function parameters of graded cellular materials.

2.4 Modeling of Functionally Graded Cellular Plates

2.4.1 Formulation of Cell Geometry

In this research, an FGC plate with a length L_{tot}, width W_{tot}, and thickness T_{tot} is considered in the xy-plane, as shown in **Fig. 2-2**. The plate consists of N_x cells in the x-direction, N_y cells in the y-direction and N_z cells in the z-direction, where (x, y, z) refer to the global Cartesian coordinate system shown in **Fig. 2-2**. The cell size in three directions can be calculated as:

$$L_{cell} = \frac{L_{tot}}{N_x}, W_{cell} = \frac{W_{tot}}{N_y}, T_{cell} = \frac{T_{tot}}{N_z} \tag{2.1}$$

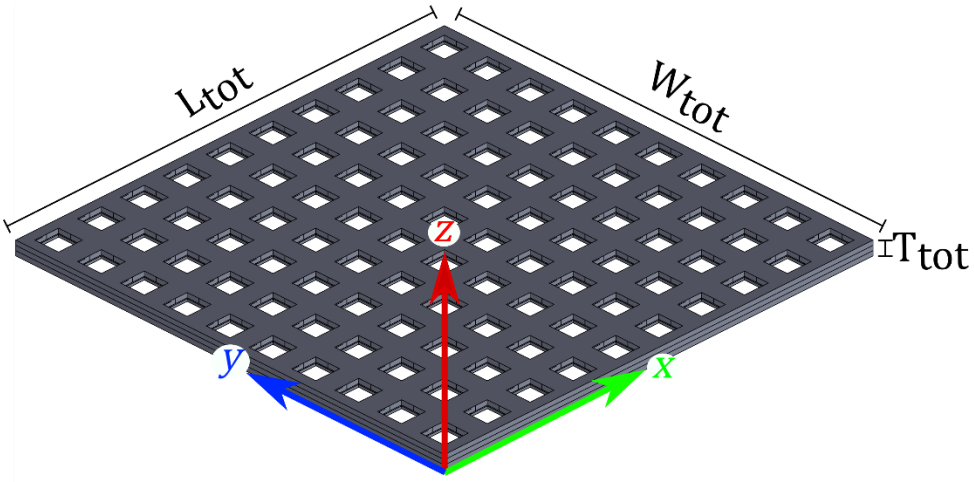

Figure 2-2- Schematic view of a homogenous cellular plate.

The properties of cellular materials depend on their relative density and void topology. Here, we focus on extruded two-dimensional (2D) square cells, in which the void topology of each cell is introduced according to the superellipse function as [52]:

$$\begin{bmatrix}\tilde{x}\\ \tilde{y}\end{bmatrix} = \begin{bmatrix}r_x \cos^n \emptyset\\ r_y \sin^n \emptyset\end{bmatrix} R(\theta) \tag{2.2}$$

where $0 \leq \emptyset \leq 2\pi$, $\tilde{x}$ and $\tilde{y}$ are the local coordinate system selected to identify the void topology of each cell. The coordinate is positioned in the middle of each cell. Three parameters (r_x, r_y, n) have been introduced to control and optimize the void size and topology. Equation (2.2) reduces to a cell with a circular void of radius r_0 for the case of $n = 1$ and $r_x = r_y = r_0$. Moreover, $R(\theta) = \begin{bmatrix}\cos\theta & -\sin\theta\\ \sin\theta & \cos\theta\end{bmatrix}$ is the rotation matrix to enable rotating the void within each cell. A systematic study is performed by considering four independent parameters: shape parameter (n), aspect ratio ($A.R. = \frac{r_y}{r_x}$), relative density (ρ_{rel}), and orientation angle (θ). Consequently, r_x and r_y are calculated based on the value of these four parameters, and by implementing a numerical integration method as explained in the **Appendix 2.A**. In this study, the four independent geometrical parameters are assumed to vary in the following ranges: $0.01 \leq n \leq 3$, $1 \leq A.R. \leq 3$, $0.01 \leq \rho_{rel} \leq 1$, and $0 \leq \theta \leq \pi$. **Figures 2-3a** and **2-3b** present the effects of n, $A.R.$, and θ on the void topology of periodic cellular materials or cellular-based metamaterials. In **Fig. 2-3,** "Geometrically Inadmissible" indicates the void topologies that intersect the boundaries of the unit cell.

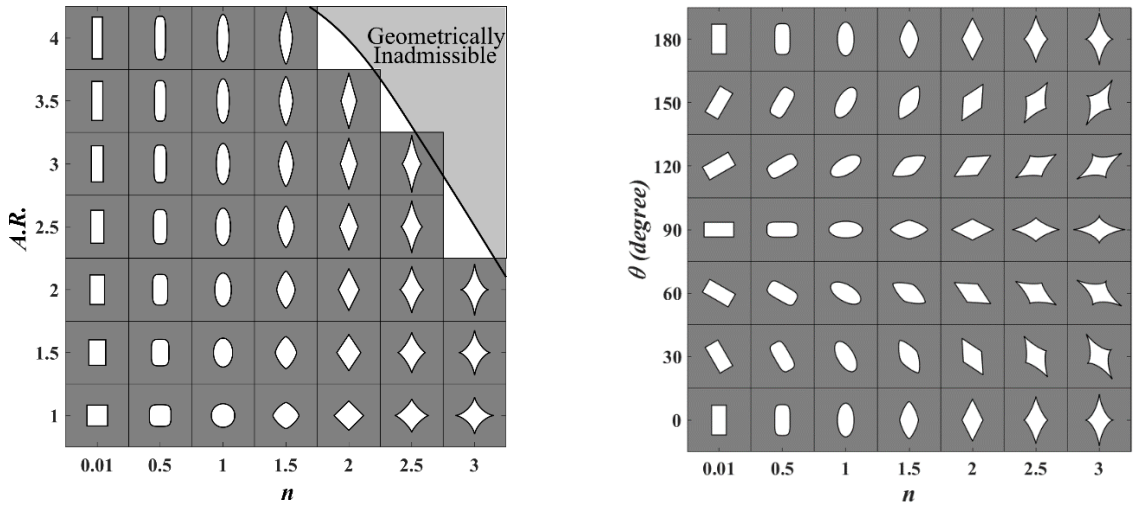

Figure 2-3- *Achievable topologies by the superellipse function for different shape parameters (n) for $\rho_{rel} = 0.9$: (a) Different aspect ratio ($A.R.$), while $\theta = 0$ and (b) Different void orientation (θ), while $A.R. = 2$.*

2.4.2 Formulation of Cell Topology Variation in FGCMs

The properties of conventional functionally graded materials (FGMs) are commonly considered to vary in one specific spatial direction via power-law [54], exponential [55], or sigmoidal functions [56]. Although these functions can produce various distribution contours, they are limited to monotonic functions. This means properties are monotonically changing from one end of a structure to another end without any extreme value. However, the property variation in FGCMs is not inherently monotonic. Therefore, a more general power-law function is here introduced to represent different property distribution throughout the length, width, and thickness of the material as:

$$P(\bar{x},\bar{y},\bar{z}) = P_1 + (P_0 - P_1)\left(1 - \frac{\bar{x}}{\bar{x}_{0P}}\right)^{mx_P}\left(1 - \frac{\bar{y}}{\bar{y}_{0P}}\right)^{my_P}\left(1 - \frac{\bar{z}}{\bar{z}_{0P}}\right)^{mz_P} \tag{2.3}$$

where P represents any of the four void topology parameters (n, $A.R.$, ρ_{rel}, and θ), P_0 is its value at the origin ($x = 0, y = 0,\ z = 0$) and P_1 is its extreme value at $x = \bar{x}_{0P}$, $y = \bar{y}_{0P}$ and $z = \bar{z}_{0P}$. In all cases, an overbar indicates dimensionless coordinates defined as:

$$\bar{x} = \frac{x}{L_{tot}}, \bar{y} = \frac{y}{W_{tot}}, \bar{z} = \frac{z}{T_{tot}} \tag{2.4}$$

Moreover, mx_P, my_P and mz_P are even integers indicating the distribution profile function. If any of mx_P, my_P or mz_P equals zero, the property in the x, y, and z direction gets a constant value, respectively; i.e., a homogenous distribution of cellular materials in the respective direction. If $P_0 = P_1$, the property has a constant value P_0 all over the domain. **Figure 2-4** shows possible distributions obtained by using Eq. (2.3) considering that the assumed variation of variable P is in a two-dimensional (2D) region. To better visualize the concept of FGCMs, four different types of one-dimensional FGCMs have been 3D printed and presented in **Appendix 2.B**, and each sample represents the variation of one of n, $A.R.$, ρ_{rel} or θ.

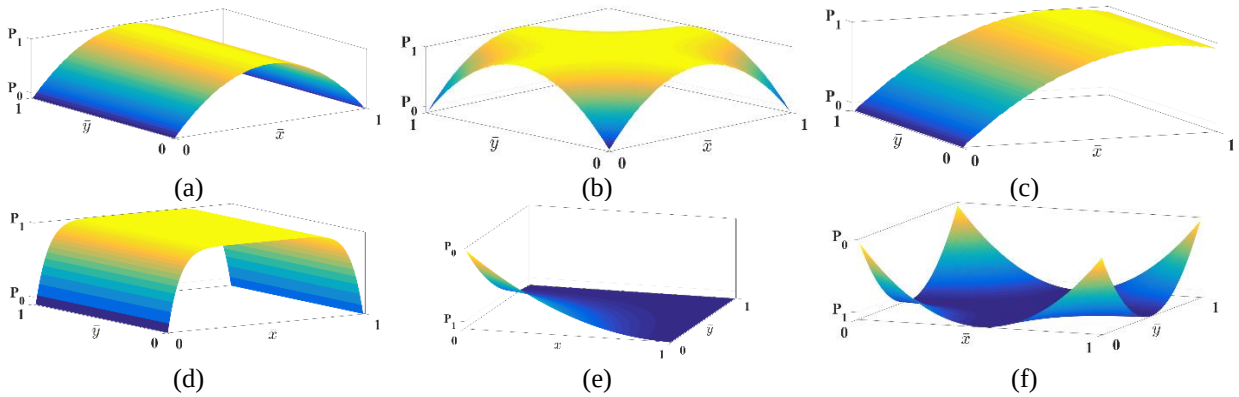

Figure 2-4- *Examples of 2D property distribution obtained by the general power-law function (Eq. 2.3): (a)* $P_1 > P_0,\ \bar{x}_0 = 0.5, mx_P = 2, my_P = 0$*; b)* $P_1 > P_0,\ \bar{x}_0 = \bar{y}_0 = 0.5, mx_P = my_P = 2$*; c)* $P_1 > P_0, \bar{x}_0 = 0.8, mx_P = 2, my_P = 0$*; d)* $P_1 > P_0, \bar{x}_0 = 0.5, mx_P = 8, my_P = 0$*; e)* $P_1 < P_0,\ \bar{x}_0 = \bar{y}_0 = 1, mx_P = my_P = 2$*; f)* $P_1 < P_0,\ \bar{x}_0 = \bar{y}_0 = 0.5, mx_P = my_P = 2$.

2.4.3 Formulation of Functionally Graded Cellular Plate

To investigate the structural responses of FGC plates, a detailed FEM can be developed. However, such an analysis is cumbersome and computationally expensive. A homogenization technique is implemented to reduce the computational cost required for analyzing FGC structures with different configurations. These effective properties, obtained by the homogenization, are implemented in the third-order shear deformation theory to perform different structural analysis on an FGC plate.

2.4.3.1 Standard Mechanics Homogenization

Standard mechanics has been widely used to obtain the effective mechanical properties of different types of anisotropic materials, including advanced composites and cellular solids. It was shown that homogenization is a reliable approach for the analysis of periodic cellular materials with a large number of repeated unit cells [53].

Based on the standard mechanics homogenization and considering the classical elasticity theory, periodic boundary conditions are applied to each unit cell to obtain the effective stiffness tensor which can be expressed as [53]:

$$\hat{C}_{ijkl} = \frac{1}{V_{RVE}} \int C_{ijmn} M^{C}_{mnkl} dV \tag{2.5}$$

where C_{ijmn} $(i, j, k, l, m, n = 1,2,3)$ is the stiffness tensor, V_{RVE} represents the volume of each unit cell (representative volume element) and M^{C}_{mnkl} is the local structural tensor defined as:

$$\varepsilon_{ij} = M^{C}_{mnkl} \hat{\varepsilon}_{ij} \tag{2.6}$$

where ε_{ij} is the strain tensor and circumflex accent identifies the effective properties for $\hat{C}_{ijkl}$ or an average field for $\hat{\varepsilon}_{ij}$. In the current study, the 3D components of the local stiffness tensor are evaluated by using Eq. (2.6) and by applying six independent 3D unit strains to a cube of unit dimensions through the commercial finite element software ANSYS version 17.1, in which the 3D unit cell is meshed by using 20-node 3D SOLID185 elements.

In this study, the effective elastic properties of all superellipse formulated cells are obtained by the standard mechanics homogenization approach. The material property chart, or so-called Ashby chart [1], is an effective method of presenting an overview of the properties of solid materials lying in a specific characteristic range. As a result, **Fig. 2-5** presents the Ashby chart for well-known solid materials along with 2D cellular materials with superellipsoidal void topologies. **Figure 2-5** shows that the range of Young's modulus for cellular materials can be extended to regions that cannot be achieved by fully dense solid materials.

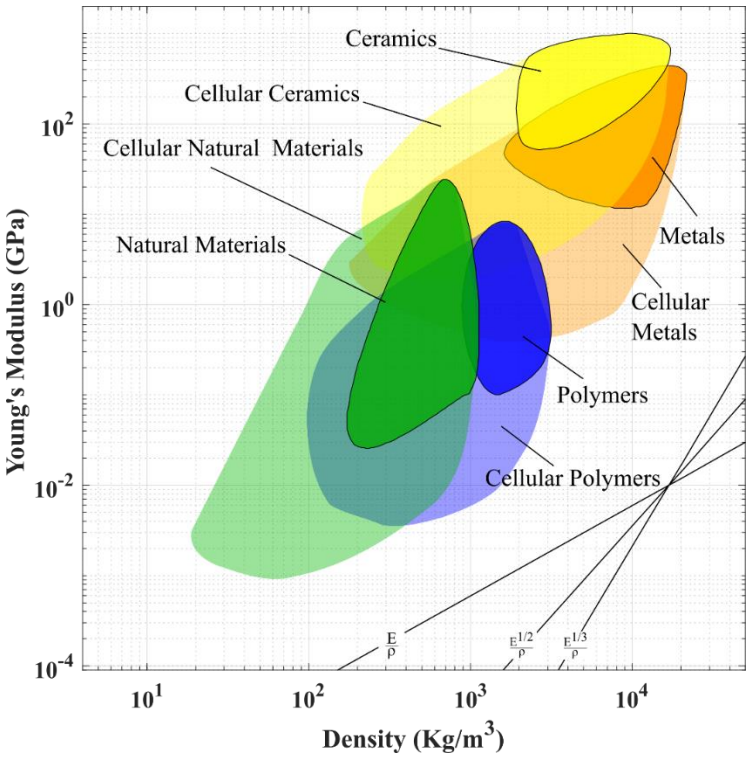

Figure 2-5- *Ashby chart for cellular materials whose void is modeled based on the superellipse function.*

2.5 Third-Order Shear Deformation Theory

To develop a methodology that can be implemented for thin and relativity-thick cellular plates, Reddy's third-order shear deformation theory (TSDT) [54] was used. According to TSDT, the transverse shear stresses are presented as a quadratic function through the plate thickness. Therefore, unlike the first-order shear deformation theory (FSDT), it is not necessary to introduce any shear correction factor in the formulation.

Based on the abovementioned assumptions and by applying Hamilton's approach, the governing equation for the present problem, in which the cell topology and subsequent elastic properties are varying in multiple directions, will be obtained as [54]:

$$N_{xx,x} + N_{xy,y} = I_0\ddot{u}_0 + J_1\ddot{\varphi}_x - c_1 I_3 \ddot{w}_{0,x} \tag{2.7a}$$

$$N_{yy,y} + N_{xy,x} = I_0\ddot{v}_0 + J_1\ddot{\varphi}_y - c_1 I_3 \ddot{w}_{0,y} \tag{2.7b}$$

$$c_1 P_{xx,xx} + 2c_1 P_{xy,xy} + c_1 P_{yy,yy} + Q_{x,x} + Q_{y,y} - 3c_1\left(R_{x,x} + R_{y,y}\right) + q = c_1\left(I_3\ddot{u}_0 + J_4\ddot{\varphi}_x - c_1 I_6 \ddot{w}_{0,x}\right)_{,x} + c_1\left(I_3\ddot{v}_0 + J_4\ddot{\varphi}_y - c_1 I_6 \ddot{w}_{0,y}\right)_{,y} + I_0\ddot{w}_0 \tag{2.7c}$$

$$M_{xx,x} + M_{xy,y} - c_1\left(P_{xx,x} + P_{xy,y}\right) - Q_x + 3c_1 R_x = J_1\ddot{u}_0 + J_2\ddot{\varphi}_x - c_1 J_4\left(\ddot{\varphi}_x + \ddot{w}_{0,x}\right) \tag{2.7d}$$

$$M_{yy,y} + M_{xy,x} - c_1\left(P_{yy,y} + P_{xy,x}\right) - Q_y + 3c_1 R_y = J_1\ddot{v}_0 + J_2\ddot{\varphi}_y - c_1 J_4\left(\ddot{\varphi}_y + \ddot{w}_{0,y}\right) \tag{2.7e}$$

where comma represents partial differentiation with respect to x or y, dots denote differentiation with respect to time and u_0, v_0, w_0, φ_x and φ_y are the displacements and rotations of the transverse normal on the plane $z = 0$. Moreover, $c_1 = \frac{4}{3T_{tot}^2}$, q is the transverse mechanical load; $N_{\alpha\beta}$, $M_{\alpha\beta}$, $P_{\alpha\beta}$, $Q_{\alpha\beta}$ and $R_{\alpha\beta}$ are stress resultants and I_i and J_i are moments of inertia, which are defined in **Appendix 2.C**. The boundary conditions of the plate are specified by the letter symbols; for example, *CSSF* denotes a plate with a Clamped edge (C) at $\bar{x} = 0$, Simply Supported edges (S) at $\bar{y} = 0$ and $\bar{x} = 1$ and free edge (F) at $\bar{y} = 1$, as shown in **Fig. 2-6**.

2.6 Solution Procedure

In this study, the finite element method is used to solve the governing differential equations (Eq. 2.7) for predicting the structural performance of multi-directional FGC plates. The generalized displacements are approximated over an element by the following expressions [54]:

$$u_0(x,y,t) = \sum_{i=1}^{m} U_i^e(t)\psi_i^e(x,y) \tag{2.8a}$$

$$v_0(x,y,t) = \sum_{i=1}^{m} V_i^e(t)\psi_i^e(x,y) \tag{2.8b}$$

$$w_0(x,y,t) = \sum_{i=1}^{m} \overline{\Delta}_{k_i}^e(t)\eta_i^e(x,y) \tag{2.8c}$$

$$\varphi_x(x,y,t) = \sum_{i=1}^{m} (t)\psi_i^e(x,y) \tag{2.8d}$$

$$\varphi_y(x,y,t) = \sum_{i=1}^{m} \emptyset_{y_i}^{\ e}(t)\psi_i^e(x,y) \tag{2.8e}$$

where ψ_i^e and η_i^e are the Lagrangian and Hermitian interpolation functions, respectively; U_i^e, V_i^e, $\overline{\Delta}_{k_i}^e$, $\emptyset_{x_i}^{\ e}$ and $\emptyset_{y_i}^{\ e}$ are the nodal degrees of freedom associated with their generalized displacement degrees of freedom. The rectangular conforming element is chosen for this study. As a result, four nodal values associated with w_0:

$$\overline{\Delta}_{1_i}^e = w_0, \quad \overline{\Delta}_{2_i}^e = w_{0,x}, \quad \overline{\Delta}_{3_i}^e = w_{0,y}, \quad \overline{\Delta}_{4_i}^e = w_{0,xy} \tag{2.9a-d}$$

The substitution of equation (2.8a to 2.8e) into the weak form of the governing differential equations, derived by using the equations (2.7), leads to the following finite element model for each element [57]:

$$[K]\{\Delta\} + [M]\{\ddot{\Delta}\} + [G]\{\Delta\} = \{\mathrm{F}\} \tag{2.10}$$

where $[K]$, $[M]$ and $[G]$ are 32×32 stiffness, inertia, and stability matrices of each element respectively, while $\{\Delta\}$ and $\{\mathrm{F}\}$ are the displacement and force vectors, respectively. More details about the elements of each matrix can be found in [54]. The overall structural responses of the architected FGC plates are predicted by assembling the finite element matrices of all elements of the plate and then applying the loading and boundary conditions. The loading vector $\{F\}$ has a non-zero value only in bending analysis, when a transverse uniform distributed load (q) is applied to the top of the plate. As shown in **Fig. 2-6**, nodal degrees of freedom at the edges are set to zero to apply the boundary conditions.

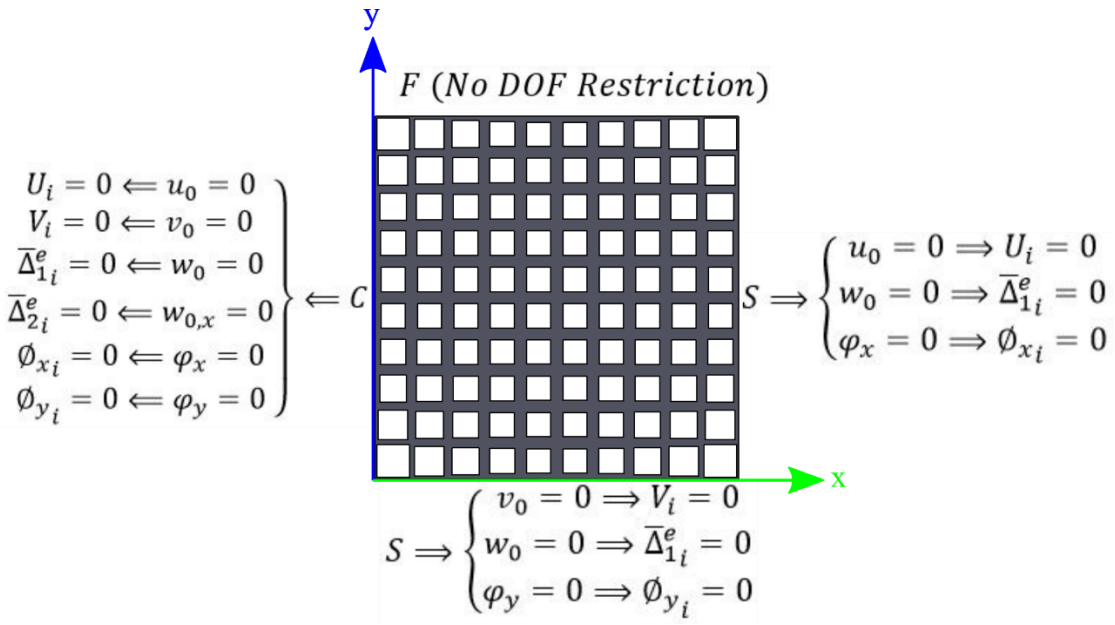

***Figure 2-6**- Schematic view of boundary conditions in a CSSF cellular plate.*

It is also worth mentioning that as the elastic properties of each cell are considered to be varying in all x, y, z-directions, the constitutive parameters $A_{ij}, B_{ij}, D_{ij}, E_{ij}, F_{ij}, H_{ij}, I_i$ and J_i (defined in

Appendix 2.C) are all functions of x and y spatial coordinates. Therefore, when the finite element model is applied to solve the problem for FGC plates, the homogenized elastic properties of each element (representing a cell) must be set in accordance with the position of that element. The main limitation of this approach is the failure of the standard mechanics homogenization technique in taking the effect of large deformation and nonlinearity into account. Therefore, the results for buckling analysis in this paper must be approached carefully as it may not be accurate in cases where local buckling is the dominant buckling mode.

2.7 Results and Discussion

In this section, the numerical results are presented in four categories. The representative optimized FGC plates are 3D printed to verify their manufacturability. The base material used in the results section is polylactic acid (PLA), a typical filament for FDM 3D printing, whose Young's modulus and Poisson's ratio are $E_s = 3.5\,GPa$ and $v_s = 0.36$, respectively [58]. The non-dimensional parameters used for presenting the responses of FGC plates are defined as:

Non-dimensional maximum deflection: $\overline{W}_{max} = 100\, W_{max} \frac{E_s W_{tot}^3}{F L_{tot}^2}$ (2.11a)

Non-dimensional natural frequency: $\overline{\Omega} = \Omega \frac{L_{tot}^2}{W_{tot}} \sqrt{\frac{\rho_s}{E_s}}$ (2.11b)

Non-dimensional buckling load: $\overline{N}_{cr}^{xx} = \frac{10^4 \hat{N}_{xx} \lambda L_{tot}^2}{E W_{tot}^3}$ (2.11c)

where F is the resultant of the uniform transverse load ($F = qA_{solid}$ and A_{solid} is the area of the top plane to which the transverse load is applied), while W_{max}, Ω and $\widehat{N}_{xx}$ are the maximum deflection of the plate, natural frequency, and in-plane compressive load, respectively. Moreover,

the size of each constituent unit cell is considered to be the same. Therefore, the total relative density of the cellular plate can be written as:

$$\rho_{rel,plate} = \frac{\sum_{i=1}^{N} \rho_{rel,i}}{N} \tag{2.12}$$

where $\rho_{rel,i}$ is the relative density of i^{th} cell and N is the total number of cells in a cellular plate.

2.7.1 Model Validation

A comparison study is presented to verify the proposed methodology for the structural analysis of FGC plates. In **Table 2-1**, the results for static bending (deflection) and natural vibration (first five natural frequencies) analyses using the homogenized properties are compared with the results of detailed 3D elasticity solutions obtained by ANSYS version 17.2. In ANSYS modeling, the Solid185 element is used, and mesh sensitivity analysis is performed. In **Table 2-1**, it can be seen that for Case I, in which the void geometry is all square, the results of the present work and ANSYS are in an excellent agreement, and the maximum deviation is less than 1%. For the other two samples (Case II and III), the maximum discrepancy between both results is less than 10%, which is acceptable in most engineering applications. The differences can potentially come from the fact that the stiffness tensor obtained for each cell from the homogenization technique is an approximation of the cell's stiffness in a structure. Therefore, these comparison studies confirm the reliability of the standard mechanics homogenization technique along with the TSDT finite element formulation used for analyzing the mechanical behavior of FGC plates.

Table 2-1- *Comparison between the results (natural frequency and out-of-plane deflection) obtained by ANSYS finite element modeling and the present methodology for the analysis of FGC plates.*

Plate geometry	Non-dimensional natural frequencies		Non-dimensional deflection at $\bar{y} = 0.5$
Case I: 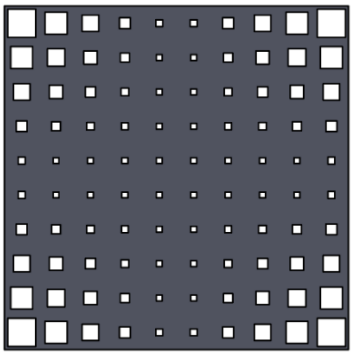	Present study	ANSYS modeling	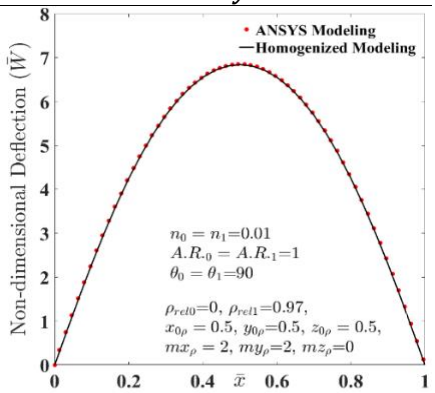
$\bar{\Omega}_1$	4.9798	5.0039	
$\bar{\Omega}_2$	12.2994	11.8107	
$\bar{\Omega}_3$	12.3056	11.8120	
$\bar{\Omega}_4$	12.9090	12.4703	
$\bar{\Omega}_5$	12.9108	12.4723	
Case II: 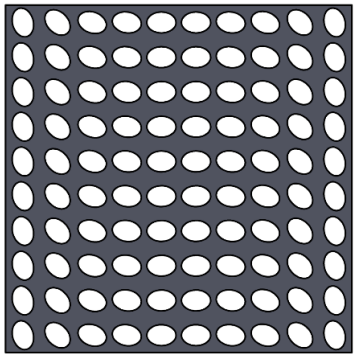	Present study	ANSYS modeling	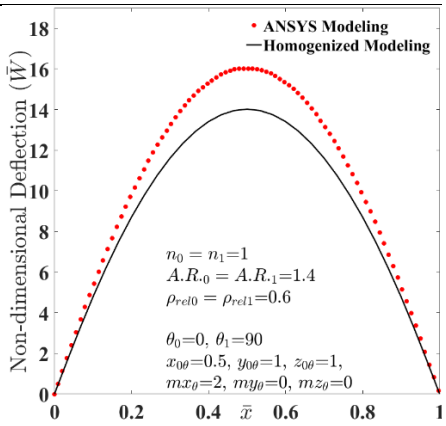
$\bar{\Omega}_1$	4.2274	3.9900	
$\bar{\Omega}_2$	9.4763	9.2590	
$\bar{\Omega}_3$	10.8372	9.5787	
$\bar{\Omega}_4$	11.6265	9.7645	
$\bar{\Omega}_5$	11.9832	10.4157	
Case III: 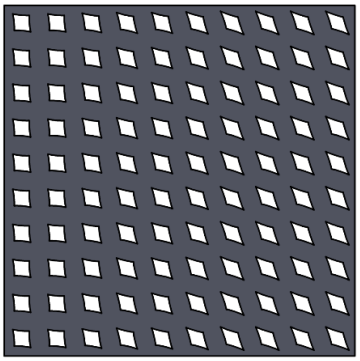	Present study	ANSYS modeling	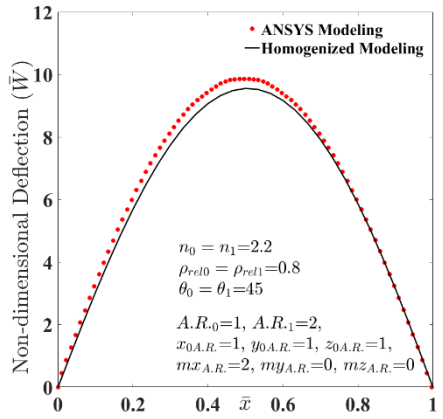
$\bar{\Omega}_1$	4.4487	4.4154	
$\bar{\Omega}_2$	10.4350	10.7298	
$\bar{\Omega}_3$	10.7801	11.2742	
$\bar{\Omega}_4$	14.8257	11.7111	
$\bar{\Omega}_5$	14.9265	11.9294	

2.7.2 Mechanical Analysis of Homogenous Cellular Structures

Figure 2-7 present the variation of the homogenized elastic properties of cells whose void is modeled by the superellipsoidal formula. **Figure 2-7a** shows that a wide range of elastic stiffness can be achieved by tessellating the cells in a periodic homogenous cellular structure. One can also see that the highest possible elastic stiffness is usually obtained by setting $n = 0.01$, which indicates square voids. Moreover, star-like void ($n > 2.2$) has the least elastic stiffness among the different shapes. In **Fig. 2-7**, the minimum relative density for the selected parameters is represented by "A", where the void surfaces touch the cell boundaries, and the void architecture is geometrically inadmissible. As shown in **Fig. 2-7a**, increasing the value of the shape parameter (n) decreases the achievable density range. The range of achievable shear modulus is depicted in **Fig. 2-7b**, which shows that the maximum achievable shear modulus does not belong to the square void. Moreover, the effect of aspect ratio is investigated in **Fig. 2-7b,** which shows that the highest shear modulus for rectangular void cells can be obtained for an aspect ratio equals to one. **Figure 2-7c** depicts the achievable range of Poisson's ratio. It can be seen that a wide range of relative Poisson's ratio ($\frac{\nu_{12}}{\nu_s}$), varying from negative values (auxetic behavior) to above unity, can be covered. The maximum and minimum of Poisson's ratios are respectively 0.448 and -0.054. **Figure 2-7c** also shows how negative Poisson's ratio can be achieved by rotating star-like shape voids, which could be of interest in some applications, e.g., hardness improvement in the isotropic materials [59] or directional wave propagation pass band for mechanical filters [60].

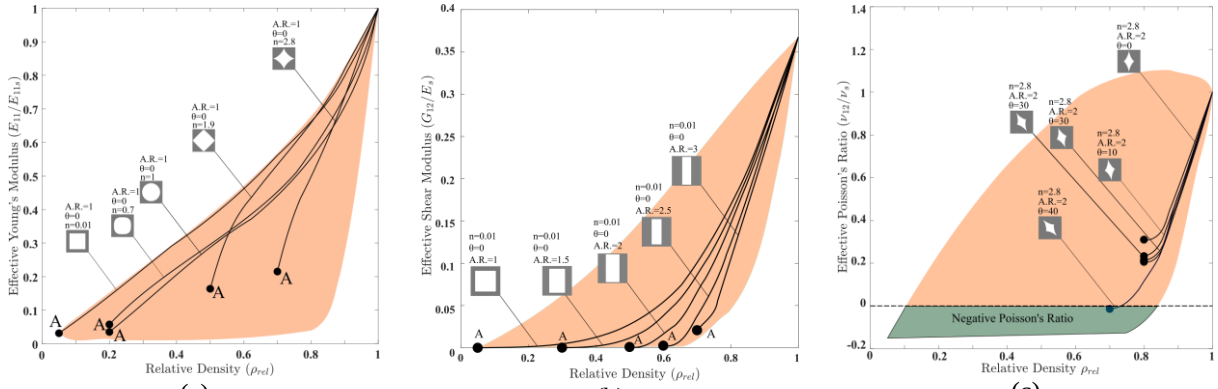

Figure 2-7- *The range of elastic properties achievable by PLA cellular solids of superellipse void shape (*$0.01 \leq n \leq 3, 0.01 \leq A.R. \leq 1, 0 \leq \theta \leq 90, 0.05 \leq \rho_{rel} \leq 1$*): (a) Young's modulus* (E_{11}) *vs. relative density* (ρ_{rel})*. Presented lines in* ***Fig. 2-7a*** *have been selected for a constant aspect ratio* $A.R. = 1$ *and rotation angle* $\theta = 0$*, while void shape parameter n varies, (b) Shear modulus* (G_{12}) *vs. relative density* (ρ_{rel})*. Presented lines in* ***Fig. 2-7b*** *have been selected for a constant shape parameter* $n = 0.01$ *and rotation angle* $\theta = 0$*, while aspect ratio A.R. varies, and (c) Poisson's ratio* (ν_{12}) *vs. relative density* (ρ_{rel})*. Presented lines in* ***Fig. 2-7c*** *have been selected for a constant shape parameter* $n = 2.8$ *and aspect ratio* $A.R. = 2$*, while orientation angle* (θ) *varies.*

An optimized structural design requires lightweight but stiff structural elements with minimum deflection, maximum mechanical buckling load, and maximum fundamental frequency. The structural responses of a homogenous cellular square plate made by 10×10 cells of the same void topology with four simply supported edges (SSSS) are depicted in **Fig. 2-8**. The variation of maximum deflection as a function of relative density is shown in **Fig. 2-8a**. As concluded from **Fig. 2-7a**, square shape voids have the highest stiffness among all the topologies studied. Consequently, the maximum deflection of a plate made of square shape voids is the lowest. **Figure 2-8b** presents the range of critical uniaxial (*x*-direction) buckling load to present the effect of the void aspect ratio on the critical buckling. **Figure 2-8c** illustrates the wide range of fundamental natural frequency attainable by the cellular plates. It is shown that varying the rotation angle (θ) can either decrease or increase the fundamental frequency depending on the relative density.

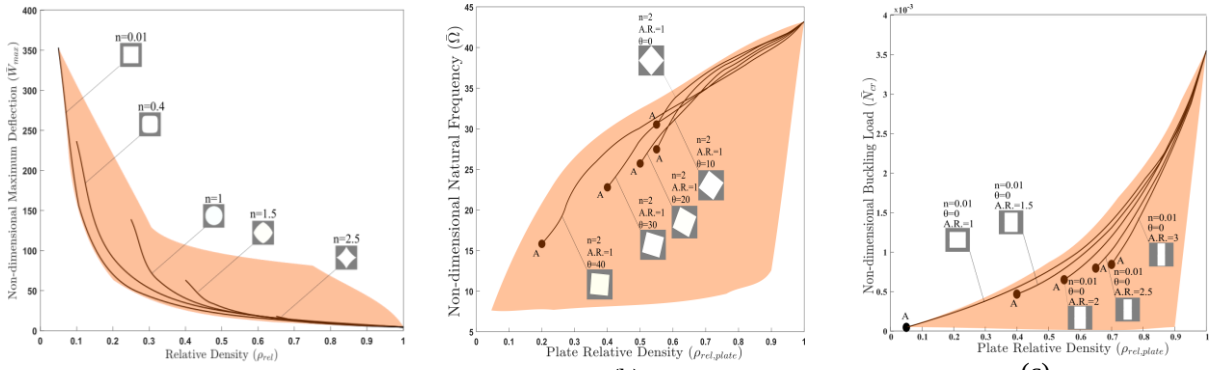

(a) (b) (c)

Figure 2-8- *Achievable structural responses of an SSSS cellular plate made of PLA with* $\frac{L_{tot}}{T_{tot}} = 10$ *made by* 10×10 *cells of all possible superellipsoidal void shapes: (a) Non-dimensional maximum deflection* ($\bar{W}_{max}$) *vs. plate relative density* ($\rho_{rel,plate}$). *Presented lines in* ***Fig. 2-8a*** *have been selected for a constant aspect ratio* $A.R. = 1$ *and rotation angle* $\theta = 0$, *while void shape parameter n varies, (b) Non-dimensional uniaxial (x-direction) critical buckling load* ($\bar{N}_{cr}$) *vs. plate relative density* ($\rho_{rel,plate}$). *Presented lines in* ***Fig. 2-8b*** *have been selected for a constant shape parameter* $n = 0.01$ *and rotation angle* $\theta = 0$, *while void aspect ratio A.R. varies, and (c) Non-dimensional natural frequency* ($\bar{\Omega}$) *vs. plate relative density* ($\rho_{rel,plate}$). *Presented lines in* ***Fig. 2-8c*** *have been selected for a constant shape parameter* $n = 2$ *and aspect ratio* $A.R. = 1$, *while cell rotation* θ *varies.*

2.7.3 Mechanical Analysis of Multi-Directional FGC Plates

So far, the range of possible structural responses by architected cellular plates has been limited to those found by cellular plates with a uniform distribution of unit cells. Here, the ability of functionally graded design to improve the structural performance of cellular plates is investigated. In **Table 2-2**, three FGC plates, made of 10×10 cells with square voids ($n = 0.01, AR = 1, \theta = 0$), with the same total relative density and dimensions but different density distribution are presented, and their structural responses are compared with homogenous cellular plates. The numerical results for these three case studies confirm the possibility of changing the maximum

deflection, maximum critical buckling load, and fundamental natural frequency while keeping constant the cellular structure total weight by grading the relative density in multiple directions.

Table 2-2- *Change in the structural response of SSSS FGC plate in comparison with a homogenous cellular plate with the same total relative density ($\rho_{rel,plate} = 0.7$).*

Architected cellular plates (Square void topology)	**Type of cellular plate**	**Maximum deflection** ($\bar{W}_{max}$)	**Fundamental natural frequency** ($\bar{\Omega}$)	**Uni-axial buckling load** ($\bar{N}_{cr}^{xx}$)
Homogenous cellular plate 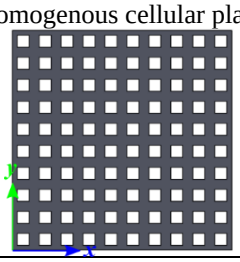	Homogenous Cellular	16.99	29.07	33.09
FGC plate with density variation in the $z-$direction 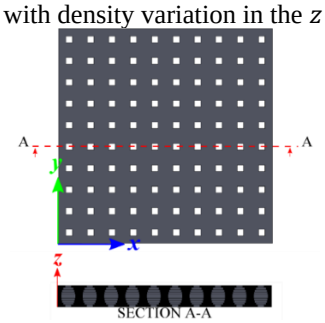	Functionally graded in the z-direction	10.96	32.09	51.08
FGC plate with density variation in the $x-$ and $y-$directions 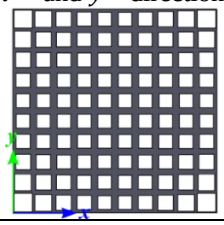	Functionally graded in the x- and y-directions	16.99	29.49	35.39
FGC plate with density variation in the $x-$, y-, and $z-$directions 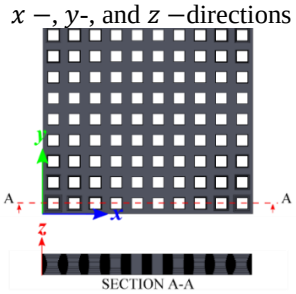	Functionally graded in the x-, y-and z-directions	18.30	29.19	32.54

The effect of density variation in different directions, on stiffening FGC plates subjected to a uniformly distributed load is presented in **Fig. 2-9**. According to this figure, a relative density variation in the z −direction can lead to maximum improvement in the elastic bending behavior of FGC plates. It can be observed that the density gradient in the z-direction has the most dominant effect on the variation of maximum deflection. While directional density variation in the *x*- and *z*-directions can decrease the maximum deflection by up to 26%, the maximum improvement attainable by one-directional density variation in the *z*-direction can be up to 56% for the maximum deflection of architected FGC plates. It is important to note that our conclusion here is only limited to the proposed variation formula defined in Eq. 2.3 for multi-directional graded materials and SSSS FGC plates. A more general mathematical expression allowing monotonic three-directional variation of relative density with simultaneous extreme values at the FGC plate center could even further optimize the performance of FGC structures. Our developed methodology for multi-directional FGC structures, contrary to a topology optimization approach [61], allows to independently investigate the effect of relative density, cell topology, cell aspect ratio, and cell orientation on the performance of FGC materials and structures.

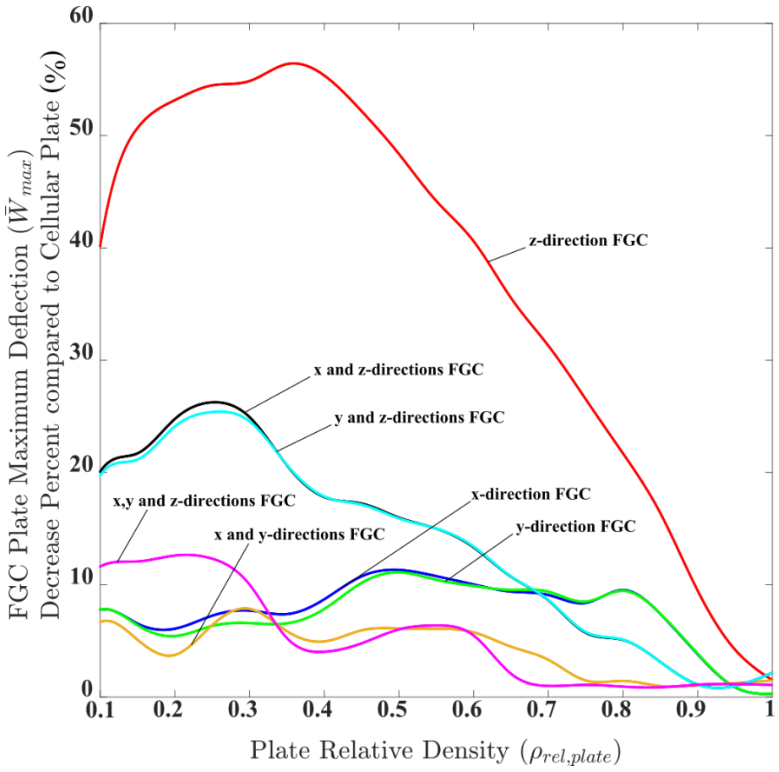

Figure 2-9- *Decrease of the maximum deflection of alternative multi-directional FGC square plate made by square void cell shape as a function of the relative density for SSSS plate with* $\frac{L_{tot}}{T_{tot}} = 10$.

The increase percent in the critical buckling load is plotted in **Fig. 2-10** as a function of $(\rho_{rel1} - \rho_{rel0})$, where ρ_{rel1} is the relative density at $\bar{x}_{0\rho} = \bar{y}_{0\rho} = \bar{z}_{0\rho} = 0.5$ and ρ_{rel0} represents the relative density at the origin. **Figure 2-10** shows that for a density gradient in the z −direction, the maximum improvement occurs when $(\rho_{rel1} - \rho_{rel0}) < 0$; i.e., when the middle plane of the FGC plate is more porous than the origin at the FGC plate top and bottom planes. When the density varies in the x-direction and/or y-direction, the conclusion is reversed. **Figure 2-10** implies that a z −directional FGC plates can have a maximum buckling load when the density at the middle of the thickness (mid-plane) is less than that of the top and bottom of the plate. On the other hand, for the x −directional or the y −directional FGC plate, lower relative density at the edges

compared to the center is more desirable for increasing the critical buckling load. It is also concluded that for all one-directional FGC plates, a higher difference between the side and center density $|\rho_{rel1} - \rho_{rel0}|$, Usually leads to a higher critical buckling load increase. However, it is worth mentioning that the effect of local buckling has not been taken into account in this study, a phenomenon which needs specific consideration since it might deteriorate the advantages of FGCMs for increasing the buckling load of lightweight architected sandwich panels.

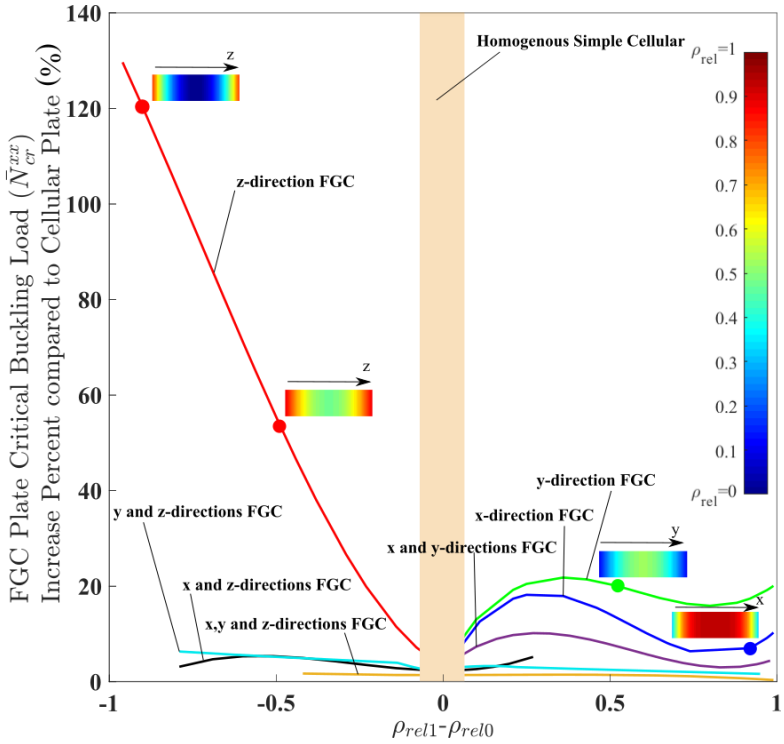

Figure 2-10- *The effect of the difference between the extreme values of relative density gradient* $(\rho_{rel1} - \rho_{rel0})$ *on the critical buckling load (x-direction) achievable by FGC design for SSSS plate with* $\frac{L_{tot}}{T_{tot}} = 10$.

Figure 2-11 presents the buckling load as a function of the extreme value location $(\bar{x}_0, \bar{y}_0, \bar{z}_0)$ on *SSSS* FGC plates. It can be seen that the highest buckling loads are achieved by setting the extreme value location in the middle of the gradient direction for all types of FGC plates. When the extreme

value location $(\bar{x}_0, \bar{y}_0, \bar{z}_0)$ is between 0.45 and 0.5, as much as an 80% increase in the buckling load can be achieved. Also, the location of the extreme value shifts toward the sides (top and bottom of the plate), the maximum achievable critical buckling load decreases. In other words, these trends mean that the quadratic distribution of relative density across a plate is more effective than the monotonic distribution for *SSSS* boundary conditions.

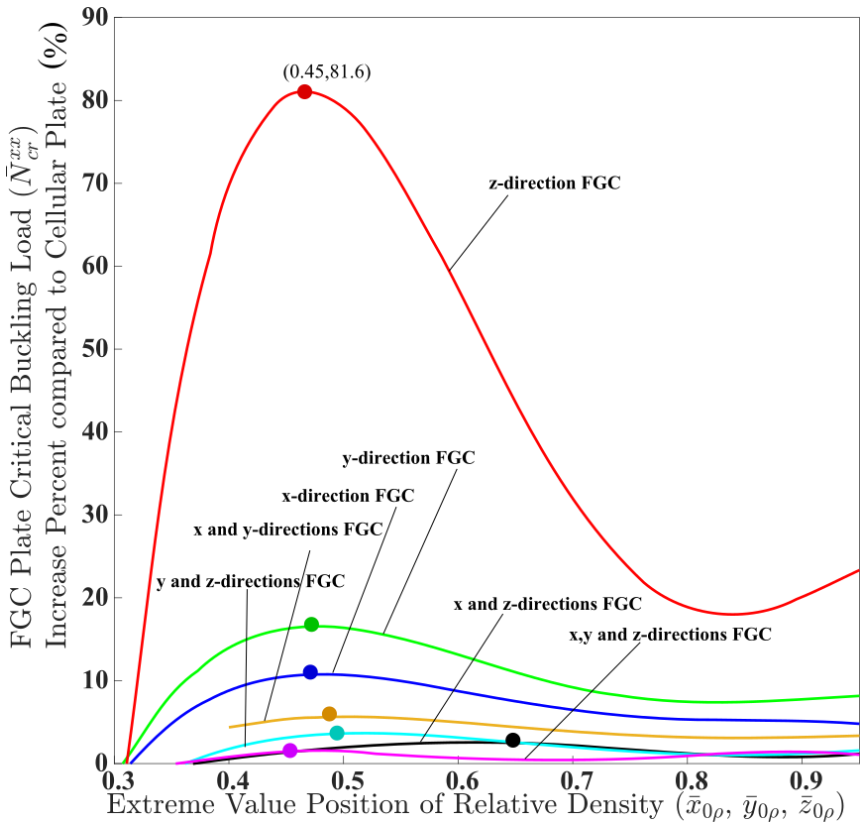

***Figure 2-11**- The effect of $\bar{x}_0$ $(= \bar{y}_0 = \bar{z}_0)$ on critical buckling load for different multi-directional FGC plate with SSSS boundary conditions and $\frac{L_{tot}}{T_{tot}} = 10$. In multi-directional FGC.*

Figure 2-12 presents the effect of the extreme value location of relative density on the critical buckling load of FGC plates with different boundary conditions. It can be observed that the conclusion obtained from **Fig. 2-11** does not fully apply for other types of boundary conditions.

According to **Fig. 2-12**, when the plate has free edges (*CFFF* and *CFCF* boundary conditions), the optimum is obtained when the extreme value is located elsewhere.

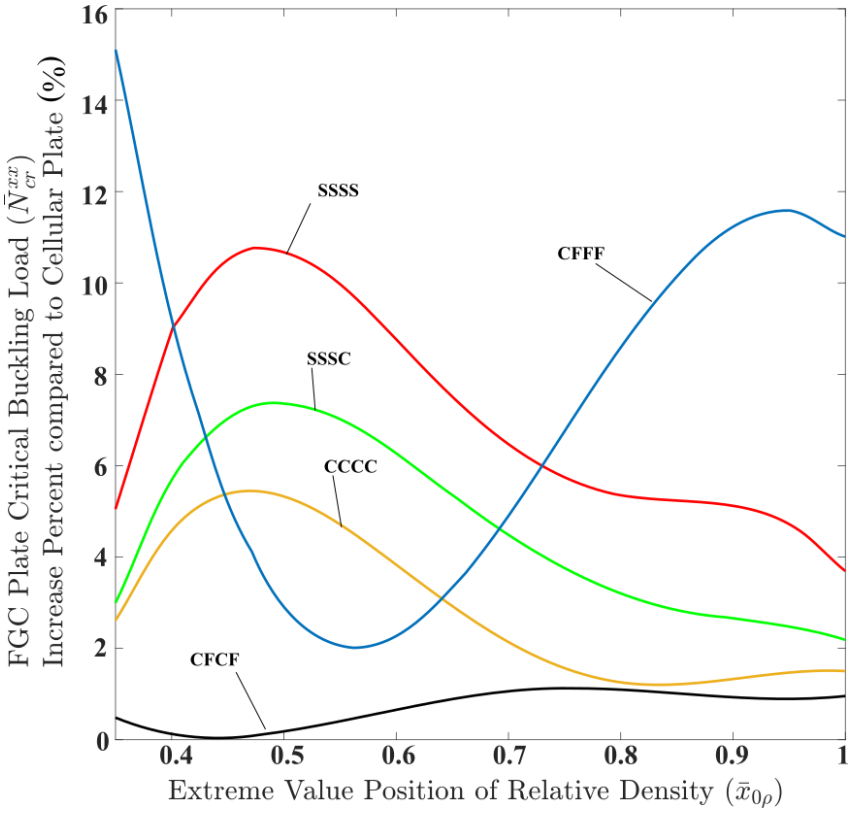

Figure 2-12- *The effect of the density extreme value location on the critical buckling* ($\bar{N}_{cr}^{xx}$) *load for* $x-$*directional FGC plate with* $\frac{L_{tot}}{T_{tot}} = 10$ *with different boundary conditions.*

2.7.4 Structural Response Optimization of Functionally Graded Cellular Plates

Since the relative density, cell topology, cell orientation, and cell aspect ratio extreme values position of FGC plate can all vary in multi-directional FGC plates, optimization of the material distribution leading to optimum structural performance for FGC plates is very complicated. Besides, the objectives for structural design (e.g., reducing the structural weight, increasing the bending toughness, decreasing the out-of-plane deflection, increasing the buckling load, and

increasing the fundamental frequencies) can be conflicting. As a result, a fast and efficient multi-objective optimization approach was adopted, the so-called non-dominated sorting genetic algorithm (NSGA-II). This technique is used to determine the maximum structural improvement achievable by tailoring the distribution parameters in an FGC plate. In this optimization problem, the parameters associated with the void shape are assumed to be constant ($n_0 = n_1 = constant$) because the cellular plates with square-shape voids show the highest bending stiffness among the all considered cell topologies (see **Section 2.7.2)**. Therefore, optimum values were searched for the other 24 distribution and void topology parameters (i.e. P_0, P_1, $\bar{x}_{0P}$, $\bar{y}_{0P}$, $\bar{z}_{0P}$, mx_P, my_P and mz_P, where P can be $A.R.$, ρ_{rel} or θ) to minimize both the total relative density ($\rho_{rel,plate}$) and the structural response parameter ($\zeta = \frac{\bar{W}_{max}}{\bar{\Omega}\bar{N}_{cr}^{xx}}$). The mathematical expression for the optimization problem can be written as:

$$min\{\rho_{rel,plate}(\bar{V}), \zeta(\bar{V})\}; \bar{V} = (P_0, P_1, \bar{x}_{0P}, \bar{y}_{0P}, \bar{z}_{0P}, mx_P, my_P, mz_P)$$

$$\text{s.t.:} \begin{cases} \text{for } P = A.R. \text{ then } \{1 \le P_0, P_1 \le 3\} \\ \text{for } P = \rho_{rel} \text{ then } \{0.01 \le P_0, P_1 \le 1\} \\ \text{for } P = \theta \text{ then } \{0° \le P_0, P_1 \le 90°\} \\ 0.01 \le \bar{x}_{0P}, \bar{y}_{0P}, \bar{z}_{0P} \le 1 \\ 0 \le mx_P, my_P, mz_P \le 8 \end{cases} \tag{2.13}$$

In **Fig. 2-13a**, the Pareto-optimal front, i.e., the most optimal outcomes which can be obtained by NSGA, is shown. It is seen that FGC plates can substantially improve the structural performance of structures made by rectangular-based ($n = 0.01$) and oval-based ($n = 1$) cells. For example, for a plate with a relative density of $\rho_{rel,plate} = 0.15$, rectangular based shape voids can improve the structural performance of the FGC plate by 46% compared to a plate made of homogenous cells of the same geometry. It should be mentioned that if the void shape parameter n is also

considered as a design variable in the optimization algorithm, the Pareto-optimal front would also indicate the square void shapes. This conclusion can be made of the results presented in **Figs. 2-7** and **2-8**.

Figure 2-13b presents the amount of improvement in the structural responses of FGC plates in percent. As shown in this figure, the maximum improvement is achieved for lower density plates, which means that the difference between the structural responses of FGC plates and homogenous cellular plates is substantially decreased for plates with higher density. Comparing points A_0 and A_1 in **Fig. 2-13a** shows that for a specific plate relative density ($\rho_{rel,plate} = 0.15$), the structural response can be improved by 45% by using an optimized FGC plate instead of a homogenous cellular plate of square cells ($n = 0.01$). On the other hand, comparing points A_0 and A_2 reveals that while the total weight of the FGC plate is reduced by 25%, the structural response remains unchanged. These observations confirm the critical advantages of multi-directional FGC structures compared to homogenous cellular structures.

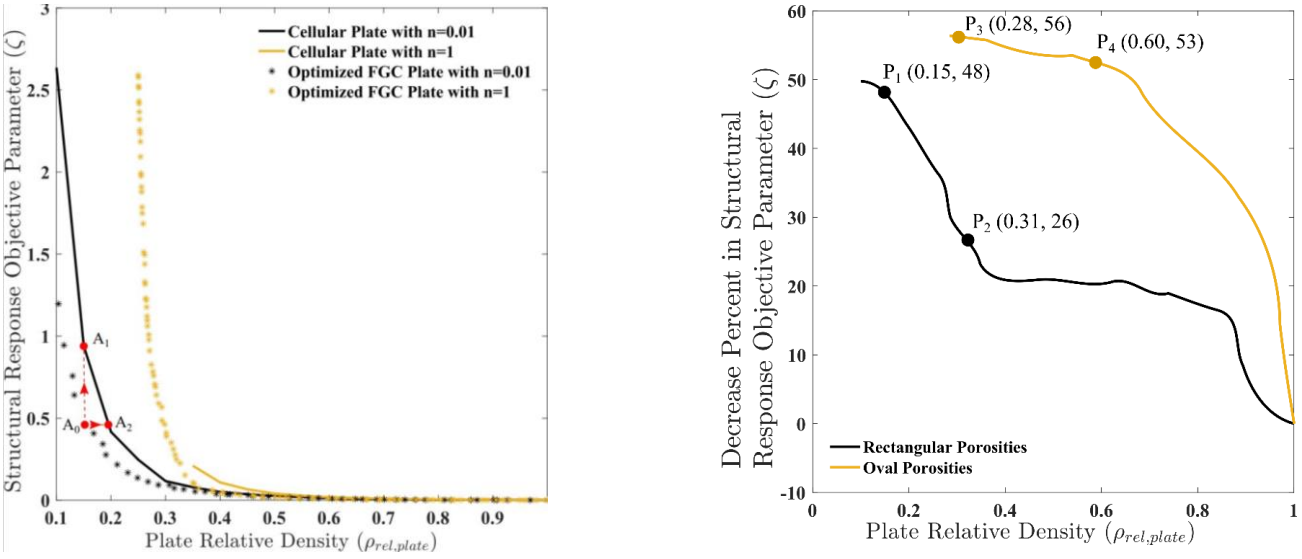

(a) (b)

Figure 2-13- *Comparison between the structural response of cellular plates and optimized FGC plates with SSSS boundary conditions and geometrical feature* $\frac{L_{tot}}{T_{tot}} = 10$ *for rectangular (*$n = 0.01$*) and oval (*n *=1) cells: (a) Pareto front and (b) Percentage of decrease in structural response parameter* (ζ).

Some prototypes have been 3D printed to verify the manufacturability of FGC structures. The pictures of these 3D printed samples corresponding to the four points in **Fig. 2-13b** (P_1, P_2, P_3 and P_4) are presented in **Fig. 2-14**. These samples have been prototyped using polylactic acid (PLA) on an FDM 3D printer MakerBot Z18 with a nominal layer resolution of 100 micrometers. The STL files of each representative optimized FGC plates have been generated by SolidWorks software. However, some defects can also be noticed in the samples, which can potentially decrease the structural performance of FGCMs. Consequently, their maximum potential as advanced architected materials is not achieved. As shown in **Fig. 2-14**, these 3D printing defects can be found on both surfaces and within the 3D printed samples. They come from different sources such as curve approximation errors in the STL files and porosities developed as a result of the layer by layer method associated with FDM 3D printing. More work is required to use more

advanced additive manufacturing technologies, like solvent-cast 3D printing [62], to reduce these manufacturing defects and to improve the surface finish of 3D printed architected FGCMs.

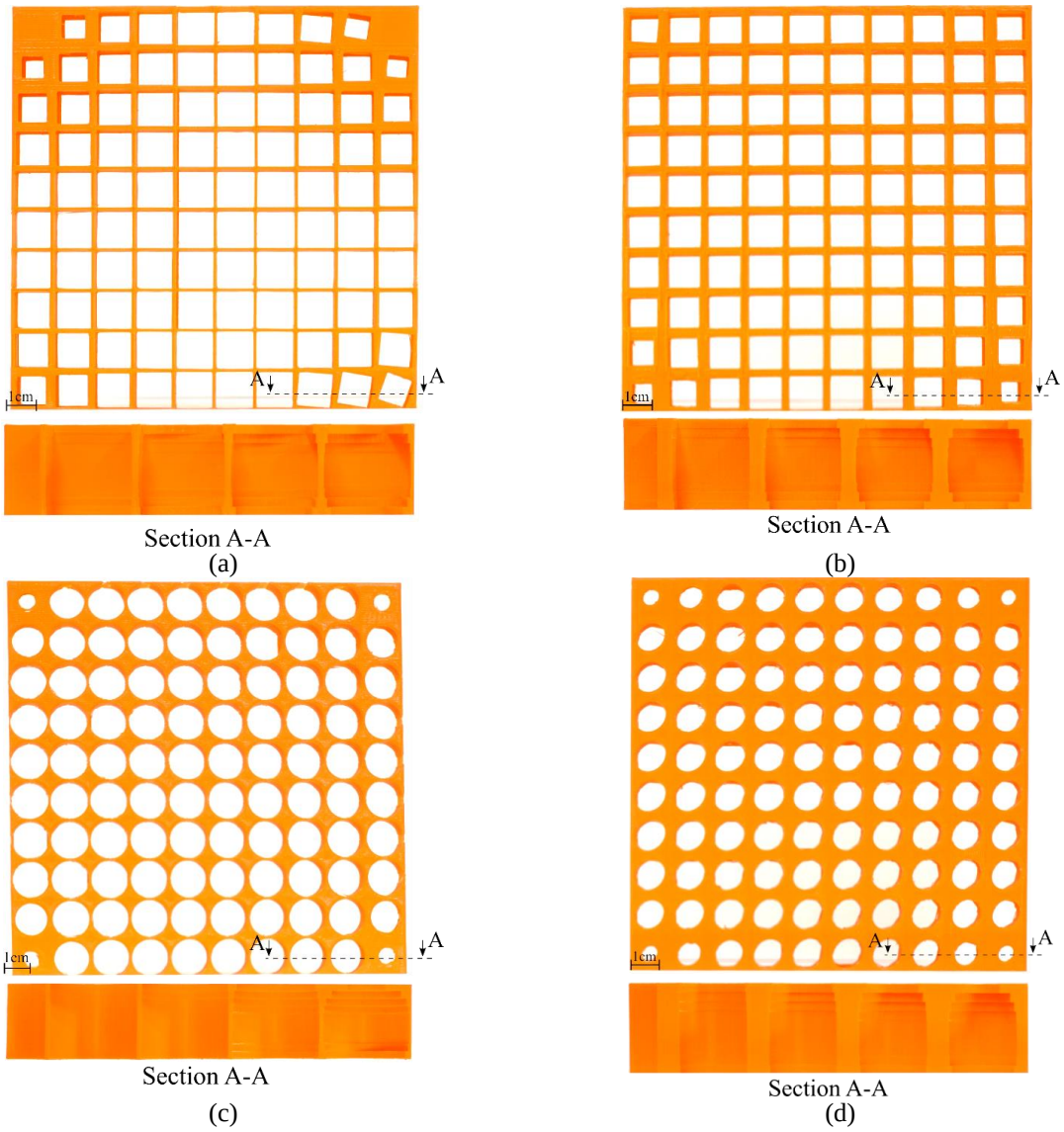

Figure 2-14- *The pictures of four optimized FGC plates, presented in* ***Fig. 2-13b****, manufactured by an FDM 3D printer: (a) Point* P_1 *(b) Point* P_2 *(c) Point* P_3 *(d) Point* P_4

2.8 Conclusions

In this paper, we have introduced the concept of multi-directional FGCMs as a new category of cellular materials. We have investigated their mechanical and structural performance, when used

as a constitutive element of cellular plates, to observe their advantages over the homogenous cellular materials. Superellipse formula is employed to model the topology of the architected cells, and a general power-law function is introduced to formulate the distribution of cell attributes in three different orthogonal directions. The effective properties of cells are predicted by standard mechanics homogenization. The FGC plate is modeled based on TSDT, and the governing differential equations are solved by FEM. The structural performance of architected FGC plates is compared with plates made of periodic cellular solids. The results of this study reveal the following interesting points:

- Architected cellular materials with superellipsoidal void can significantly expand the range of elastic and structural properties. They can offer lightweight but stiff solutions for advanced materials and structures (**Figs. 2-5, 2-7**, and **2-8**).
- Square shape voids ($n = 0.01$) lead to maximum flexural stiffness and Young's modulus compared with the other void shapes (**Figs. 2-7**, and **2-8**).
- Tailoring the topological features of cellular materials through the thickness of FGC plates significantly affects their structural responses, e.g., 56% increase in bending stiffness. This improvement is much more effective than changing the geometrical features of cells in planar directions (**Figs. 2-9**, and **2-10**).
- Relative density must be maximum at the top and bottom sides to improve the structural properties of lightweight architected FGC plates whose relative density is varying through the thickness ($z-$direction). However, in the case of architected FGC structures with planar relative density variation (i.e., $x-$ and $y-$directions), improvement in the structural performance is observed in plates whose relative density is higher at the middle of these $x-$ or $y-$directions than the plate's edges (**Fig. 2-10**).

- For 1D FGC plates with symmetric boundary conditions (e.g., SSSS and CCCC), the maximum improvement in the uniaxial buckling load can be achieved when the extreme values of density variation distribution function (Eq. 2.3) are exactly at the middle of the plate (**Figs. 2-11**, and **2-12**).
- Multi-objective optimization results anticipate a maximum improvement of up to 60% for the structural parameter ζ of an FGC plate compared to a conventional periodic cellular plate. Numerical results also reveal that the maximum possible improvement decreases as the total relative density of the FGC plate approach unity (**Fig. 2-13**).

Also, further experimental tests can be conducted to verify the conclusions made in this study and deepen the knowledge in the field of FGCMs as a new category of structurally efficient lightweight materials. The presented methodology in this paper provides a computationally efficient design guide, which can be used for developing optimized, lightweight, and structurally efficient panels.

2.9 Appendix 2.A

To create the void topology r_x and r_y must be obtained numerically using the three independent parameters; relative density (ρ_{rel}), aspect ratio ($A.R.$), and shape parameter (n). The following formula can be used for relative density (ρ_{rel}):

$$\rho_{rel} = 1 - \frac{Area_{void}}{L_{cell}W_{cell}} \tag{2.A1}$$

where the void area ($Area_{void}$) can be obtained by:

$$Area_{void} = 2\int_{-r_x}^{r_x} r_y\left(1-\left(\frac{x}{r_x}\right)^{\frac{2}{n}}\right)^{\frac{n}{2}} dx = 2r_x r_y \int_{-1}^{1}\left(1-(U)^{\frac{2}{n}}\right)^{\frac{n}{2}} dU = 2r_x r_y I \tag{2.A2}$$

in which $I = \int_{-1}^{1} \left(1 - (U)^{\frac{2}{n}}\right)^{\frac{n}{2}} dU$ and is calculated by Gaussian Quadrature numerical integration. Therefore, one can write:

$$r_x r_y = \frac{(1 - \rho_{rel}) L_{cell} W_{cell}}{2I} \tag{2.A3}$$

and by knowing the value of $r_x r_y$ and $A.R. = \frac{r_y}{r_x}$ both r_x and r_y can be calculated.

2.10 Appendix 2.B

In **Fig. 2-B1**, four types of one-dimensional FGCMs have been 3D printed by FDM technology using PLA filaments to better visualize various void. The 3D printed samples show the possibilities of independent variation of void topology parameters (n, $A.R.$, ρ_{rel} and θ) in each specific direction.

Shape parameter variation (n)

Aspect ratio variation (A.R.)

Relative density variation (ρ)

Orientation angle variation (θ)

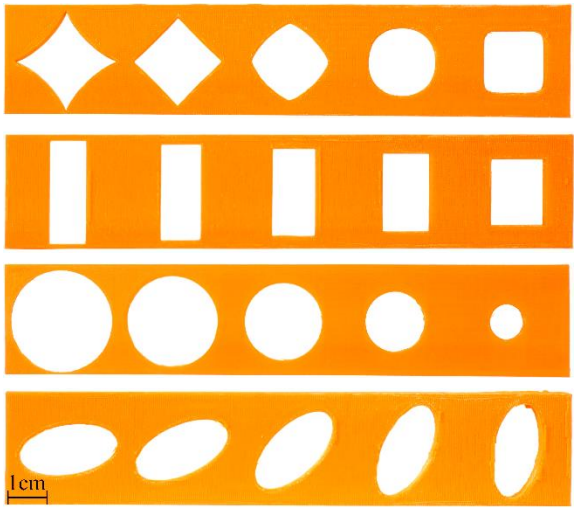

Figure 2-B1- *3D printed one-directional FGC samples designed with the superellipsoidal formula.*

2.11 Appendix 2.C

Stress resultants $N_{\alpha\beta}$, $M_{\alpha\beta}$, $P_{\alpha\beta}$, $Q_{\alpha\beta}$ and $R_{\alpha\beta}$ i.e., simplified representations of the stress state in a plate which were used in Eqs. (2.6) are defined as:

$$\begin{Bmatrix} N_{\alpha\beta} \\ M_{\alpha\beta} \\ P_{\alpha\beta} \end{Bmatrix} = \int_{-\frac{h}{2}}^{\frac{h}{2}} \sigma_{\alpha\beta} \begin{Bmatrix} 1 \\ z \\ z^3 \end{Bmatrix} dz \tag{2.C1a}$$

$$\begin{Bmatrix} Q_{\alpha} \\ R_{\alpha} \end{Bmatrix} = \int_{-\frac{h}{2}}^{\frac{h}{2}} \sigma_{\alpha z} \begin{Bmatrix} 1 \\ z^2 \end{Bmatrix} dz \tag{2.C1b}$$

These stress resultants are related to the strain components by the following constitutive equations written for the homogenized properties:

$$\begin{Bmatrix}\{N\}\\\{M\}\\\{P\}\end{Bmatrix}=\begin{bmatrix}[A] & [B] & [E]\\[B] & [D] & [F]\\[E] & [F] & [H]\end{bmatrix}\begin{Bmatrix}\{\varepsilon^0\}\\\{\varepsilon^1\}\\\{\varepsilon^3\}\end{Bmatrix} \tag{2.C2a}$$

$$\begin{Bmatrix}\{Q\}\\\{R\}\end{Bmatrix}=\begin{bmatrix}[A] & [D]\\[D] & [F]\end{bmatrix}\begin{Bmatrix}\{\gamma^0\}\\\{\gamma^2\}\end{Bmatrix} \tag{2.C2b}$$

where

$$\left(A_{ij},B_{ij},D_{ij},E_{ij},F_{ij},H_{ij}\right)=\sum_{K=1}^{N}\int_{z_k}^{z_{k+1}}Q_{ij}^{k}(1,z,z^2,z^3,z^4,z^6)dz \tag{2.C3}$$

in which Q_{ij}^{k} is the homogenized elastic properties of each cell obtained from the standard mechanics homogenization technique (**Section 2.4.3**). I_i and J_i in Eqs. (2.7) are:

$$I_i(x,y)=\int_{-\frac{h}{2}}^{\frac{h}{2}}\rho(x,y,z)z^i dz \tag{2.C4a}$$

$$J_i(x,y)=I_i(x,y)-c_1 I_{i+2}(x,y) \tag{2.C4b}$$

2.12 Acknowledgments

A.H. Akbarzadeh acknowledges the financial support by McGill University and Natural Sciences and Engineering Research Council of Canada (NSERC) through NSERC Discovery Grant RGPIN-2016-0471. The authors also acknowledge financial support from the Research Center for High-Performance Polymer and Composite Systems (CREPEC).

2.13 References

[1] L.J. Gibson, M.F. Ashby, Cellular Solids: Structure and Properties, Cambridge University Press1999.

[2] F. Robert, An isotropic three-dimensional structure with Poisson's ratio--1, Journal of Elasticity 15 (1985) 427-430.

[3] J.B. Berger, H.N.G. Wadley, R.M. McMeeking, Mechanical metamaterials at the theoretical limit of isotropic elastic stiffness, Nature 543 (2017) 533.

[4] L. Wollmann, A.K. Nayak, S.S.P. Parkin, C. Felser, Heusler 4.0: Tunable Materials, Annual Review of Materials Research 47(1) (2017) 247-270.

[5] A. Vigliotti, D. Pasini, Stiffness and strength of tridimensional periodic lattices, Computer Methods in Applied Mechanics and Engineering 229 (2012) 27-43.

[6] N. Fleck, V. Deshpande, M. Ashby, Micro-architectured materials: past, present and future, Proceedings of the Royal Society of London A: Mathematical, Physical and Engineering Sciences, The Royal Society, 2010, pp. 2495-2516.

[7] K. Bertoldi, M.C. Boyce, Wave propagation and instabilities in monolithic and periodically structured elastomeric materials undergoing large deformations, Physical Review B 78(18) (2008) 184107.

[8] M. Ruzzene, F. Scarpa, F. Soranna, Wave beaming effects in two-dimensional cellular structures, Smart materials and structures 12(3) (2003) 363.

[9] B.L. Buitrago, C. Santiuste, S. Sánchez-Sáez, E. Barbero, C. Navarro, Modelling of composite sandwich structures with honeycomb core subjected to high-velocity impact, Composite Structures 92(9) (2010) 2090-2096.

[10] A. Petras, M.P.F. Sutcliffe, Failure mode maps for honeycomb sandwich panels, Composite Structures 44(4) (1999) 237-252.

[11] H. Rathbun, D. Radford, Z. Xue, M. He, J. Yang, V. Deshpande, N. Fleck, J. Hutchinson, F. Zok, A. Evans, Performance of metallic honeycomb-core sandwich beams under shock loading, International journal of solids and structures 43(6) (2006) 1746-1763.

[12] W. Burton, A. Noor, Assessment of continuum models for sandwich panel honeycomb cores, Computer methods in applied mechanics and engineering 145(3-4) (1997) 341-360.

[13] R. Viskanta, Overview of radiative transfer in cellular porous materials, Proceedings of the ASME 2009 Heat Transfer Summer Conference, 2009, pp. 19-23.

[14] L.E. Murr, S.M. Gaytan, F. Medina, H. Lopez, E. Martinez, B.I. Machado, D.H. Hernandez, L. Martinez, M.I. Lopez, R.B. Wicker, J. Bracke, Next-generation biomedical implants using additive manufacturing of complex, cellular and functional mesh arrays, Philosophical Transactions of the Royal Society A: Mathematical, Physical and Engineering Sciences 368(1917) (2010) 1999.

[15] S. Arabnejad Khanoki, D. Pasini, Multiscale Design and Multiobjective Optimization of Orthopedic Hip Implants with Functionally Graded Cellular Material, Journal of Biomechanical Engineering 134(3) (2012) 031004-031004-10.

[16] H.G. Allen, CHAPTER 4 - ANALYSIS OF SANDWICH BEAMS AND STRUTS BY STRAIN ENERGY METHODS, Analysis and Design of Structural Sandwich Panels, Pergamon1969, pp. 57-75.

[17] G. Shi, P. Tong, The derivation of equivalent constitutive equations of honeycomb structures by a two scale method, Computational Mechanics 15(5) (1995) 395-407.

[18] I.G. Masters, K.E. Evans, Models for the elastic deformation of honeycombs, Composite Structures 35(4) (1996) 403-422.

[19] F. Scarpa, G. Tomlinson, Theoretical characteristics of the vibration of sandwich plates with in-plane negative poisson's ratio values, Journal of Sound and Vibration 230(1) (2000) 45-67.

[20] K.E. Evans, The design of doubly curved sandwich panels with honeycomb cores, Composite Structures 17(2) (1991) 95-111.

[21] T.L. Warren, Negative Poisson's ratio in a transversely isotropic foam structure, Journal of Applied Physics 67(12) (1990) 7591-7594.

[22] M. Avalle, G. Belingardi, R. Montanini, Characterization of polymeric structural foams under compressive impact loading by means of energy-absorption diagram, International Journal of Impact Engineering 25(5) (2001) 455-472.

[23] A.H. Akbarzadeh, J.W. Fu, Z.T. Chen, L.F. Qian, Dynamic eigenstrain behavior of magnetoelastic functionally graded cellular cylinders, Composite Structures 116 (2014) 404-413.

[24] V. Andrea, P. Damiano, Analysis and design of lattice materials for large cord and curvature variations in skin panels of morphing wings, Smart Materials and Structures 24(3) (2015) 037006.

[25] J.T.B. Overvelde, S. Shan, K. Bertoldi, Compaction Through Buckling in 2D Periodic, Soft and Porous Structures: Effect of Pore Shape, Advanced Materials 24(17) (2012) 2337-2342.

[26] S. Janbaz, H. Weinans, A.A. Zadpoor, Geometry-based control of instability patterns in cellular soft matter, RSC Advances 6(24) (2016) 20431-20436.

[27] D.W. Rosen, Computer-Aided Design for Additive Manufacturing of Cellular Structures, Computer-Aided Design and Applications 4(5) (2007) 585-594.

[28] B.H. Smith, S. Szyniszewski, J.F. Hajjar, B.W. Schafer, S.R. Arwade, Steel foam for structures: A review of applications, manufacturing and material properties, Journal of Constructional Steel Research 71 (2012) 1-10.

[29] T. Tan, N. Rahbar, S.M. Allameh, S. Kwofie, D. Dissmore, K. Ghavami, W.O. Soboyejo, Mechanical properties of functionally graded hierarchical bamboo structures, Acta Biomaterialia 7(10) (2011) 3796-3803.

[30] A. Miserez, T. Schneberk, C. Sun, F.W. Zok, J.H. Waite, The Transition from Stiff to Compliant Materials in Squid Beaks, Science 319(5871) (2008) 1816-1819.

[31] V. Imbeni, J.J. Kruzic, G.W. Marshall, S.J. Marshall, R.O. Ritchie, The dentin-enamel junction and the fracture of human teeth, Nat Mater 4(3) (2005) 229-232.

[32] M. Huang, N. Rahbar, R. Wang, V. Thompson, D. Rekow, W.O. Soboyejo, Bioinspired design of dental multilayers, Materials Science and Engineering: A 464(1) (2007) 315-320.

[33] N.J. Jeon, J.H. Noh, W.S. Yang, Y.C. Kim, S. Ryu, J. Seo, S.I. Seok, Compositional engineering of perovskite materials for high-performance solar cells, Nature 517 (2015) 476.

[34] T.C. Lim, Functionally graded beam for attaining Poisson-curving, Journal of Materials Science Letters 21(24) (2002) 1899-1901.

[35] S.-J. Lee, J. Wang, B.V. Sankar, A micromechanical model for predicting the fracture toughness of functionally graded foams, International Journal of Solids and Structures 44(11) (2007) 4053-4067.

[36] A. Ajdari, P. Canavan, H. Nayeb-Hashemi, G. Warner, Mechanical properties of functionally graded 2-D cellular structures: A finite element simulation, Materials Science and Engineering: A 499(1) (2009) 434-439.

[37] A. Ajdari, H. Nayeb-Hashemi, A. Vaziri, Dynamic crushing and energy absorption of regular, irregular and functionally graded cellular structures, International Journal of Solids and Structures 48(3) (2011) 506-516.

[38] L. Cui, S. Kiernan, M.D. Gilchrist, Designing the energy absorption capacity of functionally graded foam materials, Materials Science and Engineering: A 507(1) (2009) 215-225.

[39] D. Chen, J. Yang, S. Kitipornchai, Elastic buckling and static bending of shear deformable functionally graded porous beam, Composite Structures 133 (2015) 54-61.

[40] C. Lira, F. Scarpa, Transverse shear stiffness of thickness gradient honeycombs, Composites Science and Technology 70(6) (2010) 930-936.

[41] Y. Hou, Y.H. Tai, C. Lira, F. Scarpa, J.R. Yates, B. Gu, The bending and failure of sandwich structures with auxetic gradient cellular cores, Composites Part A: Applied Science and Manufacturing 49 (2013) 119-131.

[42] L. Boldrin, S. Hummel, F. Scarpa, D. Di Maio, C. Lira, M. Ruzzene, C.D.L. Remillat, T.C. Lim, R. Rajasekaran, S. Patsias, Dynamic behaviour of auxetic gradient composite hexagonal honeycombs, Composite Structures 149 (2016) 114-124.

[43] C. Lira, F. Scarpa, R. Rajasekaran, A Gradient Cellular Core for Aeroengine Fan Blades Based on Auxetic Configurations, Journal of Intelligent Material Systems and Structures 22(9) (2011) 907-917.

[44] O. Sigmund, On the Design of Compliant Mechanisms Using Topology Optimization, Mechanics of Structures and Machines 25(4) (1997) 493-524.

[45] O. Sigmund, A 99 line topology optimization code written in Matlab, Structural and Multidisciplinary Optimization 21(2) (2001) 120-127.

[46] Y.M. Xie, G.P. Steven, A simple evolutionary procedure for structural optimization, Computers & Structures 49(5) (1993) 885-896.

[47] G. Allaire, F. Jouve, A.-M. Toader, Structural optimization using sensitivity analysis and a level-set method, Journal of Computational Physics 194(1) (2004) 363-393.

[48] B. Niu, J. Yan, G. Cheng, Optimum structure with homogeneous optimum cellular material for maximum fundamental frequency, Structural and Multidisciplinary Optimization 39(2) (2008) 115.

[49] Y. Wang, H. Xu, D. Pasini, Multiscale isogeometric topology optimization for lattice materials, Computer Methods in Applied Mechanics and Engineering 316 (2017) 568-585.

[50] J.P. Groen, M. Langelaar, O. Sigmund, M. Ruess, Higher-order multi-resolution topology optimization using the finite cell method, International Journal for Numerical Methods in Engineering 110(10) (2017) 903-920.

[51] J. Zhang, Z. Wang, L. Zhao, Dynamic response of functionally graded cellular materials based on the Voronoi model, Composites Part B: Engineering 85 (2016) 176-187.

[52] N.T. Gridgeman, Lamé ovals, The Mathematical Gazette (1970) 31-37.

[53] B. Hassani, E. Hinton, A review of homogenization and topology opimization II—analytical and numerical solution of homogenization equations, Computers & structures 69(6) (1998) 719-738.

[54] J. Reddy, Analysis of functionally graded plates, International Journal for Numerical Methods in Engineering 47(1-3) (2000) 663-684.

[55] N. Noda, J. Zhi-He, Thermal stress intensity factors for a crack in a strip of a functionally gradient material, International Journal of Solids and Structures 30(8) (1993) 1039-1056.

[56] A. Akbarzadeh, A. Abedini, Z. Chen, Effect of micromechanical models on structural responses of functionally graded plates, Composite Structures 119 (2015) 598-609.

[57] J. Reddy, Z.-Q. Cheng, Three-dimensional thermomechanical deformations of functionally graded rectangular plates, European Journal of Mechanics-A/Solids 20(5) (2001) 841-855.

[58] A.M. Arias Herrera, Development of Natural Fiber Reinforced Polylactide-Based Biocomposites, (2014) 64.

[59] K.E. Evans, A. Alderson, Auxetic materials: functional materials and structures from lateral thinking!, Advanced materials 12(9) (2000) 617-628.

[60] M. Ruzzene, F. Scarpa, Directional and band-gap behavior of periodic auxetic lattices, physica status solidi (b) 242(3) (2005) 665-680.

[61] A. Radman, X. Huang, Y.M. Xie, Topology optimization of functionally graded cellular materials, Journal of Materials Science 48(4) (2013) 1503-1510.

[62] S.-Z. Guo, F. Gosselin, N. Guerin, A.-M. Lanouette, M.-C. Heuzey, D. Therriault, 3D Printing: Solvent-Cast Three-Dimensional Printing of Multifunctional Microsystems (Small 24/2013), Small 9(24) (2013) 4090-4090.

3 Chapter Three: In-Plane and Out-of-Plane Buckling of Architected Cellular Plates: Numerical and Experimental Study[1]

3.1 Preface

In **Chapter 2**, we focus on the global responses of cellular plates; in other words, we did not consider the local behavior of cells. This negligence was primarily due to the incapability of homogenized-based analysis in capturing local phenomena. Consequently, the results presented in **Chapter 2** do not apply to thick cellular plates or problems where local failure precedes global response.

This problem becomes more critical in the case of buckling analysis, where the primary buckling load may be the one associated with the local buckling. Consequently, in **Chapter 3**, we distinguish these two buckling types and consider different factors that may change the buckling response from local to global or vice-versa. As previously mentioned, the homogenization-based analysis cannot determine the local buckling behavior; therefore, two alternative methods are adopted to model the buckling behavior: Experimentation and Detailed FE modeling.

[1] Reproduced with permission from Niknam, H., Akbarzadeh, A.H.; In-Plane and Out-of-Plane Buckling of Architected Cellular Plates: Numerical and Experimental Study; *Composite Structures*, 206 (2018) 739-749.

3.2 Abstract

In this article, the nature of instability in architected cellular materials is explored through computational modeling and experimental testing. The in-plane and out-of-plane buckling, as two primary instability mechanisms in cellular materials, are distinguished, and the effects of their microarchitectural parameters on the buckling behavior are demonstrated. Different architected cellular materials in the form of cellular plates are analyzed with a finite element method (FEM) by eigen buckling and nonlinear analyses. In contrast, a few samples of elastomeric architected cellular materials are prototyped and experimentally tested to corroborate our numerical predictions for the buckling load. We show that an appropriate gradient of cell architecture within the cellular plates could lead to an increase in both out-of-plane and in-plane buckling loads. The experimental tests conducted on the cast cellular plates, confirm that different buckling mode shapes can be observed by tailoring the microarchitectures of cellular plates. This idea can pave the path for devising advanced reconfigurable materials, for shape matching and energy absorption applications, whose mode shapes and resistance to buckling can be programmed based on the desirable functionalities without compromising their total mass.

3.3 Introduction

Over the last 50 years, cellular materials have received a lot of attention as they allow tuning properties by programing their microarchitecture. Inspired by natural honeycombs, early studies focused on the design and manufacturing of honeycomb cellular structures [1, 2], which were implemented in different applications from aerospace and automotive to biomedical and construction sectors [3-5]. Following these studies, a substantial amount of research was conducted to architect cell topology and best benefit from all potentials of cellular materials [2, 3, 6]. The

concept of *functionally graded cellular materials (FGCM)* was also proposed to improve their structural performance by tailoring the relative density and cell topology across the cellular materials [7-13]. Among different structural properties, the response of cellular materials to compressive loads is of great importance because it determines their energy absorption capability, impacts energy resistance and structural stability.

Generally, an increase in compressive load leads to the failure of cellular structures either by buckling, material yielding, or brittle fracture. Preliminary studies on the response of cellular materials subjected to compressive loads involved in-plane crushing of honeycombs due to fracture or yielding. In the earliest works, the effect of uniaxial loading [14], biaxial loading [15-17], cell size [18], cell topology [19-21], constitutive base material [18, 19, 22] and out-of-plane loading [23, 24] on the crushing behavior of periodic cellular materials was investigated. Further studies on the crushing behavior of cellular materials and structures revealed that their failure behavior is almost independent of the type of compressive load, whether it is dynamic or static loading [25, 26]. However, optimized cell microarchitectures and relative density distribution across the six-sided honeycombs can improve their energy absorption capability [27, 28].

In the flexural bending theory of linear elastic materials, compressive force and deflection in beams and plates are linearly proportional to applied loads, assuming that the structures remain stable. The onset of elastic instability is referred to as “Buckling”. At the level of the highest load, a few micro-buckling might occur, which can lead to a nonlinear force-displacement curve before the peak load. Two different definitions have been presented for obtaining the buckling load from the load-displacement curve. Russel *et al.* [29] defined the buckling load as the first non-uniformity in the stress and strain curve, while Liu et al. [30] considered the buckling load as the peak load in

the load-displacement curve. In the present work, the latter definition is adopted, which means that the buckling load is considered as the highest compressive load in the load-displacement curve while the solid constituent material has not yielded or fractured. The elastic instability emerges as the out-of-plane deformation in fully dense materials; however, in cellular materials, either out-of-plane deformation or in-plane failure/buckling of constituent struts may occur. To distinguish between the failure mechanisms initiated by local (in-plane) elastic buckling of cell walls or yielding and fracture of constitutive base materials, the failure surface of honeycomb plates was investigated in [31]. Studies have been performed to obtain the failure surfaces of cellular structures made of different base materials [32], cell topologies [33], and loading conditions [22] to differentiate between failure due to the buckling and the material yield/fracture.

A few studies have investigated the behavior of cylindrical cellular structures in compression. For example, four distinct failure modes have recently been identified for cellular cylinders in compression, i.e., global buckling, shell buckling, mono-cell buckling, and struts failure [34, 35]. The in-plane buckling (local buckling) load, unlike the out-of-plane buckling (global buckling) load, is much dependent on the microarchitecture of constituent struts [36]. This conclusion was verified by further experimental and numerical studies conducted on different composite cellular cylinders [47, 48] made of alternative cell topologies [37-42].

Recently, pattern transformation, which is initiated by in-plane buckling in soft cellular structures, has received lots of attention. The yield strength of these structures is high enough to allow buckling before yielding or fracture. The pattern transformation might be triggered due to a compressive load [43-45], indentation [46] or thermal stresses [47] and can be programmed in architected cellular materials by tailoring the cell topology [48-50] and cell size [51, 52] or by

adding interfacial layers [53]. Exploiting pattern transformation in cellular materials has emerged with extraordinary properties, among which we can refer to negative Poisson's ratio [54], shape memory effect in non-ferroelastic materials [55], and mechanically triggered phononic band gaps [56]. However, the cellular materials cannot show pattern transformation and their associated exotic properties if out-of-plane buckling occurs before in-plane buckling. Therefore, a comprehensive study is critical to understand parameters affecting the in-plane and out-of-plane buckling of architected cellular materials. To best exploit all potentials of lightweight cellular structures for different applications, in-plane and out-of-plane buckling of periodic cellular materials still need to be well understood.

To the best of the authors' knowledge, no study has distinguished the in-plane and out-of-plane buckling in emerging architected cellular materials, specifically when they have been used as structural elements with graded microarchitectures. Therefore, an attempt is made to explore the buckling behavior of architected cellular plates using FEM (**Section 3.4.1**) and an experimental approach to casted elastomeric cellular plates (**Section 3.4.2**). The effect of geometrical features of cellular plates, i.e., relative density, slenderness ratio, and the number of cells on the buckling behavior of cellular plates, are investigated through a series of numerical studies (**Section 3.5**). Finally, the microarchitecture of cellular plates is engineered using the concept of FGCMs [13] to showcase the possibility of tuning the critical buckling load and buckling mode shape in cellular plates (**Section 3.6.1**) and experimental testing of casted elastomeric cellular materials (**Section 3.6.2**). The ability to tune the buckling behavior of lightweight cellular structures by grading their microarchitectures opens new avenues in the design and manufacturing of architected cellular materials.

3.4 Materials and Methods

In this study, two-dimensional (2D) extruded cells with different cell topologies and relative densities are first tessellated uniformly in $x-$ and $y-$directions to create a three-dimensional (3D) cellular material in the form of a cellular plate, as shown in **Figure 3-1a**. The relative density of each cell is defined as the volume of solid parts over the total volume of the unit cell ($\rho_{rel} = \frac{V_{solid}}{V_{unit\ cell}}$). The total relative density of the cellular plate is written as:

$$\rho_{rel,total} = \frac{\sum_{i=1}^{M} \rho_{rel,i}}{M} \tag{3.1}$$

where $\rho_{rel,i}$ is the relative density of i^{th} cell, and M is the total number of cells in the cellular plate. Besides, the slenderness ratio for the cellular plate and each cell, as well as the non-dimensional buckling load, are defined as:

$$S.R. = \frac{L}{T} \tag{3.2a}$$

$$S.R._{cell} = \frac{L_{void}}{T_{cell}} \tag{3.2b}$$

$$\bar{N}_{cr} = \frac{\widehat{N} L^2}{E_s\, W^3} \tag{3.2c}$$

where the buckling load is non-dimensionalized according to [57] and E_s is the Young's modulus of base material constituting cellular materials and $\widehat{N}$ represents the in-plane compressive load per unit width (W) in $x-$direction. This cellular plate is clamped at one edge ($x = 0$) while subjected

to a uniaxial compressive load of uniform pressure on the opposite edge, as shown in **Figure 3-1b**. Under these mechanical conditions, both in-plane and out-of-plane buckling could occur in the cellular plate. The details of the application of these boundary conditions in FEM and experimental set-up are given in this section.

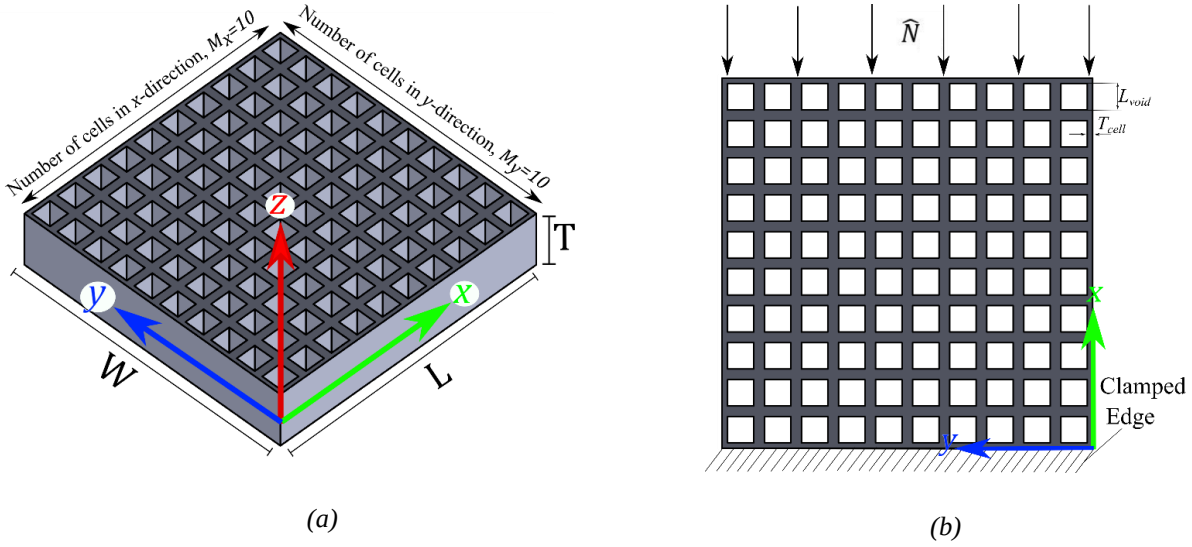

(a) *(b)*

Figure 3-1*- Schematic view of a 2D extruded cellular plate with a uniform distribution of cells: (a) Dimensions and coordinate system and (b) Loading and boundary conditions.*

3.4.1 Finite Element Simulation

Commercial ANSYS Workbench software (Ver. 18.2) is used here to simulate the buckling behavior of the cellular materials. Different geometries are modeled in SolidWorks software (Ver. 2016) and imported in ANSYS. Linear eigen buckling analysis is then implemented to obtain the critical buckling load and mode shape of the buckled cellular plate. The cellular plate is meshed with a higher-order 3D, 20-node, solid element (ANSYS element type Solid186) that exhibits quadratic displacement behavior; the number of elements in a cell varies in our FEM as the cell topology, and relative density of cells are changing. After performing mesh sensitivity analysis, a

base quantity of 1000 elements per unit cell is selected in this study for finite element simulation. In FE simulation, y and z translational degrees of freedom at the top face, where the compressive mechanical load is applied, and at the bottom face are fixed; the x translational degree of freedom of the bottom face is also fixed. Also, the x translational degree of freedom of the top face nodes is coupled together to mimic the displacement driven compression applied to the cellular plate during the experimental compression test. The boundary conditions of the cellular plate are:

$$v(0, y, z) = v(L, y, z) = 0 \tag{3.3a}$$

$$w(0, y, z) = w(L, y, z) = 0 \tag{3.3b}$$

$$u(0, y, z) = 0 \tag{3.3c}$$

$$u(L, y, z) = Constant \tag{3.3d}$$

where u, v and w are translational degrees of freedom in x, y, and z directions, respectively, and "*Constant*" represents the displacement driven compression. Either linear isotropic elasticity or Neo-Hookean elasticity can be considered as the constitutive law to model the onset of buckling in elastomeric cellular materials [58]. The stress-strain ($\sigma - \varepsilon$) relation according to linear isotropic elasticity can be written as:

$$\sigma_{ij} = \frac{E}{(1+v)}\varepsilon_{ij} + \frac{vE}{(1+v)(1-2v)}\delta_{ij}\varepsilon_{kk} \tag{3.4}$$

where E and υ are, respectively, elastic modulus and Poisson's ratio and δ_{ij} is the Kronecker delta. On the other hand, based on Neo-Hookean elasticity, stress-strain can be approximated as [58]

$$\sigma_{ij} \approx 4C_1\left(\varepsilon_{ij} - \frac{1}{3}\varepsilon_{kk}\delta_{ij}\right) + 2D_1\varepsilon_{kk} \tag{3.5}$$

where C_1 and D_1 are shear modulus and incompressibility parameter, respectively. Comparing the FEM results of eigen buckling of a cellular plate made of 10×10 square cells modeled by each of the constitutive laws in

Table 3-1 verifies that both models predict almost the same value for the onset of buckling load. As a result, we adopt a linear isotropic elasticity model for presenting our results in this paper. It is also assumed that the constituent material will not yield or fail before buckling. The solid constitutive material of the cellular materials is considered to be a two-component silicone

	$S.R. = 20$		$S.R. = 6.7$		$S.R. = 2.5$	
Relative Density	Linear Isotropic	Neo-Hookean	Linear Isotropic	Neo-Hookean	Linear Isotropic	Neo-Hookean
0.10	$4.27 \times 10{-}6$	$4.05 \times 10{-}6$	$1.39 \times 10{-}5$	$1.32 \times 10{-}5$	$3.79 \times 10{-}5$	$3.61 \times 10{-}5$
0.20	$4.11 \times 10{-}5$	$4.09 \times 10{-}5$	$1.37 \times 10{-}5$	$1.36 \times 10{-}4$	$3.77 \times 10{-}4$	$3.75 \times 10{-}4$
0.30	$6.99 \times 10{-}5$	$6.96 \times 10{-}5$	$5.13 \times 10{-}4$	$5.12 \times 10{-}4$	$1.57 \times 10{-}3$	$1.57 \times 10{-}3$
0.40	$9.79 \times 10{-}5$	$9.77 \times 10{-}4$	$1.48 \times 10{-}3$	$1.47 \times 10{-}3$	$4.11 \times 10{-}3$	$4.10 \times 10{-}3$
0.50	$1.31 \times 10{-}4$	$1.31 \times 10{-}4$	$3.03 \times 10{-}3$	$3.03 \times 10{-}3$	$8.71 \times 10{-}3$	$8.71 \times 10{-}3$
0.60	$1.70 \times 10{-}4$	$1.70 \times 10{-}4$	$4.00 \times 10{-}3$	$4.00 \times 10{-}3$	$1.65 \times 10{-}2$	$1.64 \times 10{-}2$
0.70	$2.18 \times 10{-}4$	$2.18 \times 10{-}4$	$5.11 \times 10{-}3$	$5.11 \times 10{-}3$	$2.87 \times 10{-}2$	$2.87 \times 10{-}2$
0.80	$2.81 \times 10{-}4$	$2.80 \times 10{-}4$	$6.53 \times 10{-}3$	$6.53 \times 10{-}3$	$4.63 \times 10{-}2$	$4.63 \times 10{-}2$
0.90	$3.73 \times 10{-}4$	$3.73 \times 10{-}4$	$8.59 \times 10{-}3$	$8.59 \times 10{-}3$	$8.69 \times 10{-}2$	$8.69 \times 10{-}2$
1.00	$5.10 \times 10{-}4$	$5.10 \times 10{-}4$	$1.15 \times 10{-}2$	$1.15 \times 10{-}2$	$1.13 \times 10{-}1$	$1.13 \times 10{-}1$

elastomer, with the commercial name of *Zhermack Elite Double 8*, whose Young's modulus is $E \approx 220kPa$ and Poisson's ratio is $\nu \approx 0.499$ [51].

In addition to implementing the detailed finite element analysis (eigen buckling and nonlinear elastic analysis) on cellular plates, we employ a hybrid structural method (**Appendix 3.A**) [59] and multiscale homogenization [60]) to predict the buckling response of cellular plates. This comparison (**Section 3.4.3**) reveals that the hybrid structural model fails to predict the in-plane buckling load in cellular materials.

Table 3-1- *Comparison between non-dimensional buckling load (N_{cr}) of cellular plates of* 10×10 *square cells made of Zhermack Elite Double 8 elastomers obtained by linear isotropic and neo-Hookean elasticity in linear eigen buckling analysis.*

	$S.R. = 20$		$S.R. = 6.7$		$S.R. = 2.5$	
Relative Density	Linear Isotropic	Neo-Hookean	Linear Isotropic	Neo-Hookean	Linear Isotropic	Neo-Hookean
0.10	4.27×10^{-6}	4.05×10^{-6}	1.39×10^{-5}	1.32×10^{-5}	3.79×10^{-5}	3.61×10^{-5}
0.20	4.11×10^{-5}	4.09×10^{-5}	1.37×10^{-5}	1.36×10^{-4}	3.77×10^{-4}	3.75×10^{-4}
0.30	6.99×10^{-5}	6.96×10^{-5}	5.13×10^{-4}	5.12×10^{-4}	1.57×10^{-3}	1.57×10^{-3}
0.40	9.79×10^{-5}	9.77×10^{-4}	1.48×10^{-3}	1.47×10^{-3}	4.11×10^{-3}	4.10×10^{-3}
0.50	1.31×10^{-4}	1.31×10^{-4}	3.03×10^{-3}	3.03×10^{-3}	8.71×10^{-3}	8.71×10^{-3}
0.60	1.70×10^{-4}	1.70×10^{-4}	4.00×10^{-3}	4.00×10^{-3}	1.65×10^{-2}	1.64×10^{-2}
0.70	2.18×10^{-4}	2.18×10^{-4}	5.11×10^{-3}	5.11×10^{-3}	2.87×10^{-2}	2.87×10^{-2}
0.80	2.81×10^{-4}	2.80×10^{-4}	6.53×10^{-3}	6.53×10^{-3}	4.63×10^{-2}	4.63×10^{-2}
0.90	3.73×10^{-4}	3.73×10^{-4}	8.59×10^{-3}	8.59×10^{-3}	8.69×10^{-2}	8.69×10^{-2}
1.00	5.10×10^{-4}	5.10×10^{-4}	1.15×10^{-2}	1.15×10^{-2}	1.13×10^{-1}	1.13×10^{-1}

3.4.2 Experimental Set-up

To carry out an experimental test in which the in-plane and out-of-plane buckling behavior of architected cellular materials can be captured, a cellular plate is made out of a commercial

elastomer, *Zhermack Elite Double 8*. As explained in **Appendix 3.B**, the elastomer is cast into a 3D printed mold so that the cellular plate with the desired cell microarchitecture is prepared for mechanical testing. The cellular plate is placed in a uniaxial testing machine (ADMET-SM-250-961 with 1kN load cell) and is subjected to a uniaxial compressive load. The compressive load is applied by moving down the top face of the cellular plate with a uniform speed of $1\,{}^{mm}/_{sec}$ aligned with the quasi-static loading condition considered in our numerical analysis. Plotting the reaction force at the top face versus the top face displacement, the buckling load is reported as the maximum reaction force before the first load drop in the force-displacement curve.

3.4.3 Comparison Study

To verify the FEM results, the buckling loads obtained from three different numerical analyses, including FEM eigen buckling, FEM nonlinear static, and homogenized TSDT, are compared with our experimental results in **Figure 3-2**. In the detailed FEM nonlinear static analysis, a uniform displacement is incrementally applied at the top face, and the reaction force is measured at the opposite fixed face. Similar to the experimental analysis, the reaction force at the fixed face is plotted versus the top face displacement in the x −direction and the buckling load is considered as the maximum reaction force before the first drop in the force-displacement curve. Another analysis presented in **Figure 3-2** is dedicated to the buckling load obtained by homogenized TSDT (hybrid structural method), a plate theory appropriate for structural analysis of moderately-thick composites, which requires computational time much less than the detailed 3D FEM. In the current TSDT analysis, the cellular structure is replaced by an equivalent solid plate whose effective properties are obtained by standard mechanics homogenization (**Appendix 3.A**). The boundary conditions for the equivalent solid plate, called the "homogenized TSDT" model in **Figure 3-2**,

are considered to be clamped in the direction of applying compressive force (x −direction) and free at two other edges (y −direction).

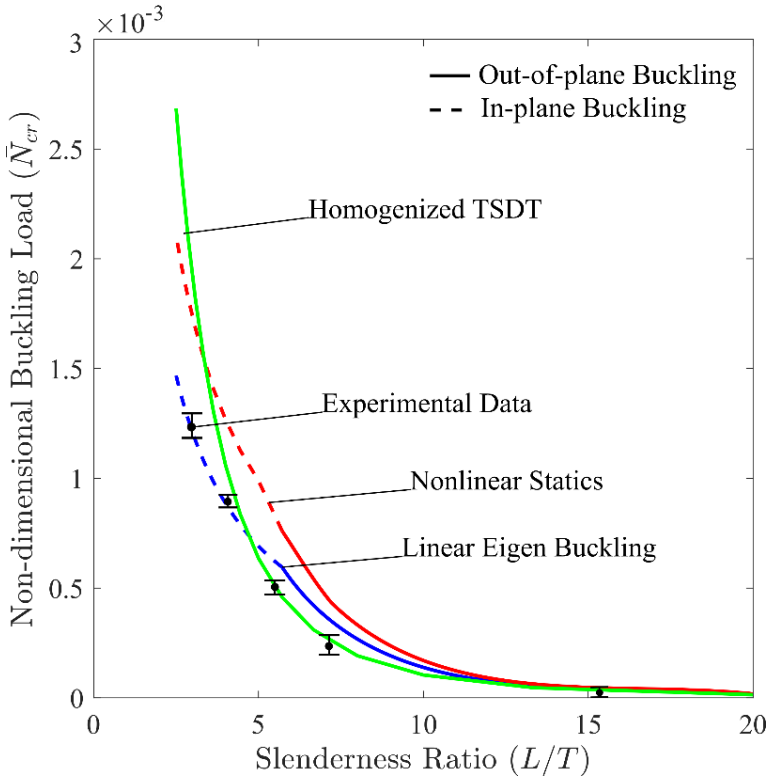

Figure 3-2- *Comparison of the buckling load of a cellular plate of* 5×5 *square cells with* $\rho_{rel,total} = 0.6$ *and* $L = H = 0.1m$ *predicted by liner eigen buckling, nonlinear static, and hybrid structural (Homogenized TSDT) analyses as well as experimental compression testing.*

Figure 3-2 confirms that the ANSYS linear eigen buckling predictions are in good agreement with experimental data both for in-plane and out-of-plane buckling. The maximum deviation between experimental results and eigen buckling analysis is 11% for $S.R. \geq 5$ and it decreases as the slenderness ratio decreases. For $S.R. < 5$, where the cellular plate experiences in-plane buckling under uniaxial compression, the percentage error is as low as 3%. A detailed nonlinear static finite element analysis also demonstrates the same trend for buckling behavior with a slight difference

in terms of the value of critical buckling load compared to the linear eigen buckling predictions. This difference decreases by increasing the slenderness ratio when the buckling is majorly "out-of-plane,"; e.g., while percentage error is 30% for $S.R.=3$ (in-plane buckling), it is 10% for $S.R.=15$ (out-of-plane buckling). **Figure 3-2** shows that the numerical results obtained by homogenized TSDT is in a good agreement with both experimental and linear eigen buckling analyses only for the out-of-plane buckling of the cellular plate; however, the method is not capable of predicting the in-plane buckling load and the associated buckling mode shape. The mode shapes of buckled cellular plates obtained by the linear eigen buckling, nonlinear static modeling, and experimental compression testing are compared in **Table *3-2*** to showcase the accuracy of the numerical model not only for predicting the critical buckling load but also for the buckled mode shape of cellular plates. It can be seen that both linear eigen buckling and nonlinear static analyses show the same mode shape as the one found in the experiment.

Table 3-2- *Comparison between the mode shapes of buckled elastomeric cellular plates from different finite element analyses and experimental testing.*

	Analysis Type		
	Nonlinear Static	Linear Eigen Buckling	Experiment
$S.R.=3$ *(In-plane buckling)*	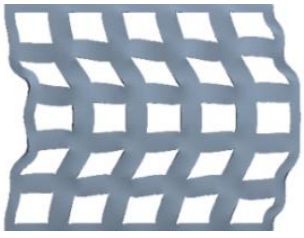	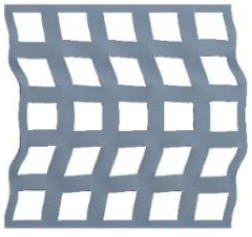	

$S.R. = 7$ *(Out-of-plane Buckling)*	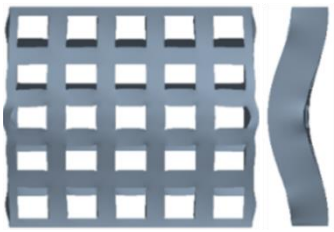	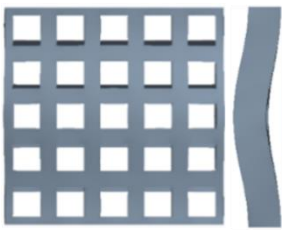	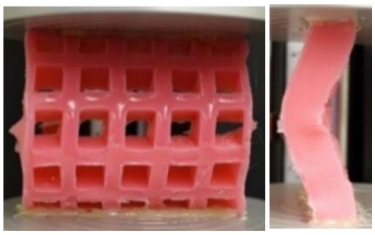

3.5 Results and Discussion

In this section, the results are obtained using ANSYS eigen buckling simulation, and they are organized into three categories. First, the effect of different microarchitectural parameters, e.g. slenderness ratio, relative density, void shape, and the number of cells, on the buckling load of cellular plates and the transition between in-plane and out-of-plane modes are investigated. Second, the potential of graded architected cellular materials for enhancing both in-plane and out-of-plane buckling loads of the cellular plates is illustrated. Finally, two different graded architected cellular plates are prototyped and examined to show how the gradual variation of the microarchitecture can improve the buckling load.

3.6 In-plane and Out-of-plane Buckling in Homogeneous Cellular Materials

The effect of the slenderness ratio ($S.R.$) of the homogenous cellular plate, made of uniformly distributed square cells on the critical buckling load is shown in **Figure 3-3**. As shown in **Figure 3-3a**, increasing $S.R.$ decreases the critical buckling load and also changes the buckling mechanism from an in-plane instability to an out-of-plane one. Besides, it is observed that the transition between in-plane and out-of-plane buckling occurs in a lower relative density when the structure is slenderer (higher $S.R.$). **Figure 3-3b** clearly demonstrates that homogenous cellular

plates are more likely to buckle in-plane when the slenderness ratio of the plate decreases. The in-plane buckling load is less dependent on the slenderness ratio of the plate ($S.R.$) and is more dependent of the slenderness ratio of constituent cells ($S.R._{cell}$). Therefore, by increasing the thickness of the plate, T, the out-of-plane buckling load increases more than the in-plane buckling load, and eventually, the out-of-plane buckling load becomes higher than the in-plane buckling load, making the in-plane buckling load the dominant buckling mode.

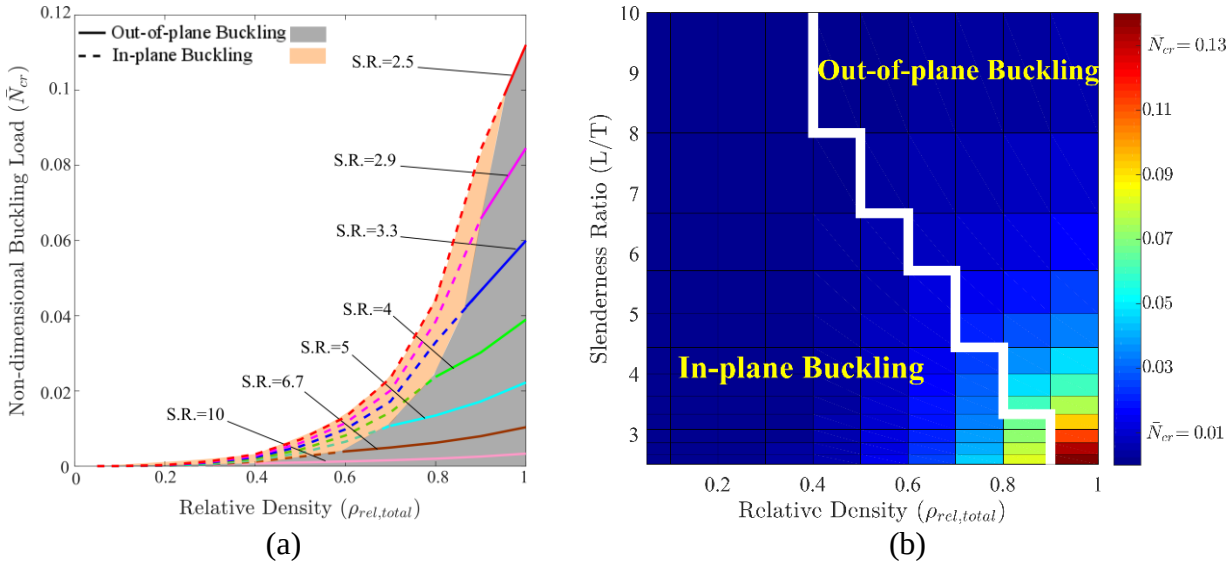

Figure 3-3- *Non-dimensional critical buckling load for* 10×10 *square cellular plate with square void shapes: (a) The variation of* $\bar{N}_{cr}$ *with relative density and (b) Phase diagram for in-plane and out-of-plane buckling load.*

The in-plane and out-of-plane buckling behavior of a cellular plate are affected by the cell topology of the constitutive unit cell. The mode shapes of the out-of-plane buckling of cellular plates of alternative cell topologies are the same; however, their in-plane buckling patterns are dissimilar and depend on their microarchitectures. To show the dependency of the in-plane buckling pattern on cell topology, we select six different cell topologies, i.e., square, circular, diamond, star, honeycomb, and re-entrant (auxetic), and present their in-plane buckling mode shapes in **Table 3-3**. When the critical load for in-plane buckling is reached, a rapid change occurs in the

microarchitecture of the cellular plate. Except for honeycomb, we can mention that in-plane buckling patterns are independent of the relative density, provided that the cellular plate does not buckle out-of-plane. It can be seen that the in-plane buckling patterns are considerably dependent on the cell microarchitecture. While cellular plates made of square or re-entrant cells show large scale lateral deformation at the onset of in-plane buckling, cells of the circular, diamond and star topologies show compaction behavior at the instant of in-plane buckling. Honeycomb cells, as opposed to the rest of the cell topologies considered in **Table 3-3**, reveal a localized deformation when they buckle in-plane.

Table 3-3- *In-plane buckling patterns for cellular plates of different cell topologies with* $\rho_{rel,total} = 0.5$ *(Except Star topology in which* $\rho_{rel,total} = 0.75$ *).*

	Cell Topology Equation	Cell Topology	In-plane Buckling Mode Shape
Square	$x = y = C^*$	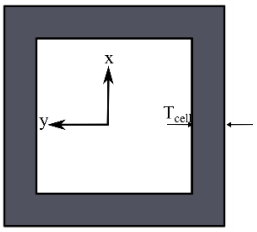	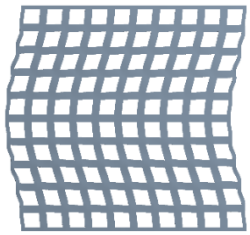
Circle	$x^2 + y^2 = C$	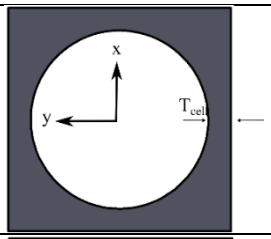	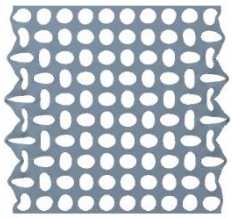
Diamond	$\lvert x\rvert + \lvert y\rvert = C$	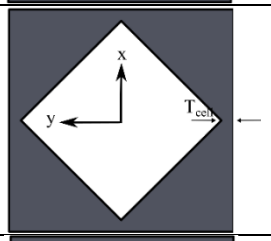	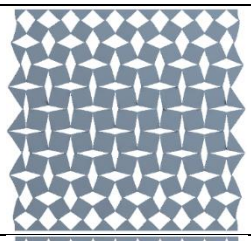
Star	$x^{\frac{2}{3}} + y^{\frac{2}{3}} = C$	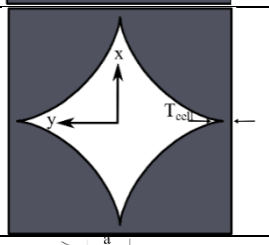	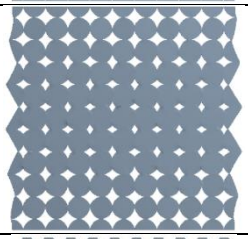
Honeycomb	$\frac{a}{b} = \sin(120) + \cos(120)$ $T_{cell} = C$	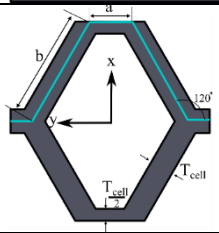	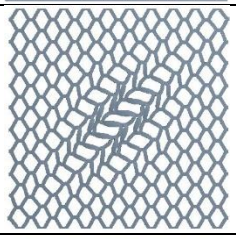
Re-entrant (Auxetic)	$\frac{a}{b} = \sin(60) + \cos(60)$ $T_{cell} = C$	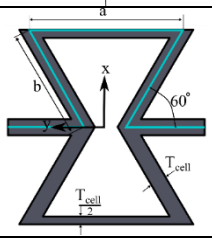	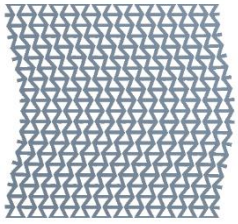

** The constant parameter* C *for each cell is determined by the relative density.*

To further investigate the effect of cell topology on the buckling behavior of cellular plates, **Figure 3-4** presents the buckling load for six different cell topologies for a wide range of relative densities achievable by each cell topology. In this figure, points A and B indicate the achievable limits for each cell topology; it is not possible to design a cell topology with a relative density less than the relative density of A or more than the relative density of B. It can be seen that the honeycomb cell has the highest in-plane buckling load for cellular plates with low relative densities ($\rho_{rel} \leq 0.5$). The transition between in-plane and out-of-plane buckling modes of honeycomb cellular plates happens at the lowest relative density among the other cell topologies. Among the cell topologies with the same relative density, other than honeycombs, those cells with a higher minimum cell wall thickness, T_{cell}, have a higher in-plane buckling load. Opposed to the other five cell topologies, a cellular plate with a re-entrant cell topology with the geometry specified in **Table 3-3**, always buckles in-plane, and the dependence of critical buckling load on the relative density is the least among all the cell topologies considered in this paper.

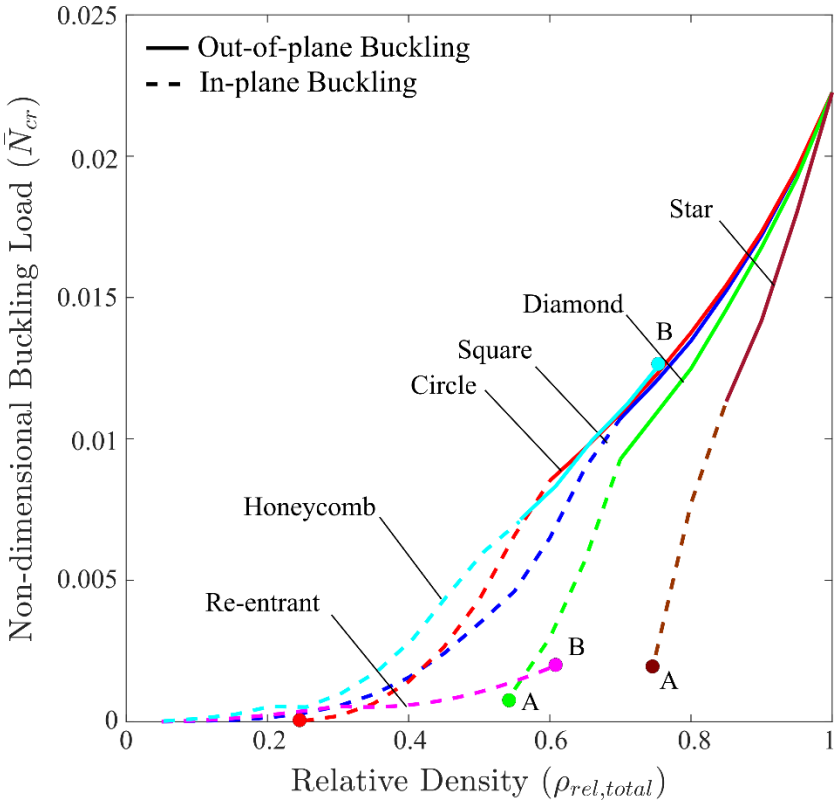

Figure 3-4- *Effect of cell topology on non-dimensional critical buckling load, $\bar{N}_{cr}$, for 10×10 square cellular plates with $S.R. = 5$.*

Figure 3-5 and**Figure 3-6** present the effect of the number of cells on the buckling behavior of the homogenous cellular plates. **Figure 3-5** shows that the effect of the number of square cells on the critical buckling load and the buckling mode is negligible for a cellular plate with the same number of cells in x and y directions ($M_x = M_y$). In the case of out-of-plane buckling, this behavior is due to the fact that the out-of-plane buckling behavior mainly depends on the slenderness ratio of the cellular plate. Moreover, the slenderness ratio of cells ($S.R._{cell}$) remains unchanged by increasing the number of cells in both directions; therefore, the critical in-plane buckling load of the cellular plate does not change either.

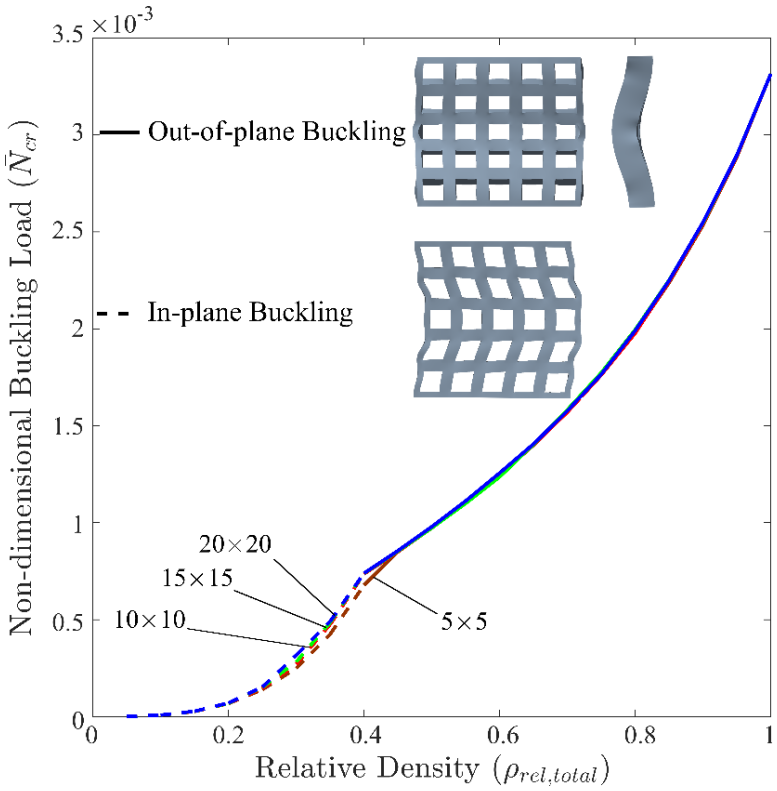

Figure 3-5- *Non-dimensional buckling load, $\bar{N}_{cr}$, of homogenous cellular plates with a square void shape and $S.R. = 10$.*

Figure 3-6 presents the effect of changing the number of cells in one direction on the buckling behavior of cellular plates with the same total dimensions. It is found that increasing the number of cells in x direction (M_x), which is the direction of compressive load, leads to an increase in the buckling load when the buckling mode is in-plane. When the number of cells in y direction (M_y) is constant, increasing the number of cells in x direction (M_x) could change the buckling mode from an in-plane mode to an out-of-plane one. When the out-of-plane buckling mode is reached, increasing M_x does not affect the buckling load considerably. Increasing the number of cells in y direction (M_y), which is perpendicular to the direction of compressive load, decreases the buckling load as long as the dominant buckling mode is in-plane instability. For a higher M_y, the transition of buckling mode from in-plane to out-of-plane occurs at a higher M_x. It is worth

mentioning that the cell topology of the cellular plate is considered to be rectangular with an aspect ratio of $\frac{L_x}{L_y} = \frac{M_y}{M_x}$, where L_x and L_y are the length and width of rectangular cells in x and y directions, respectively.

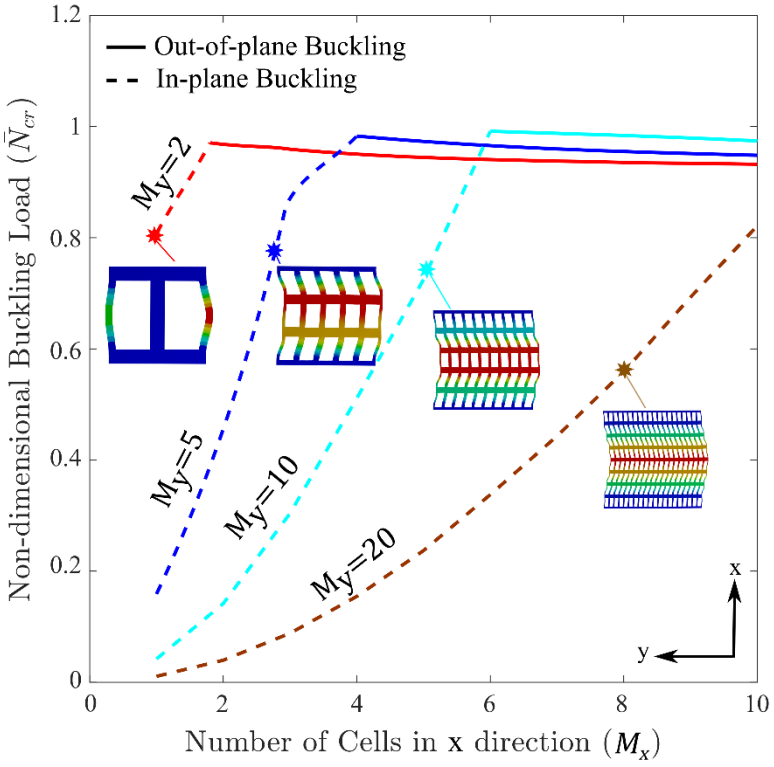

Figure 3-6- *Effect of the number of cells in different directions on the buckling load of cellular plates with rectangular voids,* $S.R. = 10$ *and* $\rho_{rel,total} = 0.5$.

3.6.1 Buckling Behavior of Functionally Graded Cellular (FGC) Plates

In this section, the possibility of improving the buckling behavior of cellular plates by varying the relative density across the cellular medium is investigated. It is shown that by tailoring the relative density according to an appropriate function, both in-plane and out-of-plane buckling loads of cellular plates can be increased. The variation of density of each cell is considered to be according to the following general function:

$$\rho(\alpha) = \rho_1 + (\rho_0 - \rho_1)\left(1 - \frac{\alpha}{\alpha_0}\right)^n \quad (3\text{-}6)$$

where α can be either x or y coordinate, ρ_0 is the relative density at the origin ($x = 0,\ y = 0$) and ρ_1 is the extreme value of relative density at $\alpha = \alpha_0$; the center of each cell is considered as its coordinate. **Figures 3-7** and **3-8** show the effect of different variation functions on the critical buckling load of FGC plates in both in-plane and out-of-plane regimes.

Figure 3-9 compares the critical buckling load for eight different variation functions of FGC plates and a homogenous cellular plate. The value of relative densities of ρ_0 and ρ_1 are determined based on the total relative density ($\rho_{rel,total}$) the absolute value of the difference between ρ_0 and ρ_1 for all cases is considered to be constant and equal to 0.2 ($|\rho_0 - \rho_1| = 0.2$). The variation of relative density for each function is shown by a color map next to the function, while the parameters for each variation functions F_1 to F_8 are given in **Table 3-4**. It is seen that by the variation functions introduced in **Table 3-4**, the buckling load of FGC plates can be increased or decreased while the total weight of the cellular plate remains the same. However, in most cases, the buckling load of FGC plates with this set of gradient functions is lower than the corresponding value for a homogenous cellular plate. It has been recently reported that the optimized variation of cells in the out-of-plane directions is the most efficient strategy for increasing the out-of-plane buckling load of FGC plates [13].

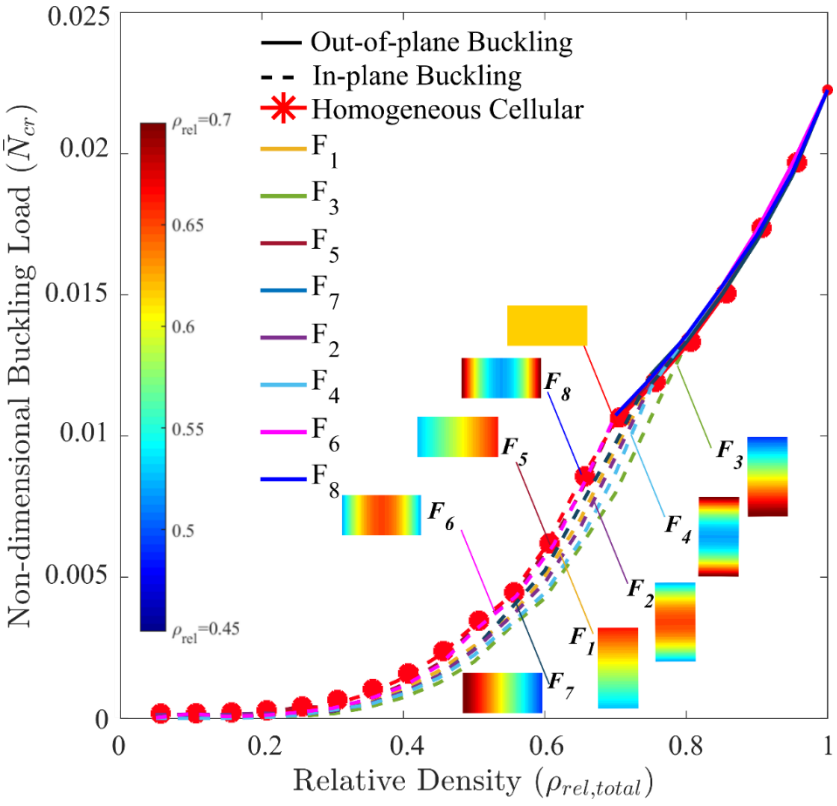

Figure 3-7- *Buckling load of* 10×10 *FGC plates with* $S.R. = 5$ *for different density variation functions.*

Table 3-4- *Parameters for defining different functions used in Eq. (3.6) and* ***Figure*** *3-7.*

	F_1	F_2	F_3	F_4	F_5	F_6	F_7	F_8
α	x	x	x	x	y	y	y	y
α_0	L	$\frac{L}{2}$	L	$\frac{L}{2}$	W	$\frac{W}{2}$	W	$\frac{W}{2}$
n	1	2	1	2	1	2	1	2
$\rho_1 - \rho_0$	0.2	0.2	-0.2	-0.2	0.2	0.2	-0.2	-0.2

The effect of the difference between the minimum and maximum relative density ($\rho_1 - \rho_0$) in an FGC plate with the variation function F_6 or F_8 is presented in **Fig. 3-8**. The FGC plate is made of 10×10 cells, where the relative density of each cell varies across the FGC plate, according to Eq.

(3.6). On one hand, **Fig. 3-8a** shows that the FGC plates with $\rho_1 > \rho_0$ tend more to buckle in-plane; the in-plane buckling load also decreases monotonically by increasing $|\rho_1 - \rho_0|$Across the FGC plate. On the other hand, when $\rho_1 < \rho_0$, the in-plane buckling load does not change monotonically with the variation of $|\rho_1 - \rho_0|$. For $\rho_1 < \rho_0$, by increasing the absolute value of $\rho_1 - \rho_0$, the in-plane buckling loads increase first by 8, 11, and 13% for cellular plates with a total relative density of 0.4, 0.5, and 0.6, respectively. FGC plates with higher relative densities i.e. $\rho_{rel,total} = 0.7$ and $\rho_{rel,total} = 0.8$, buckle out-of-plane when they are homogeneous cellular. The out-of-plane and in-plane buckling loads in these cellular plates are slightly affected by the relative density gradient ($\rho_1 - \rho_0$); however, the buckling mode changes from out-of-plane to in-plane when $|\rho_1 - \rho_0|$ is more than a critical value, e.g. for $\rho_{rel,tot} = 0.5$ and $\rho_1 > \rho_0$.

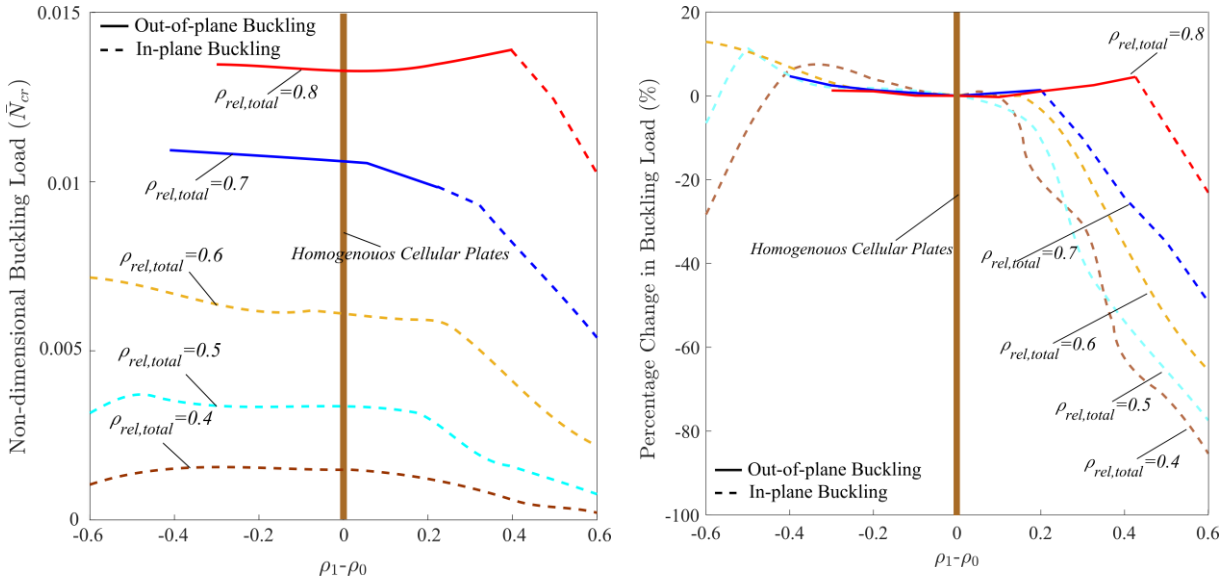

Figure 3-8*- Effect of difference between the maximum and minimum relative density ($\rho_1 - \rho_0$) on the buckling behavior of FGC plates with the square void, $S.R. = 5$ and the variation function F_6 or F_8: (a) Non-dimensional Buckling load and (b) Percentage Change with respect to a homogenous cellular plate.*

Figure 3-9 also presents the result for buckling behavior of FGC plates with circular holes to investigate the possibility of increasing the buckling load for cellular plates with void topologies other than square cells, as presented in **Fig. 3-8**. The numerical results show that the buckling load of the cellular plates with circular void shapes cannot be considerably increased by varying the relative density across the cellular plate. This result reveals that the improvement in the buckling load using the concept of FGCMs is very much dependent on the void shape of the architected cellular materials.

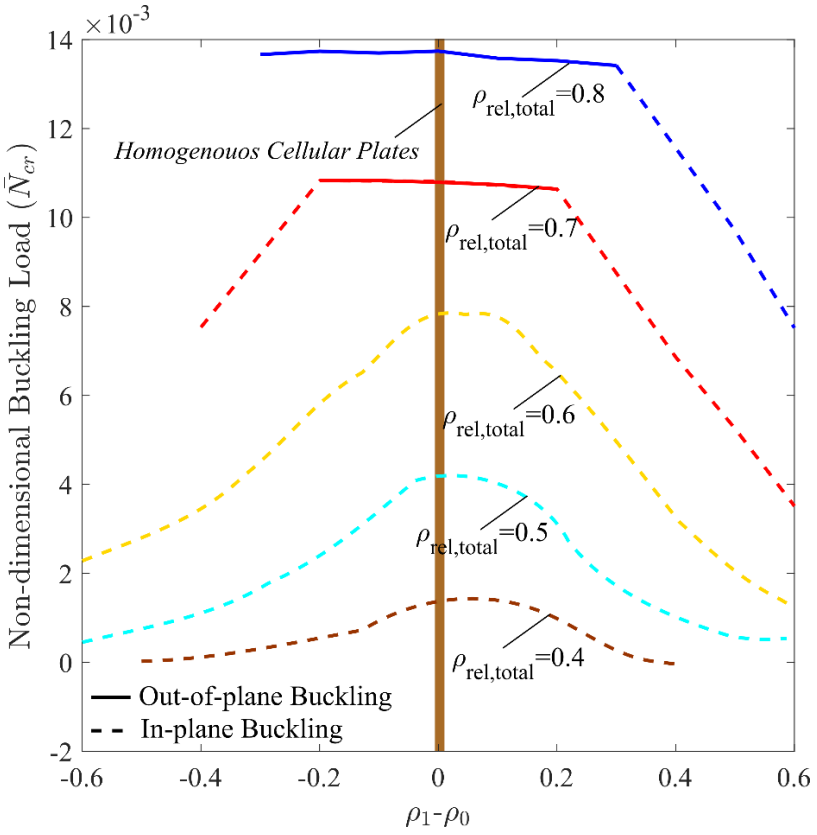

Figure 3-10*- Effect of difference between the maximum and minimum relative density ($\rho_1 - \rho_0$) on the non-dimensional load of FGC plates with $S.R. = 5$ and circular holes based on the variation function F_6 or F_8.*

3.6.2 Experimental Analysis of Buckling Behavior of Elastomeric FGC Plates

Two FGC plates and one homogenous cellular plate are prepared out of the two-component silicone elastomer, *Zhermack Elite Double 8*, and experimentally tested to show the capability of FGCMs in changing the critical buckling load of a cellular plate. One homogenous cellular and two 5×5 FGC (Variation function F_6 and $\rho_1 - \rho_0 = 0.6$) plates with $S.R. = 4.45$ are fabricated with $\rho_{rel,total} = 0.6$. They are tested under quasi-static uniaxial compression. The experimental and numerical results for buckling load and buckled mode shapes are presented in

Table 3-5. It can be seen that for the FGC1 plate, with maximum relative density in the middle of y direction, the buckling load is 32% higher than the homogenous cellular plate. On the other hand, the buckling mode shapes reveal that while the buckling load of the FGC1 plate is higher than the FGC2, the deformation is more localized in the FGC1 plate, which means that fewer number of cells carry a bigger portion of the compressive load and initiate the buckling behavior. The mode shape predicted by FEM is in good agreement with the experimental results confirming that the linear eigen buckling analysis can successfully predict the buckling mode shape in cellular plates. Nonetheless, the error in the value of buckling load obtained by FEM is as high as 35% for FGC samples; the culprit is mainly the manufacturing defects within the FGC samples. The comparison of experimental and numerical load-displacement curve associated with the three architected cellular plates reveals that not only can the buckling load of cellular plates be controlled by grading their microarchitecture, but the quasi-static energy absorption capability of cellular materials could also be tuned by the concept of FGCM. This exciting phenomenon needs further detailed studies to develop multifunctional cellular solids with a high energy absorption capability.

Table 3-5- *Critical buckling load and mode shape of three* 5×5 *architected cellular plates with the same weight*

		FGC1	Homogenous Cellular	FGC2
Non-dimensional Buckling Load ($\bar{N}_{cr}$)	Experiment	8.60×10^{-4}	7.68×10^{-4}	5.22×10^{-7}
	FEM	11.97×10^{-4}	8.08×10^{-4}	7.02×10^{-4}
Buckling Mode Shape	Experiment		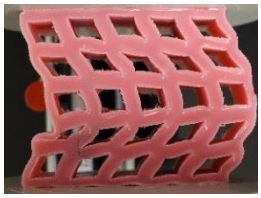	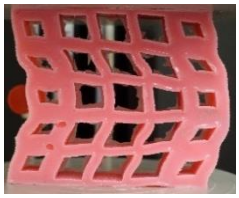
	FEM	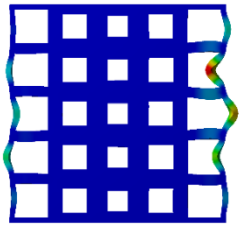	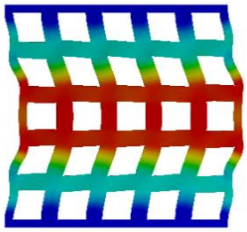	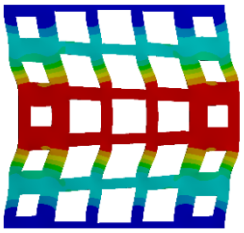
Load-Displacement Curve	Experiment	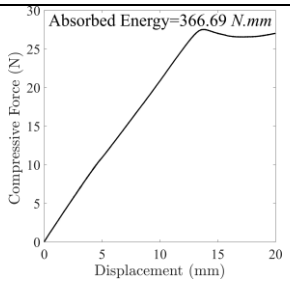	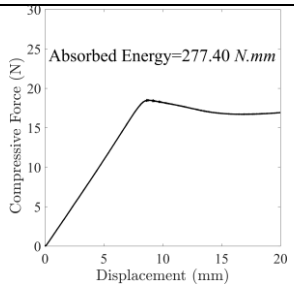	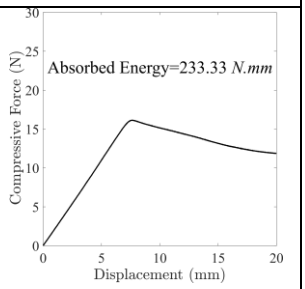

3.7 Conclusions

In this study, the in-plane and out-of-plane buckling modes in architected cellular materials are distinguished. We attempt to gain an insight into the critical parameters affecting the buckling behavior of architected cellular plates. Both FEM and experimental testing are implemented to study the effect of cell topology, relative density, slenderness ratio, and the number of cells on the

buckling load buckling mode and transition between the in-plane and out-of-plane buckling in architected cellular plates (**Figs. 3-3** to **3-6**). It is found that the cellular plates with a lower slenderness ratio or a lower relative density tend to in-plane buckling (**Fig. 3-3**). Architected cellular plates with the same relative density and different cell topologies exhibit different buckling behavior, especially in their in-plane buckling patterns; those cellular plates with slenderer constituent cells are more likely to buckle in-plane (**Fig. 3-4**). Finally, by implementing the concept of FGC plates, the effect of relative density gradient on the buckling behavior of architected cellular plates is investigated (**Figs. 3-7** to **3-9**). It is shown that both buckling loads and buckled mode shapes of architected cellular materials can be changed by using the concept of functionally graded cellular materials (**Fig. 3-8**). We have also designed and manufactured an architected optimized FGC plate whose buckling load is 20% more than a corresponding homogenous cellular plate with the same weight, by changing the relative density gradient across the cellular medium. This strategy can be exploited to design architected advanced materials with tunable energy absorption and shape-matching properties in multiple scales, as in [61].

3.8 Appendix 3.A

The representative volume element (RVE) of cellular material is replaced by an equivalent solid material whose effective properties are the same as the primitive cell to use third-order shear deformation theory (TSDT) [59] for predicting the buckling load of a cellular plate. Therefore, the standard mechanics homogenization is implemented to find the equivalent stiffness properties, $\hat{C}_{ijmn}$, of a cellular material [62]:

$$\hat{C}_{ijmn} = \frac{1}{V_{RVE}} \int C_{ijkl} M^{C}_{klmn} dV \tag{3.A1}$$

where C_{ijmn} $(i, j, k, l, m, n = 1,2,3)$ is the stiffness tensor, V_{RVE} represents the volume of unit cell or RVE and M^{C}_{mnkl} is the local structural tensor defined as:

$$\varepsilon_{ij} = M^{C}_{ijkl} \hat{\varepsilon}_{kl} \tag{3.A2}$$

where ε_{ij} is the strain tensor and the circumflex accent identifies the effective stiffness properties $\hat{C}_{ijkl}$ or an average strain field $\hat{\varepsilon}_{ij}$. In the current study, the 3D components of the local stiffness tensor are evaluated by using Eq. (3.A1) and by applying six independent 3D unit strains to a periodic cube of unit dimensions through APDL coding in ANSYS version 18.2, where the 3D unit cell is meshed with 20-node 3D SOLID185 elements.

Equations of plates are obtained here based on TSDT [59], while FEM is used to solve the governing differential equations and to predict the out-of-plane buckling load. Consequently, the generalized displacements, u_0, v_0, w_0, φ_x and φ_y are approximated over an element with effective properties by the following expressions [59]:

$$u_0(x, y, t) = \sum_{i=1}^{m} U_i^e(t) \psi_i^e(x, y) \tag{3.A3a}$$

$$v_0(x, y, t) = \sum_{i=1}^{m} V_i^e(t) \psi_i^e(x, y) \tag{3.A3b}$$

$$w_0(x, y, t) = \sum_{i=1}^{m} \overline{\Delta}^e_{k_i}(t) \eta_i^e(x, y) \tag{3.A3c}$$

$$\varphi_x(x, y, t) = \sum_{i=1}^{m} \emptyset_{x_i}^{e}(t) \psi_i^e(x, y) \tag{3.A3d}$$

$$\varphi_y(x,y,t) = \sum_{i=1}^{m} \emptyset_{y_i}^{e}(t)\psi_i^e(x,y) \tag{3.A3e}$$

where ψ_i^e and η_i^e are the Lagrangian and Hermitian interpolation functions, respectively; U_i^e, V_i^e, $\overline{\Delta}_{k_i}^e$, $\emptyset_{x_i}^{e}$ and $\emptyset_{y_i}^{e}$ are the nodal degrees of freedom associated with displacement degrees of freedom. The rectangular conforming element is chosen for this study, where four nodal values are associated with w_0:

$$\overline{\Delta}_{1_i}^e = w_0, \quad \overline{\Delta}_{2_i}^e = w_{0,x}, \quad \overline{\Delta}_{3_i}^e = w_{0,y}, \quad \overline{\Delta}_{4_i}^e = w_{0,xy} \tag{3.A4}$$

Clamped boundary conditions are adopted at edges with $x = 0, L$ to mimic the experimental compression test, and the 3D detailed finite element modeling conducted in ANSYS, and free boundary conditions are assumed at edges with $y = 0, W$. Substituting Eq. (3.3) into the weak form of the governing differential equations leads to the following finite element model [63]:

$$[K]\{\Delta\} - \lambda[G]\{\Delta\} = 0 \tag{3.A5}$$

where $[K]$ and $[G]$ are 32×32 stiffness and stability matrices of each element, respectively, $\{\Delta\}$ is the displacement vector, and λ is the eigenvalue of Eq. (3.A5) which is equivalent to the eigen buckling load of the cellular plate. More details about the elements of each matrix can be found in Reference [59].

3.9 Appendix 3.B

The liquid elastomer is prepared according to the instruction guide of *Zhermack Elite Double 8* and cast in a 3D printed mold made of PLA polymer. The elastomer is completely set after 20

minutes. The 3D printed mold is disassembled, and the elastomeric cellular plate is ready for experimental tests. For the fabrication of elastomeric plates made of FGCMs, the geometrical features of internal members are arbitrarily changed. **Fig. 3-B1** shows the 3D model of the mold and cast elastomeric cellular plates.

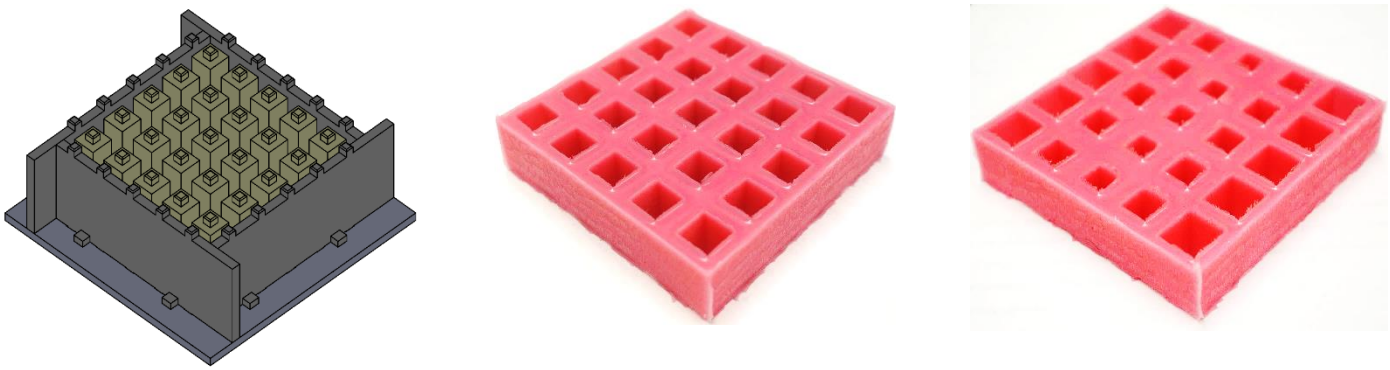

(a) (b) (c)

Figure 3-B1- *(a) 3D model of mold for casting cellular plates, (b) Molded elastomeric homogenous cellular plate, and (c) Molded elastomeric FGC plate*

3.10 Acknowledgment

A.H. Akbarzadeh acknowledges the financial support by McGill University and Natural Sciences and Engineering Research Council of Canada (NSERC) through NSERC Discovery Grant RGPIN-2016-0471.

3.11 References

[1] L.J. Gibson, M.F. Ashby, Cellular Solids: Structure and Properties, Cambridge University Press1999.

[2] F. Robert, An isotropic three-dimensional structure with Poisson's ratio--1, Journal of Elasticity 15 (1985) 427-430.

[3] L. Wollmann, A.K. Nayak, S.S.P. Parkin, C. Felser, Heusler 4.0: Tunable Materials, Annual Review of Materials Research 47(1) (2017) 247-270.

[4] K. Bertoldi, M.C. Boyce, Wave propagation and instabilities in monolithic and periodically structured elastomeric materials undergoing large deformations, Physical Review B 78(18) (2008) 184107.

[5] M. Ruzzene, F. Scarpa, F. Soranna, Wave beaming effects in two-dimensional cellular structures, Smart materials and structures 12(3) (2003) 363.

[6] T.L. Warren, Negative Poisson's ratio in a transversely isotropic foam structure, Journal of Applied Physics 67(12) (1990) 7591-7594.

[7] T.C. Lim, Functionally graded beam for attaining Poisson-curving, Journal of Materials Science Letters 21(24) (2002) 1899-1901.

[8] A. Ajdari, P. Canavan, H. Nayeb-Hashemi, G. Warner, Mechanical properties of functionally graded 2-D cellular structures: A finite element simulation, Materials Science and Engineering: A 499(1) (2009) 434-439.

[9] D. Chen, J. Yang, S. Kitipornchai, Elastic buckling and static bending of shear deformable functionally graded porous beam, Composite Structures 133 (2015) 54-61.

[10] Y. Hou, Y.H. Tai, C. Lira, F. Scarpa, J.R. Yates, B. Gu, The bending and failure of sandwich structures with auxetic gradient cellular cores, Composites Part A: Applied Science and Manufacturing 49 (2013) 119-131.

[11] L. Boldrin, S. Hummel, F. Scarpa, D. Di Maio, C. Lira, M. Ruzzene, C.D.L. Remillat, T.C. Lim, R. Rajasekaran, S. Patsias, Dynamic behaviour of auxetic gradient composite hexagonal honeycombs, Composite Structures 149 (2016) 114-124.

[12] S. Arabnejad Khanoki, D. Pasini, Multiscale Design and Multiobjective Optimization of Orthopedic Hip Implants with Functionally Graded Cellular Material, Journal of Biomechanical Engineering 134(3) (2012) 031004-031004-10.

[13] H. Niknam, A.H. Akbarzadeh, D. Rodrigue, D. Therriault, Architected multi-directional functionally graded cellular plates, Materials & Design 148 (2018) 188-202.

[14] S.D. Papka, S. Kyriakides, In-plane compressive response and crushing of honeycomb, Journal of the Mechanics and Physics of Solids 42(10) (1994) 1499-1532.

[15] S.D. Papka, S. Kyriakides, Biaxial crushing of honeycombs*Part I: Experiments, International Journal of Solids and Structures (1998) 4367-4396.

[16] S.D. Papka, S. Kyriakides, Biaxial crushing of honeycombs, International Journal of Solids and Structures 36(29) (1999) 4367-4396.

[17] A.M.W. Jaeung Chung, In-plane biaxial crush response of polycarbonate honeycombs, 127(February) (2001) 180-193.

[18] S.D. Papka, S. Kyriakides, Experiments and full-scale numerical simulations of in-plane crushing of a honeycomb, Acta Materialia 46(8) (1998) 2765-2776.

[19] S.D. Papka, S. Kyriakides, In-plane crushing of a polycarbonate honeycomb, International Journal of Solids and Structures 35(3-4) (1998) 239-267.

[20] X.E. Guo, L.J. Gibson, T.A. McMahon, W.C. Hayes, Post Yield Behaviour of Intact and Damaged Honeycombs: A Finite Element Study, 41(1) (1999) 85-105.

[21] T. Yokozeki, Y. Shimizu, M. Ishii, K. Kimizuka, S. Suzuki, Y. Yamasaki, K. Terashima, T. Kamita, T. Aoki, Mechanical behavior in compression of skin-added X-lattice composite panel with corrugated ribs, Composite Structures 168 (2017) 863-871.

[22] N. Triantafyllidis, M.W. Schraad, Onset of failure in aluminum honeycombs under general in-plane loading, Journal of the Mechanics and Physics of Solids 46(6) (1998) 1089-1124.

[23] Y. Aminanda, B. Castanié, J.J. Barrau, P. Thevenet, Experimental analysis and modeling of the crushing of honeycomb cores, Applied Composite Materials 12(3-4) (2005) 213-227.

[24] F. Scarpa, S. Blain, T. Lew, D. Perrott, M. Ruzzene, J.R. Yates, Elastic buckling of hexagonal chiral cell honeycombs, Composites Part A: Applied Science and Manufacturing 38(2) (2007) 280-289.

[25] J. Chung, A.M. Waas, Compressive Response of Honeycombs Under In-Plane Uniaxial Static and Dynamic Loading, Part 1: Experiments, AIAA Journal 40(5) (2002) 966-973.

[26] J. Chung, a.M. Waas, Compressive response of honeycombs under in-plane uniaxial static and dynamic loading. II - Simulations, AIAA Journal 40 (2002) 974-980.

[27] A. Ajdari, H. Nayeb-Hashemi, A. Vaziri, Dynamic crushing and energy absorption of regular, irregular and functionally graded cellular structures, International Journal of Solids and Structures 48(3) (2011) 506-516.

[28] D. Zhang, Q. Fei, P. Zhang, In–plane dynamic crushing behavior and energy absorption of honeycombs with a novel type of multi-cells, Thin-Walled Structures 117 (2017) 199-210.

[29] B. Russell, V. Deshpande, H. Wadley, Quasistatic deformation and failure modes of composite square honeycombs, Journal of mechanics of materials and structures 3(7) (2008) 1315-1340.

[30] J.X. Liu, S.C. Deng, J. Zhang, N.G. Liang, Lattice type of fracture model for concrete, Theoretical and Applied Fracture Mechanics 48(3) (2007) 269-284.

[31] L.J.A.M.F. Gibson, T.C. Triantafillou, Failure surfaces for cellular materials under multixial loads - I. Modelling, Int. J. Mech. Sci. 31(9) (1989) 635-663.

[32] L.J. Gibson, Biomechanics of cellular solids, Journal of Biomechanics 38(3) (2005) 377-399.

[33] H.L. Fan, D.N. Fang, F.N. Jing, Yield surfaces and micro-failure mechanism of block lattice truss materials, Materials and Design 29(10) (2008) 2038-2042.

[34] Q. Sui, H. Fan, C. Lai, Failure analysis of 1D lattice truss composite structure in uniaxial compression, Composites Science and Technology 118 (2015) 207-216.

[35] Q. Zheng, D. Jiang, C. Huang, X. Shang, S. Ju, Analysis of failure loads and optimal design of composite lattice cylinder under axial compression, Composite Structures 131 (2015) 885-894.

[36] M.E. Rackliffe, D.W. Jensen, W.K. Lucas, Local and global buckling of ultra-lightweight IsoTruss?? structures, Composites Science and Technology 66(2) (2006) 283-288.

[37] H. Fan, D. Fang, L. Chen, Z. Dai, W. Yang, Manufacturing and testing of a CFRC sandwich cylinder with Kagome cores, Composites Science and Technology 69(15-16) (2009) 2695-2700.

[38] E.V. Morozov, A.V. Lopatin, V.A. Nesterov, Finite-element modelling and buckling analysis of anisogrid composite lattice cylindrical shells, Composite Structures 93(2) (2011) 308-323.

[39] V.V. Vasiliev, V.A. Barynin, A.F. Razin, Anisogrid composite lattice structures – Development and aerospace applications, Composite Structures 94(3) (2012) 1117-1127.

[40] G. Totaro, Local buckling modelling of isogrid and anisogrid lattice cylindrical shells with hexagonal cells, Composite Structures 95(2) (2013) 403-410.

[41] G. Totaro, Local buckling modelling of isogrid and anisogrid lattice cylindrical shells with hexagonal cells, Composite Structures 95 (2013) 403-410.

[42] G. Totaro, F.D. Nicola, P. Caramuta, Local buckling modelling of anisogrid lattice structures with hexagonal cells : An experimental verification, Composite Structures 106 (2013) 734-741.

[43] N. Ohno, D. Okumura, H. Noguchi, Microscopic Symmetric Bifurcation Analysis for Cellular Solids Based on a Homogenization Theory of Finite Deformation. 1st Report. Theory, Transactions of the Japan Society of Mechanical Engineers Series A 67(656) (2001) 618-624.

[44] T. Mullin, S. Deschanel, K. Bertoldi, M.C. Boyce, Pattern transformation triggered by deformation, Physical Review Letters 99(8) (2007) 1-4.

[45] S. Willshaw, T. Mullin, Pattern switching in two and three-dimensional soft solids, Soft Matter 8(6) (2012) 1747-1750.

[46] K.L. Chen, Y.P. Cao, M.G. Zhang, X.Q. Feng, Indentation-triggered pattern transformation in hyperelastic soft cellular solids, Comptes Rendus - Mecanique 342(5) (2014) 292-298.

[47] Y. He, S. Guo, Z. Liu, K.M. Liew, Pattern transformation of thermo-responsive shape memory polymer periodic cellular structures, International Journal of Solids and Structures 71 (2015) 194-205.

[48] J.T.B. Overvelde, S. Shan, K. Bertoldi, Compaction Through Buckling in 2D Periodic, Soft and Porous Structures: Effect of Pore Shape, Advanced Materials 24(17) (2012) 2337-2342.

[49] J. Hu, Y. He, J. Lei, Z. Liu, Novel mechanical behavior of periodic structure with the pattern transformation, Theoretical and Applied Mechanics Letters 3(5) (2013) 054007-054007.

[50] B. Haghpanah, J. Papadopoulos, D. Mousanezhad, H. Nayeb-Hashemi, A. Vaziri, Buckling of regular, chiral and hierarchical honeycombs under a general macroscopic stress state, Proceedings of the Royal Society A: Mathematical, Physical and Engineering Sciences 470(2167) (2014) 20130856-20130856.

[51] B. Florijn, C. Coulais, M. Van Hecke, Programmable mechanical metamaterials, Physical Review Letters 113(17) (2014) 1-5.

[52] B. Florijn, C. Coulais, M. van Hecke, Programmable mechanical metamaterials: the role of geometry, Soft Matter 12(42) (2016) 8736-8743.

[53] Y. He, Y. Zhou, Z. Liu, K.M. Liew, Pattern transformation of single-material and composite periodic cellular structures, Materials & Design 132 (2017) 375-384.

[54] K. Bertoldi, P.M. Reis, S. Willshaw, T. Mullin, Negative Poisson's Ratio Behavior Induced by an Elastic Instability, Advanced Materials 22(3) (2010) 361-366.

[55] D. Yang, L. Jin, R.V. Martinez, K. Bertoldi, G.M. Whitesides, Z. Suo, Phase-transforming and switchable metamaterials, Extreme Mechanics Letters 6 (2016) 1-9.

[56] K. Bertoldi, M.C. Boyce, Mechanically triggered transformations of phononic band gaps in periodic elastomeric structures, Physical Review B 77(5) (2008) 052105-052105.

[57] J.N. Reddy, Mechanics of laminated composite plates and shells: theory and analysis, CRC press2004.

[58] A.N. Gent, Elasticity, Engineering with Rubber (Third Edition), Hanser2012, pp. 37-88.

[59] J. Reddy, Analysis of functionally graded plates, International Journal for Numerical Methods in Engineering 47(1-3) (2000) 663-684.

[60] A.H. Akbarzadeh, J.W. Fu, L. Liu, Z.T. Chen, D. Pasini, Electrically conducting sandwich cylinder with a planar lattice core under prescribed eigenstrain and magnetic field, Composite Structures 153 (2016) 632-644.

[61] C. Zhang, A. Akbarzadeh, W. Kang, J. Wang, A. Mirabolghasemi, Nano-architected metamaterials: Carbon nanotube-based nanotrusses, Carbon 131 (2018) 38-46.

[62] B. Hassani, E. Hinton, A review of homogenization and topology opimization II—analytical and numerical solution of homogenization equations, Computers & structures 69(6) (1998) 719-738.

[63] J. Reddy, Z.-Q. Cheng, Three-dimensional thermomechanical deformations of functionally graded rectangular plates, European Journal of Mechanics-A/Solids 20(5) (2001) 841-855.

4 Chapter Four: Thermo-Mechanical Bending of Architected Functionally Graded Cellular Beams[1]

4.1 Preface

In our exploration of the mechanical response of the graded cellular structures, we investigated the bending and buckling of an FGC plate subjected to mechanical loading. We considered the effect of merely mechanical forces on the bending and buckling responses of the FGC structure in the first two chapters.

In **Chapter 4,** we continue investigating the behavior of an FGC structure working under another physical stimulus. Here, we study the effect of both thermal and mechanical loads on the bending response of an FGC beam. We examine the effect of temperature gradient on thermal stresses and bending deformation of different graded cellular beams.

[1] Reproduced with permission from Niknam, H., Akbarzadeh, A.H.; Thermo-Mechanical Bending of Architected Functionally Graded Cellular Beams; *Composite Part B: Engineering*, 174 (2019) 107060.

4.2 Abstract

This article investigates the effect of cell architecture on the bending behavior of architected cellular beams subjected to a thermo-mechanical load. The architected functionally graded cellular (FGC) beam is made of porous cells whose properties vary across the thickness or length of the beam. The FGC beam is modeled according to Reddy's third-order shear deformation theory (TSDT), and the effective thermo-mechanical properties are obtained by standard mechanics homogenization. The governing equations are solved by a finite element method, and deflection curves are presented for the architected cellular beams with relative density gradients, subjected to thermal and mechanical loads. Numerical results demonstrate that tailoring relative density through the thickness of an FGC beam can reduce the lateral deflection of lightweight beams to less than half; consequently, tuning the flexural stiffness of cellular structures without changing their total weight. Interestingly, numerical results reveal that the flexural deformation of an FGC beam subjected to a thermo-mechanical load can be controlled utilizing the variations function of cell architectures. We also present the optimized architectural variation and cell topologies, leading to the least flexible architected cellular beams for alternative thermo-mechanical loading conditions. This paper sheds light on the application of cellular-based mechanical metamaterials for programming the multifunctional behavior of beams.

4.3 Introduction

Cellular materials, known as the composite of air and solid, have recently received a great deal of attention from material scientists and structural designers [1]. Tailoring the architecture and material composition of cellular solids can control their overall mechanical stiffness, strength, thermal conductivity, and thermal expansion. For instance, a periodic cellular material with

triangular [2] and tetrahedral [3] cell topology made of sets of rods with different thermal expansion coefficients has been proposed to program the overall thermal expansion coefficient of architected cellular solids. Besides, a few research studies [4-7] have investigated the effect of cell architectures on the thermal conductivity of cellular materials, exploring the possibility of designing materials with anisotropic thermal conductivity. The unprecedented properties of periodic cellular solids have enabled engineers to design architected materials for bending the streamline of heat flux [8], concentrating and diffusing thermal energy [9-11], and thermal cloaking [12, 13].

From another point of view, beams, as a fundamental structural element, must resist against mechanical and thermal loads in various construction, aerospace, and automotive industries. There have been many studies on mathematical modeling [14-18], experimental testing [19-21], and analyzing [22-24] beams under various thermal loading conditions. Initial studies were focused on metals with isotropic thermo-mechanical properties [25, 26], where classic Euler and Timoshenko beam theories were adopted to predict the mechanical behavior of slender beams [27, 28]. The desire for developing lightweight structures led to the application of advanced composite laminates as the base materials for structural elements [29]. As a result, the new higher-order shear deformation theories were developed to analyze moderately-thick structural elements made of anisotropic composites [30-32]. Following advances in material processing, two-phase ceramic-metal functionally graded materials (FGMs) with a smooth variation of one phase (particulate or any form of heterogeneity) in a continuous phase (matrix) were first proposed in the 1980s to combine temperature resistance and fracture toughness in composite materials [33, 34]. However, multi-material manufacturing techniques are yet to be developed to fabricate multi-phase FGMs with arbitrary and continuous variation of one phase (fiber/inclusion) into another phase (matrix).

The thermo-mechanical response of structures made of FGMs has been largely studied not only due to their improved structural performance but also because of the generality of the mathematical formulations governing their structural behavior. These studies investigated the stress distribution [35-37], in-plane and out-of-plane deformation [38-42], and structural stability [43, 44] of the FGM structures subjected to arbitrary thermo-mechanical loads. The thermal loading can include uniform [42, 44], linear [36, 38, 40], and nonlinear [45-47] temperature variation across structures made of materials with graded properties. These studies have investigated the effect of various parameters, e.g., material distribution profile, geometric nonlinearity, and cross-section geometries. It has been shown that geometric nonlinearity does not play a significant role in the bending behavior of FGM structures unless the applied loading is large [46]. The effects of in-plane constraints on the flexure of FGM beams have been less prominent than out-of-plane boundary conditions [38].

Although few studies have investigated mechanical responses of cellular materials with a periodic distribution of cells as structural elements [48-50], the response of lightweight architected cellular structures subjected to combined thermo-mechanical loading has yet to be explored. The objective of this study is to illuminate how these cellular materials perform as the constitutive materials of cellular structures. Advanced manufacturing techniques, like additive manufacturing [51] and laser cutting [52], opened new opportunities to manufacture cellular materials of arbitrary architectures, so-called *Functionally graded cellular materials* (FGCMs) [49, 53]. Consequently, this study aims to investigate the effect of variation of microarchitectural features in FGCMs on the flexural behavior of meta-structures. Functionally graded cellular (FGC) beams made of two-dimensional (2D) and three-dimensional (3D) cell architectures, with relative density variation across thickness and length, are studied (**Section 4.4**). The governing equations of the FGC beam are driven based

on a third-order shear deformation theory (TSDT) [54], in which the effective stiffness and thermal conductivity are obtained by standard mechanics homogenization (**Section 4.5 and 4.6**) [55]. According to this approach, each cell of a cellular beam is replaced with a solid of the same mechanical and thermal properties. In the results and discussion section (**Section 4.7**), first, commercial ANSYS finite element software is used to validate the developed methodology; then, the thermo-mechanical response of FGC beams is studied for different heterogeneous microarchitectures. The possibility of tailoring the architecture of cellular beams to obtain desirable flexural behavior is demonstrated. The variation of relative density across an architected cellular beam is shown to control structural stiffness or flexibility of cellular structures under thermo-mechanical loads without changing the total weight of structures. Numerical results reveal the possibility of programming the deformation mode and curvature of architected cellular beams by adopting a proper relative density variation for certain loading and boundary conditions.

4.4 Geometry definition

An architected cellular beam with length L, width W, and thickness H (along $x-$, $y-$, and $z-$directions) is considered to investigate the thermo-mechanical flexure of cellular materials, as shown in **Figure 4-1.**

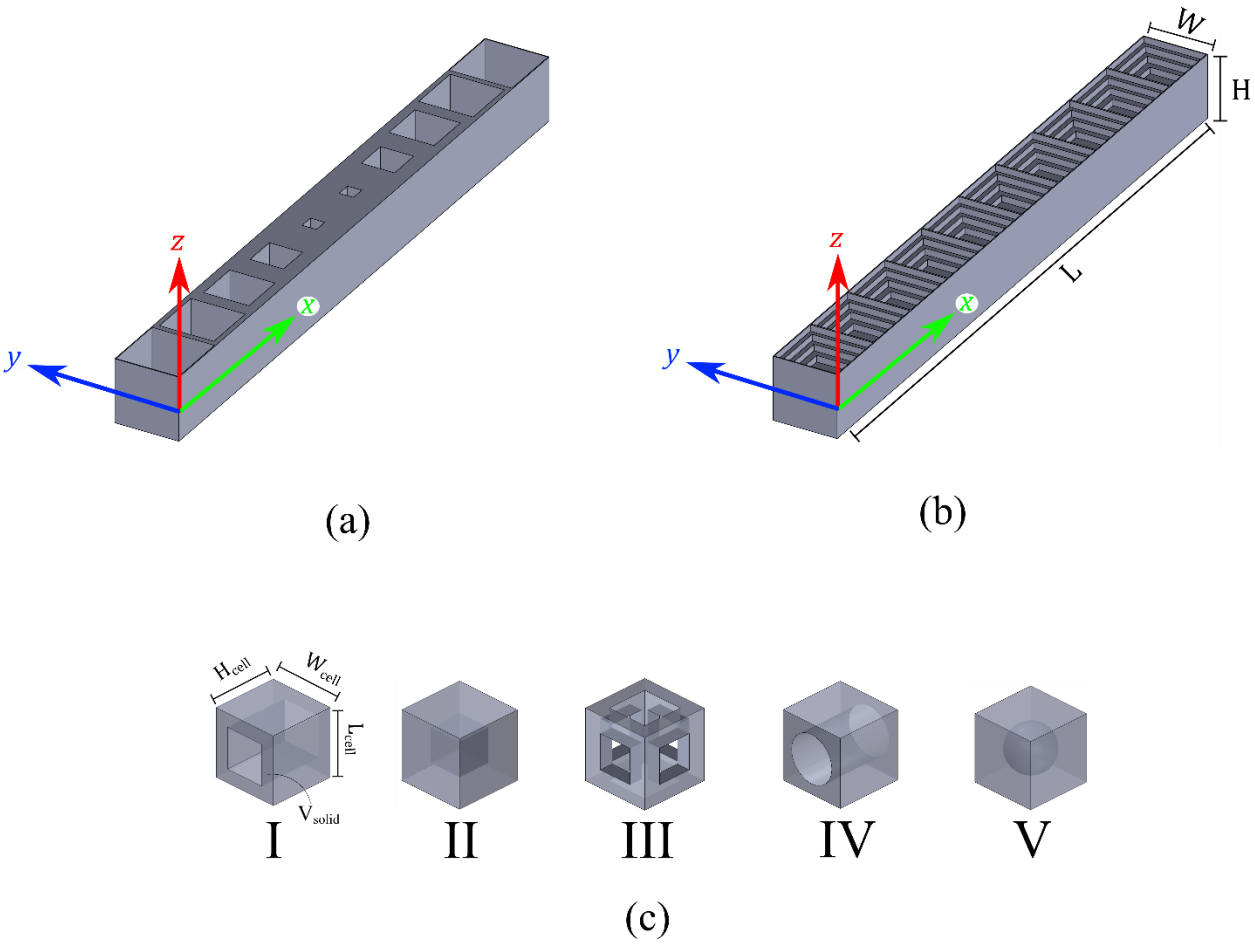

Figure 4-1- *Schematic view of FGC beams: (a) x −directional FGC beam, (b) z −directional FGC beam, and (c) Different cell topologies constructing the FGC beam.*

We consider one cell in the width direction (y −direction) and $2N$ cells in x − and z −directions. The dimensions of the architected cellular beam are determined as follows:

$$W = W_{cell} \tag{4.1a}$$

$$L = 2NL_{cell} \tag{4.1b}$$

$$H = 2NH_{cell} \tag{4.1c}$$

One of the most critical parameters in defining the properties of a cellular solid is relative density (ρ). The relative density of each cell can be obtained by the following equation:

$$\rho_{cell} = \frac{V_{solid}}{V_{total}} = \frac{V_{solid}}{L_{cell} W_{cell} H_{cell}} \tag{4.2}$$

where V_{solid} and V_{total} are the volumes of solid materials and representative cells, respectively. As shown in **Figure 4-1**, we assume that the relative density changes in either length, x, or thickness, z, directions. Therefore, the total relative density of the architected cellular beam can be written as follows:

$$\rho_{total} = \sum_{i=1}^{2N} \frac{\rho_{cell,i}}{2N} \tag{4.3}$$

4.4.1 The relative density distribution function

In this study, we consider symmetric distribution for relative density. We define a double linear function with the extreme (maximum or minimum) relative density in the middle, as shown below:

$$\begin{aligned} &\rho_{cell,i} = \rho_{total} + \rho^* \left(\frac{2i - N - 1}{N - 1}\right), && for\ i \le N \\ &\rho_{cell,i} = \rho_{cell,2N-i+1}, && for\ N + 1 \le i \le 2N \end{aligned} \tag{4.4}$$

where $\rho_{cell,i}$ defines the relative density of the i^{th} cell in the FGC beam with $2N$ cells and ρ^* is a coefficient which determines the slope of the relative density variation; $\rho_{cell,i}$ should be within the limit of a minimum value (ρ_{min}), which has been assumed to be 0.01 in this study to reflect the manufacturability of cellular materials, and 1 (fully solid material). As a result, certain conditions are imposed on ρ^*:

$$|\rho^*| \le min\{(1 - \rho_{total}), (\rho_{total} - 0.01)\} \tag{4.5}$$

Eq. (4.4) presents different symmetric distribution profiles, as shown in **Figure 4-2**. It can be observed that ρ^* defines the slope of relative density variation, meaning that the higher the ρ^*, the

more significant difference between the relative density of side and middle cells. On the other hand, positive ρ^* indicates that the relative density of the middle cells is maximum, while the relative density of the side cells is maximum for negative ρ^*.

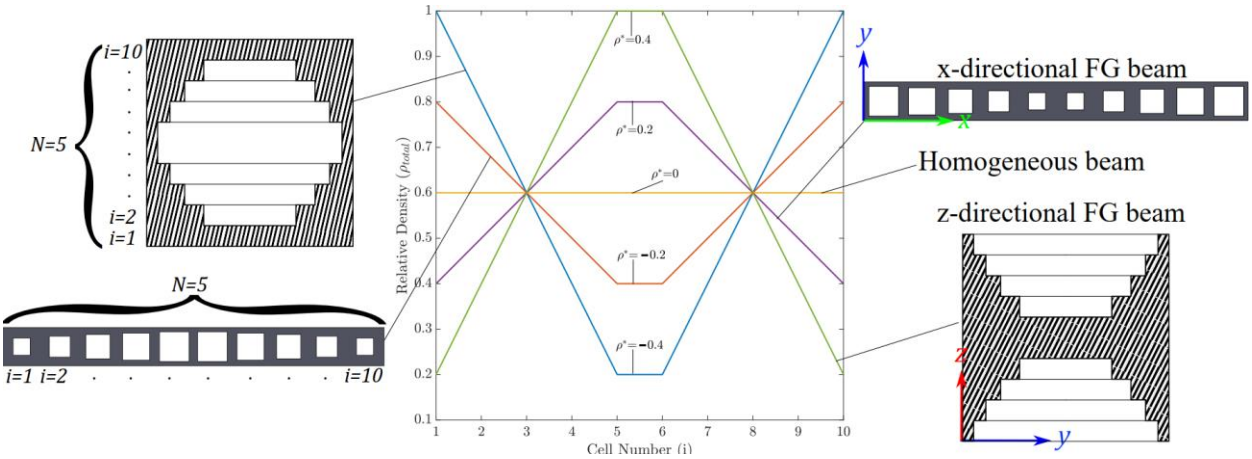

Figure 4-2- *Relative density distribution profiles provided by Eq. (4.4).*

4.5 Methodology

Two different approaches can be used to investigate the structural behavior of the architected FGC beams subjected to thermo-mechanical loads:

***Detailed 3D modeling*:** In this approach, the beam is modeled as a 3D structure, and the thermal and mechanical loads are applied to different faces and edges of the beam. In this approach, the governing equations are obtained by using 3D thermoelasticity instead of adopting conventional beam theories. While 3D detailed modeling yields the most accurate numerical results, this procedure is computationally expensive, making it inappropriate for numerical analysis of large-scale structures.

***Homogenized modeling*:** In this approach, each cell is replaced with an equivalent solid with effective thermoelastic properties. This method can expedite the computational procedure even though it has some limitations in taking local deformation (e.g., local buckling [53] and wrinkling [56]) into account. Consequently, the current method cannot capture the large deformation or plastic behavior of the beam. There are several homogenization techniques used to obtain the equivalent properties. In this study, we adopt the standard mechanics homogenization technique [57]. **Figure 4-3** depicts a homogenized $z-$directional FGC beam where the heterogeneous cellular structure is replaced with solid layers of effective material properties.

In the current study, homogenized modeling is mainly used to investigate the thermo-mechanical behavior of architected cellular beams. The homogenized mechanical and thermal properties of cells are first obtained, and these effective thermoelastic properties are used in the governing equations of the FGC beam. Finally, the finite element formulation is implemented to discretize the governing equation to obtain the deformation of the FGC beam. In several cases, the results of the homogenized modeling approach are compared with the detailed 3D approach, conducted by the Commercial ANSYS software, to evaluate the accuracy of homogenized modeling results.

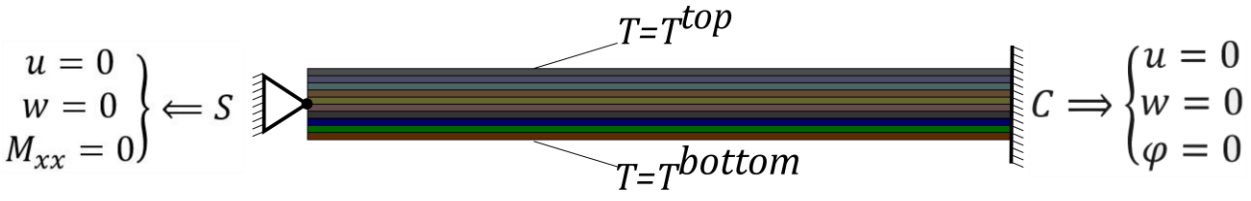

Figure 4-3- *Thermal and mechanical boundary conditions of the FGC beam.*

4.6 Problem definition based on homogenized modeling

4.6.1 Governing equation of beam

Two different loading conditions are considered in this study, i.e., thermal and/or mechanical loads. The thermal load is a temperature gradient through the thickness (z −direction), caused by prescribed temperature on the top ($z = \frac{H}{2}$) and/or bottom ($z = -\frac{H}{2}$) faces of the architected cellular beam. The mechanical loading is considered to be uniformly distributed (q) on the top face with the resultant force F_{total}, which is determined as follows:

$$F_{total} = qA_{top} \tag{4.6}$$

where A_{top} is the solid area of the top face of the cellular beam. In addition, the mechanical boundary conditions on the left ($x = 0$) or right side (L) of the architected cellular beam can be either Clamped (C), Simply-supported (S), or Free (F).

To evaluate mechanical deformation imposed by thermo-mechanical loading on the FGC beam, we need first to determine the temperature gradient caused by thermal loading. If we neglect the heat convection and heat irradiation, temperature distribution within the FGC beam is considered to follow the Fourier heat conduction as [58]

$$q^H = -k_{eff}\nabla T \tag{4.7}$$

where ∇ is the 3D del operator, q^H is heat flux vector, T is temperature, and k_{eff} is an effective thermal conductivity tensor determined by a homogenization technique (See **Section 4.4.6.2.1**). Using the Fourier heat conduction and the principle of conservation of energy, the steady-state heat conduction equation can be derived as shown below [58]:

$$\nabla.\left(k_{eff}\nabla T\right)=0 \tag{4.8}$$

By solving Eq. (4.8), one can obtain the temperature distribution of the equivalent solid body for architected cellular beams.

The governing equations of the FGC beam are obtained by using Reddy's TSDT [54, 59]:

$$N_{xx,x}=0 \tag{4.9a}$$

$$M_{xx,xx}+q=0 \tag{4.9b}$$

$$M_{xx,x}+\frac{4}{3H^2}\left(3R_x-P_{xx,x}\right)-Q_x=0 \tag{4.9c}$$

where N_{xx}, M_{xx}, and P_{xx} are normal stress resultants defined as:

$$\begin{Bmatrix}N_{xx}\\M_{xx}\\P_{xx}\end{Bmatrix}=\begin{bmatrix}A & B & E\\B & D & F\\E & F & H\end{bmatrix}\begin{Bmatrix}u_{,x}\\\varphi_{,x}\\-\frac{4}{3H^2}\left(\varphi_{,x}+w_{,xx}\right)\end{Bmatrix}-\begin{Bmatrix}N^T\\M^T\\P^T\end{Bmatrix} \tag{4.10}$$

and Q_x and R_x are shear stress resultants written as:

$$\begin{Bmatrix}Q_x\\R_x\end{Bmatrix}=\begin{bmatrix}A & D\\D & F\end{bmatrix}\begin{Bmatrix}\varphi+w_{,x}\\-\frac{4}{H^2}\left(\varphi+w_{,x}\right)\end{Bmatrix} \tag{4.11}$$

In Eqs. (4.10) and (4.11), u and w are, respectively, displacement components in $x-$ and $z-$directions, and φ is the rotation of mid-plane at $z=0$. The stiffness matrices are defined as shown:

$$\left([A],[B],[D],[E],[F],[H]\right)=\sum_{K=1}^{N}\int_{z_k}^{z_{k+1}}[\bar{C}](1,z,z^2,z^3,z^4,z^6)dz \tag{4.12}$$

N^T, M^T, and P^T are thermal stress resultants which are obtained based on the temperature distribution using the following formulation:

$$\begin{Bmatrix} N^T \\ M^T \\ P^T \end{Bmatrix} = \int_{-\frac{H}{2}}^{\frac{H}{2}} \alpha[\bar{C}] \begin{Bmatrix} 1 \\ z \\ z^3 \end{Bmatrix} \Delta T dz \tag{4.13}$$

where $\bar{C}$ is the matrix of elastic properties obtained by implanting a homogenization technique (see **Section 4.6.2.2**); α is the thermal expansion coefficient of the solid material which has the same value for cellular solids made of a single base material, regardless of the void geometry and relative density [60]. It is worth mentioning that thermal and mechanical properties are considered to be temperature-independent in this study, as temperature variation is assumed to be relatively small. However, in the case of large temperature variation or for base materials whose properties are highly temperature-dependent, thermal and mechanical properties should be considered a function of temperature. Such an assumption can lead to nonlinear equations for determining temperature distribution and deformation caused by thermo-mechanical bending [61, 62].

4.6.2 Standard mechanics homogenization

In this study, the effective elastic properties and thermal conductivity of architected cellular materials are obtained using standard mechanics homogenization, which is based on the finite element analysis of representative volume elements (RVEs) [57]. The methodology for obtaining these thermal and elastic properties is briefly described in this Section.

4.6.2.1 Effective thermal conductivity

According to the standard mechanics homogenization theory and by adopting the Fourier's law of heat conduction, the following thermal loadings are applied to RVE [55]:

$$(\overline{\nabla T})_i = \left(\frac{\overline{\partial T}}{\partial x}, \frac{\overline{\partial T}}{\partial y}, \frac{\overline{\partial T}}{\partial z}\right)_i = \begin{cases} (1,0,0), & i = 1 \\ (0,1,0), & i = 2 \\ (0,0,1), & i = 3 \end{cases} \tag{4.14}$$

where $\overline{\nabla T}$ indicates the average temperature gradient in an RVE, which is applied in different $x-$, $y-$ and $z-$directions for each loading case, $i = 1,2,3$, respectively. For each thermal loading case, the temperature of corresponding nodes on the remaining opposite faces of the RVE is set to be the same to fulfill the periodic boundary conditions. For instance, thermal loading and periodicity in $x-$direction is stated as $T(x_0, y, z) - T(x_0 + L, y, z) = L\frac{\partial T}{\partial x}$ while $T(x, y_0, z) - T(x, y_0 + W, z) = T(x, y, z_0) - T(x, y, z_0 + H) = 0$ [63]. Consequently, the effective thermal conductivity tensor can be obtained by [64]:

$$\bar{k}_{ij} = \frac{1}{V_{RVE}} \int k_{ik} M_{kj}^T dV_{RVE} \tag{4.15}$$

where k_{ik} $(i, j, k = 1,2,3)$ is the thermal conductivity tensor of the base material, V_{RVE} represents the RVE's volume, and M_{kj}^T is the local temperature tensor defined as follows:

$$\nabla T = M^T \overline{\nabla T} \tag{4.16}$$

Here ∇T is defined as temperature gradient at any point on RVE. It is worth mentioning that a similar approach can also be developed to take into account the effect of forced heat convection [65] and irradiation [66] on the heat transfer phenomena within periodic cellular solids.

4.6.2.2 Effective elastic properties

Similar to the effective thermal conductivity, periodic displacement boundary conditions should be applied on each side of RVE to evaluate the effective elastic properties. For example, the

boundary conditions and the loading in $x-$direction can be stated as $u(x_0, y, z) - u(x_0 + L, y, z) = L\frac{\partial u}{\partial x}$ while $u(x, y_0, z) - u(x, y_0 + W, z) = u(x, y, z_0) - u(x, y, z_0 + H) = 0$ [49]. Consequently, the effective elastic stiffness matrix is obtained by the equation below [55]:

$$\bar{C}_{ijkl} = \frac{1}{V_{RVE}} \int C_{ijmn} M^{C}_{mnkl} dV \tag{4.17}$$

where C_{ijmn} $(i, j, k, l, m, n = 1,2,3)$ is the stiffness tensor of base material and M^{C}_{mnkl} is the local elastic tensor defined as follows:

$$\varepsilon_{ij} = M^{C}_{ijkl} \hat{\varepsilon}_{kl} \tag{4.18}$$

In the present study, the 3D components of the effective thermal conductivity and elastic stiffness tensors are evaluated by implementing Eqs. (4.15) and (4.17) through a commercial finite element software, ANSYS version 18.2. This effective thermal and mechanical property for RVE with square voids is plotted in the **Appendix 4.A**.

4.6.3 Finite element (FE) formulation

The FE analysis is implemented to solve the governing differential equations for temperature distribution and bending deformation of FGC beams. In the first step, temperature distribution is obtained by discretizing and solving the heat conduction equation (Eq. (4.8)). The thermal stress resultants (N^T, M^T, and P^T) are then calculated and imported into the beam governing equations (Eqs. (4.9a) - (4.9c)) to form governing differential equations, which are discretized and solved by FE analysis. The details of the FE formulations are provided in this section.

4.6.3.1 FE formulation for temperature distribution

In this study, FEM is used at the beam level, while homogenization provides the local and upscaled properties of the beam. The temperature at the top and bottom surfaces are prescribed, as shown in **Figure 4-3**, while the other faces of FGC beams are assumed to be thermally insulated. Therefore, the temperature only varies across the thickness direction of FGC beams. If we assume a linear variation of temperature across each element, the temperature can be approximated as follows [67]:

$$T(x,y,z) = \sum_{i=1}^{m} T_i^e \psi_i^e\,(x,y,z) \tag{4.19}$$

where T_i^e is the nodal value of temperature and ψ_i^e is the Lagrangian interpolation function in 3D space. The substitution of Eq. (4.19) into Eq. (4.8) yields the following discretized set of equations:

$$[K^T]\{\mathrm{T}^e\} = \{\mathrm{F}^T\} \tag{4.20}$$

where $[K^T]$ is the thermal stiffness matrix and $\{\mathrm{F}^T\}$ is the thermal force vector calculated according to the prescribed thermal boundary conditions.

4.6.3.2 FE formulation of thermo-mechanical deformation

A similar approach is adopted to discretize the governing equation of the FGC beam under mechanical bending. The displacement components are approximated as follows [54, 67]:

$$u(x) = \sum_{i=1}^{m} U_i^e \psi_i^e\,(x) \tag{4.21a}$$

$$w(x) = \sum_{i=1}^{m} \overline{\Delta}_{k_i}^e \eta_i^e\,(x) \tag{4.21b}$$

$$\varphi(x) = \sum_{i=1}^{m} \emptyset_i^e \psi_i^e\,(x) \tag{4.21c}$$

where η_i^e is the Hermitian interpolation function and U_i^e, $\overline{\Delta}_{k_i}^e$, and $\emptyset_i^e$ are the nodal degrees of freedom. A conforming element is chosen for this study [54, 67]. Therefore, the nodal values associated with w are:

$$\overline{\Delta}_{1_i}^e = w_0, \qquad \overline{\Delta}_{2_i}^e = w_{0,x} \tag{4.22}$$

Substituting Eq. (4.21) into Eq. (4.9) leads to the following set of algebraic equations:

$$[K^M]\{\Delta\} = \{\mathrm{F}^{ME}\} + \{\mathrm{F}^{TH}\} \tag{4.23}$$

where $[K^M]$ is the mechanical stiffness matrix, $\{\mathrm{F}^{ME}\}$ is the mechanical force vector, and $\{\mathrm{F}^{TH}\}$ is the force caused by thermal expansion associated with temperature variation across the architected cellular beam.

It is worth mentioning that the thermoelastic properties of each cell are considered to vary in $x-$ or $z-$directions in the FGC beams. As a result, the constitutive matrices $A, B, D, E, F,$ and H are a function of $x-$coordinate. When the FE model is employed to solve the thermo-mechanical problem of FGC beams, the homogenized thermoelastic properties of each element are specified in accordance with the element position.

4.7 Results and discussion

In this Section, the numerical results for the bending of architected FGC beams subjected to thermo-mechanical loads are presented. The structural steel with the following thermal and mechanical properties is assumed as the base material of FGC beams: Elastic modulus $E_s = 200\mathrm{GPa}$, Poisson's ratio: $\nu_s = 0.3$, thermal expansion coefficient: $\alpha = 1.2 \times 10^{-5}\,\frac{1}{^{\circ}\mathrm{K}}$, and thermal

conductivity: $K_s = 60.5 \frac{\text{W}}{\text{m.K}}$. Unless otherwise stated, each cell dimension is considered to be $0.1L \times W \times 0.1H$ and 10 cells are assumed in both $z-$ and $-x$ directions. Also, the void topology is mainly assumed to be square extruded (Cell shape I in **Fig. 4-1**) except in **Figs. 4-11** and **4-12**, where alternative cell topologies are considered to construct FGC beams.

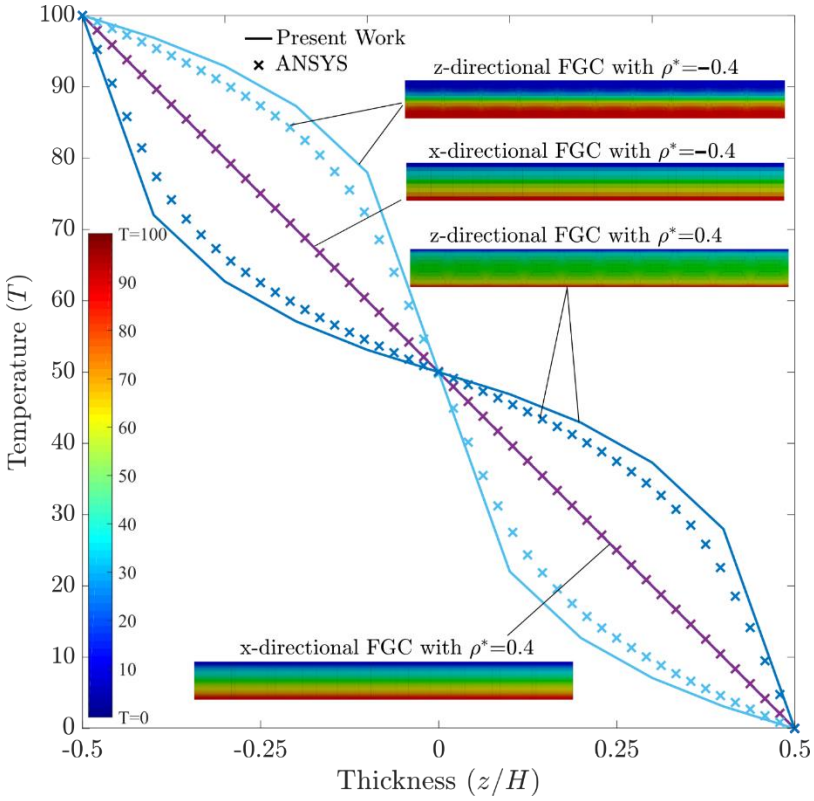

Figure 4-4- *Comparison of temperature distribution obtained by homogenized modeling and ANSYS detailed 3D FE modeling for FGC beams with* $\rho_{total} = 0.5$ *and thermal loading of* $T^{bottom} = 100$℃ *and* $T^{top} = 0$℃.

The deflection curves for the FGC beams, with the same total relative density $\rho_{total} = 0.5$ and subjected to the thermal loading are shown in **Figs. 4-5a** and **4-5b**, for different mechanical boundary conditions. An excellent agreement is found between the numerical results obtained based on the presented methodology and detailed FE analysis conducted by ANSYS. **Figure 4-5a** shows that the variation of relative density in $x-$ direction, as opposed to the z−direction, does

not have a significant effect on the deflection curve of FGC beams. However, for unsymmetrical boundary conditions (SC), x −directional variation of relative density can lead to substantial changes in the flexural behavior of FGC beams and even can change the beam curvature. This behavior is an exciting phenomenon that can be exploited to program deformation modes in metamaterials and meta-structures [68].

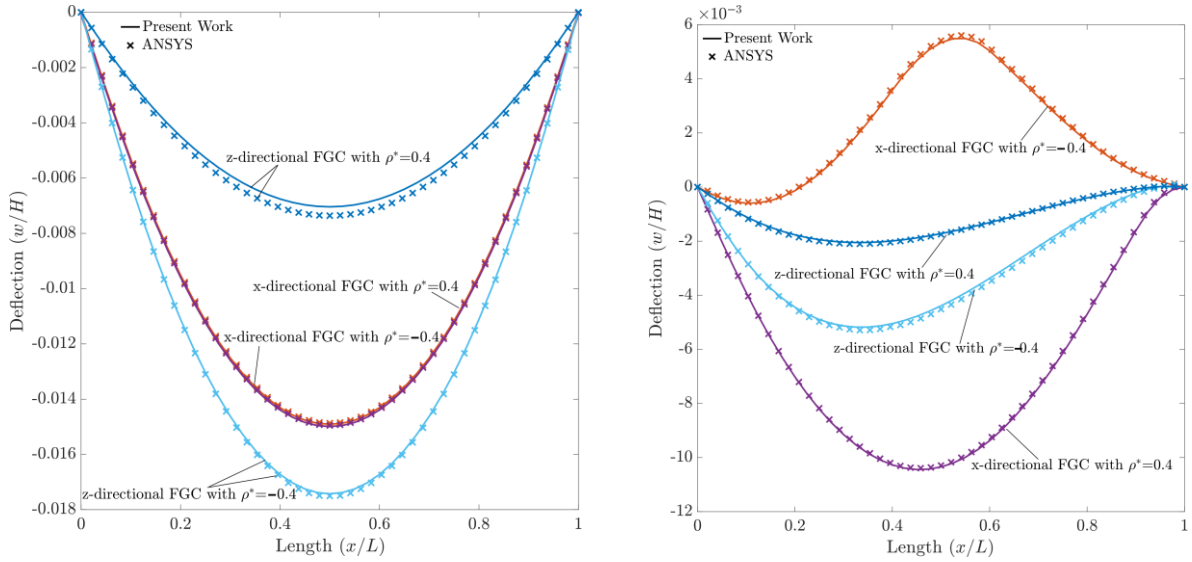

(a) (b)

Figure 4-5- *Comparison of deflection curves obtained by present work (hybrid homogenized modeling) and ANSYS detailed 3D FE modeling for FGC beams with* $\rho_{total} = 0.5$, *thermal loading of* $T^{bottom} = 100℃$ *and* $T^{top} = 0℃$ *and different* ρ^* *and mechanical boundary conditions; (a) SS and (b)* SC.

4.7.1 Benchmark results

Figures 4-6a and **4-6b** present the effect of ρ^* on the maximum deflection of z −directional FGC beams with SS boundary conditions and subjected to thermal and mechanical loads, respectively. **Figure 4-6a** shows that changing the total relative density, i.e., the weight of the architected beam does not alter the flexural behavior of homogenous ($\rho^* = 0$) cellular beams subjected to a

prescribed thermal load. This means that although increasing the total relative density of the architected beam makes it stiffer; the resultant thermal moment also increases to counterbalance the increase of stiffness. However, different behavior is observed when a mechanical load is applied to the homogenous cellular beam; the maximum deflection of the architected FGC beam decreases by increasing the relative density of the cellular material.

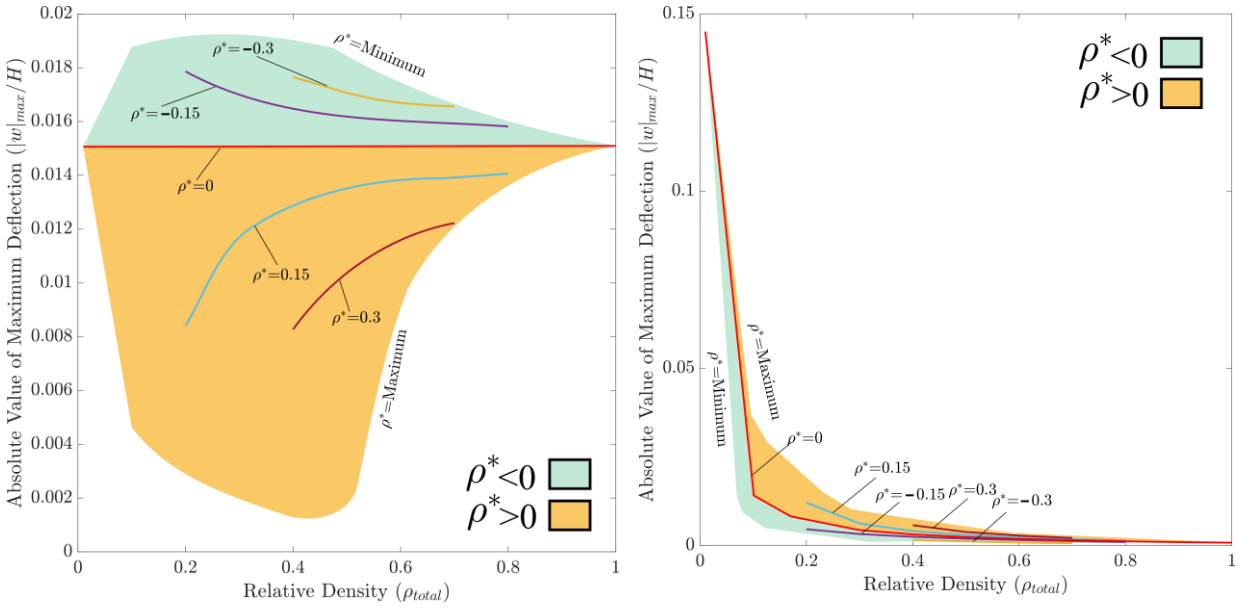

***Figure 4-6**- The effect of alternative relative density gradient function on the maximum deflection of SS z −directional FGC beams subjected to: (a) Thermal loading of $T^{bottom} = 100℃$ and $T^{top} = 0℃$ and (b) Uniform mechanical loading of $F = -10kN$.*

Figure 4-6 also reveals the conflicting effect of ρ^*on the flexural deflection (bending stiffness) of z −directional FGC beams subjected to thermal (**Fig. 4-6a**) and mechanical (**Fig. 4-6b**) loadings. This is an important observation that highlights the necessity of using an optimized strategy for tailoring/grading cell architecture in lightweight multifunctional structures to satisfy design requirements under thermal and mechanical loadings simultaneously. The yellow shaded zoon

represents $\rho^* > 0$ which refers to FGC beams whose relative density in the middle is more than the relative density at the top and bottom; the green shaded zoon represents $\rho^* < 0$ with the opposite density distribution. The position of shaded zones with respect to the red line ($\rho^* = 0$) is the opposite of whether we have thermal or mechanical loading. This means that while the relative density in the middle of FGC beams should be higher than the top and bottom surfaces ($\rho^* > 0$) to decrease the maximum thermal bending, the top and bottom surfaces must be denser ($\rho^* < 0$) to reduce the flexural deflection of FGC beams under uniform mechanical loading.

The trade-off thermo-mechanical behavior of FGC beams with respect to the relative density gradient is shown in **Fig. 4-7**. **Figure 4-7** shows that the value of ρ^* corresponding to the most flexible and least flexible FGC beams depends on the value of thermal and mechanical loads for the case of combined thermo-mechanical loading. For designing a stiff $z-$directional FGC beam, ρ^* must For designing a stiff $z-$directional FGC beam, ρ^* must be the highest or the lowest possible value, depending on whether the thermal loading or the mechanical loading is dominant, respectively.

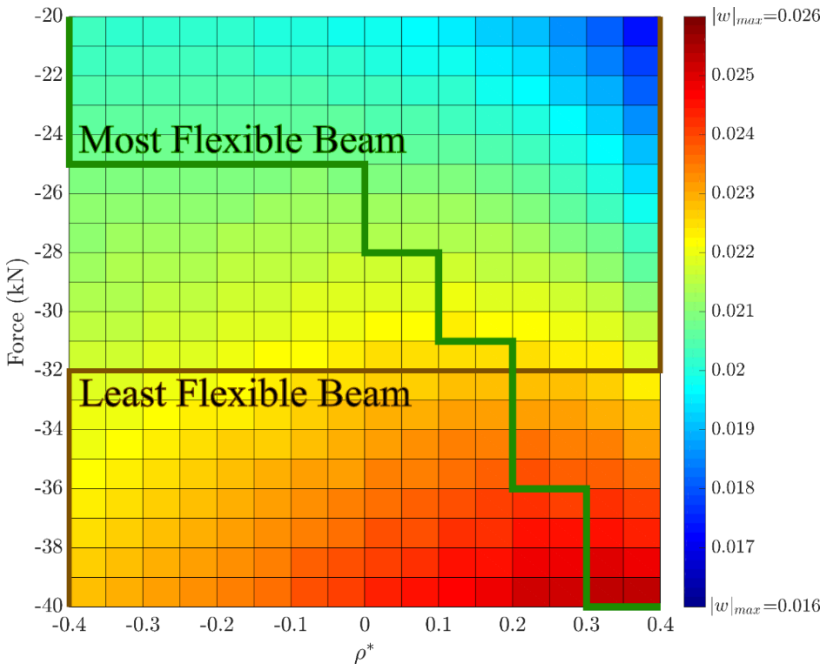

Figure 4-7- *The effects of relative density gradient on the maximum deflection of z −directional FGC beams with $\rho_{total} = 0.5$, SS boundary conditions, and thermal loading: $T^{bottom} = 100℃$ and $T^{top} = 0℃$.*

Although x −directional variation of relative density does not affect the deflection behavior under thermo-mechanical loading for symmetric boundary conditions, it can lead to a significant change in the flexural behavior of x −directional FGC beams with unsymmetrical boundary conditions. **Figure 4-8** presents the deflection curves of x −directional FGC beams with the same weight (constant ρ_{total}) and with SC boundary conditions subjected to the thermal loading of $T^{bottom} = 100℃$ and $T^{top} = 0℃$ for different values of ρ^*. Remarkably, not only does the deflection value changes by ρ^*, but the deformation mode (curvature) of FGC beams may also vary for specific values of ρ^*. **Figure 4-8** shows that the FGC beam deflects upward even though the temperature of the bottom face of the FGC beam is higher for large negative values of ρ^*, which means the relative density of the middle of the FGC beam is lower than its sides. This unexpected behavior is studied in more detail in **Fig. 4-9**.

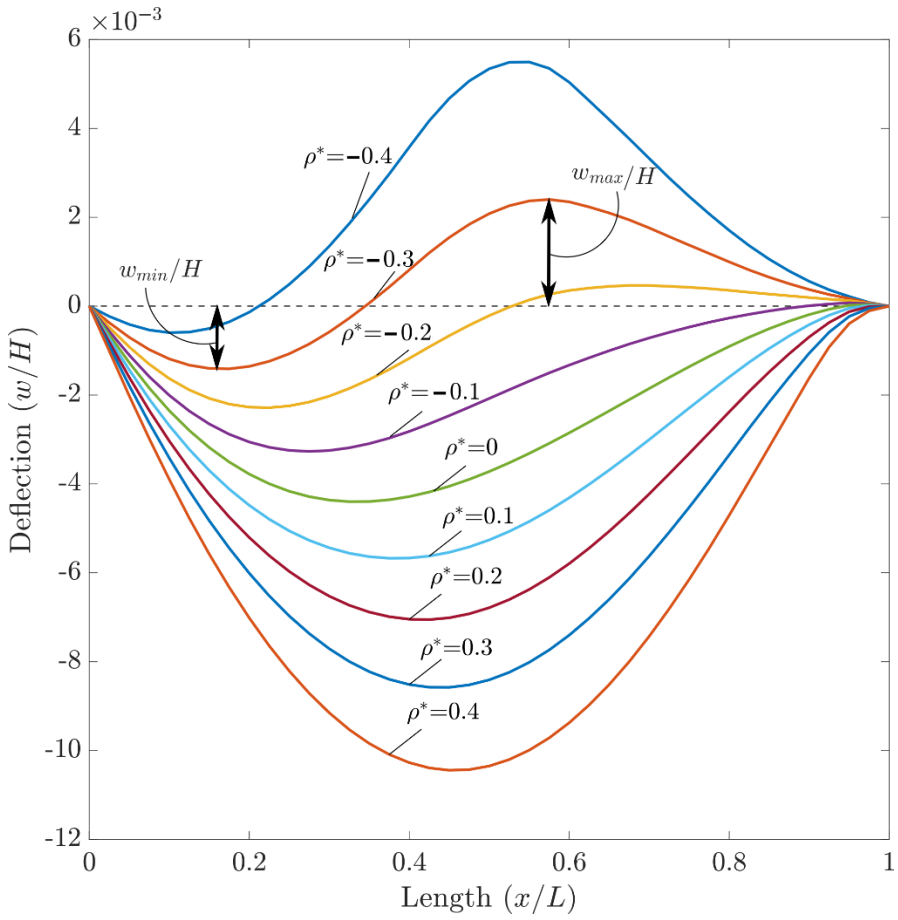

***Figure 4-8**- Deflections curves of x −directional FGC beams with the same weight ($\rho_{total} = 0.5$) and with SC boundary conditions subjected to thermal loading $T^{bottom} = 100℃$ and $T^{top} = 0℃$.*

The non-dimensional values of maximum and minimum deflection ($^{w_{max}}/_{H}$ and $^{w_{min}}/_{H}$) for x −directional FGC beams under thermal loading ($T^{bottom} = 100℃$ and $T^{top} = 0℃$) are presented in **Fig. 4-9a** for beams with different total relative density and alternative variation of relative density. As shown in **Fig. 4-9a**, if ρ^* is less than a critical value (i.e., $\rho^* < -0.1$), a part of the FGC beam will deflect upward while the rest of the beam will be deflected downward. This critical value for ρ^* depends on the total weight of the FGC beam. **Figure 4-9b** presents the position where the maximum positive and negative deflection of the FGC beam occurs. This figure shows that the total weight (total relative density ρ_{total}) of the FGC beam does not play a

significant role in where the extremes happen and the value of ρ^* has a more dominant effect on the position of maximum and minimum deflection.

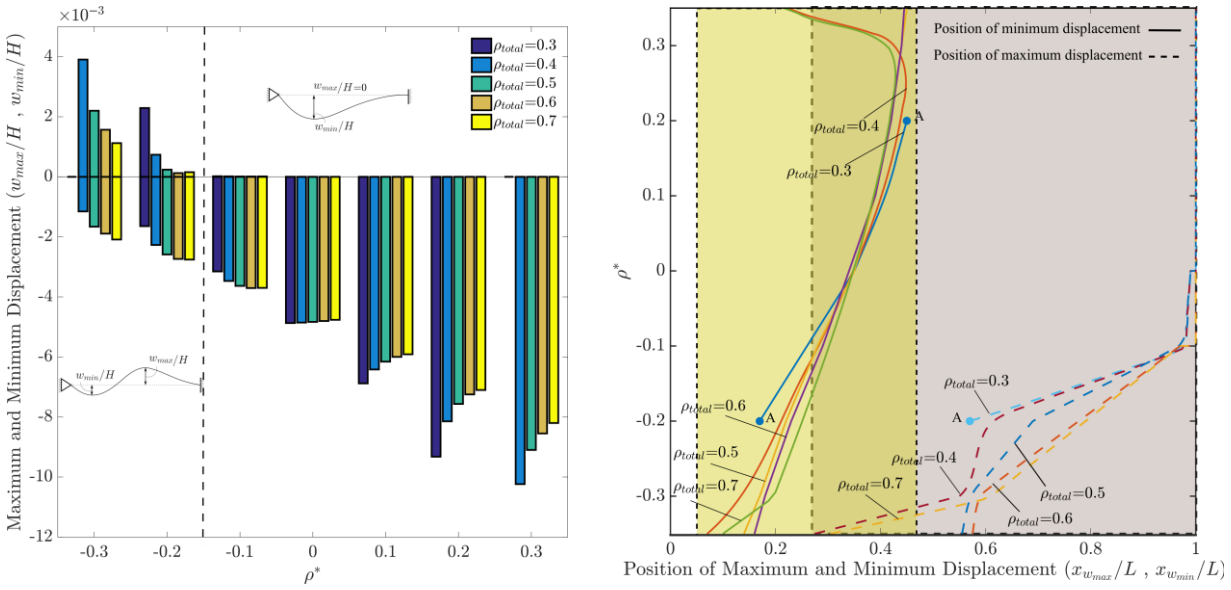

Figure 4-9- *(a) Value and (b) position of maximum and minimum deflection of x −directional FGC beams with SC boundary conditions subjected to thermal loading ($T^{bottom} = 100℃$ and $T^{top} = 0℃$).*

Figure 4-10 is dedicated here to find an optimized relative density distribution function in the case of combined mechanical and thermal loads. The values of ρ^* which makes a beam the least flexible, i.e., the absolute value of deflection is minimum, are presented for x −directional (**Fig. 4-10a**), and z −directional (**Fig. 4-10b**) FGC beams. In these beams, top face temperature is kept at 0℃, and the bottom face temperature, as well as an applied mechanical force on the top face, vary.

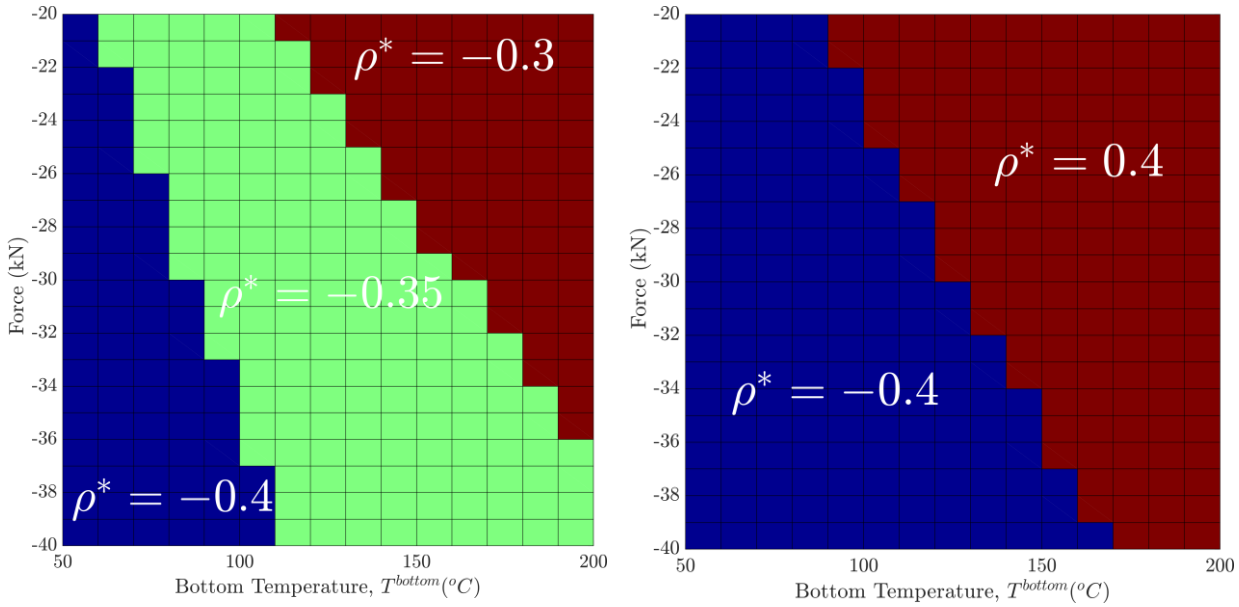

(a) (b)

Figure 4-10- *The optimized value of ρ^* for least flexible FGC beams with $\rho_{total} = 0.5$ and SC boundary conditions for different combined mechanical and thermal loadings: (a) $x-$directional FGC beam and (b) $z-$directional FGC beam.*

Figures 4-11 and **4-12** are dedicated to studying the effect of void topology on the flexural behavior of FGC beams. **Figure 4-11** presents the maximum deflection for $x-$directional FGC beams made of five different cell topologies, as introduced in **Fig. 4-1**, subjected to alternative thermal and mechanical loading conditions. As expected, cell architecture can tune the flexural deformation of the FGC beams without compromising their total weight. However, the effect of architecture can be different for FGCM beams with dissimilar grading profiles (ρ^*) of relative density. For example, for a homogenous cellular beam ($\rho^* = 0$) under thermal loading ($T^{top} =$ 100℃), FGC beams made of shape V show the lowest absolute value of maximum deflection (stiffest), and FGC beams made of cells with shape III show the highest maximum deflection (most flexible).

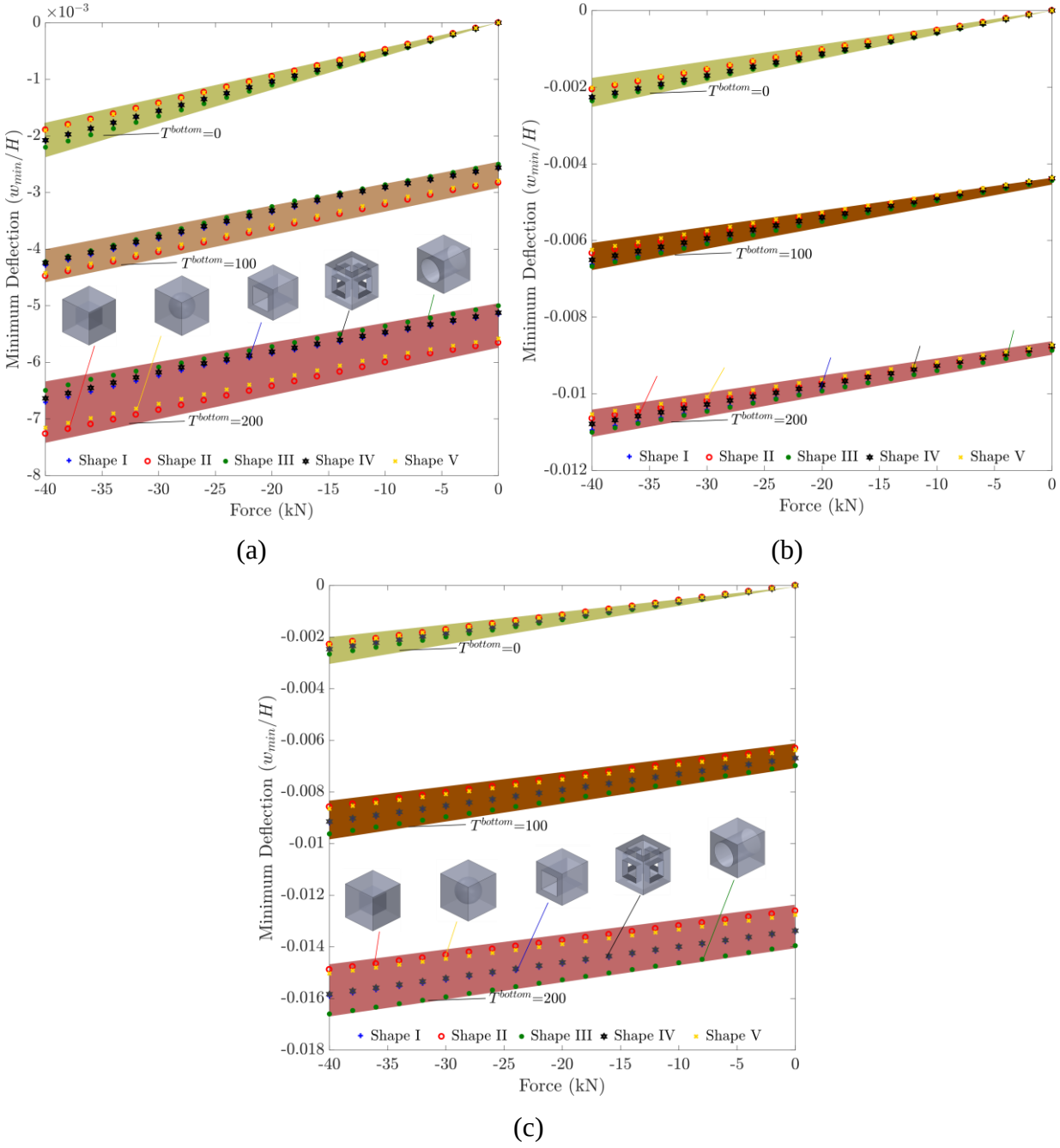

Figure 4-11- *The effects of different shapes on the minimum deflection of x −directional FGC beams with $\rho_{total} =$ 0.75, SC boundary conditions, and $T^{top} = 0$℃: (a) $\rho^* = -0.2$, (b) $\rho^* = 0$, and (c) $\rho^* = 0.2$.*

Figure 4-12 shows the effect of cell topology on maximum upward (positive) and downward (negative) deflection of x −directional FGC beams with unsymmetrical (SC) boundary conditions subjected to a thermal load. Similar to **Fig. 4-9a**, it can be seen that the direction of the FGC beam deflection changes by varying the value of ρ^*. According to **Fig. 4-12**, cell topology does not have a significant effect on the flexural response of the FGC beams, although it can affect the absolute value of flexural deflection.

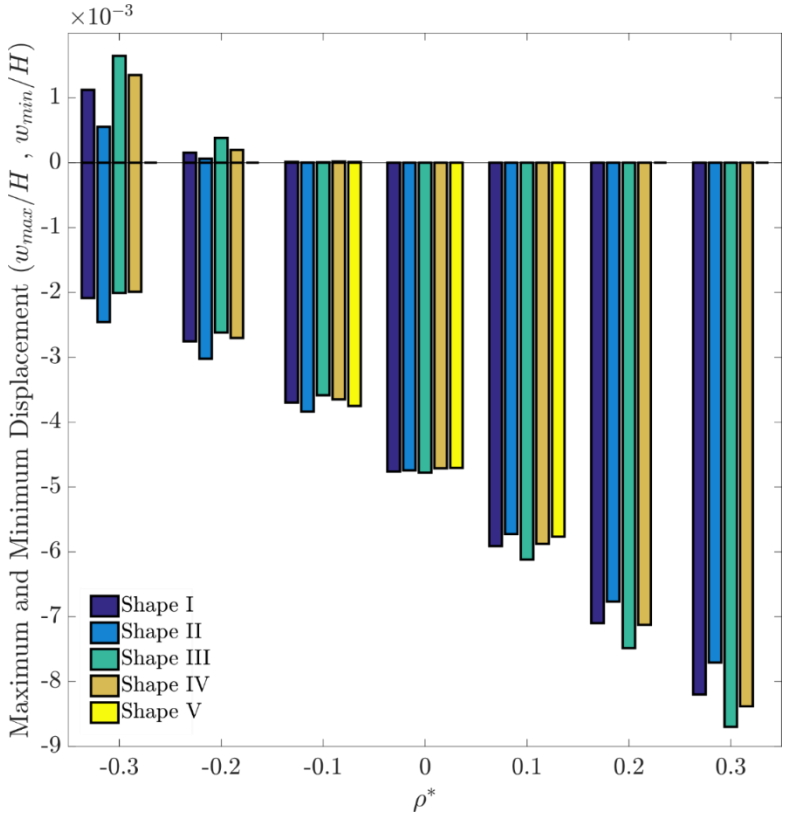

Figure 4-12- *The value of maximum positive and negative deflection for x −directional FGC beams with $\rho_{total} =$ 0.7 and SC boundary conditions subjected to thermal loading ($T^{bottom} = 100℃$ and $T^{top} = 0℃$).*

4.8 Concluding remarks

The thermo-mechanical bending of architected FGC beams has been investigated in this paper. The effective thermoelastic properties of architected cells constructing FGC beams are obtained by standard mechanics homogenization, and the governing equations are derived based on TSDT. The introduced hybrid methodology is corroborated by comparing its numerical results with those obtained by a detailed FE modeling. The main findings of our numerical analyses on the FGC beams under thermal and mechanical loadings can be summarized as:

- The deflection behavior of homogenous cellular beams with prescribed temperatures on the top and bottom surfaces does not depend on the total weight or relative density of the architected cellular beam (**Fig. 4-6a**).
- The variation of relative density across the thickness of a $z-$directional FGC beam has opposite effects on the flexural bending of the FGC beam subjected to thermal and mechanical loads (**Fig. 4-6**).
- If thermal loading is dominant, FGC beams with a higher relative density in the middle show higher bending stiffness; the opposite is true if the mechanical loading is the dominant flexural force on the FGC beam (**Fig. 4-7**).
- In the case of beams with symmetric boundary conditions (e.g., SS), subjected to thermal loading, the $x-$directional variation of properties does not have any effect on the flexural behavior of FGC beams. However, the $x-$directional variation of properties can make a significant difference in terms of deflection value and curvature if the boundary conditions of the FGCM beam are not symmetric (e.g., SC) (**Figs. 4-5** and **4-8**).

- For SC mechanical boundary conditions and prescribed temperature at the top and bottom faces of the beam, if the relative density of the center of the beam ($x = \frac{L}{2}$) is less than the sides ($x = 0, L$), the FGCM beam's flexural stiffness can be increased significantly, and the beam might even deflect in the opposite direction for certain variation functions in the *x*-direction (**Figs. 4-8** and **4-9**).
- The optimized relative density variation function to achieve the highest flexural stiffness in FGC beams varies depending on the value of thermal and mechanical loading for both $z-$directional and $x-$directional FGC beams (**Fig. 4-10**).
- Although the topology of the void might affect the flexural stiffness of the beam, the general conclusions mentioned above are still valid for different cell topologies. Besides, changing the cell architecture can further increase or decrease the stiffness of FGC beams depending on the value of the thermal and mechanical loading applied to the architected beam. (**Figs. 4-11** and **4-12**)

The results of this paper show how cell architecture can be tailored to improve thermal and mechanical functionality. This improvement facilitates the development of lightweight multifunctional materials in the form of meta-structures for structural load-bearing [49, 69], thermal insulation [60, 70-72], and energy absorption [53, 73, 74] applications. FGCMs can also contribute to the improved performance of lightweight cellular materials used in a wide range of applications, from aerospace and automotive to biomedical and construction [75-77].

4.9 Appendix 4.A

The effective thermal and elastic properties of cells with arbitrary architectures are obtained in this paper by applying standard mechanics homogenization for a wide range of relative density. The

effective homogenized thermal properties are presented in **Fig. 4-A1**. The results are compared with the rough estimation provided by *Voigt* and *Reuss* micromechanical models and a more accurate theoretical bound presented by Lim [78]. The thermal circuit method with parallel and series configurations has also recently been proposed as an alternative approach providing an accurate bound for prediction of thermal conductivity of particulate composites and cellular solids [63]. It can be found that the homogenized results lay between the proposed theoretical bounds. In addition, **Fig. A1** reveals that cells with spherical or extruded cellular voids have the highest thermal conductivity among those considered in this paper.

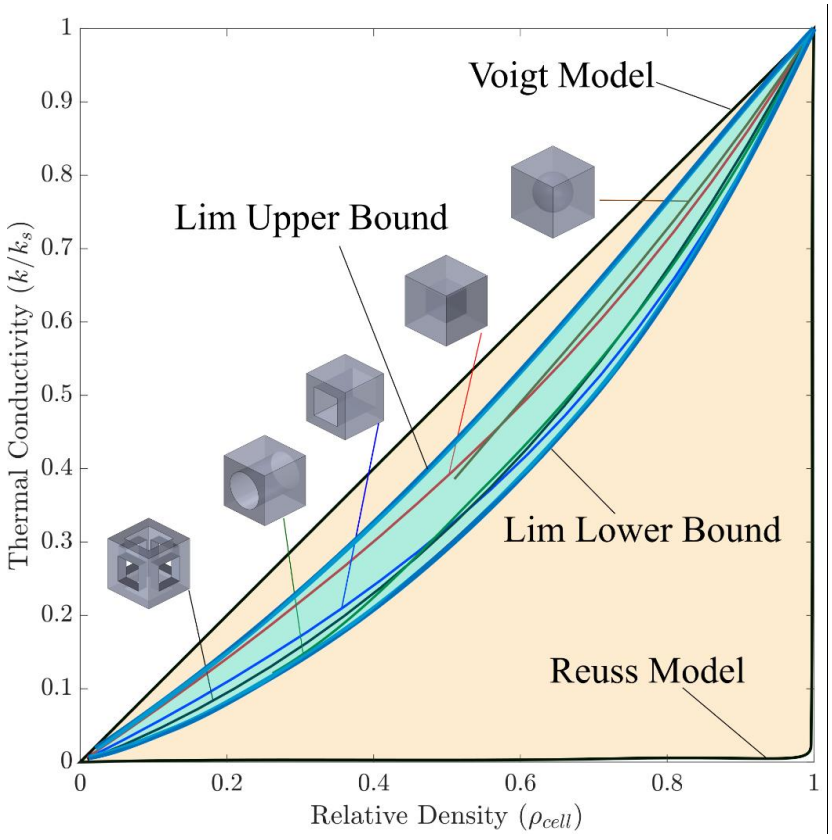

***Figure 4-A1**- Effective thermal conductivity for cells with different topologies.*

The effective in-plane Young's modulus and in-plane Poisson's ratio are shown in **Fig. 4-A2**. It is observed that cells with a spherical void (Shape V) are the stiffest in high relative densities.

Different micromechanical bounds are also presented in **Fig. 4-A2a** for prediction of elastic modulus. Several studies have reported upper and lower bounds for Young's modulus of composite materials [79, 80]; however, only upper bound has been determined for the case of cellular materials [81] as the lower bound of Young's modulus is zero for cellular solids.

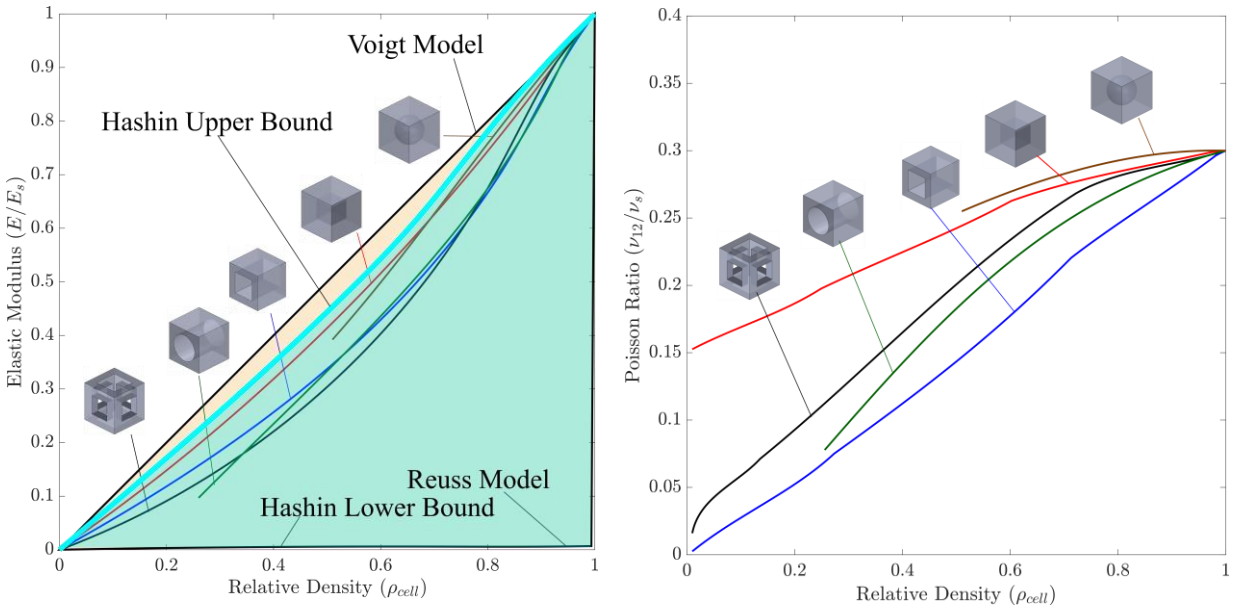

(a) *(b)*

***Figure 4-A2**- The effective mechanical properties of cells for alternative cell topologies.*

4.10 Acknowledgment

A.H. Akbarzadeh acknowledges the financial support by Natural Sciences and Engineering Research Council of Canada (NSERC) through NSERC Discovery Grant RGPIN-2016-0471.

4.11 References

[1] L.J. Gibson, M.F. Ashby, Cellular Solids: Structure and Properties, Cambridge University Press1999.

[2] J.N. Grima, P.S. Farrugia, R. Gatt, V. Zammit, A system with adjustable positive or negative thermal expansion, Proceedings of the Royal Society A: Mathematical, Physical and Engineering Science 463(2082) (2007) 1585.

[3] T.-C. Lim, Negative thermal expansion in transversely isotropic space frame trusses, physica status solidi (b) 250(10) (2013) 2062-2069.

[4] A. Bezazi, C. Remillat, P. Innocenti, F. Scarpa, In-plane mechanical and thermal conductivity properties of a rectangular–hexagonal honeycomb structure, Composite Structures 84(3) (2008) 248-255.

[5] K.P. Vemuri, P.R. Bandaru, Geometrical considerations in the control and manipulation of conductive heat flux in multilayered thermal metamaterials, Applied Physics Letters 103(13) (2013) 133111.

[6] T. Yang, K.P. Vemuri, P.R. Bandaru, Experimental evidence for the bending of heat flux in a thermal metamaterial, Applied Physics Letters 105(8) (2014) 103-106.

[7] P. Bandaru, K. Vemuri, F. Canbazoglu, R. Kapadia, Layered thermal metamaterials for the directing and harvesting of conductive heat, AIP Advances 5(5) (2015) 053403.

[8] K.P. Vemuri, P.R. Bandaru, Anomalous refraction of heat flux in thermal metamaterials, Applied Physics Letters 104(8) (2014) 083901.

[9] F. Chen, D.Y. Lei, Experimental realization of extreme heat flux concentration with easy-to-make thermal metamaterials, Scientific reports 5 (2015) 11552.

[10] G. Park, S. Kang, H. Lee, W. Choi, Tunable Multifunctional Thermal Metamaterials: Manipulation of Local Heat Flux via Assembly of Unit-Cell Thermal Shifters, Scientific Reports 7 (2017) 41000.

[11] G. Xu, H. Zhang, M. Xie, Y. Jin, Geometrical effects on the concentrated behavior of heat flux in metamaterials thermal harvesting devices, AIP Advances 7(10) (2017) 105322.

[12] K. Vemuri, F. Canbazoglu, P. Bandaru, Guiding conductive heat flux through thermal metamaterials, Applied Physics Letters 105(19) (2014) 193904.

[13] D.-P. Liu, P.-J. Chen, H.-H. Huang, Realization of a thermal cloak–concentrator using a metamaterial transformer, Scientific Reports 8(1) (2018) 2493.

[14] H.-T. Thai, S.-E. Kim, A review of theories for the modeling and analysis of functionally graded plates and shells, Composite Structures 128 (2015) 70-86.

[15] K.P. Soldatos, T. Timarci, A unified formulation of laminated composite, shear deformable, five-degrees-of-freedom cylindrical shell theories, Composite Structures 25(1) (1993) 165-171.

[16] J.N. Reddy, Theory and analysis of elastic plates and shells, CRC press2006.

[17] M. Aydogdu, A new shear deformation theory for laminated composite plates, Composite Structures 89(1) (2009) 94-101.

[18] J.N. Reddy, Nonlocal nonlinear formulations for bending of classical and shear deformation theories of beams and plates, International Journal of Engineering Science 48(11) (2010) 1507-1518.

[19] S. Kapuria, M. Bhattacharyya, A. Kumar, Bending and free vibration response of layered functionally graded beams: a theoretical model and its experimental validation, Composite Structures 82(3) (2008) 390-402.

[20] J. Hutchinson, Shear coefficients for Timoshenko beam theory, Journal of Applied Mechanics 68(1) (2001) 87-92.

[21] S. Spinner, A comparison of experimental and theoretical relations between Young's modulus and the flexural and longitudinal resonance frequencies of uniform bars.

[22] N.G. Stephen, S. Puchegger, On the valid frequency range of Timoshenko beam theory, Journal of Sound and Vibration 297(3) (2006) 1082-1087.

[23] R.A.W. Mines, A. Alias, Numerical simulation of the progressive collapse of polymer composite sandwich beams under static loading, Composites Part A: Applied Science and Manufacturing 33(1) (2002) 11-26.

[24] V. Birtel, P. Mark, Parameterised finite element modelling of RC beam shear failure, ABAQUS users' conference, 2006, pp. 95-108.

[25] M. Sayir, C. Mitropoulos, On elementary theories of linear elastic beams, plates and shells, Zeitschrift für angewandte Mathematik und Physik ZAMP 31(1) (1980) 1-55.

[26] J.B. Carr, The Effect of Shear Flexibility and Rotatory Inertia on the Natural Frequencies of Uniform Beams, Aeronautical Quarterly 21(1) (2016) 79-90.

[27] S.P. Timoshenko, LXVI. On the correction for shear of the differential equation for transverse vibrations of prismatic bars, The London, Edinburgh, and Dublin Philosophical Magazine and Journal of Science 41(245) (1921) 744-746.

[28] J.M. Gere, S. Timoshenko, Mechanics of Materials, ; Brooks, Cole, Pacific Grove, CA (2001) 815-39.

[29] L. Librescu, O. Song, Thin-walled composite beams: theory and application, Springer Science & Business Media2005.

[30] D.H. Robbins, J.N. Reddy, Modelling of thick composites using a layerwise laminate theory, International Journal for Numerical Methods in Engineering 36(4) (1993) 655-677.

[31] G. Giunta, F. Biscani, S. Belouettar, A.J.M. Ferreira, E. Carrera, Free vibration analysis of composite beams via refined theories, Composites Part B: Engineering 44(1) (2013) 540-552.

[32] S.R. Marur, T. Kant, Free vibration analysis of fiber reinforced composite beams using higher order theories and finite element modelling, Journal of Sound and Vibration 194(3) (1996) 337-351.

[33] M. Koizumi, FGM activities in Japan, Composites Part B: Engineering 28(1) (1997) 1-4.

[34] M. SASAKI, Y. WANG, T. HIRANO, T. HIRAI, Design of SiC/C functionally gradient material and its preparation by chemical vapor deposition, Journal of the Ceramic Society of Japan 97(1125) (1989) 539-543.

[35] M. Zidi, A. Tounsi, M.S.A. Houari, E.A. Adda Bedia, O. Anwar Bég, Bending analysis of FGM plates under hygro-thermo-mechanical loading using a four variable refined plate theory, Aerospace Science and Technology 34 (2014) 24-34.

[36] T.-C. Lim, Thermal stresses in auxetic plates and shells, Mechanics of Advanced Materials and Structures 22(3) (2015) 205-212.

[37] K. Tanaka, Y. Tanaka, H. Watanabe, V. Poterasu, Y. Sugano, An improved solution to thermoelastic material design in functionally gradient materials: Scheme to reduce thermal stresses, Computer Methods in Applied Mechanics and Engineering 109(3-4) (1993) 377-389.

[38] J. Yang, H.-S. Shen, Nonlinear bending analysis of shear deformable functionally graded plates subjected to thermo-mechanical loads under various boundary conditions, Composites Part B: Engineering 34(2) (2003) 103-115.

[39] L. Ma, T. Wang, Nonlinear bending and post-buckling of a functionally graded circular plate under mechanical and thermal loadings, International Journal of Solids and Structures 40(13-14) (2003) 3311-3330.

[40] A.M. Zenkour, Analytical solution for bending of cross-ply laminated plates under thermo-mechanical loading, Composite Structures 65(3) (2004) 367-379.

[41] S. Brischetto, R. Leetsch, E. Carrera, T. Wallmersperger, B. Kröplin, Thermo-Mechanical Bending of Functionally Graded Plates, Journal of Thermal Stresses 31(3) (2008) 286-308.

[42] H.-S. Shen, Z.-X. Wang, Nonlinear bending of FGM plates subjected to combined loading and resting on elastic foundations, Composite Structures 92(10) (2010) 2517-2524.

[43] H.V. Tung, N.D. Duc, Nonlinear analysis of stability for functionally graded plates under mechanical and thermal loads, Composite Structures 92(5) (2010) 1184-1191.

[44] H. Jopek, T. Strek, Thermal and structural dependence of auxetic properties of composite materials, physica status solidi (b) 252(7) (2015) 1551-1558.

[45] J. Woo, S. Meguid, Nonlinear analysis of functionally graded plates and shallow shells, International Journal of Solids and structures 38(42-43) (2001) 7409-7421.

[46] G. Praveen, J. Reddy, Nonlinear transient thermoelastic analysis of functionally graded ceramic-metal plates, International journal of solids and structures 35(33) (1998) 4457-4476.

[47] M.M. Almutairi, M. Osman, I. Tlili, Thermal Behavior of Auxetic Honeycomb Structure: An Experimental and Modeling Investigation, Journal of Energy Resources Technology 140(12) (2018) 122904.

[48] J. Yan, S. Yang, C. Yang, Multiscale Analysis of Thermal Stress of Lattice Materials and Its Size Effects, Journal of Thermal Stresses 37(8) (2014) 885-904.

[49] H. Niknam, A.H. Akbarzadeh, D. Rodrigue, D. Therriault, Architected multi-directional functionally graded cellular plates, Materials & Design 148 (2018) 188-202.

[50] C. Lira, F. Scarpa, Transverse shear stiffness of thickness gradient honeycombs, Composites Science and Technology 70(6) (2010) 930-936.

[51] D.W. Rosen, Computer-Aided Design for Additive Manufacturing of Cellular Structures, Computer-Aided Design and Applications 4(5) (2007) 585-594.

[52] M. Taylor, L. Francesconi, M. Gerendás, A. Shanian, C. Carson, K. Bertoldi, Low Porosity Metallic Periodic Structures with Negative Poisson's Ratio, Advanced Materials 26(15) (2014) 2365-2370.

[53] H. Niknam, A.H. Akbarzadeh, In-plane and out-of-plane buckling of architected cellular plates: Numerical and experimental study, Composite Structures 206 (2018) 739-749.

[54] J. Reddy, Analysis of functionally graded plates, International Journal for Numerical Methods in Engineering 47(1-3) (2000) 663-684.

[55] B. Hassani, E. Hinton, A review of homogenization and topology opimization II—analytical and numerical solution of homogenization equations, Computers & structures 69(6) (1998) 719-738.

[56] A.G. Evans, M. He, V.S. Deshpande, J.W. Hutchinson, A.J. Jacobsen, W.B. Carter, Concepts for enhanced energy absorption using hollow micro-lattices, International Journal of Impact Engineering 37(9) (2010) 947-959.

[57] S.J. Hollister, N. Kikuchi, A comparison of homogenization and standard mechanics analyses for periodic porous composites, Computational Mechanics 10(2) (1992) 73-95.

[58] T.L. Bergman, F.P. Incropera, A.S. Lavine, D.P. Dewitt, Introduction to heat transfer, John Wiley & Sons2011.

[59] M. Aydogdu, V. Taskin, Free vibration analysis of functionally graded beams with simply supported edges, Materials & Design 28(5) (2007) 1651-1656.

[60] J. Shi, A.H. Akbarzadeh, Architected cellular piezoelectric metamaterials: Thermo-electro-mechanical properties, Acta Materialia 163 (2019) 91-121.

[61] M. Komijani, S.E. Esfahani, J.N. Reddy, Y.P. Liu, M.R. Eslami, Nonlinear thermal stability and vibration of pre/post-buckled temperature- and microstructure-dependent functionally graded beams resting on elastic foundation, Composite Structures 112 (2014) 292-307.

[62] D.-G. Zhang, Nonlinear bending analysis of FGM beams based on physical neutral surface and high order shear deformation theory, Composite Structures 100 (2013) 121-126.

[63] A. Mirabolghasemi, A.H. Akbarzadeh, D. Rodrigue, D. Therriault, Thermal Conductivity of Architected Cellular Metamaterials, Acta Materialia (2019).

[64] A. Akbarzadeh, J. Fu, L. Liu, Z. Chen, D. Pasini, Electrically conducting sandwich cylinder with a planar lattice core under prescribed eigenstrain and magnetic field, Composite Structures 153 (2016) 632-644.

[65] A.S. Suleiman, N. Dukhan, Forced convection inside metal foam: Simulation over a long domain and analytical validation, International Journal of Thermal Sciences 86 (2014) 104-114.

[66] V.M. Patel, P. Talukdar, Determination of radiative properties of representative and real open cell foam structures using the finite volume method, International Journal of Thermal Sciences 132 (2018) 117-128.

[67] J.N. Reddy, An introduction to the finite element method, McGraw-hill New York1993.

[68] C. Coulais, J.T.B. Overvelde, L.A. Lubbers, K. Bertoldi, M. van Hecke, Discontinuous Buckling of Wide Beams and Metabeams, Physical Review Letters 115(4) (2015) 044301.

[69] A. Radman, X. Huang, Y.M. Xie, Topology optimization of functionally graded cellular materials, Journal of Materials Science 48(4) (2013) 1503-1510.

[70] J. Tian, T.J. Lu, H.P. Hodson, D.T. Queheillalt, H.N.G. Wadley, Cross flow heat exchange of textile cellular metal core sandwich panels, International Journal of Heat and Mass Transfer 50(13) (2007) 2521-2536.

[71] G. Carbajal, C.B. Sobhan, G.P. Peterson, D.T. Queheillalt, H.N.G. Wadley, Thermal response of a flat heat pipe sandwich structure to a localized heat flux, International Journal of Heat and Mass Transfer 49(21) (2006) 4070-4081.

[72] L. Cheng, J. Liu, X. Liang, A.C. To, Coupling lattice structure topology optimization with design-dependent feature evolution for additive manufactured heat conduction design, Computer Methods in Applied Mechanics and Engineering 332 (2018) 408-439.

[73] H. Yazdani Sarvestani, A.H. Akbarzadeh, H. Niknam, K. Hermenean, 3D printed architected polymeric sandwich panels: Energy absorption and structural performance, Composite Structures 200 (2018) 886-909.

[74] S. Shan, S.H. Kang, J.R. Raney, P. Wang, L. Fang, F. Candido, J.A. Lewis, K. Bertoldi, Multistable Architected Materials for Trapping Elastic Strain Energy, Advanced Materials 27(29) (2015) 4296-4301.

[75] L. Wollmann, A.K. Nayak, S.S.P. Parkin, C. Felser, Heusler 4.0: Tunable Materials, Annual Review of Materials Research 47(1) (2017) 247-270.

[76] K. Bertoldi, M.C. Boyce, Wave propagation and instabilities in monolithic and periodically structured elastomeric materials undergoing large deformations, Physical Review B 78(18) (2008) 184107.

[77] M. Ruzzene, F. Scarpa, F. Soranna, Wave beaming effects in two-dimensional cellular structures, Smart materials and structures 12(3) (2003) 363.

[78] T.C. Lim, Unified practical bounds for the thermal conductivity of composite materials, Materials Letters 54(2) (2002) 152-157.

[79] A.H. Akbarzadeh, A. Abedini, Z.T. Chen, Effect of micromechanical models on structural responses of functionally graded plates, Composite Structures 119 (2015) 598-609.

[80] T.-C. Lim, Geometrical Correction to the Elastic Stiffness of Particulate Composites, Journal of Reinforced Plastics and Composites 29(1) (2008) 94-104.

[81] J.B. Berger, H.N.G. Wadley, R.M. McMeeking, Mechanical metamaterials at the theoretical limit of isotropic elastic stiffness, Nature 543 (2017) 533.

5 Chapter Five: Bending Behavior of Optimally Graded 3D Printed Cellular Beams[1]

5.1 Preface

In the previous chapters, we considered predefined functions for the relative density distribution across the cellular structures. We gained insight into how different gradients affect the behavior of FGC structures and identified specific gradients that could improve the mechanical response of cellular beams and plates.

In **Chapter 4**, we utilized an optimization algorithm to find out the most efficient distribution across a cellular beam. We observe the difference between using and not exploiting a predefined function for the optimization process of relative density distribution. Besides, more systematic experimental studies are conducted on additively manufactured cellular samples. We ensure the validity of our results through this experimentation and also examine the manufacturability of optimized FGC structures.

[1] Reproduced with permission from Seyedkanani, A., Niknam, H., Akbarzadeh, A.H.; Bending Behavior of Optimally Graded 3D Printed Cellular Beams; *Additive Manufacturing*, 36 (2020) 101327.

5.2 Abstract

Periodic cellular materials can substantially improve the stiffness-to-weight ratio of structures. This improvement depends on the geometry of periodic cells. This article presents the idea of enhancing the bending stiffness of an architected cellular beam by an optimum distribution of relative density through its length and across its thickness. We employ a hybrid-homogenized model to expedite the computational evaluation of the bending performance of the graded cellular beams. Detailed finite element analysis (FEA) and experimental bending tests on specimens 3D printed by stereolithography validate the hybrid-homogenized modeling approach. The hybrid-homogenized model facilitates transforming the general optimization problem into a shape optimization process with the relative density of unit cells as design variables. The teaching-learning-based optimization (TLBO) algorithm is used to obtain the optimum relative density distribution, which maximizes the bending stiffness. The optimization results show a substantial increase in bending stiffness, as high as 43%, 155%, and 182% for a cellular beam graded through the length, across the thickness, and in both directions, respectively. It is found that varying the relative density of cells across the beam thickness is more effective than variation through the length. Detailed FEA and experimental bending tests corroborate the optimization findings and confirm the practicality of such graded designs for developing advanced lightweight structures. Investigating the effect of cell architecture also reveals that optimally graded cellular beams have the potential to outperform uniform cellular beams made out of ideal unit cells (Voigt bound for elastic properties). The relatively simple graded cellular designs are beneficial in applications where high bending stiffness and low density are essential. Recent advances in additive manufacturing promise extending the presented grading strategy for polymeric, composite, and

metallic 3D printed cellular materials to fabricate high performance lightweight structural elements at a relatively low cost.

5.3 Introduction

Architected cellular materials have recently been used in a variety of structural systems to improve their mechanical properties, including stiffness and energy absorption [1-3]. This group of advanced materials can decrease the weight of structural elements while maintaining their structural integrity. Weight reduction is critical in energy absorbents, thermal insulators, and structural elements to optimize their functionalities. Theoretical and practical perspectives of the bending response of a beam, as one of the fundamental and widely used structural elements, have always been of great importance. Researchers have proposed several theoretical models based on the theory of elasticity to study the bending behavior of beams subjected to static and dynamic loads [4]. These models enable analyzing beams with different thicknesses, a variety of constituent materials [5], and alternative geometries [6]. Multiple practical approaches have also been proposed to improve the mechanical responses of beams. These approaches include adding reinforcement into the constituent materials of beams [7-9], changing the variation of material properties across the beam [10, 11], engineering the microstructure of solid beams by mimicking biomaterials [12, 13] and introducing architected cells in engineered porous beams [14, 15].

As a category of architected materials, cellular solids have received significant attention in the design of lightweight structural elements as they can reduce the weight and improve specific structural responses [1]. They have been used as a core of sandwich panels and beams to improve flexural responses in lightweight structures. Originally, the core of sandwich beams was made of hexagonal honeycombs to enhance the ultimate strength of the sandwich structures and to postpone

plastic deformation [16, 17]. Evans et al. [18] showed that hexagonal honeycomb cores outperform foam cores in bending response. Further research revealed that the application of cellular materials with alternative geometries as a core of sandwich structures could improve their flexural responses [19, 20]. Subsequently, cellular materials have been proposed to replace the hexagonal cells in the core of sandwich structures [18, 21-23]. Exploiting cells with optimized microarchitectures, such as octet and Isomax cells, led to developing sandwich structures with enhanced flexural stiffness that surpass conventional sandwich beams with hexagonal cellular cores [22, 23].

From another point of view, varying mechanical properties across structural elements has shown substantial improvement in the flexural properties. Two well-known examples of exploiting variation of properties to improve the mechanical functionality of structural elements are using *Laminated sandwiches* [24, 25] and *Functionally graded materials* (FGMs) [26-28], both found as structural design elements in biological materials like a sea sponge, abalone nacre *(Laminate design*), tooth dental/enamel junctions, and crab claw (*Gradient design*) [29]. Laminated sandwiches are multilayer composites in which the orientation of fibers varies from one layer to the other one in constant stiffness composites [24] or within each lamina by steering the fibers [30]. Consequently, desired mechanical properties can be achieved through the optimization of lay-ups and fiber steering within the laminated sandwich composite. In FGMs, the material properties vary continuously and usually by a pre-defined function [11]. Although this class of heterogeneous materials is more difficult to fabricate, the continuous variation of properties makes them less susceptible to failure by delamination [26]. As a result, the continuous variation of properties has been considered as an effective method to enhance the mechanical performance of structures.

The development of advanced manufacturing techniques, such as additive manufacturing or so-called 3D printing, facilitates the fabrication of lightweight cellular materials with variable and complex microarchitectures [31, 32]. During the past few years, additive manufacturing technologies have moved from prototyping to product manufacturing [33] and enabled the designers to fabricate structures with unprecedented geometries [34, 35]. Appropriate 3D printing technology is selected depending on the application, geometry, and base material. Stereolithography (SLA) is among the earliest additive manufacturing techniques that can fabricate structures with a high degree of precision. It exploits UV light to initiate a chain reaction on a layer of monomer solution of photopolymers [36]. Although the range of materials used in SLA 3D printing is limited, it can print high-quality parts at a fine resolution [37]. In the case of cellular materials, this high-precision additive manufacturing technology can facilitate the fabrication of a novel type of cellular materials, i.e., *functionally graded cellular* (FGC) materials. In this type of cellular material, cell properties, including relative density, topology, and connectivity, can be tailored across the architected structure. A series of theoretical studies investigated the effects of this variation of cell topology on bending [38, 39], free vibration [39], and buckling [40] of cellular plates. These merely computational studies demonstrated that the structural stiffness of a cellular plate and consequently its buckling load and bending stiffness can be remarkably increased by selecting an appropriate variation function for FGC materials [39, 40]. Tailoring the density variation was also proved to be effective for controlling the magnitude and deformation modes of FGC beams subjected to a thermo-mechanical load [38]. Further studies showed that the overall Poisson's ratio and subsequently the compression resistance can be controlled by varying the cellular architecture across the cellular solids [41].

The abovementioned studies have strived to show the potential of improving structural responses by varying properties across the cellular structures; however, the maximum achievable improvement has yet to be determined through optimization. Conventionally, topology optimization (TO) algorithms have been used to obtain the most optimized material distribution; however, several drawbacks such as compensation of intermediate relative densities and the manufacturability of optimized geometry [42-44] impede the application of TO algorithms to every structural element. *Homogenization-based optimization approaches* can overcome these drawbacks while drastically reduce the computational efforts [45-47]. These strategies usually adopt a TO-to-lattice mapping to relate optimum relative densities to the corresponding unit cell architectures. In this study, we implement the Teaching-Learning-Based Optimization (TLBO) algorithm as a heuristic optimization method that is efficient in handling multiple design variables and constrained mechanical design problems [48-50].

Although few works have reported the advantage of graded cellular structure over homogenous cellular design [38-40], to the best of authors' knowledge, no study in the literature has found the optimal distribution of cells for specific mechanical applications, i.e., flexural bending. In this paper, the problem is first defined in **Section 5.4**, and then different approaches adopted for obtaining the bending stiffness of the cellular beams are introduced in **Section 5.5**. **Section 5.6** begins with the validation of the proposed hybrid-homogenized model by a detailed FEA and experimental bending tests on 3D printed samples and continues with finding optimum relative density distribution to maximize the bending stiffness of graded cellular beams. Next, the results of experimental bending tests and FEA are presented, which confirm optimization findings for a group of 3D printed optimally graded cellular beam samples. Then, we study the effect of using octet truss unit cells as 3D lattice architectures on the maximum feasible bending stiffness.

Eventually, concluding remarks are brought in **Section 5.7** to summarize the most important findings of this study.

5.4 Problem definition

The present study investigates the bending response of a graded cellular beam. The cellular beam can be graded along its length and/or across its thickness. **Figure 5-1** depicts the schematic view of the graded cellular beam together with the loading condition. The figure illustrates how a graded cellular beam ($L \times W \times T$) is constructed by tessellating 2D extruded square unit cells of $l \times W \times t$ dimensions with various relative densities along the length (*x*-direction) and across the thickness (*z*-direction). A cross-sectional view in **Figure 5-1** visualizes the relative density distribution across the thickness of the beam. The heterogeneous cellular structure is then replaced with a solid beam with layers of varying relative density. In **Figure 5-1**, the gradient of colors in different layers across the thickness or different cells along the length of the graded cellular beam represents the variation of the relative density. If the beam in **Figure 5-1** is graded only in the *x*-direction, the unit cell may be recognized as a square cell of $l \times W \times T$ extruded through the whole thickness of the beam.

Bending tests are conducted with a line load applied on the top face and in the middle of the graded cellular beam with simply-supported boundary conditions at both edges. The relative density of the i^{th} cell is defined as the fraction of solid volume over the total volume of the representative unit cell (RVE):

$$\bar{\rho}_i = \frac{V_{solid}}{V_{RVE}} \tag{5.1}$$

In a graded cellular beam with $N = N_x \times N_z$ numbers of unit cells, where N_x and N_z are respectively, the numbers of unit cells in *x*- and *z*-directions, the total relative density is calculated as follows:

$$\bar{\rho} = \frac{\sum_{i=1}^{N} \bar{\rho}_i}{N} \tag{5.2}$$

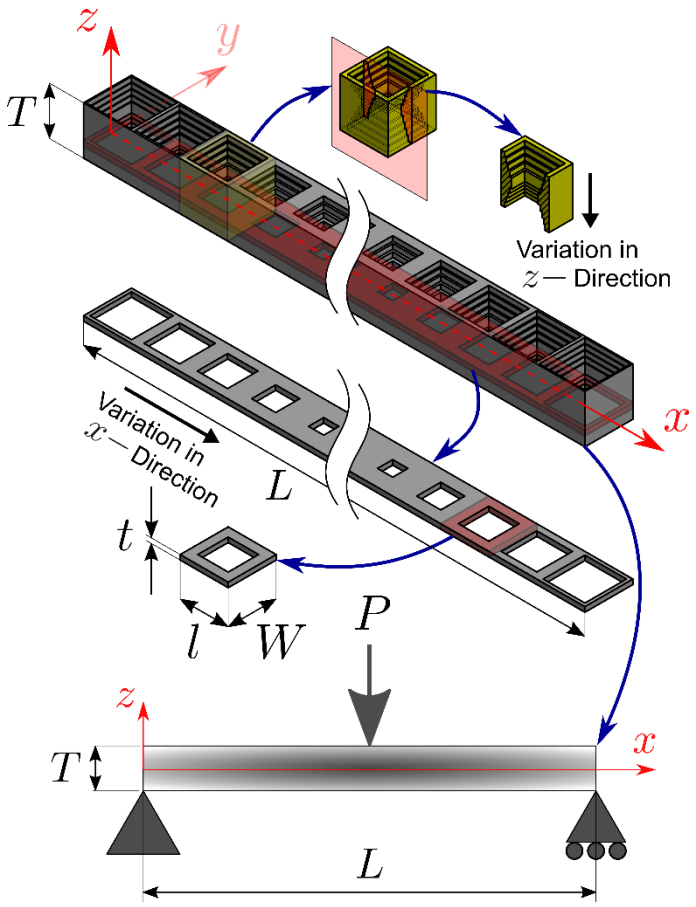

Figure 5-1- *Schematic view of a cellular beam ($L \times W \times T$) graded through its length (x-direction) and across its thickness (z-direction) and the associated loading and support conditions.*

The objective of this study is to find an optimum relative density distribution to minimize the maximum lateral deflection under a specified load. In other words, we aim at optimizing the relative density distribution such that the maximum bending stiffness is achieved while the total weight remains unchanged. The optimization problem is defined in Eq. (5.3), where K^b is the bending stiffness of the graded cellular beam. This optimization problem has N design variables that are relative densities of constituting cells. The design variables are optimized while a constraint is applied that satisfies a specified total relative density $\bar{\rho}$. The minimum and maximum allowable relative densities, i.e., optimization bounds on design variables, are set 0.1 and 1, respectively. The lower bound is set based on the limitations of the SLA 3D printer used for fabrication, which will be further discussed in **Section 5.5.1**. Therefore, the optimization problem can be formulated as:

$$\begin{aligned} &\max \quad K_b(\bar{\rho}_1, \bar{\rho}_2, \dots, \bar{\rho}_N) \\ &\text{wrt.} \quad \bar{\rho}_i \ (i = 1, \dots, N) \\ &\text{s.t.} \quad \begin{cases} \bar{\rho} = \sum_{i=1}^{N} \frac{\bar{\rho}_i}{N} \\ 0.1 \le \bar{\rho}_i \le 1 \end{cases} \end{aligned} \tag{5.3}$$

This optimization problem is solved using the TLBO algorithm [48] as a population-based optimization method. The equality constraint in Eq. (5.3) is treated as two inequality constraints with a tolerance of 0.001; in other words, the total relative density can be $\bar{\rho} \pm 0.001$.

5.5 Materials and methods

The abovementioned bending problem is solved with two numerical models, and an experimental study on 3D printed samples is adopted to verify the numerical results. The details of each method are discussed in this section.

5.5.1 Experimental study and detailed finite element modeling

Sample fabrication: In this study, stereolithography (SLA) is used to 3D print samples for experimental testing. SLA has higher accuracy and reliability compared to other widely accessible 3D printing technologies like fused deposition modeling (FDM). Also, layers in SLA 3D printed specimens are chemically bonded together by cross-linking photopolymers, which is much stronger than inter-layer bonds in FDM 3D printed products. Chemically bonded photopolymers are fully dense parts with isotropic properties and are more suitable for mechanical and structural applications than FDM 3D printed products that have inherent anisotropic properties [51, 52]. Accordingly, graded cellular beams are fabricated by *Formlabs Form 2*, a commercial SLA 3D printer. The base material used in this study is a brittle methacrylate photopolymer, with a commercial name of *Grey Pro* resin. The mechanical properties of the base material are determined by conducting uniaxial tensile tests on five 3D printed specimens according to the ASTM D638 standard. Dogbone samples are fabricated with the same 3D printer and cured for 60 minutes at 60 ℃. The stress-strain curves obtained from these tests are presented in **Figure 5-2a**, where error bars depict deviation from the mean value. As shown in **Figure 5-2a**, the material exhibits linear elastic behavior while the strain value is low, but nonlinearity increases as the strain increases. The Young's modulus ($E = 2.09\ GPa$) of the material is estimated to be the slope of the tangent line to the stress-strain curve in the small strain region near the origin. The nonlinear region is captured

through true stress – true strain data points, which are used to model the nonlinear behavior of the material in detailed FEA. **Figure 5-2b** presents the effect of changing the printing direction on the tensile stress-strain curve of the 3D printed dogbone samples. The dogbone samples in this test are fabricated by orienting parts in three different directions on the build platform of the 3D printer. We can observe that changing the printing direction has a negligible effect on the Young's modulus of the samples; however, it can alter the ultimate tensile strength. Samples placed vertically on the build platform appear to be the strongest. **Figure 5-3** shows the images of free and fractured surfaces of the dogbone samples taken by Scanning Electron Microscopy (SEM) to better explore the 3D printing quality and fracture type. The river pattern in the fracture surface, shown in **Figure 5-3a-b**, is considered as a sign of brittle failure [53-55]. Investigating the image of a free surface normal to the printing direction in **Figure 5-3c** reveals voids that are probably resulting from trapped air bubbles in the resin.

The existence of these voids, which diameters are changing from 10 μm to almost 300 μm, can affect the quality of the 3D printed parts. Printed layers and laser points are visible in the image of a free surface aligned with the printing direction shown in **Figure 5-3d**. The layer thickness is 100 μm as previously set in the print settings. **Figure 5-4a** shows the cellular SLA 3D printed beams with the same dimensions ($L = 150\ mm$ and $T = W = 15\ mm$) and consisting of 10 equal-sized cells in each *x*- and *z*-directions. The minimum wall thickness that can be 3D printed with acceptable accuracy and minimum shape deformation of 3D printed part during the curing process is about $0.4\ mm$. Consequently, the minimum relative density of cells considered in this study is assumed to be $\bar{\rho} = 0.1$ to assure the acceptable quality of SLA 3D printed cellular beams.

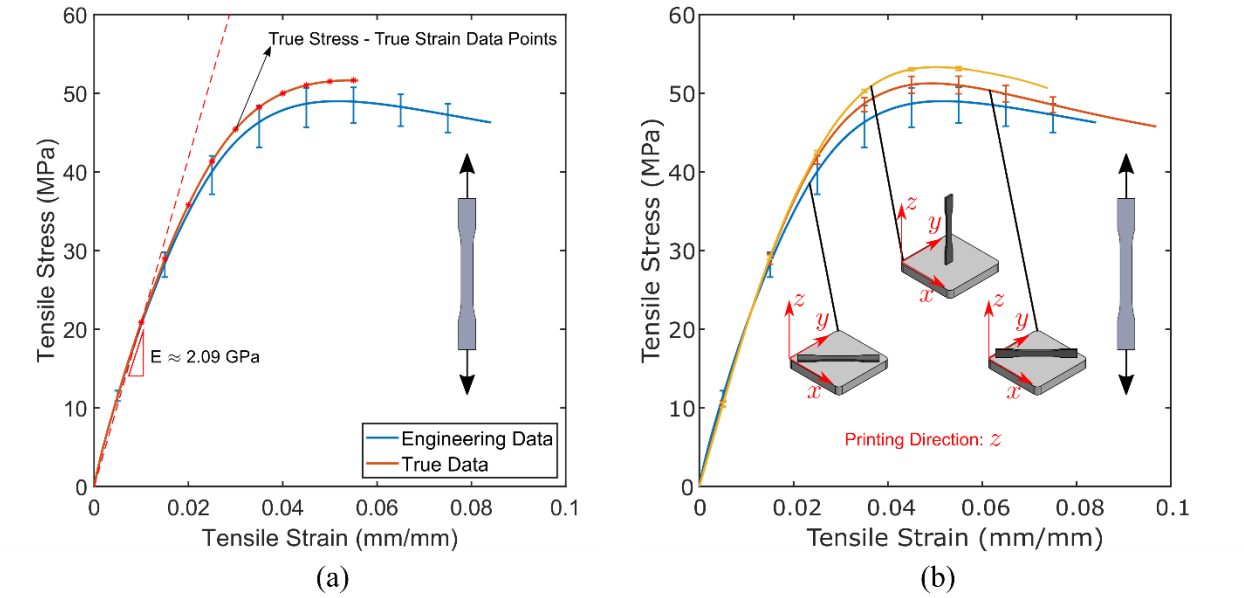

Figure 5-2- *(a) Tensile test results of SLA 3D printed dogbone samples manufactured out of Grey Pro resin, (b) the effect of changing the printing direction on the tensile stress-strain curve.*

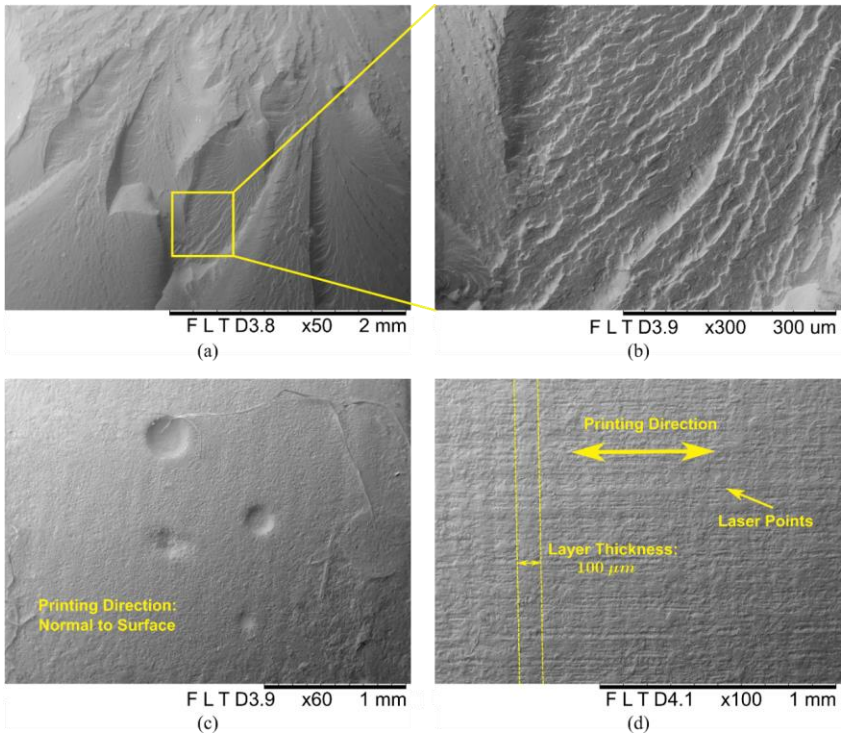

Figure 5-3- *(a and b) SEM images of the fractured surface, (c) free surface normal to the printing direction, and (d) free surface aligned with printing direction of SLA 3D printed dogbone samples.*

Testing procedure: Tensile and bending tests are performed by *ADMET eXpert 8612* with a 20kN load cell. A line load is applied to the beam with an appropriate fixture, and both edges of the sample are placed on two supports for bending tests, as shown in **Figure 5-4b**.

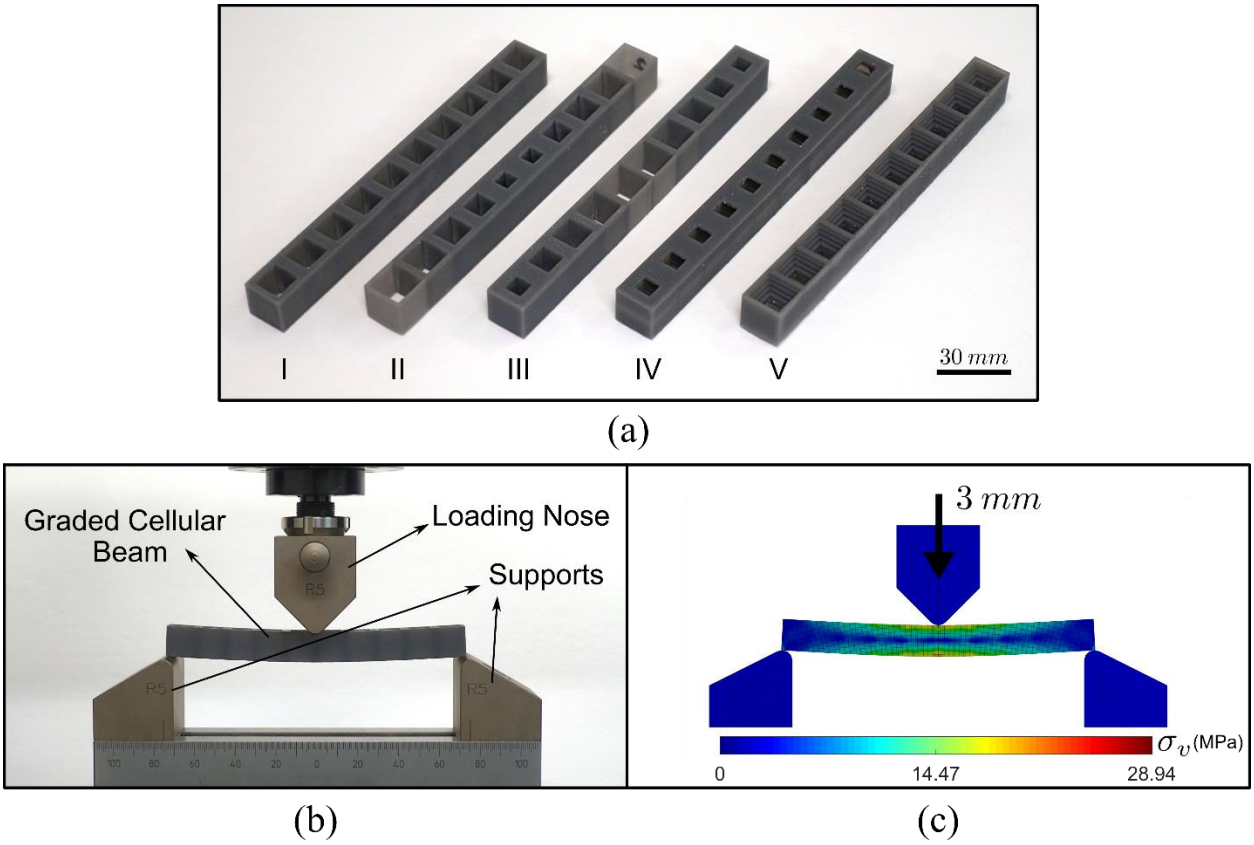

Figure 5-4- *(a) SLA 3D printed specimen of graded cellular beams manufactured out of Grey Pro resin, (b) experimental bending test setup, and (c) an example of detailed finite element modeling of the bending test (contour plot shows the von Mises stress of the cellular beam subjected to a downward 3mm displacement at the mid-length).*

Detailed finite element analysis: The detailed 3D FEA enables us to study the bending behavior of graded cellular beams of arbitrary architectures (**Figure 5-4c**). The 3D model of the cellular beam is created in SolidWorks 2019 and imported to the commercial ANSYS 2019R2 FE analysis

software for a detailed analysis. The nonlinear behavior of the constituent material of the beam is modeled using an isotropic hardening model with $E = 2.09\ GPa$ and $\upsilon = 0.3$, based on true stress-true strain data points (**Figure 5-2**). The supports with fillet radii of 5mm are made of steel (with Young's modulus of $200\ GPa$ and Poisson's ratio of 0.3) to make them almost rigid compared to the 3D printed polymeric beam. The FE analysis also takes into account the effect of large deflection and geometric nonlinearity. The type of contact between the beam and the supports is frictionless, while a bonded type is considered for the line contact between the tip of the loading nose and the beam to restrain its degrees of freedom and prevent rigid body motion. The bottom faces of the supports are fixed while a prescribed downward displacement is assigned to the loading nose. The amount of this prescribed displacement is such that we can assume that other parts of the loading nose do not make contact with the beam. The reaction force at the loading nose is probed to draw the force-deflection diagram, the slope of which represents the bending stiffness of the beam. The structure (beam and support) is discretized with higher-order 20-node SOLID186 3D elements together with CONTA174/TARGE170 paired 3D contact elements, and a convergence study is conducted to avoid the dependency of the reaction force at the loading nose on the mesh size.

5.5.2 Hybrid-homogenized modeling

In this approach, each cell is replaced with an equivalent solid with effective elastic properties. This method can expedite the computational procedure as it overlooks the local deformation (e.g., local buckling [40] and wrinkling [56]). A solid cell, whose properties are obtained through a homogenization method, replaces the actual cell of a cellular beam. The standard mechanics homogenization with periodic boundary conditions is adopted here to obtain the effective mechanical properties of constitutive cellular materials [57]. These equivalent elastic properties

are then used in the constitutive models to find the structural responses of the beam [39]. The equivalent stiffness matrix, $\hat{C}_{ijmn}$, of each periodic unit cell is approximated by [58]:

$$\hat{C}_{ijmn} = \frac{1}{V_{cell}} \int C_{ijkl} M^{C}_{klmn} dV \quad \text{with } i,j,k,l,m,n = 1,2,3 \tag{5.4}$$

where C_{ijkl} is the stiffness tensor of the base material, V_{cell} represents the volume of a unit cell and M^{C}_{mnkl} is the local structural tensor. The structural unit tensor is defined to relate the local strain tensor to the effective strain and is defined as:

$$\varepsilon_{ij} = M^{C}_{ijkl} \hat{\varepsilon}_{kl} \tag{5.5}$$

where ε_{ij} is the strain tensor and the circumflex accent indicates the equivalent stiffness properties $\hat{C}_{ijkl}$ or an average strain field $\hat{\varepsilon}_{ij}$. In the current study, the 3D components of the local stiffness tensor, $\hat{C}_{ijmn}$, are evaluated by using Eqs. (5.4) and (5.5). We apply six independent 3D unit strains to a representative cell of unit dimensions and with periodic boundary conditions, through APDL coding in ANSYS, where the 3D unit cell is meshed with 8-node SOLID185 3D elements. Upon calculation of local strain tensor, ε_{ij}, the structural tensor, M^{C}_{mnkl}, is obtained by Eq. (5.5); finally, the effective stiffness tensor is calculated by Eq. (5.4).

The effective mechanical properties (i.e., stiffness tensor) obtained by standard mechanics homogenization are used in a structural theory to evaluate the bending response of a cellular beam. In this study, the third-order shear deformation theory (TSDT) is employed to obtain the governing equations of the graded cellular beams as follows [59, 60]:

$$N_{xx,x} = 0 \tag{5.6a}$$

$$M_{xx,xx} + q = 0 \tag{5.6b}$$

$$M_{xx,x} + \frac{4}{3H^2}\left(3R_x - P_{xx,x}\right) - Q_x = 0 \tag{5.6c}$$

where N_{xx}, M_{xx}, and P_{xx} are normal stress resultants defined as:

$$\begin{Bmatrix} N_{xx} \\ M_{xx} \\ P_{xx} \end{Bmatrix} = \begin{bmatrix} A & B & E \\ B & D & F \\ E & F & G \end{bmatrix} \begin{Bmatrix} u_{,x} \\ \varphi_{,x} \\ -\frac{4}{3H^2}\left(\varphi_{,x} + w_{,xx}\right) \end{Bmatrix} \tag{5.7}$$

and Q_x and R_x are shear stress resultants written as:

$$\begin{Bmatrix} Q_x \\ R_x \end{Bmatrix} = \begin{bmatrix} A & D \\ D & F \end{bmatrix} \begin{Bmatrix} \varphi + w_{,x} \\ -\frac{4}{H^2}\left(\varphi + w_{,x}\right) \end{Bmatrix}. \tag{5.8}$$

In Eqs. (5.7) and (5.8), u and w are displacement components in *x*- and *z*-directions, respectively, and φ is the rotation of mid-plane at $z = 0$ in the $xz-$plane. The stiffness matrices $A, B, D, E, F,$ and G are defined by:

$$([A], [B], [D], [E], [F], [G]) = \sum_{K=1}^{N} \int_{z_k}^{z_{k+1}} \left[\hat{C}\right](1, z, z^2, z^3, z^4, z^6) dz \tag{5.9}$$

where $\hat{C}$ is the equivalent stiffness matrix calculated by Eq. (5.4). In the next step of the hybrid-homogenized modeling approach, the governing equations (Eqs. (5.6a-c) are discretized and solved based on a finite element technique which is programmed in MATLAB software. Further information about calculating the stiffness and loading matrices for FEA can be found in [27]. The details of approximation functions and algebraic equations derived by FEA can be found in the following references [38, 61, 62].

It is worth mentioning that the proposed hybrid-homogenized modeling is not capable of taking the local deformation (e.g., local buckling and warping) into account due to the limitation of homogenization modeling. However, the results of the FEA and experimental test corroborate the predictions of hybrid-homogenized modeling when the cell wall is thick enough to avoid local deformation.

5.6 Results and discussion

5.6.1 Validation of the proposed model

Using hybrid-homogenized modeling as the basis of the optimization technique necessitates a validation study. As a result, we compare the results of the proposed model with the results of detailed 3D FE analysis and experiment for the bending response of several beams with different gradients of relative density as ordered below:

5.6.1.1 Theme A: graded in the x-direction

Fabricated samples in this group are classified as (**Figure 5-4a**):

- *Sample I*: Cellular beam specimens of this sample have a uniform architecture with a relative density of 0.5, uniformly distributed among all the unit cells of the beam.
- *Sample II*: In these graded cellular beam specimens, the relative density is increasing linearly and symmetrically from 0.2 at both ends to 0.8 in the middle unit cells of the beam such that the total relative density maintains $\bar{\rho} = 0.5$.
- *Sample III*: The relative density distribution in this sample is the opposite of sample II; in other words, the relative density is decreasing linearly from 0.8 at both ends to 0.2 in the middle unit cells of the beam.

Figure 5-5a depicts the experimental results for a transverse load (P) versus lateral deflection (δ) for the three above-mentioned 3D printed samples. The maximum deflection of the middle of the architected cellular beams is set to be 10% of the thickness, i.e., 1.5 mm, to avoid the effect of geometrical nonlinearities in the results. As shown in **Fig. 5-5a**, the maximum deflection predicted by different methods are in a good agreement. The deviation of bending stiffness ($K_b = P/\delta$) obtained by FEA and hybrid-homogenized model from that of experiments is presented in **Figure 5-5b**. This figure shows that the error in the detailed FEA is less than the hybrid-homogenized model in general, which stems from the fact that the detailed FEA contemplates the effect of local deformations and considers the boundary conditions the same as those used during the experiment. Also, the overall maximum error in bending stiffness is shown to be less than 10% for samples I and II and 30% for sample III, which confirms the validity of the results obtained in this group by the proposed homogenized model.

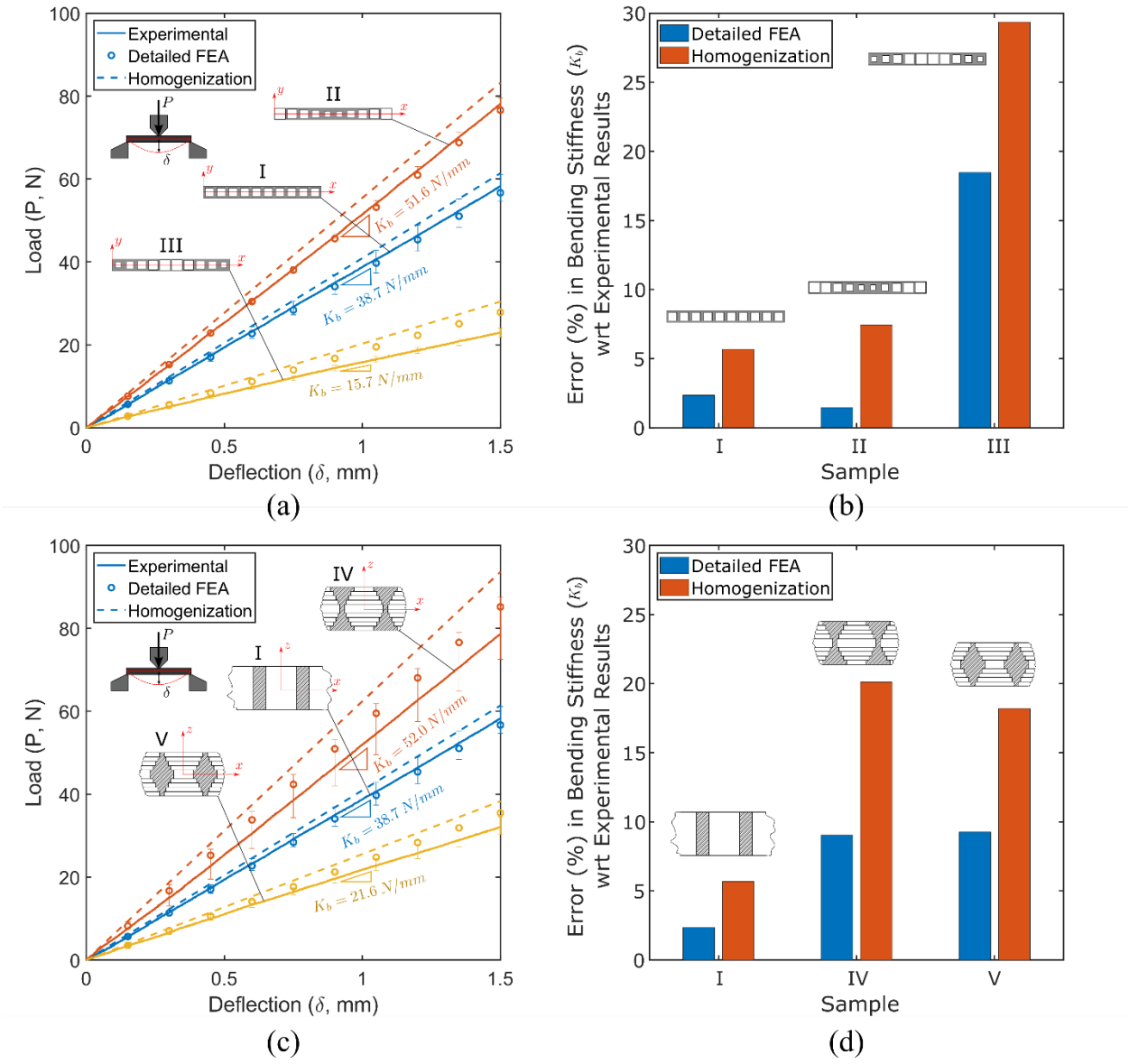

Figure 5-5- *Comparison of the results obtained from experimental bending test, detailed FEA and hybrid-homogenized modeling: load vs. deflection curve for the cellular beams graded in (a) x-direction and (c) z-direction along with the percent error in experimental bending stiffness (K_b) and bending stiffness calculated using detailed FEA and homogenization for cellular beams graded in (b) x-direction and (d) z-direction.*

In **Figure 5-5a**, grading the architecture of the beam brings about the difference between the bending stiffness of three cellular beams with the same total relative density. Distributing relative densities across the length of the beam can lead to a higher ($51.6\ N/mm$ in sample II) or a lower ($15.7\ N/mm$ in sample III) bending stiffness compared to the uniform distribution ($38.7\ N/mm$ in sample I). Maintaining higher relative densities at mid-span of the graded cellular beam, where the bending moment is maximum, results in higher bending stiffness. The effect of different gradients will be further discussed in **Section 5.6.2**.

5.6.1.2 Theme B: graded in the z-direction

In this group, two other samples are considered in addition to Sample I (**Figure 5-4c**):

- *Sample IV*: Cellular beam specimens of this sample have symmetric relative density distribution across the thickness of the beam such that the relative density is 0.8 at top and bottom layers, while it is 0.2 in the middle layers of the beam.
- *Sample V*: In this sample, the relative density distribution is reversed compared to sample IV; in other words, relative density increases linearly from 0.2 at top and bottom layers to 0.8 in the middle layers of the architected cellular beam.

Figure 5-5c presents the comparison of the experimental and computational results for the above-mentioned samples compared to sample I. The deviation between bending stiffness values obtained by both numerical models and experimental testing is presented in **Figure 5-5d**. The errors are less than 25% for three samples (including one uniform and two graded samples), which is less than the maximum error in samples of Theme A. **Figure 5-5b** and **Figure 5-5d** demonstrate the validity of the hybrid-homogenized modeling in analyzing cellular beams that are graded through the

length or across the thickness. The higher bending stiffness measured for sample IV ($52.0\ N/mm$) compared to sample I ($38.7\ N/mm$) demonstrates the fact that maintaining higher relative densities at the top and bottom layers, where maximum bending stresses occur, increases the bending stiffness of the graded cellular beam.

5.6.2 Optimized relative density distribution

This section presents the optimization results of the relative density distribution in the cellular beam for maximizing the bending stiffness. First, we obtain the optimized relative density distribution in the *x*-direction for a whole range of total relative densities from 0.1 to 1. Next, we carry out a similar study for optimum relative density distribution in the *z*-direction. These are followed by a discussion on optimization in both *x*- and *z*-directions. Some of the optimized graded cellular beams are 3D printed for experimental testing and comparative study.

5.6.2.1 Optimization in x-direction

Figure 5-6 shows the results of optimization for a $150\ mm \times 15\ mm \times 15\ mm$ cellular beam with 10 cells in the *x*-direction (or $N = N_x = 10$) and three different total relative densities, including 0.2, 0.55, and 0.9, known as low-range, mid-range, and high-range total relative densities, respectively.

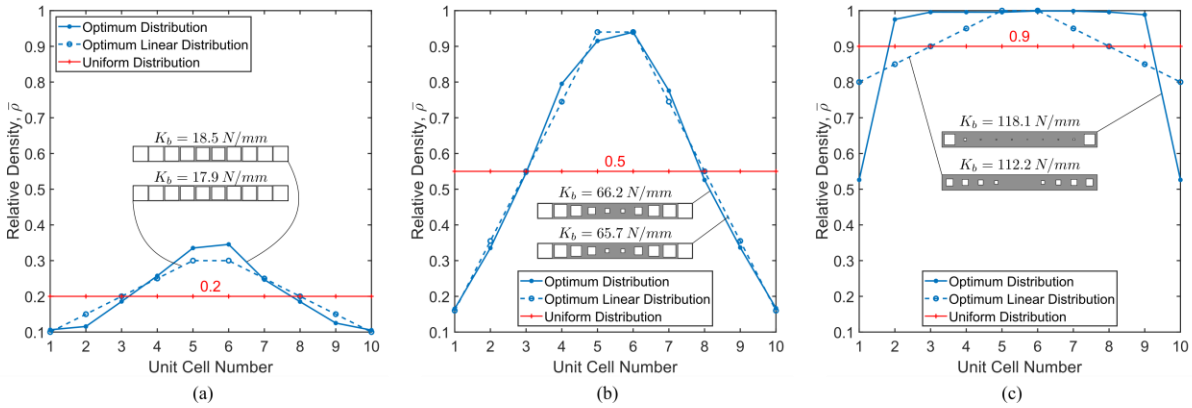

***Figure 5-6**- Optimized relative density distribution in x-direction for total relative densities of: (a) 0.2, (b) 0.55, and (c) 0.9.*

The optimum distribution for all three cases is where the relative density is symmetric, with a maximum relative density in the middle (**Figure 5-6**). However, the variation slope differs for alternative total relative densities. For a total relative density of 0.2 and 0.55 (**Figure 5-6a** and **Figure 5-6b**), the optimum relative density of cells varies almost linearly from a minimum at the edges to a maximum in the middle. In contrast, the optimum variation of cell relative densities is not linear for a higher total relative density. The optimum distributions for high-range relative densities are achieved by minimizing the relative density of cells at both ends as much as possible to obtain the maximum feasible relative density for the middle cells. This distribution results in a sharp change of cell relative densities as we move toward the edges.

As we discussed earlier, from a physical point of view, the optimum distribution of relative densities in an architected cellular beam graded in *x*-direction complies with the change of bending moment through its length. The maximum bending moment occurs at the mid-length of the cellular beam for a middle load on a simply-supported beam. Thus, stronger cells must be placed in the middle of the beam to increase the bending stiffness. An analytical study based on the Euler-

Bernoulli beam theory graded through its length is presented in **Appendix 5.A**, which justifies this distribution for relatively thin beams. A special case of asymmetric loading and how it affects the optimum relative density distribution is also studied in **Appendix 5.B**.

Generally, the optimization process can take into account an arbitrary distribution of relative density; in other words, the only constraint to satisfy can be the specified total relative density. However, employing a predefined function for optimizing the structural behavior of cellular beams not only clarifies the effect of different parameters on the objective function but also speeds up the optimization process. Consequently, we defined the following bi-linear distribution function to gain deeper insight into the optimized relative density distribution:

$$\bar{\rho}_i(m,n) = \begin{cases} m\left(\dfrac{2i-n-1}{n-1}\right) + \bar{\rho} & \text{for } i \le n \\ -m\left(\dfrac{2i-n-1-N}{N-n-1}\right) + \bar{\rho} & \text{for } i > n \end{cases} \tag{5.10}$$

where m is the slope of relative density variation, and n is the cell number in which the extremum value of relative density occurs. Consequently, the optimization problem (defined in Eq. (5.3)) can be modified as follows:

$$\begin{aligned} &\max \quad K_b\left(\bar{\rho}_i(m,n)\right) \text{ for } i = 1, \dots, N \\ &\text{wrt.} \quad m, n \end{aligned} \tag{5.11}$$

Comparing Eqs. (5.3) and (5.11) for the case of 1×10 cellular beam, the number of design variables decreases from 10 to 2, which accelerates the optimization process. Dashed lines in **Figure 5-6** show the results of optimization for the linear distribution of relative densities. As previously mentioned, the optimum distribution is almost linear in low-range, and mid-range total relative densities and optimization results with a linear distribution function give a good

approximation of general optimization. The maximum difference in bending stiffness obtained by each of these two optimization methods is less than 5%. In the case of high-range total relative density, where the optimum linear distribution deviates from the optimum arbitrary distribution, this maximum difference is still below 10%. Thus, employing optimized linear distribution functions yields relatively acceptable results for increasing the bending stiffness of the *x*-directionally graded beam.

Figure 5-7 shows normalized bending stiffness ($\overline{K}_b(\bar{\rho}) = K_b(\bar{\rho})/K_b(\bar{\rho} = 1)$) and normalized maximum deflection $\left(\bar{\delta}_{max} = \delta_{max}/\delta_{max}\,(\bar{\rho} = 0.1)\right)$ versus total relative densities along with the corresponding discrepancies to compare the results of optimization with and without a predefined distribution function. The bending stiffness is normalized by the bending stiffness of a solid beam (total relative density of 1 ($\bar{\rho} = 1$)) and the maximum deflection is normalized by the maximum deflection of the most compliant geometry with a total relative density of 0.1. These values are also presented in **Figure 5-7** for a uniform distribution, i.e., no relative density gradient, to elucidate the improvement achieved by optimization.

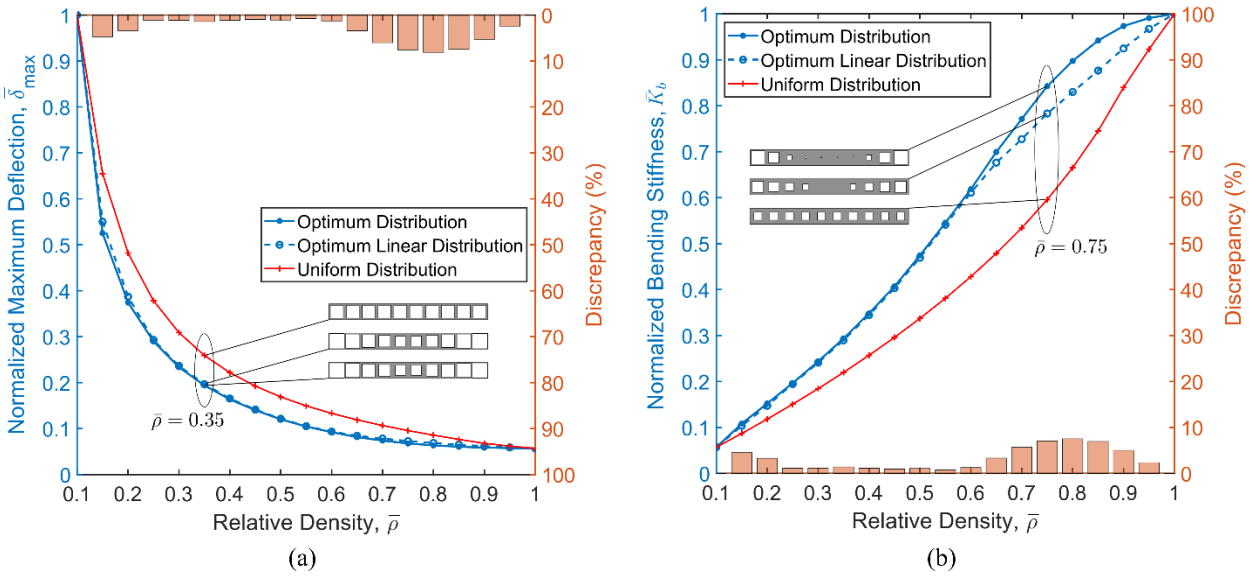

Figure 5-7- *(a) Normalized bending stiffness and (b) normalized maximum deflection versus total relative density for the cellular beam optimally graded in the x-direction along with the discrepancies between optimization results with and without using a linear relative density distribution function.*

Stiffness-to-density ratio, or so-called specific bending (flexural) stiffness, is a critical index in a variety of applications that require stiffness-driven design [1, 63]. The normalized bending stiffness-to-density ratio ($\overline{K}_b/\bar{\rho}$) is plotted versus total relative density in **Figure 5-8**. The value of $\overline{K}_b/\bar{\rho} = 1$ for this ratio in **Figure 5-8** corresponds to a cellular beam with ideal unit cells, i.e., cells in which effective properties are a linear function of the relative density (Voigt upper bound anisotropic materials) [64]. The normalized bending stiffness-to-density ratio can exceed 1 for optimized longitudinally graded cellular beams with a total relative density of 0.55 or more. In other words, graded cellular beams with the optimum distribution of relative densities can outperform a cellular beam with ideal unit cells. The maximum bending stiffness-to-density ratio achieved by this method is 1.12 for total relative density of $\bar{\rho} = 0.75$. Furthermore, employing a

predefined linear distribution function leads to a similar trend, corroborating our previous statement on the validity of using such a function for relative density distribution in *x*-direction.

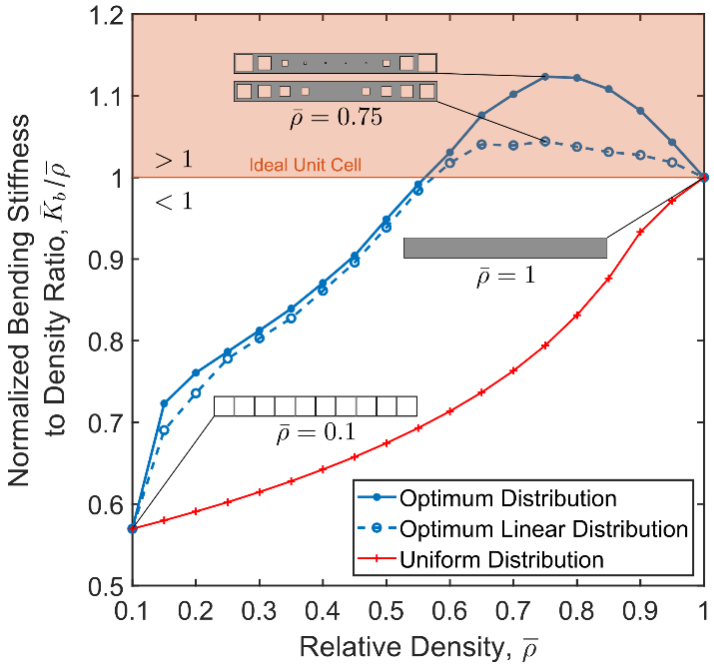

Figure 5-8- *Normalized bending stiffness-to-density ratio versus total relative density for the cellular beam graded in the x-direction.*

5.6.2.2 Optimization in z-direction

Figure 5-9 presents the optimum relative density distributions for $150\ mm \times 15\ mm \times 15\ mm$ cellular beams graded with 10 unit cells in z-direction for total relative densities of 0.2, 0.55, and 0.9. This figure demonstrates that optimization tends to distribute relative densities such that cells with maximum feasible relative densities are at the top and bottom layers, where bending stresses are maximum. This distribution reminds the well-known I-beam cross-section material concentration at the flanges, which contributes to an increased bending resistance. Consequently, contrary to the graded cellular beams in the *x*-direction, optimization results using a predefined

linear distribution function (Eq. (5.10)) deviate more from the results obtained without any predefined function.

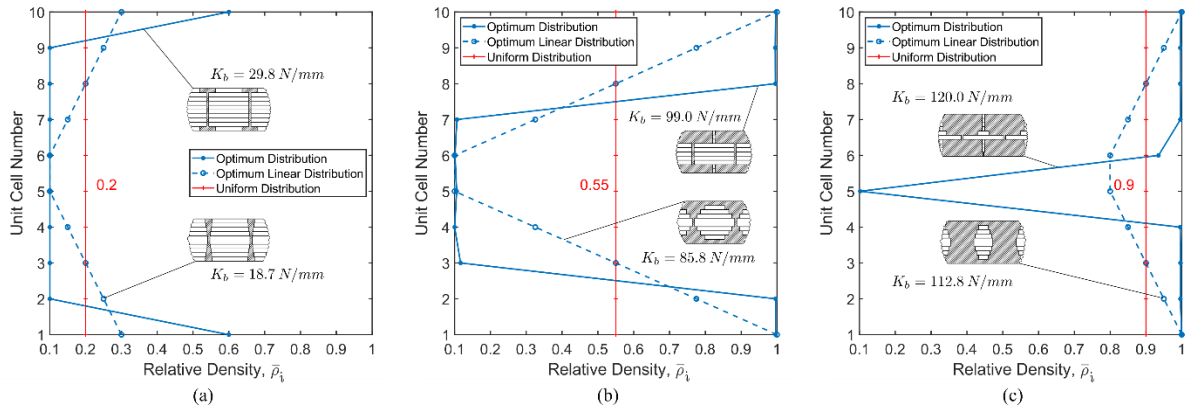

Figure 5-9- *Optimum relative density distribution in z-direction for total relative densities of: (a) 0.2, (b) 0.55, and (c) 0.9.*

Figure 5-10 depicts normalized bending stiffness and normalized maximum deflection for *z*-directionally graded cellular beams with total relative densities of 0.1 to 1 as well as the discrepancies between optimization results obtained with and without a predefined linear function. As shown in **Figure 5-10**, the discrepancies are less than 20% for total relative densities above 0.55; therefore, using a predefined linear function for optimizing cellular beams graded across the thickness could be a viable alternative if the total relative density is more than 0.55.

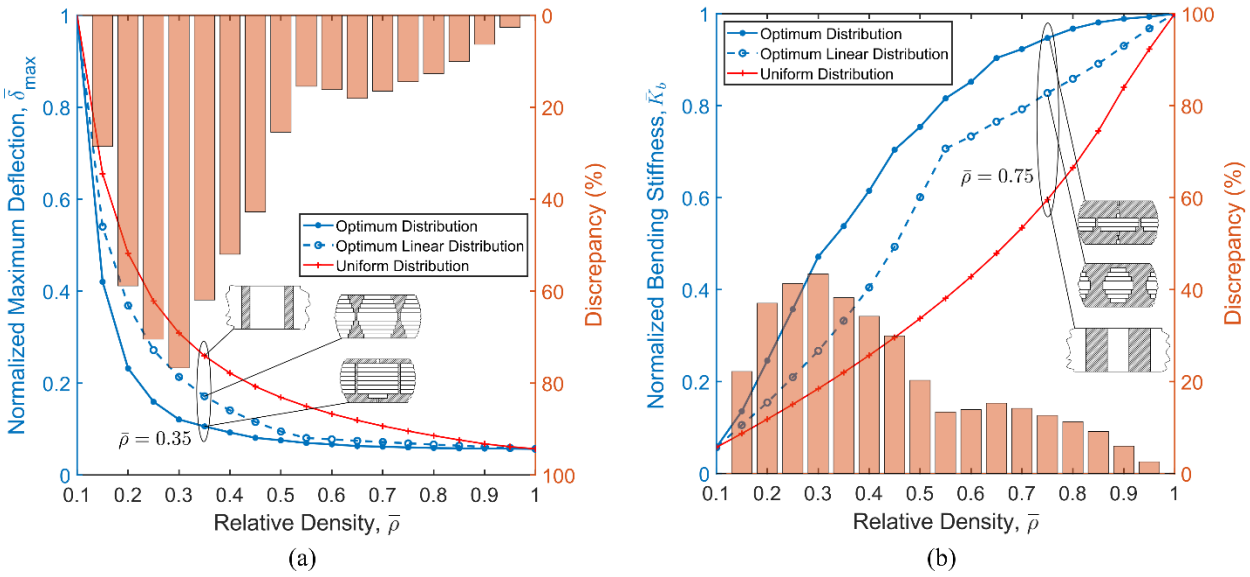

Figure 5-10- *(a) Normalized bending stiffness, and (b) normalized maximum deflection versus total relative density for the cellular beam optimally graded in z-direction along with discrepancies between optimization results with and without using a linear relative density distribution function.*

Figure 5-11 depicts the normalized bending stiffness-to-density ratio for a range of total relative densities from 0.1 to 1. For optimized cellular beams graded without a predefined function, this value peaks at about 1.6 for a total relative density of 0.3. **Figure 5-11** also illustrates that optimizing a cellular beam graded in the *z*-direction can result in bending stiffness-to-density ratios greater than 1, corresponding to a cellular beam with a uniform distribution of ideal unit cells, even for total relative densities as low as 0.2. Graded cellular beams with optimum linear distribution, however, show a normalized bending stiffness higher than 1 for relative densities higher than 0.45, although they still provide significant enhancement compared to uniform cellular beams.

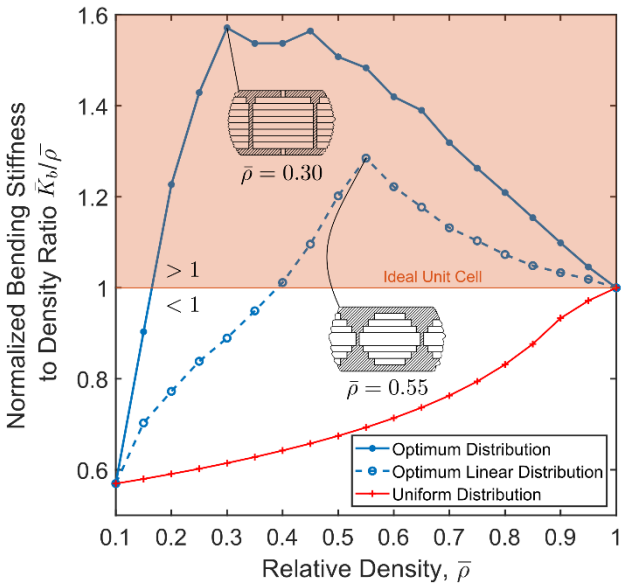

***Figure 5-11**- Normalized bending stiffness-to-density ratio versus total relative density for the cellular beam graded in the z-direction.*

5.6.2.3 Optimization in both x- and z-directions

Optimizing the relative density distribution of the cellular beam in both *x*- and *z*-directions is based on a level-by-level approach. First, we evaluate the effective properties of unit cells optimized in *z*-direction for every total relative density from 0.1 to 1. Next, we find the optimized distribution of these cells in the *x*-direction. In the end, the final distribution of relative densities will be optimum in both *x*- and *z*-directions. **Figure 5-12** depicts the results of optimization implementing the abovementioned approach along with previous findings for a comparative study. As shown in **Figure 5-12**, optimizing in both *x*- and *z*-directions slightly improves the bending stiffness of the graded cellular beam compared to optimization in the *z*-direction.

Table 5-1 provides a summary of the optimization results. **Figure 5-12** and also illustrate that optimization in *z*-direction affects the stiffness more than optimization in the *x*-direction. Consequently, we can conclude that following the opposite approach in finding optimized distribution, i.e., first optimizing in the *x*-direction, then *z*-direction would lead to less efficient behavior. In this case, the optimization in *x*-direction leads the optimization process, which confines the more effective *z*-direction optimization, and the stiffness of the final distribution will be less than the approach taken in this section.

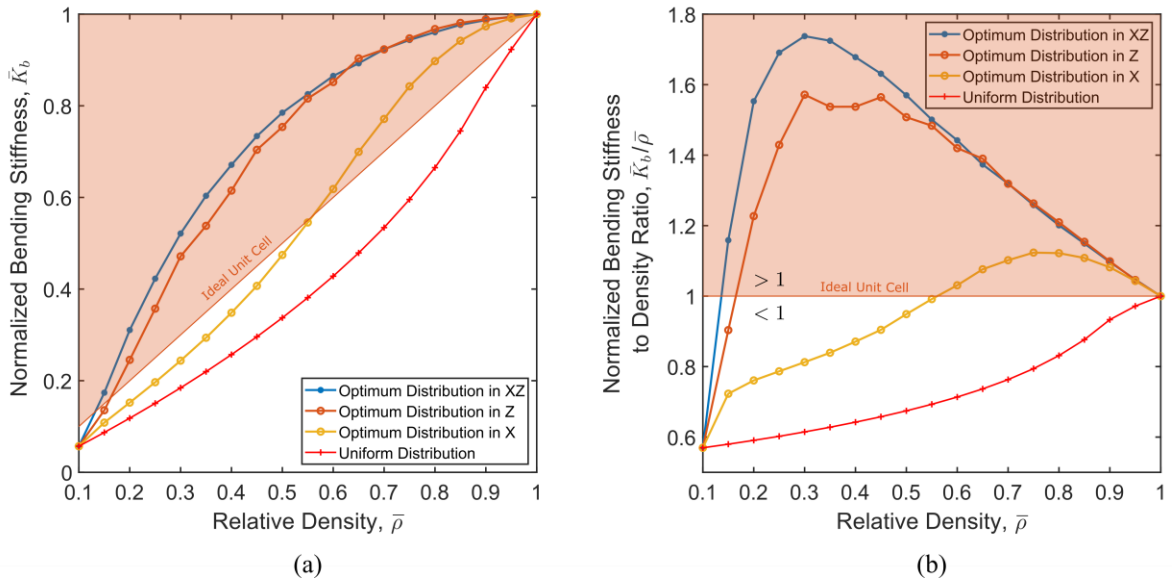

Figure 5-12- *Comparing the results of optimization for the cellular beam with optimum relative density distribution in the x-direction, z-direction, and x- and z-directions: (a) Normalized bending stiffness and (b) Normalized bending stiffness-to-density ratio versus total relative density.*

Table 5-1- *Summary of the results of the optimization study carried out on the graded cellular beams.*

	Max. Improvement in $\overline{K}_b$ (%)	Max. $\overline{K}_b/\bar{\rho}$
Optimum linear distribution in *x*-direction	42.6% at $\bar{\rho} = 0.60$	1.04 at $\bar{\rho} = 0.75$
Optimum distribution in *x*-direction	46.1% at $\bar{\rho} = 0.65$	1.12 at $\bar{\rho} = 0.75$
Optimum linear distribution in *z*-direction	85.4% at $\bar{\rho} = 0.55$	1.29 at $\bar{\rho} = 0.55$
Optimum distribution in *z*-direction	155% at $\bar{\rho} = 0.30$	1.57 at $\bar{\rho} = 0.30$
Optimum distribution in both *x*- and *z*-directions	182% at $\bar{\rho} = 0.30$	1.74 at $\bar{\rho} = 0.30$

5.6.2.4 Experimental testing on 3D printed optimally graded cellular beams

Graded cellular beams with total relative densities of 0.35, 0.55, and 0.75 are 3D printed for experimental testing to verify the optimization results. These total relative densities are close to optimum values associated with the maximum improvements in bending stiffness (

Table 5-1). For each of these total relative densities, specimens with uniform and optimum distributions in the *x*-direction, *z*-direction, and both *x*- and *z*-directions are fabricated, as shown in **Figure 5-13**.

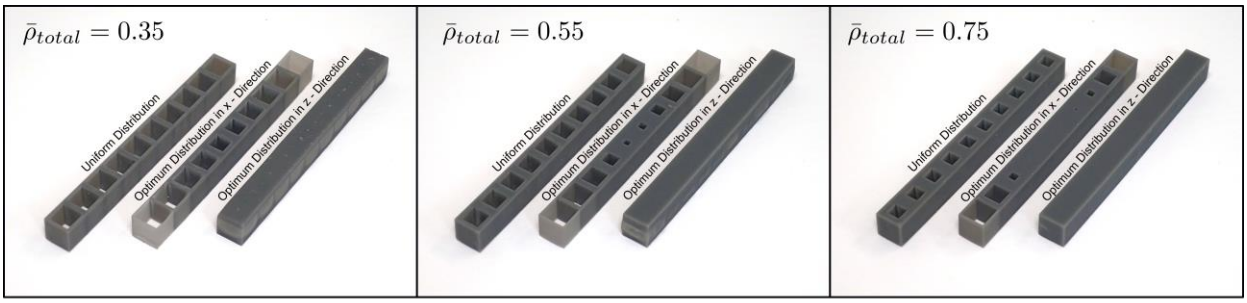

(a) (b) (c)

Figure 5-13*- 3D-printed uniform and graded cellular beam specimens with: (a)* $\bar{\rho} = 0.35$*, (b)* $\bar{\rho} = 0.55$*, and (c)* $\bar{\rho} = 0.75$.

Figure 5-14 presents the results of experimental tests together with the detailed FEA and hybrid-homogenization. This figure also reveals a good agreement between the results obtained by the three above mentioned methods. Experimental tests and detailed FEA verify the calculated maximum bending stiffness of graded cellular beams with the optimum distribution of relative density obtained by optimization based on the proposed hybrid-homogenized model. The experimental data confirms that optimum distribution of relative density of graded cellular beams in the *z*-direction yields more improvement in bending stiffness than optimum distribution in the *x*-direction, particularly at low-range total relative densities. For example, experiments show that at $\bar{\rho} = 0.35$, optimum distribution of the relative densities in *x*-direction will improve the bending stiffness of the graded cellular beam by 15%; however, with optimum distribution in the *z*-direction, this improvement will be raised to 123%. Samples with the optimum distribution in both *x*- and *z*-directions can further enhance the bending stiffness; however, this improvement is

insignificant compared to the improvement made by the gradient in the *z*-direction. At high range total relative densities, optimum distribution of relative density in the *x*-direction leads to a considerable increase in the bending stiffness of the graded cellular beam.

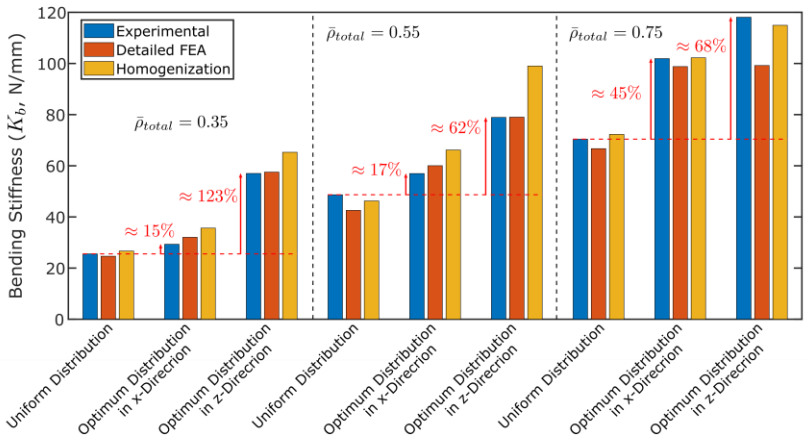

Figure 5-14- *Bending stiffness of optimally graded cellular beams calculated by experimental testing on SLA 3D printed samples, detailed FEA, and hybrid-homogenized.*

5.6.3 3D cell architectures

The optimization results presented so far are for graded cellular beams constructed by unit cells of an extruded square (ES) geometry (**Figure 5-1**). In this section, the proposed method is extended to 3D cell architectures, and the effect of the unit cell geometry on the optimization results is studied by analyzing cellular beams with octet truss (OT) unit cells. The variation of relative densities is merely considered in the *x*-direction since these unit cells are 3D cubic cells, and their variation in the *z*-direction is not possible. In **Figure 5-15**, we compare the optimization results for the cells with OT architecture with those previously obtained for ES geometry. ES has higher bending stiffness compared to OT since it develops stresses that efficiently utilize material volume (particularly for low-density cells) to increase the overall stiffness [64, 65]. **Figure 5-15** clearly

shows that the maximum feasible bending stiffness of a graded cellular beam depends on the cell architecture. We can also observe that optimized graded cellular beams with OT unit cells can achieve bending stiffness-to-density ratios higher than the uniform cellular beam made of ideal unit cells only for a small range of high total relative density ($\bar{\rho} > 0.70$).

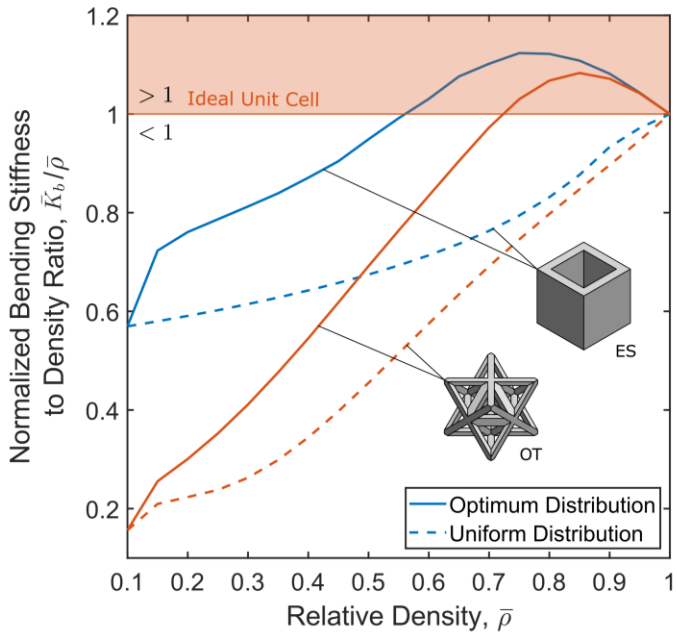

Figure 5-15- *Normalized bending stiffness-to-density ratio versus total relative density for optimally graded cellular beams with unit cells of different geometries (ES: Extruded Square and OT: Octet Truss).*

3D printed specimens of uniform and graded cellular beams with the OT cell geometry with the total relative density of 0.55 are shown in **Figure 5-16**. **Figure 5-17** compares the results of experimental tests, detailed FEA, and homogenized modeling for graded cellular beams of ES and OT cell topologies. Optimal grading of the cellular beam with OT architecture improves its bending stiffness by 58% at $\bar{\rho}_{total} = 0.55$. **Figure 5-17** shows a good agreement between the results obtained with FEA and experimental tests; however, the errors are more significant between homogenization findings and experimental results, particularly in the case of beams with OT unit

cell geometries. In addition to overlooking local deformation in hybrid-homogenized modeling, imperfect periodicity of the finite number of unit cells in the beam, and the discrepancy between the second moment of area for homogenized and non-homogenized unit cell geometries can contribute to the errors of homogenized modeling [66, 67]. These errors are minimized for extruded 2D unit cells (5% maximum error); however, they can be more considerable in the case of unit cells with 3D architectures (40% maximum error here). Consequently, one should cautiously generalize the proposed methodology to cellular beams made of 3D unit cells.

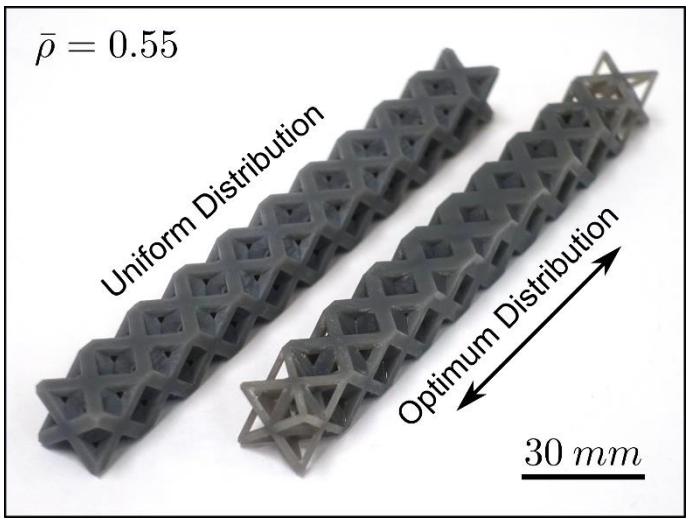

Figure 5-16- *3D printed, uniform and graded in the x-direction, cellular beam specimens of octet-truss geometry at* $\bar{\rho} = 0.55$.

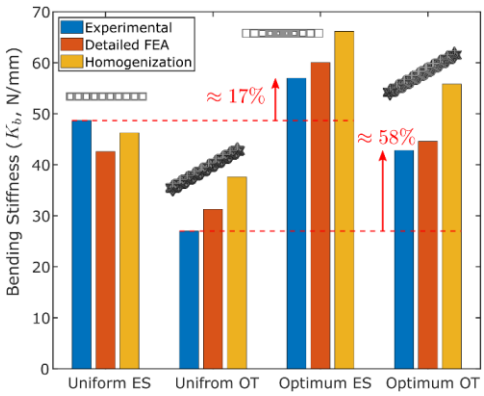

Figure 5-17- *Comparing the experimental, detailed FEA, and hybrid homogenized modeling results for graded cellular beams of ES and OT geometries at* $\bar{\rho} = 0.55$.

5.7 Concluding remarks

The optimum relative density distribution through the length and across the thickness of the newly designed cellular beams is obtained to maximize their bending stiffness. We utilize a hybrid-homogenized modeling method, validated by experimental testing and detailed FEA, to transform the optimization process into a shape optimization problem with relative densities of unit cells as design variables. This problem is solved using a population-based TLBO algorithm, and the optimization results are validated by conducting experimental bending tests on optimally graded cellular beams additively manufactured by SLA 3D printing. The main findings of the current study can be summarized as follows:

- The optimum relative density distribution of longitudinally graded cellular beams is almost linear, particularly for low- to mid-range total relative densities. The optimization results show less than 10% difference for the maximum feasible bending stiffness when a linear function is assumed for the relative density distribution instead of leaving it to be changed arbitrarily (**Figure 5-6** and **Figure 5-7**).
- Assuming a predefined linear distribution function can reduce the computational time of the optimization process, e.g., more than ten times for a 1×10 cellular beam while the obtained distribution is quiet close to general optimization for most of the cases (**Figure 5-9** and **Figure 5-10**).
- Optimum distribution of the relative density across the thickness of the cellular beam results in more significant improvements in bending stiffness (e.g., 155% improvement at $\bar{\rho}_{total} = 0.30$) compared to optimally graded cellular beams in the longitudinal direction (e.g.,

46% improvement at $\bar{\rho}_{total} = 0.65$), particularly at low-range total relative densities (**Figure 5-12**).

- Cellular beams can be optimally graded to achieve a bending stiffness-to-density ratio higher than one while outperforming uniform cellular beams with ideal unit cells (**Figure 5-12**).

The results of this paper open a new avenue for the design and fabrication of the next generation of optimized lightweight 3D printed structures made of polymers, composites, and even metals. We can use this strategy to increase the stiffness or flexural rigidity of structural elements without increasing the weight (enhancing specific stiffness). This is a leap forward in applications with required stiffness-driven designs, e.g., in airplane wings and load-bearing structural elements such as joist, girder, beam, and slab. Functionally graded cellular materials can offer a new design paradigm for developing meta-structures with enhanced multifunctional properties, along with other microarchitectural design approaches [68-70],

The main objective of this work is to improve the bending stiffness-to-weight ratio of graded cellular beams; however, the development of a framework to accomplish other objectives such as increasing the buckling load and controlling the natural frequencies are quite feasible by making slight modifications in the hybrid homogenized model. In some instances where the strength is also of importance for design, it can dictate the lower bounds on the relative densities in the optimization problem. Therefore, an exciting future endeavor may be to develop a framework to improve stiffness not only by considering the manufacturing limitations but also by considering the strength requirements. Further studies may also be conducted to reveal the capabilities of graded structures in other functionalities such as energy absorption and impact resistance.

5.8 Appendix 5.A: Analytical study based on Euler Bernoulli beam theory

Using Euler-Bernoulli beam theory, the maximum deflection (δ_{max}) of a simply-supported cellular beam of length L subjected to a point load of P at mid-length can be analytically calculated for a different number of cells (N) as follows:

$$N = 2 \Rightarrow \delta_{max} = \frac{PL^3}{96I}\left(\frac{1}{E_1} + \frac{1}{E_2}\right) \tag{5.A1a}$$

$$N = 4 \Rightarrow \delta_{max} = \frac{PL^3}{768I}\left(\frac{1}{E_1} + \frac{7}{E_2} + \frac{7}{E_3} + \frac{1}{E_4}\right) \tag{5.A1b}$$

$$N = 6 \Rightarrow \delta_{max} = \frac{PL^3}{2592I}\left(\frac{1}{E_1} + \frac{7}{E_2} + \frac{19}{E_3} + \frac{19}{E_4} + \frac{7}{E_5} + \frac{1}{E_6}\right) \tag{5.A1c}$$

, …,

$$N = 10 \Rightarrow \delta_{max} = \frac{PL^3}{12000I}\left(\frac{1}{E_1} + \frac{7}{E_2} + \frac{19}{E_3} + \frac{37}{E_4} + \frac{61}{E_5} + \frac{61}{E_6} + \frac{37}{E_7} + \frac{19}{E_8} + \frac{7}{E_9} + \frac{1}{E_{10}}\right) \tag{5.A1d}$$

In Eqs. (5.A.1a-d), E_i is the effective Young's modulus of the corresponding unit cell i and I represents the second moment of area, which is constant throughout the beam since the unit cells of the beam are replaced with equivalent solid unit cells with their effective properties. Considering Eqs. (5.A1a-d), the effective Young's modulus of cells should have a symmetric trend with a maximum in the mid-length of the beam to maximize the bending stiffness. In this problem, E_i is a function of the relative density $\bar{\rho}_i$ of the unit cell; therefore, the optimum relative density distribution will have the same pattern of Young's modulus.

Assuming Euler-Bernoulli beam theory and using the analytical formulations in the optimization process boost the speed of calculations. The optimum relative density distributions for a 1×10

cellular beam with extruded square unit cells graded in the *x*-direction and for three different total relative densities are depicted in **Fig. 5-A1** and are compared with previously obtained results using TSDT hybrid-homogenized modeling. Using the Euler-Bernoulli beam theory decreases the calculation time significantly and with negligible changes in the results for the optimum relative density distribution. Consequently, using the Euler-Bernoulli beam theory could be considered as a viable alternative for computationally efficient optimization of cellular beams graded in the *x*-direction.

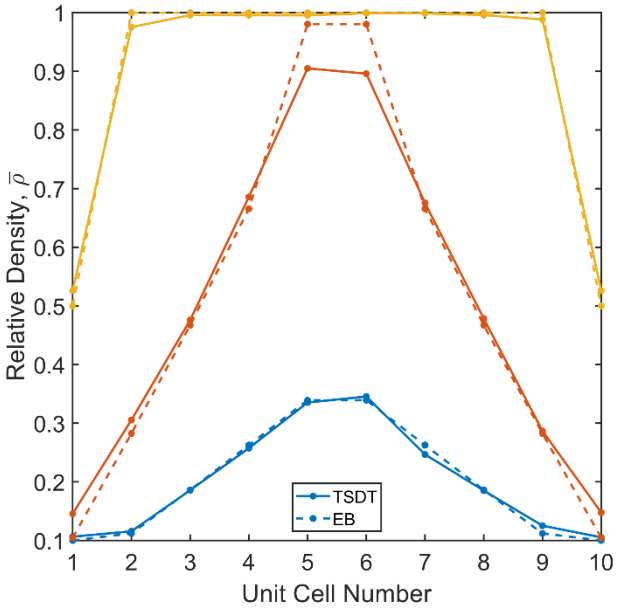

***Figure 5-A1**- Comparison of optimum relative density distributions for a longitudinally graded* 1×10 *cellular beam with Euler-Bernoulli beam theory and TSDT hybrid-homogenized modeling.*

5.9 Appendix 5.B: Asymmetric loading

If the line load is not applied in the middle of the graded cellular beam, the optimization process will deliver an unsymmetrical density distribution through the length of the beam to minimize the

maximum deflection. The optimum relative density distribution is not symmetric because the bending moment is not maximum in the middle of the beam for an asymmetric loading condition. The optimum relative density distribution in the *x*-direction for a graded cellular beam of $\bar{\rho}_{total} = 0.55$ is shown in **Fig. 5-B1**. The line load is applied asymmetrically at $x = L/10$. In this case, the unit cell with the maximum relative density is leaned towards a side of the cellular beam where the line load is applied.

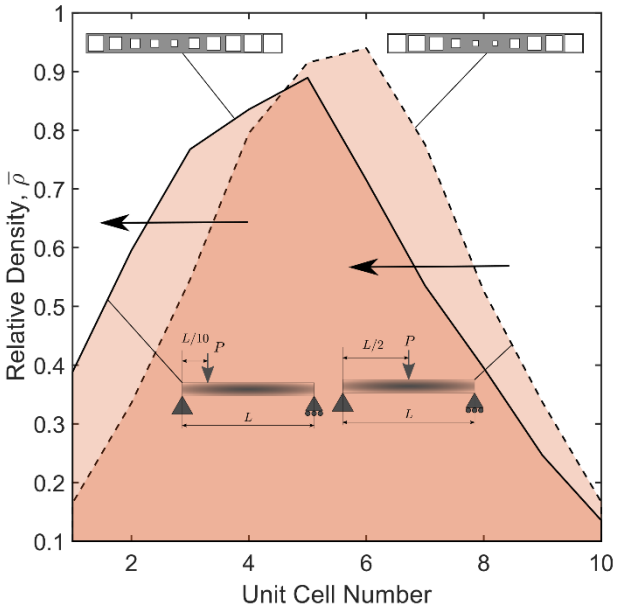

Figure 5-B1- *Asymmetric loading and the corresponding optimum distribution of relative densities of graded* 1×10 *cellular beam with* $\bar{\rho}_{total} = 0.55$.

5.10 Acknowledgment

A.H. Akbarzadeh acknowledges the financial support by Natural Sciences and Engineering Research Council of Canada through NSERC Discovery Grant RGPIN-2016-0471, Canada Foundation for Innovation (CFI) through John R. Evans Leaders Fund, and McGill University. This research was undertaken, in part, thanks to funding from the Canada Research Chairs program

to A.H.Akbarzadeh in Multifunctional metamaterials. Niknam is supported by Quebec Research Fund - Nature and Technologies (FRQNT) doctoral awards (B2X) and McGill University. The authors also acknowledge the contribution of J. Shi and discussion with S. Eskandari from the AM^{3}L lab of McGill University for determining effective properties of 3D architected cells using homogenization.

5.11 Reference

[1] L.J. Gibson, M.F. Ashby, Cellular Solids: Structure and Properties, Cambridge University Press1999.

[2] J. Yan, S. Yang, C. Yang, Multiscale Analysis of Thermal Stress of Lattice Materials and Its Size Effects, Journal of Thermal Stresses 37(8) (2014) 885-904.

[3] C. Lira, F. Scarpa, Transverse shear stiffness of thickness gradient honeycombs, Composites Science and Technology 70(6) (2010) 930-936.

[4] J.N. Reddy, Theory and analysis of elastic plates and shells, CRC press2006.

[5] Y.M. Ghugal, R.P. Shimpi, A Review of Refined Shear Deformation Theories for Isotropic and Anisotropic Laminated Beams, Journal of Reinforced Plastics and Composites 20(3) (2001) 255-272.

[6] Y.P. Liu, J.N. Reddy, A NONLOCAL CURVED BEAM MODEL BASED ON A MODIFIED COUPLE STRESS THEORY, International Journal of Structural Stability and Dynamics 11(03) (2011) 495-512.

[7] C.A. Berg, J. Tirosh, M. Israeli, Analysis of Short Beam Bending of Fiber Reinforced Composites, in: H.T. Corten (Ed.), ASTM International, West Conshohocken, PA, 1972, pp. 206-218.

[8] E. Sideridis, G.A. Papadopoulos, Short-beam and three-point-bending tests for the study of shear and flexural properties in unidirectional-fiber-reinforced epoxy composites, Journal of Applied Polymer Science 93(1) (2004) 63-74.

[9] T. Vodenitcharova, L.C. Zhang, Bending and local buckling of a nanocomposite beam reinforced by a single-walled carbon nanotube, International Journal of Solids and Structures 43(10) (2006) 3006-3024.

[10] F. Gandhi, S.-G. Kang, Beams with controllable flexural stiffness, Smart Materials and Structures 16(4) (2007) 1179-1184.

[11] S.M. Aldousari, Bending analysis of different material distributions of functionally graded beam, Applied Physics A 123(4) (2017) 296-296.

[12] Z. Yin, F. Hannard, F. Barthelat, Impact-resistant nacre-like transparent materials, Science 364(6447) (2019) 1260.

[13] Z. Jia, Y. Yu, S. Hou, L. Wang, Biomimetic architected materials with improved dynamic performance, Journal of the Mechanics and Physics of Solids 125 (2019) 178-197.

[14] Y. Hou, Y.H. Tai, C. Lira, F. Scarpa, J.R. Yates, B. Gu, The bending and failure of sandwich structures with auxetic gradient cellular cores, Composites Part A: Applied Science and Manufacturing 49 (2013) 119-131.

[15] R.M. Lawson, J. Lim, S.J. Hicks, W.I. Simms, Design of composite asymmetric cellular beams and beams with large web openings, Journal of Constructional Steel Research 62(6) (2006) 614-629.

[16] K.K. Rao, K.J. Rao, A. Sarwade, B.M.J.I.J.o.E. Varma, A.T. ISSN, Bending Behavior of Aluminum Honey Comb Sandwich Panels, International Journal of Engineering and Advanced Technology 1(4) (2012) 2249-8958.

[17] B. Kim, R.M. Christensen, Basic two-dimensional core types for sandwich structures, International Journal of Mechanical Sciences 42(4) (2000) 657-676.

[18] A.G. Evans, J.W. Hutchinson, N.A. Fleck, M.F. Ashby, H.N.G. Wadley, The topological design of multifunctional cellular metals, Progress in Materials Science 46(3-4) (2001) 309-327.

[19] V.S. Deshpande, N.A. Fleck, Collapse of truss core sandwich beams in 3-point bending, International Journal of Solids and Structures 38(36) (2001) 6275-6305.

[20] J. Romanoff, P. Varsta, Bending response of web-core sandwich plates, Composite Structures 81(2) (2007) 292-302.

[21] M. Schenk, S.D. Guest, G.J. McShane, Novel stacked folded cores for blast-resistant sandwich beams, International Journal of Solids and Structures 51(25) (2014) 4196-4214.

[22] H. Yazdani Sarvestani, A.H. Akbarzadeh, A. Mirabolghasemi, Structural analysis of size-dependent functionally graded doubly-curved panels with engineered microarchitectures, Acta Mechanica 229(6) (2018) 2675-2701.

[23] H. Yazdani Sarvestani, A.H. Akbarzadeh, H. Niknam, K. Hermenean, 3D printed architected polymeric sandwich panels: Energy absorption and structural performance, Composite Structures 200 (2018) 886-909.

[24] A.S. Sayyad, Y.M. Ghugal, Bending, buckling and free vibration of laminated composite and sandwich beams: A critical review of literature, Composite Structures 171 (2017) 486-504.

[25] K. Draiche, A.A. Bousahla, A. Tounsi, A.S. Alwabli, A. Tounsi, S. Mahmoud, Static analysis of laminated reinforced composite plates using a simple first-order shear deformation theory, Computers and Concrete 24(4) (2019) 369-378.

[26] D.K. Jha, T. Kant, R.K. Singh, A critical review of recent research on functionally graded plates, Composite Structures 96 (2013) 833-849.

[27] J. Reddy, Z.-Q. Cheng, Three-dimensional thermomechanical deformations of functionally graded rectangular plates, European Journal of Mechanics-A/Solids 20(5) (2001) 841-855.

[28] B. Karami, M. Janghorban, A. Tounsi, Galerkin's approach for buckling analysis of functionally graded anisotropic nanoplates/different boundary conditions, Engineering with Computers 35(4) (2019) 1297-1316.

[29] S.E. Naleway, M.M. Porter, J. McKittrick, M.A. Meyers, Structural Design Elements in Biological Materials: Application to Bioinspiration, Advanced Materials 27(37) (2015) 5455-5476.

[30] A.H. Akbarzadeh, M. Arian Nik, D. Pasini, Vibration responses and suppression of variable stiffness laminates with optimally steered fibers and magnetostrictive layers, Composites Part B: Engineering 91 (2016) 315-326.

[31] B.G. Compton, J.A. Lewis, 3D-Printing of Lightweight Cellular Composites, Advanced Materials 26(34) (2014) 5930-5935.

[32] T.A. Schaedler, W.B. Carter, Architected Cellular Materials, Annual Review of Materials Research 46(1) (2016) 187-210.

[33] T.D. Ngo, A. Kashani, G. Imbalzano, K.T.Q. Nguyen, D. Hui, Additive manufacturing (3D printing): A review of materials, methods, applications and challenges, Composites Part B: Engineering 143 (2018) 172-196.

[34] W. Jiang, S.T. Tu, G.C. Li, J.M. Gong, Residual stress and plastic strain analysis in the brazed joint of bonded compliant seal design in planar solid oxide fuel cell, Journal of Power Sources 195(11) (2010) 3513-3522.

[35] A. Francavilla, C.V. Ramakrishnan, O.C. Zienkiewicz, Optimization of shape to minimize stress concentration, Journal of Strain Analysis 10(2) (1975) 63-70.

[36] F.P.W. Melchels, J. Feijen, D.W. Grijpma, A review on stereolithography and its applications in biomedical engineering, Biomaterials 31(24) (2010) 6121-6130.

[37] X. Wang, M. Jiang, Z. Zhou, J. Gou, D. Hui, 3D printing of polymer matrix composites: A review and prospective, Composites Part B: Engineering 110 (2017) 442-458.

[38] H. Niknam, A.H. Akbarzadeh, Thermo-mechanical bending of architected functionally graded cellular beams, Composites Part B: Engineering 174 (2019) 107060.

[39] H. Niknam, A.H. Akbarzadeh, D. Rodrigue, D. Therriault, Architected multi-directional functionally graded cellular plates, Materials & Design 148 (2018) 188-202.

[40] H. Niknam, A.H. Akbarzadeh, In-plane and out-of-plane buckling of architected cellular plates: Numerical and experimental study, Composite Structures 206 (2018) 739-749.

[41] L. Francesconi, A. Baldi, X. Liang, F. Aymerich, M. Taylor, Variable Poisson's ratio materials for globally stable static and dynamic compression resistance, Extreme Mechanics Letters 26 (2019) 1-7.

[42] M.P. Bendsøe, N. Kikuchi, Generating optimal topologies in structural design using a homogenization method, Computer Methods in Applied Mechanics and Engineering 71(2) (1988) 197-224.

[43] M.P. Bendsøe, Optimal shape design as a material distribution problem, Structural Optimization 1 1(4) (1989) 193-202.

[44] M.P. Bendsøe, O. Sigmund, Material interpolation schemes in topology optimization, Archive of Applied Mechanics (Ingenieur Archiv) 69(9-10) (1999) 635-654.

[45] L. Cheng, P. Zhang, E. Biyikli, J. Bai, J. Robbins, A. To, Efficient design optimization of variable-density cellular structures for additive manufacturing: theory and experimental validation, Rapid Prototyping Journal 23(4) (2017) 660-677.

[46] M.E. Lynch, M. Mordasky, L. Cheng, A. To, Design, testing, and mechanical behavior of additively manufactured casing with optimized lattice structure, Additive Manufacturing 22 (2018) 462-471.

[47] A. Panesar, M. Abdi, D. Hickman, I. Ashcroft, Strategies for functionally graded lattice structures derived using topology optimisation for Additive Manufacturing, Additive Manufacturing 19 (2018) 81-94.

[48] R.V. Rao, V.J. Savsani, J. Balic, Teaching–learning-based optimization algorithm for unconstrained and constrained real-parameter optimization problems, Engineering Optimization 44(12) (2012) 1447-1462.

[49] R.V. Rao, V.J. Savsani, D.P. Vakharia, Teaching–learning-based optimization: A novel method for constrained mechanical design optimization problems, Computer-Aided Design 43(3) (2011) 303-315.

[50] R.V. Rao, V.J. Savsani, D.P. Vakharia, Teaching–Learning-Based Optimization: An optimization method for continuous non-linear large scale problems, Information Sciences 183(1) (2012) 1-15.

[51] H. Bikas, P. Stavropoulos, G. Chryssolouris, Additive manufacturing methods and modelling approaches: a critical review, The International Journal of Advanced Manufacturing Technology 83(1-4) (2016) 389-405.

[52] J.R.C. Dizon, A.H. Espera, Q. Chen, R.C. Advincula, Mechanical characterization of 3D-printed polymers, Additive Manufacturing 20 (2018) 44-67.

[53] G. Tang, Y. Yan, X. Chen, J. Zhang, B. Xu, Z. Feng, Dynamic damage and fracture mechanism of three-dimensional braided carbon fiber/epoxy resin composites, 22(1) (2001) 21-25.

[54] M. Krishnadev, M. Larouche, V.I. Lakshmanan, R. Sridhar, Fracture of high carbon high strength anchor rods, 15(8) (2008) 1009-1018.

[55] J. Pelleg, Fracture, Mechanical Properties of Materials, Springer Netherlands, Dordrecht, 2013, pp. 449-520.

[56] A.G. Evans, M. He, V.S. Deshpande, J.W. Hutchinson, A.J. Jacobsen, W.B. Carter, Concepts for enhanced energy absorption using hollow micro-lattices, International Journal of Impact Engineering 37(9) (2010) 947-959.

[57] S.J. Hollister, N. Kikuchi, A comparison of homogenization and standard mechanics analyses for periodic porous composites, Computational Mechanics 10(2) (1992) 73-95.

[58] B. Hassani, E. Hinton, A review of homogenization and topology opimization II—analytical and numerical solution of homogenization equations, Computers & structures 69(6) (1998) 719-738.

[59] M. Aydogdu, V. Taskin, Free vibration analysis of functionally graded beams with simply supported edges, Materials & Design 28(5) (2007) 1651-1656.

[60] J. Reddy, Analysis of functionally graded plates, International Journal for Numerical Methods in Engineering 47(1-3) (2000) 663-684.

[61] J.N. Reddy, Mechanics of laminated composite plates and shells: theory and analysis, CRC press2004.

[62] G. Shi, K.Y. Lam, Finite element vibration analysis of composite beams based on higher-order beam theory, Journal of Sound and Vibration 219(4) (1999) 707-721.

[63] M.F. Ashby, T. Evans, N.A. Fleck, J. Hutchinson, H. Wadley, L. Gibson, Metal foams: a design guide, Elsevier2000.

[64] J.B. Berger, H.N.G. Wadley, R.M. McMeeking, Mechanical metamaterials at the theoretical limit of isotropic elastic stiffness, (2017).

[65] J.L. Grenestedt, Effective elastic behavior of some models for perfect cellular solids, International Journal of Solids and Structures 36(10) (1999) 1471-1501.

[66] A.G. Kolpakov, Calculation of the characteristics of thin elastic rods with a periodic structure, Journal of Applied Mathematics and Mechanics 55(3) (1991) 358-365.

[67] A.G. Kolpakov, Variational principles for stiffnesses of a non-homogeneous beam, 46(6) (1998) 1039-1053.

[68] Z. Jia, L. Wang, 3D printing of biomimetic composites with improved fracture toughness, Acta Materialia 173 (2019) 61-73.

[69] L.R. Meza, A.J. Zelhofer, N. Clarke, A.J. Mateos, D.M. Kochmann, J.R. Greer, Resilient 3D hierarchical architected metamaterials, 112(37) (2015) 11502-11507.

[70] C.M. Portela, A. Vidyasagar, S. Krödel, T. Weissenbach, D.W. Yee, J.R. Greer, D.M. Kochmann, Extreme mechanical resilience of self-assembled nanolabyrinthine materials, 117(11) (2020) 5686-5693.

6 Chapter Six: Graded Lattice Structures: Simultaneous Enhancement in Stiffness and Energy Absorption[1]

6.1 Preface

Thus far, our studies mainly involved different elastic responses of functionally graded cellular structures. In the previous chapters, we studied the bending and the onset of buckling of graded cellular beams and plates subjected to the mechanical and thermal loadings. We have not considered the response of these cellular structures beyond the linear regime in any of these studies. In **Chapter 6**, we investigate the energy absorption capabilities and stiffness of graded cellular structures under large deformation. The manufacturability of 3D graded lattices with more complicated geometries is checked by additive manufacturing methods, and the effect of gradient on their stiffness and energy absorption capability is evaluated.

1 Submitted to journal under the name of Niknam, H., Akbarzadeh, A.H.; Graded Lattice Structures: Simultaneous Enhancement in Stiffness and Energy Absorption; May 2020

6.2 Abstract

Tremendous capabilities of 3D printed cellular solids as high-performance energy absorbers can be further enhanced by engineering their underlying architectures. In this study, we classify different groups of cellular solids based on their topology into 2D extruded, 3D truss-like, and 3D shell-like lattices and propose a strategy to enhance their energy absorption-to-weight ratio under compression. We particularly elicit the effect of variation of relative density across the lattice structures, 3D printed by stereolithography. The experimental compression test results, as well as numerical data conducted by large deformation nonlinear finite element analysis, show that a *uniform design* with even distribution of relative density yields the highest initial stiffness among all 3D printed architected lattices. However, the *graded design* with a rational variation of relative density can significantly enhance the stiffness and energy absorption capability of architected cellular solids experiencing high compressive strains. Particular gradients, where the relative density varies normal to the direction of external compressive force, can increase the stiffness and energy absorption capabilities of cellular solids up to 60 and 110 percent for all of the investigated cell topologies. These results promise the possibility of designing single-phase lattice architectures by rational variation of porosity throughout the cellular structure, which can combine lightweight with high stiffness and energy absorption properties and offer a strategy for prevailing the material performance trade-off between stiffness and energy absorption.

6.3 Introduction

The energy absorption capabilities of cellular solids have always been of interest to material scientists and engineers. The vast usage of cellular solids in shock absorbing and energy dissipating applications invokes a lot of research on the energy absorption behavior of this category of

advanced lightweight materials. Initial studies proposed empirical relationships between stress and strain of hexagonal honeycombs, as the most famous periodic cellular solids, made out of metals and polymers subjected to both uniaxial [1] and biaxial [2] compression. Analytical formulae were also derived for yield surface and stiffness of cellular solids with primitive cell topologies like Square and Diamond [3], Hexagon, and Octet-truss [4], and Triangular and Rectangular [5].

Over the last decade, many ideas have been proposed to design the microarchitecture of solids to improve their mechanical properties and widen their application [6-9]. Modifying the architecture of 2D corrugated honeycomb structures by adding a reinforcing triangular tube at the edges [10], developing quadri-arc multi-cell [11] or reinforcing them with a second phase [12] have been reported to be effective for the enhancement of the energy absorption and crashworthiness of a cellular structure. In a leading work, Evans *et al.* [13] demonstrated the superior performance of micro-lattice, with hollow cylindrical struts, in improving the energy absorption of cellular solids. As shown in **Figs. 6-1a** to **6-1c**, cellular solids are divided here into three categories depending on their geometrical features: *(a)* 2D extruded lattices, *(b)* Truss-like lattices, and *(c)* 3D shell/plate-like lattices. The first two categories of cellular materials can be fabricated by traditional manufacturing methods such as casting [14], forming [15], and extrusion [16]. The inception of additive manufacturing (AM) paved the path for fabricating cell topologies with more complex architectures, i.e., 3D shell-like and plate-like lattice structures [17-25]. Direct laser writing was customized and used for manufacturing 3D plate-lattices, a class of low-density materials with near-optimal stiffness for isotropic materials [26]. Metallic smooth-shell structures with complex Gyroid and shell-like lattice architectures were manufactured with selective laser melting, and the effect of different AM parameters on their compressive behavior was investigated [18, 27, 28]. Recent investigations also revealed that shell/plate-like cellular materials fabricated by fused

deposition molding (FDM) 3D printing techniques could significantly enhance the energy absorption compared to the conventional 1D and 2D designs, and the stiffness of the structure close to maximum theoretical limit [24, 29].

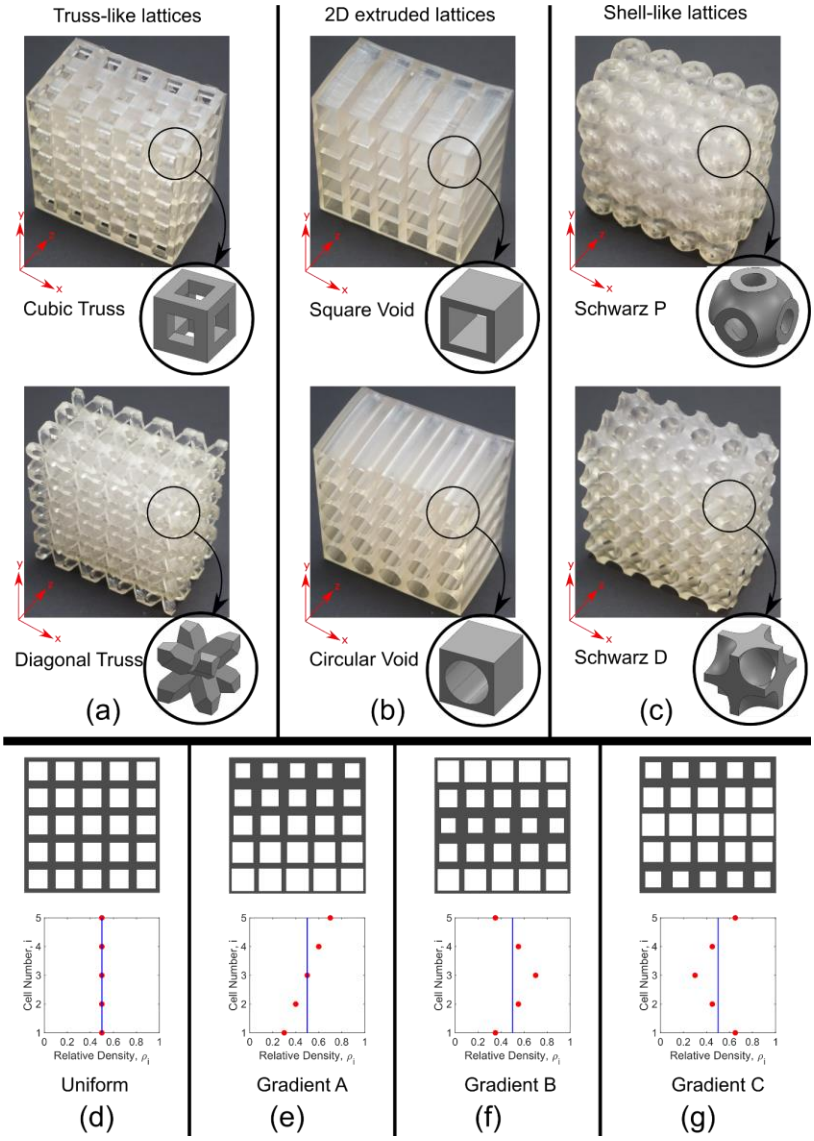

Figure 6-1- *Different categories of lattice structures: (a) Truss-like lattices, (b) 2D extruded lattices, and (c) Shell-like lattices, and the relative density distribution in lattices: (d) Uniform distribution, (e) Linear distribution*

(Gradient A), (f) Symmetric distribution with a maximum in the middle (Gradient B), (g) Symmetric distribution with a minimum in the middle (Gradient C).

AM also enables the realization of cellular materials whose properties are changing across a structure. Investigations on 2D extruded lattices have revealed that varying the cell architecture across a structure made out of hexagonal honeycombs cell [30, 31] or other 2D topologies [32-34] enables to tune the buckling load and flexural responses. Modifying the arrangement of cells in 2D periodic honeycomb can lead to exceptional mechanical properties, such as negative (*auxetics*) or zero Poisson's ratio [35] and improved out-of-plane compressive strength [36]. In most recent works, specific energy absorption and deformation behavior of nature-inspired graded 2D extruded cellular lattices [37], and shell-like lattices [38] have been evaluated through experimentation and detailed finite element modeling. It has been found that variation of properties can effectively enhance the structural performances.

In the literature, no study has systematically investigated the effect of relative density gradient on the mechanical performance of alternative types of 3D printed lattice structures. This study fabricates graded cellular structures of different cell topologies and relative density gradients to evaluate their performance under a compressive load. The lattice architecture of the cellular structure is introduced in **Section 6.4.1** for different relative density gradients. The fabrication process, by stereolithography of flexible materials, and experimental method, together with the material characterization of the base material are introduced in **Sections 6.4.2-6.4.4**. **Section 6.5** is dedicated to results and discussion about the mechanical performance of 3D printed graded cellular structures. These results reveal that no matter which cell topology constitutes a lattice

structure, a rational selection of gradients can improve not only its energy absorption capacity but also its stiffness. These outcomes offer a design strategy to combine energy absorption and stiffness in a single-phase (base material and void) lightweight advanced material. Conclusion and a highlight of the research findings are presented in **Section 6.6**.

6.4 Materials and methods

This section identifies our strategy to explore the energy absorption behavior of different categories of lattice structures. Different cell topologies and relative density gradients are introduced, and the 3D printing fabrication method, along with procedures for determining the mechanical performance of lattice structures, by finite element (FE) simulation and experimental testing, are described. The fabricated structure consists of $5 \times 5 \times 3$ unit cells in x, y, and z directions, where x and y are in-plane directions and z is thickness direction, and each unit cell is a cube of $10mm \times 10mm \times 10mm$.

6.4.1 The architecture of the lattice structure

6.4.1.1 Cell topology

As shown in **Figs. 6-1a** to **6-1c**, six topologies are designed, and 3D printed in this study where each lattice type is being represented by two different cell topologies as discussed below:

Truss-like lattices (**Fig. 6-1a**):

i. *Cubic truss* consists of straight rods with square cross-sections which connect each vertex of a cube to its closest adjacent vertex.
ii. *Diagonal truss* is built by rods with a square cross-section in place of each four diagonals of a cube.

2D extruded lattices (**Fig. 6-1b**):

iii. *Square void* is a cube in which a square hole is cut in the middle of one of its faces through the whole cube.

iv. *Circular void* is a cube in which a circle is cut in the middle of one of its faces through the whole cube.

Shell-like lattices (**Fig. 6-1c**):

v. *Schwarz P* which consists of a unit cell containing a Schwarz Primitive surface approximated by [39]:

$$\cos(x) + \cos(y) + \cos(z) = 0 \tag{6.1}$$

i. *Schwarz D* which consists of a unit cell containing a Schwarz Diamond surface approximated by [39]:

$$\sin(x)\sin(y)\sin(z) + \sin(x)\cos(y)\cos(z) + \cos(x)\sin(y)\cos(z) + \cos(x)\cos(y)\sin(z) = 0 \tag{6.2}$$

6.4.1.2 Density gradient

Equation 6.3 defines the relative density of the i^{th} cell of a cellular structure as a fraction of solid volume over the total volume of the unit cell:

$$\bar{\rho}_i = \frac{V_{solid}}{V_{cell}} \tag{6.3}$$

In a graded cellular structure with $N = N_x \times N_y \times N_z$ numbers of unit cells, where N_x, N_y and N_z are the number of cells in three different directions, the total relative density is calculated by:

$$\bar{\rho} = \frac{\sum_{i=1}^{N} \bar{\rho}_i}{N} \tag{6.4}$$

In this study, the total relative density for all samples with different variation is set as $\bar{\rho} = 0.5$ and different variations of relative density are considered as follows.

i. *Uniform distribution* presents a lattice structure with no variation in the relative density of cells throughout the cellular medium (**Fig. 6-1d**).

ii. *Gradient A* presents a linear variation of relative density from one side to another side of the cellular structure (**Fig. 6-1e**).

iii. *Gradient B* presents a symmetric variation of the relative density of cells where the cell with the highest relative density is placed in the middle (**Fig. 6-1e**).

iv. *Gradient C* presents a symmetric variation of relative density where the cell with the lowest relative density is placed in the middle (**Fig. 6-1f**).

6.4.2 Fabrication

We have employed commercial SolidWorks 2019 software to design the graded cellular structures samples with different microarchitectures. The designs have been imported in the PreForm software to slice and prepare them for additive manufacturing. The samples have been 3D printed out of a commercial elastic resin using the Formlabs Form 3 SLA 3D printer. Each sample underwent 30 minutes of washing by isopropyl alcohol and 60 minutes of curing by UV light at a temperature of 60℃.

The base material is Formlabs commercial elastic resin with 50A shore durometer. Uniaxial tensile tests are performed on the 3D printed dogbone samples according to ASTM D638, and the stress-strain curves are obtained, as shown in **Fig. 6-2a**. The results of these tests are used as the material

properties in numerical simulation. **Figures 6-2b** to **6-2d** present the SEM image of both intact and failed surfaces of 3D printed dogbone samples. No defect can be detected on the cross-section of failure surface nor the other sides of the specimens.

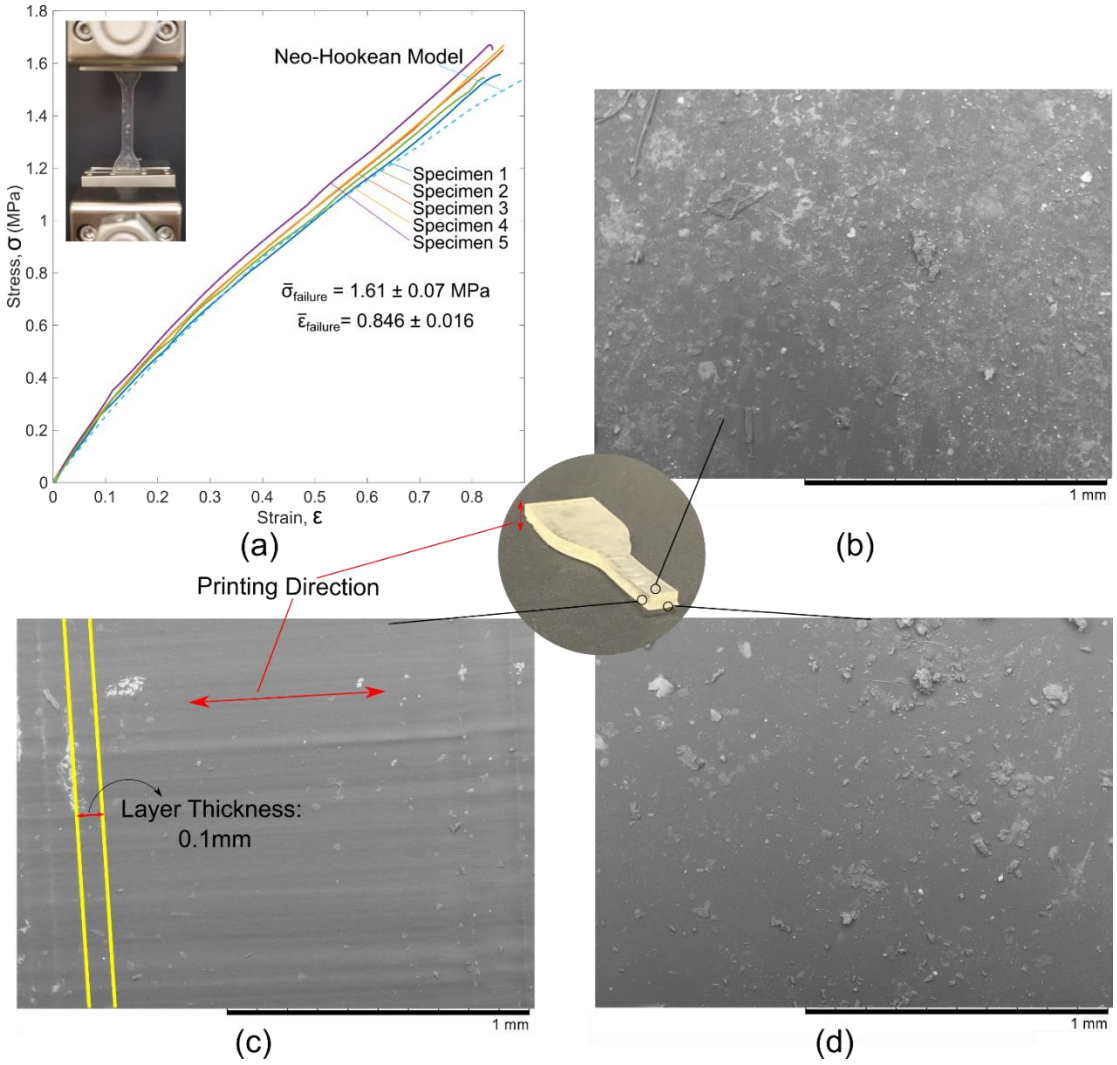

Figure 6-2- *Additively manufactured dogbone samples: (a) Stress-strain curves conducted on dogbone samples according to ASTM D638 and SEM images of (b) the surface normal to the printing direction, (c) the surface parallel to printing direction, and (d) cross-section after failure.*

We have measured dimensions of samples to ensure the accuracy of the 3D printing process and have found that the deviation of as-built dimensions and as-designed models is less than 5 percent.

All samples have been weighed, and the mass of 3D printed samples has been reported in **Table 6-1**. The average mass of 3D printed samples is $42.31\ g$, and the standard deviation of them is 0.47, confirming the precision of the 3D printing process.

Table 6-1- Mass of 3D printed cellular samples in gram.

Density variation	***Cubic Truss***	***Diagonal Truss***	***Square Void***	***Circular Void***	***Schwarz P***	***Schwarz D***
Uniform	43.73	42.78	41.75	40.96	40.31	41.3
Gradient A	44.11	42.95	41.71	43.77	40.74	41.32
Gradient B	44.51	43.3	41.66	44.25	41.25	41.9
Gradient C	44	42.38	41.17	43.53	40.82	41.34

6.4.3 The characterization of experiments

Each 3D printed sample undergoes 50% compression to evaluate the energy absorption potential of the designed uniform and graded lattices. This strain is large enough to allow the densification of 3D printed cellular structures. ADMET eXpert 8612 mechanical tester with a 20kN load cell is employed, and aluminum anodized flat surface (CPC-20T) fixtures are set up to apply compression. A sequence of loading and unloading is applied to each sample at a constant rate of $1\,mm/sec$.

6.4.4 Finite element simulation

We use ANSYS AutoDyn solver to simulate the behavior of lattice structures under compression. The lattice structures are meshed with approximately 400,000 elements, and mesh sensitivity analysis is performed to ensure the validity of the finite element results. The linear Tetrahedron

element geometry with Nodal Based Strain (NBS) formulation is selected as the element type for modeling the structure. Two rigid bodies are attached to the top and bottom of the lattice structures to model the effect of a rigid fixture. Element and body self-contact effects are taken into account by enabling body interaction during the analysis.

6.4.4.1 Material modeling

The material is considered to be nearly incompressible, and the Neo-Hookean model is used as the constitutive law. Consequently, the strain energy density function, W, can be written as [40]:

$$W(I_1, I_3) = \frac{\mu}{2}(I_1 - 3 - 2\ln J) + \frac{K}{2}(J-1)^2 \tag{6.5}$$

where μ and K are shear and bulk moduli, respectively; J is the determinant of deformation gradient tensor $\boldsymbol{F}$ ($J = det(\boldsymbol{F})$) and I_1 is the first invariant of right Cauchy-Green stress tensor ($I_1 = tr(\boldsymbol{C})$; $\boldsymbol{C} = \boldsymbol{F^T F}$). The Cauchy stress tensor, $\boldsymbol{\sigma}$, is determined by:

$$\boldsymbol{\sigma} = \frac{2}{J}\frac{\partial W}{\partial I_1}\boldsymbol{B} + \frac{\partial W}{\partial J}\boldsymbol{I} \tag{6.6}$$

where $\boldsymbol{B}$ is the left Cauchy-Green stress tensor ($\boldsymbol{B} = \boldsymbol{F F^T}$) and $\boldsymbol{I}$ is the identity matrix.

From the experimental results shown in **Fig. 6-2a**, the shear modulus is approximated to be $\mu = 0.95MPa$, and as the material is considered to be nearly incompressible the ratio of bulk modulus to initial shear modulus is set as $K/\mu \sim 500$. **Fig. 6-2a** confirms the good agreement between the Neo-Hookean model with the abovementioned constants with experimental results.

6.5 Results and discussion

In this section, we explore the response of graded cellular structures under compressive loading from different aspects, including energy absorption, stiffness, and maximum elemental stress at different strains. The total energy dissipated in a cycle of loading and unloading is also calculated and presented for different gradients and topologies. We consider the uniform distribution of cells together with six graded cellular designs. The first three gradients are named as Gradient A, Gradient B, and Gradient C, as defined in **Section 6.4.1.2**, in which the compressive force is being applied in the same direction as relative density variation. In the other three gradients, the force is applied in a direction normal to the direction of relative density variation. Subscript "N" in the figures presents experimental tests where the compressive force is normal to the relative density variation.

Force divided by the nominal area of the top surface of each specimen (i.e., $50mm \times 30mm$) defines the *Nominal stress* and the displacement of the top face of any structure divided by the length of each specimen (i.e., $50mm$) indicates the *Nominal strain*. We consider the energy absorption as the area under the stress-strain curves for each 3D printed sample and define the *Specific energy absorption* ($S.E.A.$) as the energy absorption normalized by the mass of each specimen (**Table 6-1**).

In **Fig. 6-3**, we investigate the behavior of different topologies with the uniform distribution of relative density under compressive loading. The stress-strain curves show that *Square void* lattice structure has the maximum initial incremental stiffness compared to the other cell topologies; however, its nominal stress drops sooner than the other topologies. This drop happens due to the initial buckling, making its energy absorption capacity minimum at higher strains. The response

of the *Circular void* is similar to the *Square void* in small strains; however, its energy absorption capability is higher than Square void in the higher strains, which is mainly due to the self-interacting nature of its buckled configuration [41]. As the strain increases, *Schwarz D* and *Cubic truss* are found to be the best energy absorbers, while the peak force, and its associated nominal stress, is the highest for *diagonal truss* at 50% strain. As shown in **Fig. 6-3**, each topology has its distinct deformed configuration; in *Cubic truss* and *Square void* rows of cells deform sequentially, and middle row distorts last, while the whole lattice structure deforms at the same time in the other topologies.

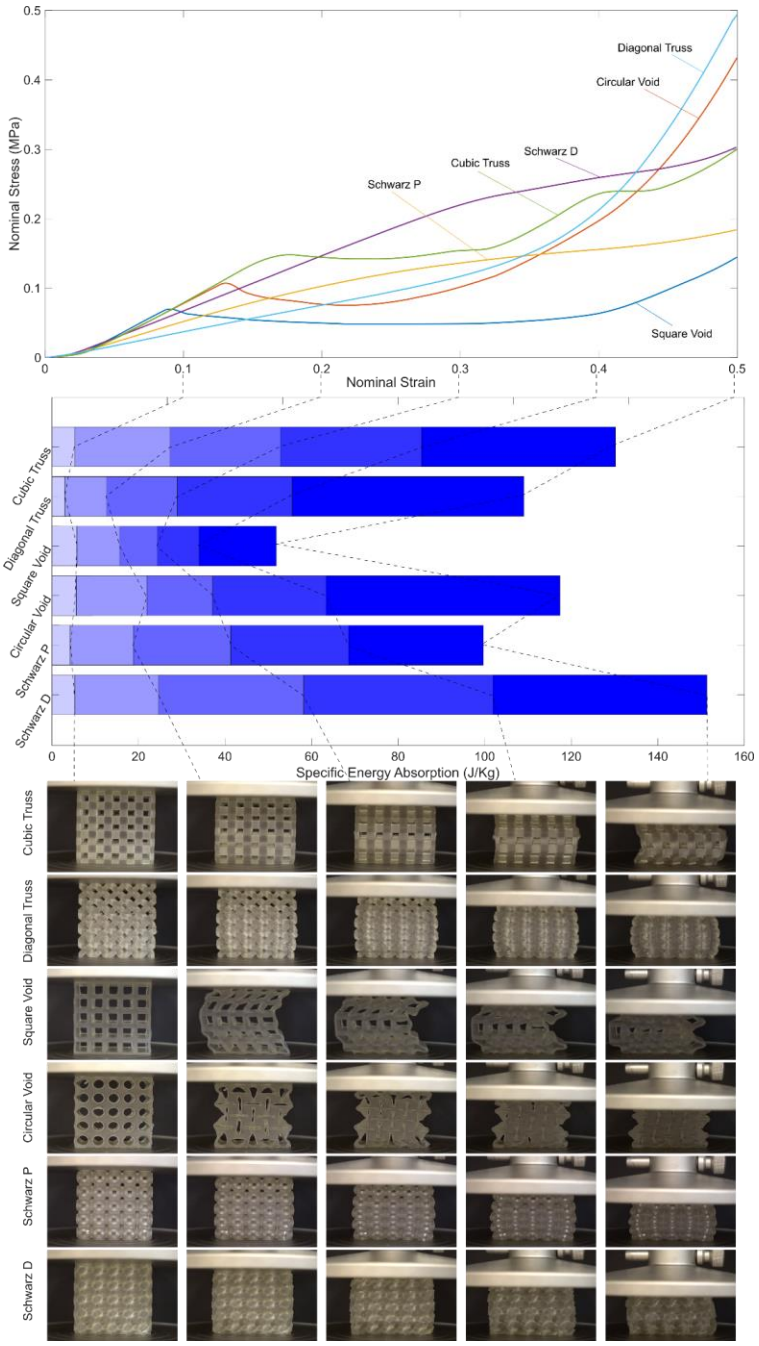

Figure 6-3*- Performance of lattice structures with uniform relative density distribution and different cell topologies.*

Figure 6-4 depicts the stress-strain curves for different cell topologies and relative density variation. We can observe that the highest initial slope is generally associated with the uniform distribution of relative density—a gradient of relative density in the direction of compressive force yields lower initial stiffness. In contrast, density variation normal to compressive force direction negligibly changes the stiffness compared to the uniform distribution. For shell-like lattices, *Schwarz P* and *D*, variation of stress-strain curves for different gradients are less than the others, as opposed to 2D-extruded lattices that show substantial changes when relative density distribution varies. We also notice that the variation of relative density in the force direction facilitates buckling in lattice structure in lower strains, while gradients in a direction normal to compressive force delay the instability in the lattice structure. It should be noted that for *Diagonal truss* topology with *Gradients* A_N and B_N drops in the stress-strain curve are observed in high normal strain ($\varepsilon = 0.48$) mainly due to the material failure and not structural instability.

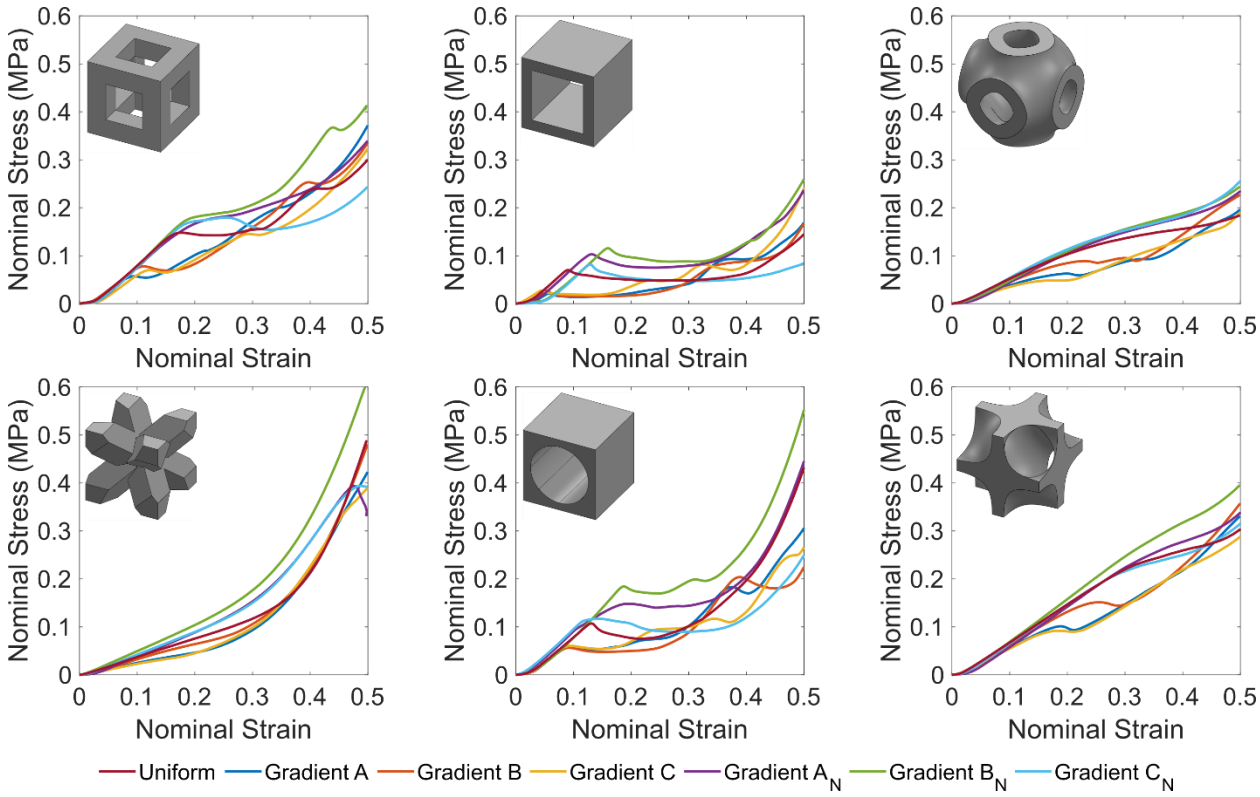

Figure 6-4- *Stress-strain curves for compression of graded cellular structures for different cell topologies and relative density gradients.*

Energy absorption capabilities of cellular solids with different relative density gradients, compressed up to a specific strain, are presented in **Fig. 6-5**. One can observe that the monotonic increase of absorbed energy by strain can is dictated by both cell architecture and relative density distribution. The slope of variation of specific energy absorption with strain for grade lattice structures in which the relative density varies in the direction of compressive force is generally less than lattices with a uniform distribution. However, the opposite is true for gradients whose relative densities vary normal to the direction of the force. We can conclude that, for the same relative density gradient, *Schwarz D* is the best energy absorber followed by *Diagonal truss*, *Cubic truss*, and *Circular void*. In contrast, *Schwarz P* and *Square void* absorb the least amount of energy for the same gradient.

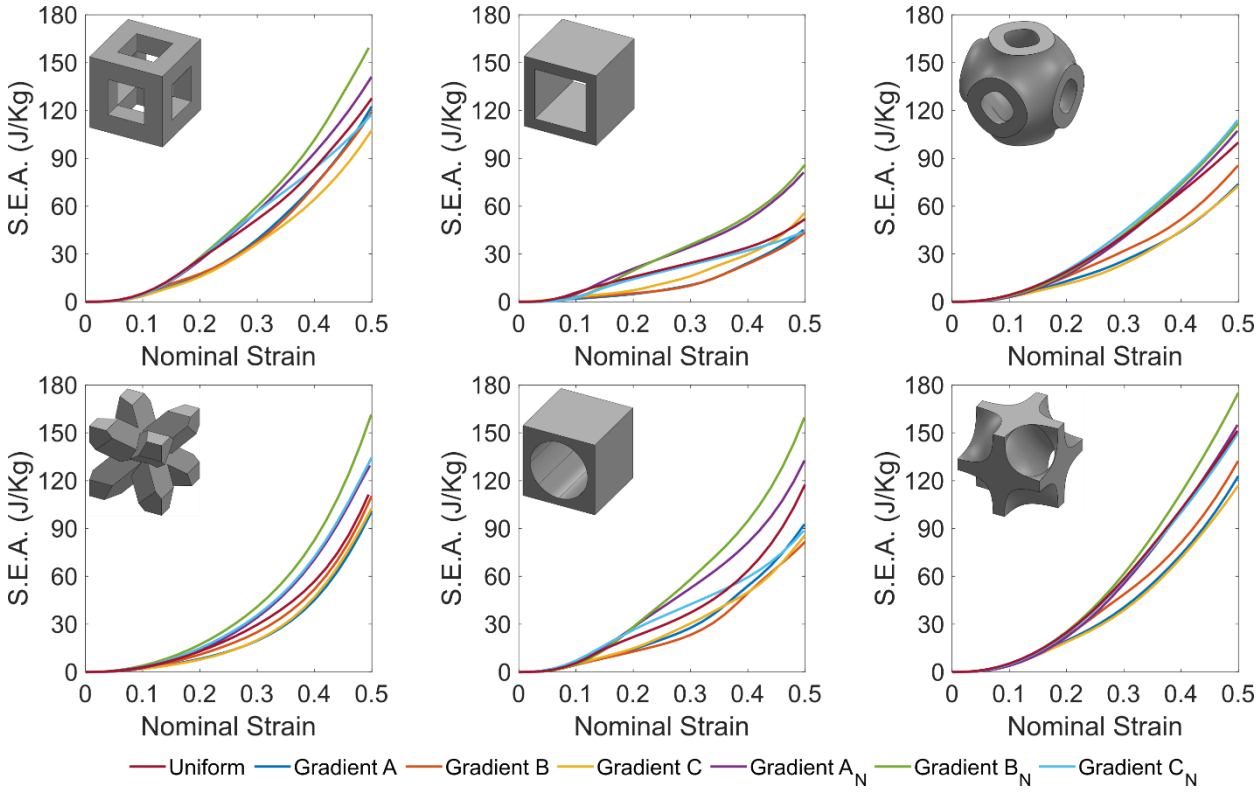

Figure 6-5- *Specific energy absorption versus nominal strain of graded cellular structures under compression for different cell topologies and relative density gradient.*

Figure 6-6 compares the effect of relative density gradients on nominal stress (S) and specific energy absorption (S.E.A.) at specific strains with the performance of corresponding lattice structures with uniform relative density distribution. The subscript "U" in S_U and $S.E.A._U$ indicate the stress and specific energy absorption of structures with a uniform gradient. For small compression (i.e., the nominal strain of 0.1), uniform density distribution often performs better both in carrying higher stress and absorbing more energy. For most cases, lattice structure with gradients normal to the force direction can absorb more energy and sustain higher loads as the strain increases. In particular, *Gradients* B_N can increase the energy absorption capabilities between 10% to 110% depending on the strain value and cell topology. Nevertheless, varying the

relative density in the direction of compressive force often decreases the energy absorption capabilities between 0% to 60% percent for different cell topologies and at different strain values.

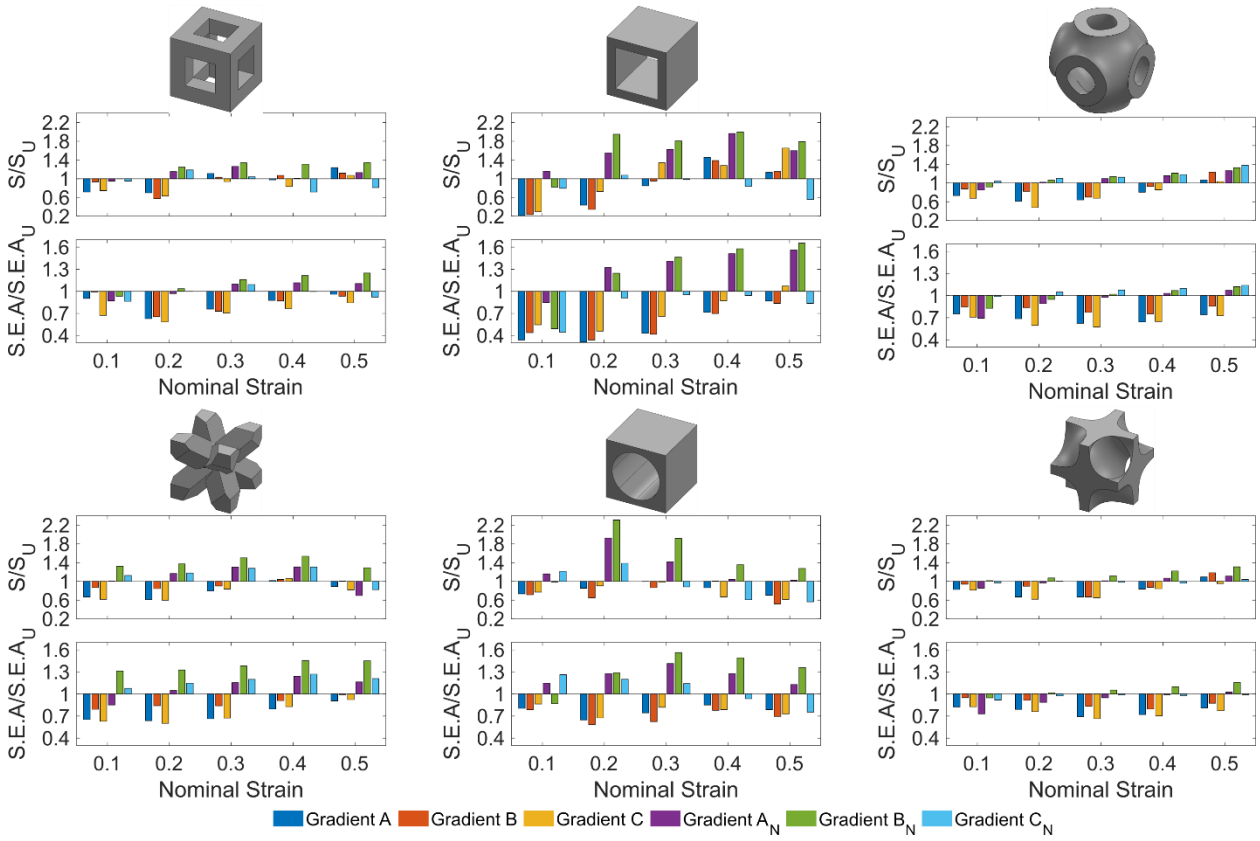

Figure 6-6- *Performance of cellular structures with different relative density gradients compared to the corresponding uniform distribution of relative density.*

The Specific Energy Dissipation (*S.E.D*) is defined as the energy dissipated per unit of mass in a sequence of loading and unloading and equals to the enclosed area in the stress-strain curve divided by the mass of the structure. This value is reported in **Fig. 6-7** for all the lattice structures tested in this study. The results show that structures with *Gradients* A_N and B_N perform better in dissipating energy in addition to absorbing energy. The figure shows that *Diagonal truss* with *Gradients* A_N, B_N, and C_N exceptionally dissipate more energy compared to other structures, mainly stemming

from material failure in these three gradients during the compression. Putting this aside, it can be observed that *Cubic truss* and *Circular void* performs better than other topologies in energy dissipation.

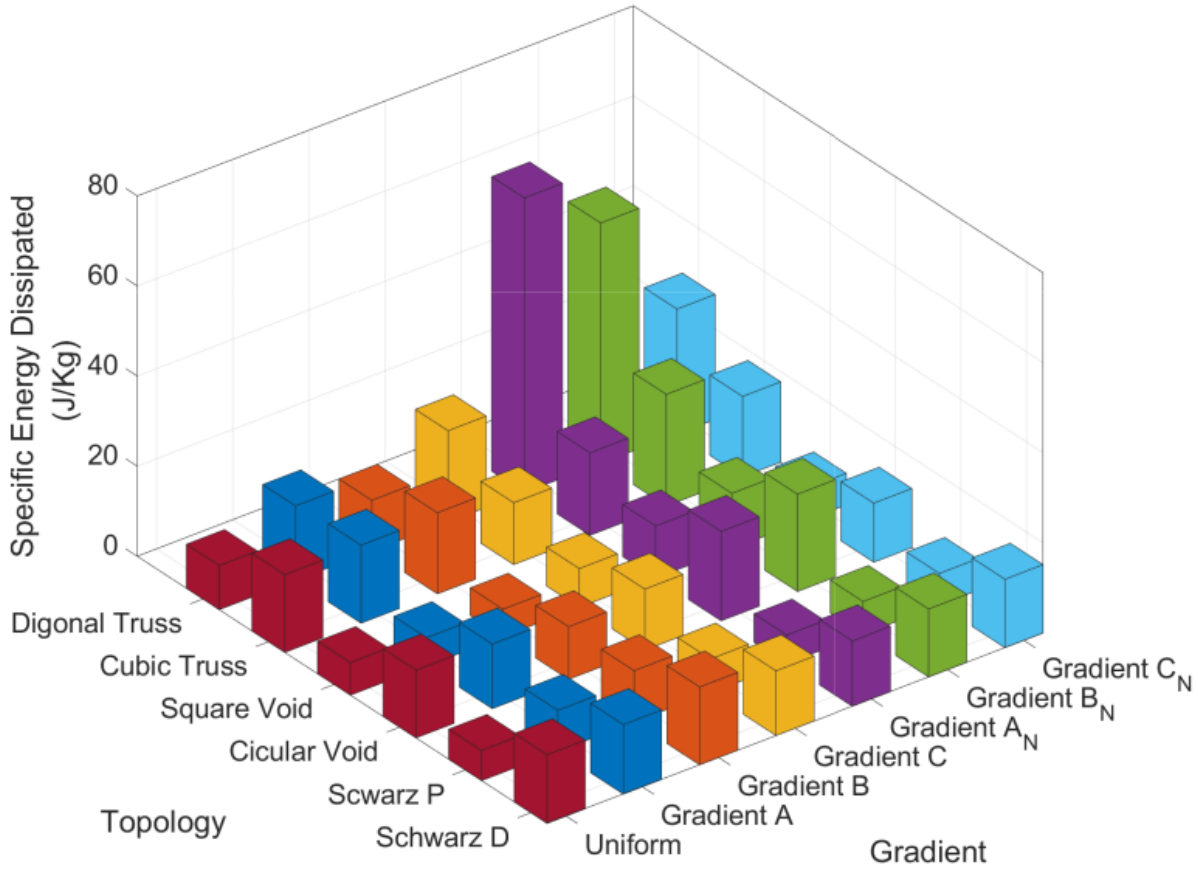

Figure 6-7- *Specific energy dissipation during loading of up to 50% compressive load and unloading for different cellular structures.*

ln **Fig. 6-8**, we compare the stress-strain curves and energy absorption at different strains, determined by ANSYS FE analyses and experimental compression test, for lattice structures with *Square-void* topology and different relative density gradients. We can observe that there is an acceptable agreement between FE predictions and experimental data. However, the deviation

between the two results can reach up to 30 percent in a few cases. In general, FE analysis on as-designed graded cellular structures overestimates the stress and energy-absorbing capabilities for all different gradients, which is mainly due to the presence of dimensional non-conformities caused by manufacturing defects in the as-built 3D printed samples. There are also more fluctuations in the stress-strain curves, predicted by FE analysis, compared to the experimental data which can stem from the nature of Explicit Dynamics analysis and temporal effects in rubber modeling and can be reduced by increasing the analysis time span, which has been set to 1 second in the present study.

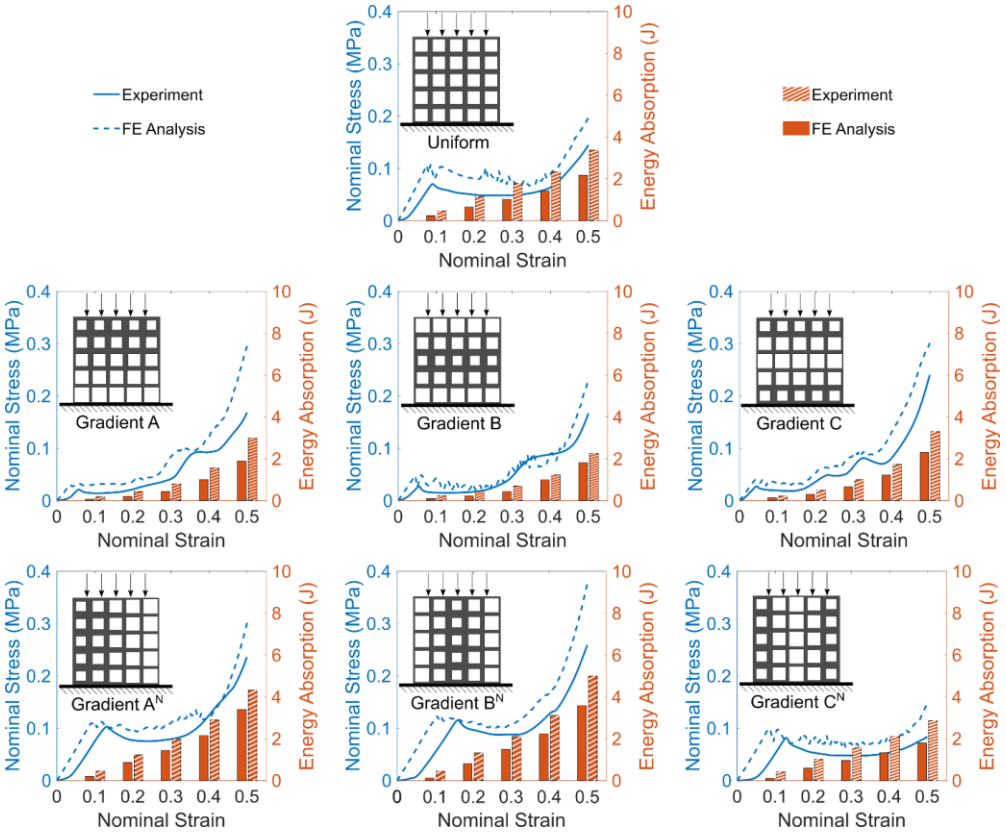

Figure 6-8- *Comparison of experimental results and FE predictions for stress-strain curves and energy absorption of different graded cellular structures with square void topology.*

Figure 6-9 presents deformed configurations and von Mises stress distribution obtained by FE simulation at various strains for *Square Void* topology with different gradients of relative density. As shown in this figure, when loading is applied parallel to the relative density gradient, the deformation prevails row by row for the *Square void* topology starting from rows with the lowest relative density. Consequently, the cells with the lowest relative densities determine the initial buckling load and control the deformation modes of graded lattice structures. However, when the loading is applied normal to the gradient direction, the cells with the highest relative density delays the onset of instability in the structures. Taking a closer look at the equivalent stress at different strains shows that gradients that are stiffer (e.g., *Gradient* A^N and *Gradient* B^N) have the highest von Mises stress within the lattice structure.

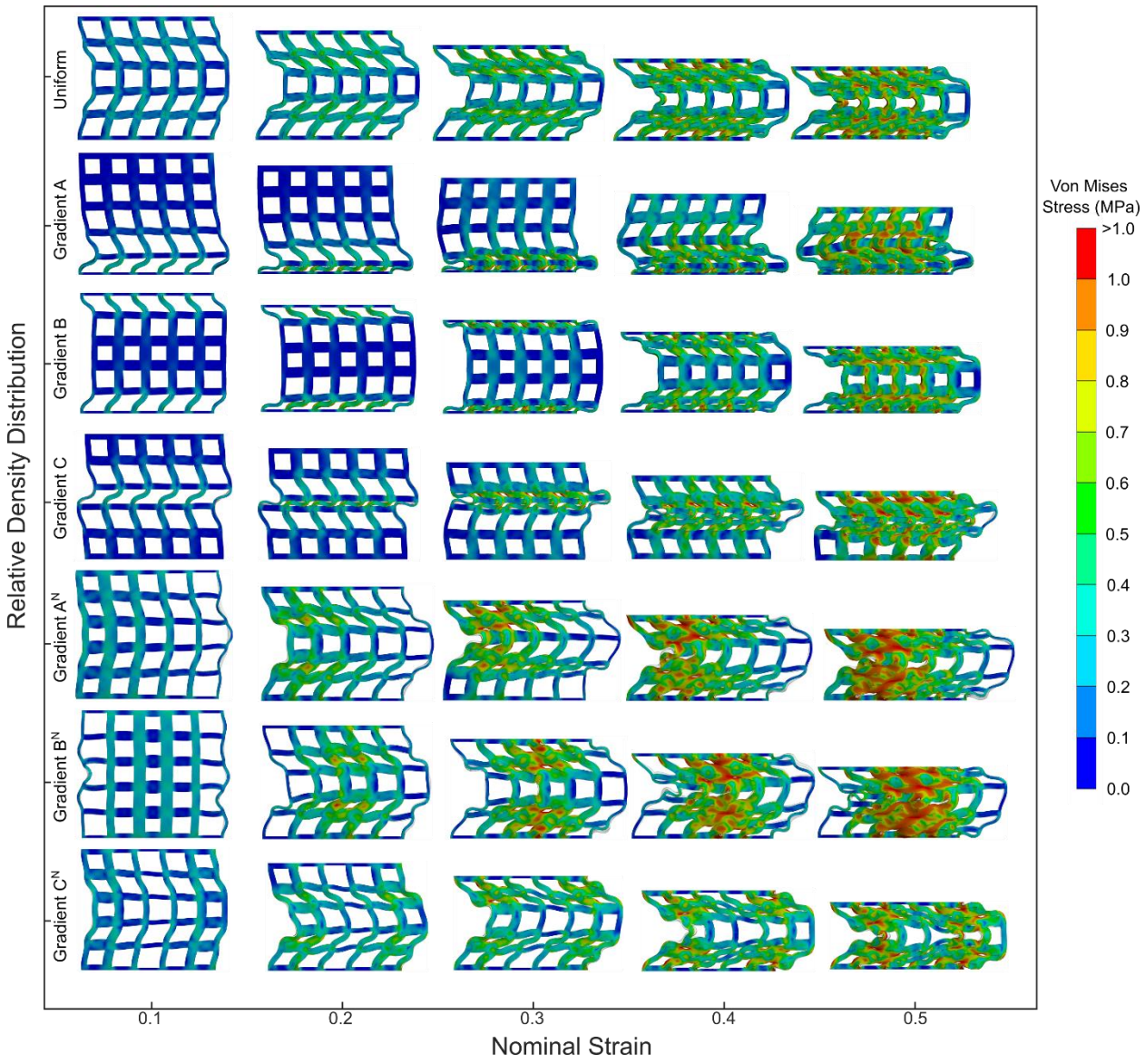

Figure 6-9– *Equivalent von Mises stress and deformed configurations obtained from FE analysis for different graded cellular structures with square cell topology.*

The results of FE simulation for compression of all other geometries with uniform distribution of relative density are presented in **Fig. 6-10** to better compare the evolution of stresses in cellular solids. **Figure 6-10a** illustrates the value of maximum von Misses stress in each lattice structure at different strains. We can see that the values of maximum stress in different topologies are very close at low strain and change almost linearly with strain. Nevertheless, the difference and

fluctuation increase in the higher strains caused by different deformation modes leading to distinct stiffness and energy absorption capabilities for each cellular material. For instance, the elemental stress values in *Diagonal Truss* are initially lower than the rest of topologies; however, the slope of variation substantially increases when the nominal strain exceeds 0.35, which is mainly due to the densification. This sharp increase makes the stress in *Diagonal Truss* higher than any other topology in high strain values, which can justify the material failure in the experimental results. Finally, **Fig. 6-10b** depicts the deformed configurations and the state of stress for different topologies at different strain values. This figure shows that in the structures with sharp edges, e.g., Square void and Cubic truss, the increased stress is locally distributed. In contrast, in shell-like structures, the increase of stress is more uniform, especially for *Schwarz D*, across the lattice structure.

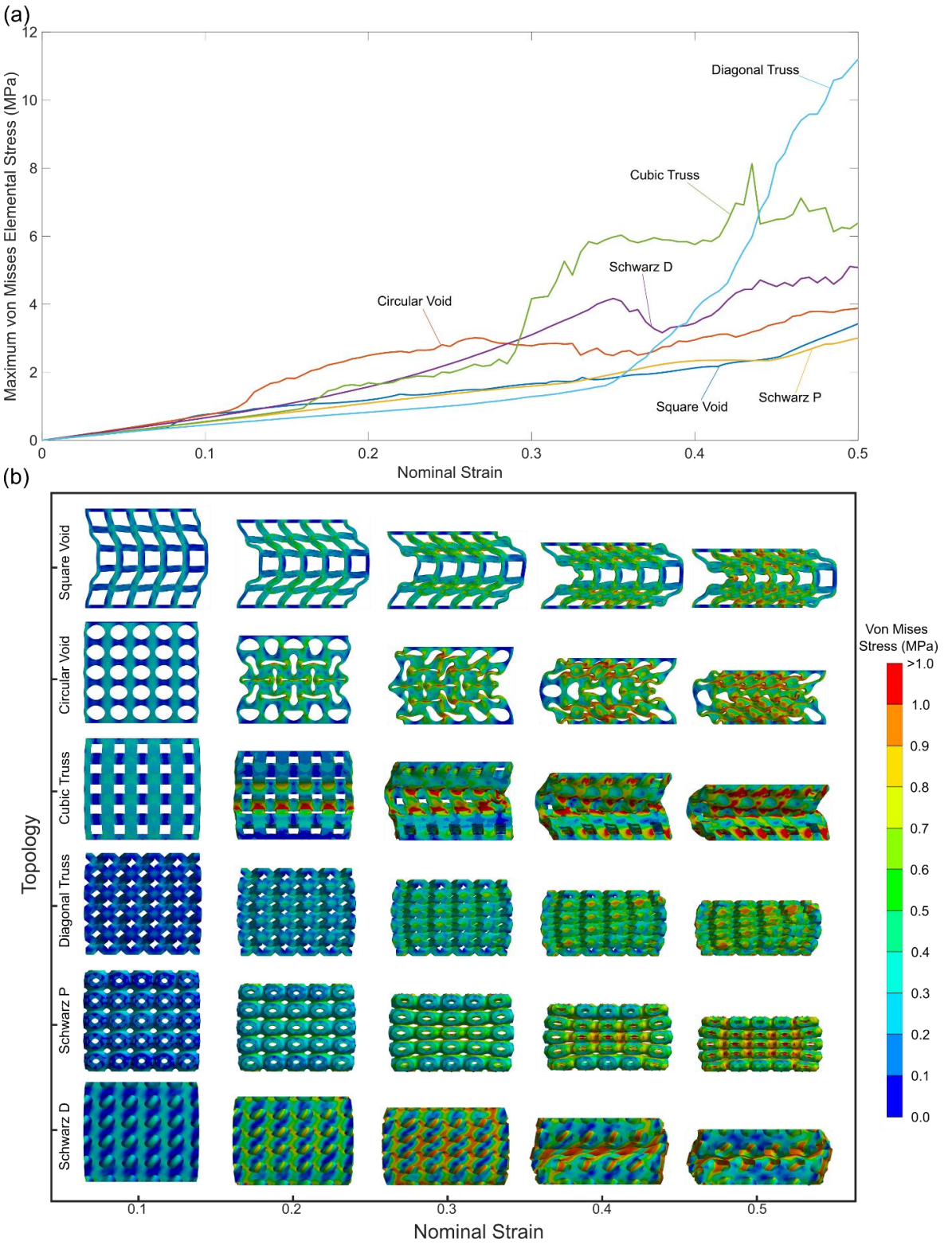

Figure 6-10– *Results of FE simulation for (a) Maximum elemental von Mises stress at different strains, and (b) Deformed configurations for different cell topologies.*

6.6 Concluding remarks

This research explores the effect of cell topology and relative density variation on the response of cellular structures subjected to a compressive force. The lattice structures are 3D printed by stereolithography with elastic materials and are tested under compression and cyclic loading. The experimental results show that uniform density distribution leads to the highest stiffness and specific energy absorption as far as the compressive strain value is as low as 0.1. When the strain increases, the stiffness and specific energy absorption of gradient lattices can surpass the performance of lattices with a uniformly distributed relative density as much as 100 percent and 60 percent, respectively. The enhancement in stiffness and energy absorption capacity is maximized for *Gradients* B_N design, in which the relative densities of cells vary in a direction normal to the direction of the force and through a symmetric function that is minimum at the sides and maximum in the middle. This graded design of lattices promises the possibility of a significant reduction in the weight of cellular structures used in the different applications, including the cores of sandwich panels and automotive shock absorbers, without compromising their energy absorption and stiffness properties.

6.7 Acknowledgments

A.H. Akbarzadeh acknowledges the financial support by Natural Sciences and Engineering Research Council of Canada through NSERC Discovery Grant (RGPIN-2016-0471) and Canada Foundation for Innovation (CFI) through John R. Evans Leaders Fund. This research was also undertaken, in part, thanks to funding from the Canada Research Chairs program to A.H.Akbarzadeh in Multifunctional Metamaterials. H. Niknam is supported by Quebec Research

Fund - Nature and Technologies (FRQNT) doctoral awards (B2X) and McGill University. This research was enabled in part by support provided by CalculQuebec and Compute Canada.

6.8 References

[1] S.D. Papka, S. Kyriakides, In-plane compressive response and crushing of honeycomb, Journal of Mechanics and Physics of Solids 42(10) (1994) 1499-1532.

[2] S. Papka, S. Kyriakides, Structures, Biaxial crushing of honeycombs:—Part 1: Experiments, International Journal of Solids and Structures 36(29) (1999) 4367-4396.

[3] A.J. Wang, D.L. McDowell, In-Plane Stiffness and Yield Strength of Periodic Metal Honeycombs, Journal of Engineering Materials and Technology 126(2) (2004) 137-156.

[4] H.L. Fan, D.N. Fang, F.N. Jing, Yield surfaces and micro-failure mechanism of block lattice truss materials, Materials & Design 29(10) (2008) 2038-2042.

[5] Y. Liu, X.-C. Zhang, The influence of cell micro-topology on the in-plane dynamic crushing of honeycombs, International Journal of Impact Engineering 36(1) (2009) 98-109.

[6] M.-S. Pham, C. Liu, I. Todd, J. Lertthanasarn, Damage-tolerant architected materials inspired by crystal microstructure, Nature 565(7739) (2019) 305-311.

[7] Z. Yin, F. Hannard, F. Barthelat, Impact-resistant nacre-like transparent materials, Science 364(6447) (2019) 1260.

[8] T.C. Shyu, P.F. Damasceno, P.M. Dodd, A. Lamoureux, L. Xu, M. Shlian, M. Shtein, S.C. Glotzer, N.A. Kotov, A kirigami approach to engineering elasticity in nanocomposites through patterned defects, Nature Materials 14(8) (2015) 785-789.

[9] D. Rus, M.T. Tolley, Design, fabrication and control of soft robots, Nature 521 (2015) 467.

[10] X. Yang, J. Ma, Y. Sun, J. Yang, Ripplecomb: A novel triangular tube reinforced corrugated honeycomb for energy absorption, Composite Structures 202 (2018) 988-999.

[11] D. Zhang, Q. Fei, P. Zhang, In–plane dynamic crushing behavior and energy absorption of honeycombs with a novel type of multi-cells, Thin-Walled Structures 117 (2017) 199-210.

[12] T. Li, Y. Chen, X. Hu, Y. Li, L. Wang, Exploiting negative Poisson's ratio to design 3D-printed composites with enhanced mechanical properties, Materials & Design 142 (2018) 247-258.

[13] A.G. Evans, M.Y. He, V.S. Deshpande, J.W. Hutchinson, A.J. Jacobsen, W.B. Carter, Concepts for enhanced energy absorption using hollow micro-lattices, International Journal of Impact Engineering 37(9) (2010) 947-959.

[14] H.N.G. Wadley, Cellular Metals Manufacturing, Advanced Engineering Materials 4(10) (2002) 726-733.

[15] H.N.G. Wadley, N.A. Fleck, A.G. Evans, Fabrication and structural performance of periodic cellular metal sandwich structures, Composites Science and Technology 63(16) (2003) 2331-2343.

[16] F. Wang, Precision extruding deposition and characterization of cellular poly-ε-caprolactone tissue scaffolds, Rapid Prototyping Journal 10(1) (2004) 42-49.

[17] J.B. Berger, H.N.G. Wadley, R.M. McMeeking, Mechanical metamaterials at the theoretical limit of isotropic elastic stiffness, Nature 543 (2017) 533.

[18] I. Maskery, N.T. Aboulkhair, A.O. Aremu, C.J. Tuck, I.A. Ashcroft, Compressive failure modes and energy absorption in additively manufactured double gyroid lattices, Additive Manufacturing 16 (2017) 24-29.

[19] R.A.W. Mines, S. Tsopanos, Y. Shen, R. Hasan, S.T. McKown, Drop weight impact behaviour of sandwich panels with metallic micro lattice cores, International Journal of Impact Engineering 60 (2013) 120-132.

[20] A. Ingrole, A. Hao, R. Liang, Design and modeling of auxetic and hybrid honeycomb structures for in-plane property enhancement, Materials & Design 117 (2017) 72-83.

[21] M. Mohsenizadeh, F. Gasbarri, M. Munther, A. Beheshti, K. Davami, Additively-manufactured lightweight Metamaterials for energy absorption, Materials & Design 139 (2018) 521-530.

[22] F.N. Habib, P. Iovenitti, S.H. Masood, M. Nikzad, Fabrication of polymeric lattice structures for optimum energy absorption using Multi Jet Fusion technology, Materials & Design 155 (2018) 86-98.

[23] C. Neff, N. Hopkinson, N.B. Crane, Experimental and analytical investigation of mechanical behavior of laser-sintered diamond-lattice structures, Additive Manufacturing 22 (2018) 807-816.

[24] S.M. Sajadi, P.S. Owuor, S. Schara, C.F. Woellner, V. Rodrigues, R. Vajtai, J. Lou, D.S. Galvão, C.S. Tiwary, P.M. Ajayan, Multiscale Geometric Design Principles Applied to 3D Printed Schwarzites, Advanced Materials 30(1) (2018) 1704820.

[25] S.C. Han, J.W. Lee, K. Kang, A New Type of Low Density Material: Shellular, Advanced Materials 27(37) (2015) 5506-5511.

[26] T. Tancogne-Dejean, M. Diamantopoulou, M.B. Gorji, C. Bonatti, D. Mohr, 3D Plate-Lattices: An Emerging Class of Low-Density Metamaterial Exhibiting Optimal Isotropic Stiffness, Advanced Materials 30(45) (2018) 1803334.

[27] C. Bonatti, D. Mohr, Mechanical performance of additively-manufactured anisotropic and isotropic smooth shell-lattice materials: Simulations & experiments, Journal of the Mechanics and Physics of Solids 122 (2019) 1-26.

[28] C. Bonatti, D. Mohr, Smooth-shell metamaterials of cubic symmetry: Anisotropic elasticity, yield strength and specific energy absorption, Acta Materialia 164 (2019) 301-321.

[29] M.A. Kader, P.J. Hazell, A.D. Brown, M. Tahtali, S. Ahmed, J.P. Escobedo, M. Saadatfar, Novel design of closed-cell foam structures for property enhancement, Additive Manufacturing 31 (2020) 100976.

[30] A. Ajdari, H. Nayeb-Hashemi, A. Vaziri, Dynamic crushing and energy absorption of regular, irregular and functionally graded cellular structures, International Journal of Solids and Structures 48(3) (2011) 506-516.

[31] L. Boldrin, S. Hummel, F. Scarpa, D. Di Maio, C. Lira, M. Ruzzene, C.D.L. Remillat, T.C. Lim, R. Rajasekaran, S. Patsias, Dynamic behaviour of auxetic gradient composite hexagonal honeycombs, Composite Structures 149 (2016) 114-124.

[32] H. Niknam, A.H. Akbarzadeh, D. Rodrigue, D. Therriault, Architected multi-directional functionally graded cellular plates, Materials & Design 148 (2018) 188-202.

[33] H. Niknam, A.H. Akbarzadeh, In-plane and out-of-plane buckling of architected cellular plates: Numerical and experimental study, Composite Structures 206 (2018) 739-749.

[34] H. Niknam, A.H. Akbarzadeh, Thermo-mechanical bending of architected functionally graded cellular beams, Composites Part B: Engineering 174 (2019) 107060.

[35] J. Huang, X. Gong, Q. Zhang, F. Scarpa, Y. Liu, J. Leng, In-plane mechanics of a novel zero Poisson's ratio honeycomb core, Composites Part B: Engineering 89 (2016) 67-76.

[36] J. Huang, Q. Zhang, F. Scarpa, Y. Liu, J. Leng, In-plane elasticity of a novel auxetic honeycomb design, Composites Part B: Engineering 110 (2017) 72-82.

[37] K. Hu, K. Lin, D. Gu, J. Yang, H. Wang, L. Yuan, Mechanical properties and deformation behavior under compressive loading of selective laser melting processed bio-inspired sandwich structures, Materials Science and Engineering: A 762 (2019) 138089.

[38] S. Yu, J. Sun, J. Bai, Investigation of functionally graded TPMS structures fabricated by additive manufacturing, Materials & Design 182 (2019) 108021.

[39] M. Maldovan, C.K. Ullal, J.H. Jang, E.L. Thomas, Sub-Micrometer Scale Periodic Porous Cellular Structures: Microframes Prepared by Holographic Interference Lithography, Advanced Materials 19(22) (2007) 3809-3813.

[40] K. Bertoldi, M.C. Boyce, S. Deschanel, S.M. Prange, T. Mullin, Mechanics of deformation-triggered pattern transformations and superelastic behavior in periodic elastomeric structures, Journal of the Mechanics and Physics of Solids 56(8) (2008) 2642-2668.

[41] C. Coulais, J.T.B. Overvelde, L.A. Lubbers, K. Bertoldi, M. van Hecke, Discontinuous Buckling of Wide Beams and Metabeams, Physical Review Letters 115(4) (2015) 044301.

7 Chapter Seven: 3D Printed Accordion-like Materials: A Design Route to Achieve Ultrastretchability[1]

7.1 Preface

In **Chapter 6**, the subject of the study was the energy absorption of cellular structures under compression. We evaluate a relative density variation strategy to tune the performance of graded architectures under compressive loading. In **Chapter 7**, we concentrate on improving energy absorption by a structure during tension. We propose a design strategy to substantially increase the stretchability of a brittle material. Through this strategy, we can enhance the stretchability of a brittle material to the same level of elastomers. Unlike other chapters, we have not employed the relative density gradient in this study because this strategy is not capable of improving stretchability.

[1] Reproduced with permission from Niknam, H., Yazdani Sarvestani, H., Jakubinek M., B., Ashrafi, B., Akbarzadeh, A., H.; 3D Printed Accordion-like Materials: A Design Route to Achieve Ultrastretchability; *Additive Manufacturing*. 34 (2020) 101215.

7.2 Abstract

Brittle polymers suffer from the lack of stretchability, which limits their application when large deformation is required. To address this limitation, we investigate the stretchability of a set of cellular materials with conventional and novel cell architectures through 3D printing, experimental testing, and computational simulation. A new class of accordion-like cellular architecture with sinusoidal struts is designed to enhance the planar stretchability of cellular solids. These accordion-like sinusoidal architectures exhibit an enhancement in the stretchability of the cellular materials even for those samples fabricated from brittle polymers. The manufacturability of the proposed architectures is demonstrated utilizing SLA and FDM additive manufacturing techniques. We customize the 3D printing settings to fabricate specimens with tailored architectures for experimental testing. Comparing the stress-strain curves obtained by experimental testing on the 3D printed samples with numerical simulation confirms that the failure strains for sinusoidal architectures can be as high as 20 times that of conventional honeycombs without compromising the energy absorption efficiency of the cellular materials. The Stress-strain curves for 3D printed samples fabricated from flexible polymers are presented to show that energy dissipation in a hysteresis loop also can be enhanced by exploiting the accordion-like sinusoidal architectural designs. The sinusoidal struts in accordion-like cellular architectures offer a design route to extend the material property chart to achieve ultrahigh stretchability in brittle polymers.

7.3 Introduction

Stretchable materials are gaining importance in different applications, including electronic devices [1-4], soft robotics [5], drug delivery systems [6], and shape morphing [7, 8]. An increase in stretchability makes the material more ductile and potentially more damage tolerant, which allows

engineers to design durable structures experiencing large deformation. Two routes are commonly chosen for the design and fabrication of highly-stretchable materials: (1) using elastomers and hydrogels [9-12] as the base material or (2) engineering the underlying architecture (from nano to mesoscale) [13, 14]. This study focuses on the latter approach, where 3D printing and computational modeling are used to tailor the architectural parameters of honeycomb cellular materials. A new class of lightweight architected materials with sinusoidal struts is designed, which allows high stretchability.

Different approaches have been proposed to engineer the underlying architecture of materials to enhance their stretchability [15-19]. Origami-based [15, 17], kirigami-based [16, 18, 20], and wavy-shape [19] architectures have enabled achieving highly-stretchable materials. Wavy-shape or accordion-like materials have been fabricated for high-performance electronics [21, 22]. Through introducing the accordion-like designs in electronic devices, it has been found that the stretchability can be increased by 30% while the electrical conductivity is preserved [23]. One of the simplest accordion-like materials is arrowhead or double-V architecture (**Fig. 7-1a**) [24, 25]. This architecture can result in a small improvement in in-plane stretchability compared to conventional hexagonal honeycombs while offering tunable stiffness and Poisson's ratio properties [26]. The effective stiffness of arrowhead architectures with a range of angles and relative densities are determined by a homogenization technique [27, 28] and compared to the stiffness of conventional hexagonal and re-entrant honeycombs [29] in **Fig. 7-1b**. **Figure 7-1** demonstrates that arrowhead architectures offer a wider design space for developing cellular materials with various relative densities (i.e., the volume of solid parts divided by the total volume of the representative unit cell).

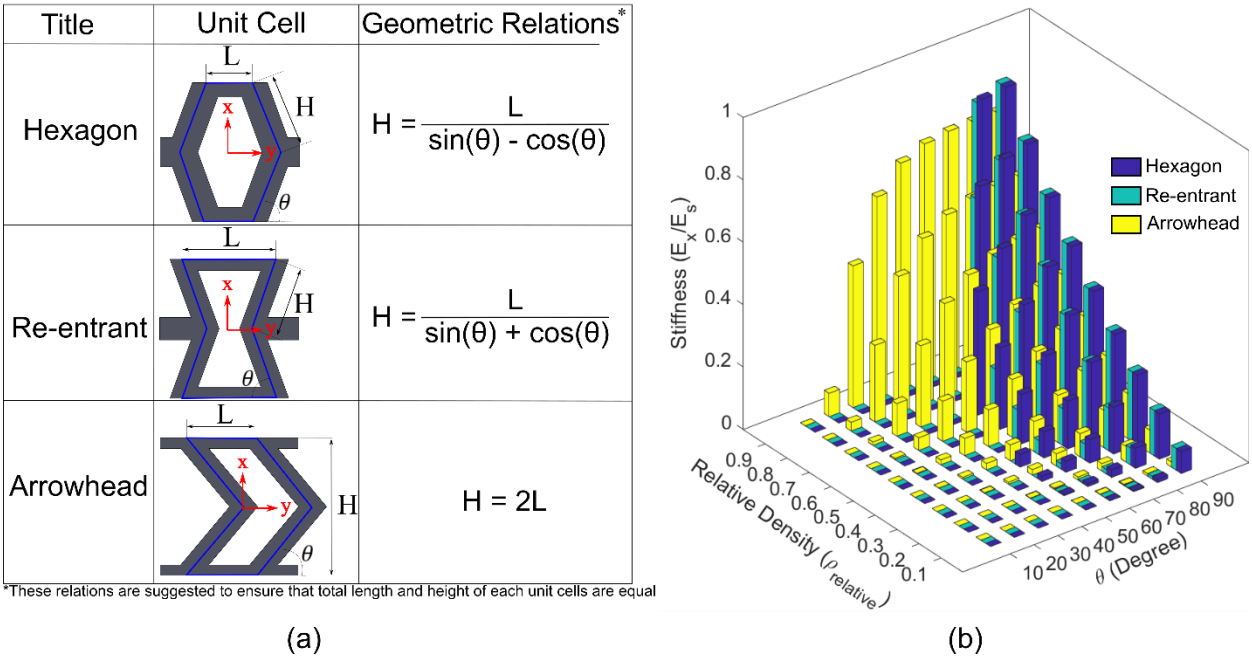

Figure 7-1- *(a) Schematic view of hexagonal, re-entrant, and arrowhead cells; (b) Homogenized stiffness of different architected cells.*

Sharp corners, commonly found in conventional cellular materials, limit their tensile strength and stretchability. However, this restriction can be overcome by using cellular architectures, where sharp corners are avoided [30, 31]. The design of such architectures is facilitated by recent developments in additive manufacturing techniques, which provide geometrical and material selection flexibility for the manufacturing of products with free-form and complex architectures. The accuracy of additive manufacturing technologies have been consistently increased in the past few years [32, 33]; however, non-conformity between *as-designed* and *as-built* products (e.g., waviness of surfaces, positioning errors, shrinkage and stress-based distortions, and porosities in the final product) is still unavoidable [34-38]. Additive manufacturing has enabled the fabrication of architected geometries with unique structural properties [39-43]. Tailoring the topology of cellular materials can enable controlling the overall mechanical properties (e.g., stiffness, strength, toughness, and stretchability) while keeping the weight of structural elements unchanged. In

efforts to program the mechanical properties of lightweight materials, a series of 3D printable rationally designed microarchitectures have been proposed. Isomax (an architected isotropic material achieving the theoretical upper bound of elastic stiffness) [44], Gyroid (a shell-like stretching-dominated cell less sensitive to flaws and imperfection than truss-like architectures) [41], and Crystal-inspired metamaterials (Damage-tolerant architected materials inspired by hardening mechanism in crystalline materials) [45] are a few examples of recently-developed engineered cellular materials.

In addition to the controllability of stiffness, strength, and energy absorption reported in the aforementioned architected materials, additive manufacturing can also facilitate improving the stretchability of 3D printed materials [46-48]. To the best of author's knowledge, the capabilities of additive manufacturing in increasing the stretchability of architected cellular materials, fabricated from brittle polymers, have not been explored in the literature. In this study, we propose a novel accordion-like design to enhance the stretchability of 3D printed conventional cellular architectures without sacrificing their weight. Novel accordion-like architectures are designed, and their mechanical properties are assessed using a combination of finite element modeling and experimental testing on 3D printed brittle and flexible polymeric samples. The 3D printed samples are uniaxially tested, and their stretchability is compared to show how the rational design of underlying architectures of cellular solids can lead to the development of ultrastretchable materials even from brittle polymers.

7.4 Design and manufacturing strategy

7.4.1 Material properties and 3D printing techniques

The architectures investigated in this study are fabricated with two different additive manufacturing technologies out of two different materials:

Methacrylate polymeric samples 3D printed via stereolithography (SLA): The first group of samples is manufactured from a methacrylate-based polymer, with the commercial name of Grey Pro resin, which exhibits a brittle behavior. A commercial SLA 3D printer (Form 2, Formlabs) is used to 3D print the samples with appropriate supports and raft. Architected cellular samples are designed in SOLIDWORKS and sliced in PreForm software. The 3D printed samples are washed in isopropyl alcohol and cured by UV light. **Table 7-1** presents the SLA 3D printing process parameters.

Table 7-1*- SLA 3D printing settings.*

Resin	Sample thickness	Washing duration	UV curing temperature	UV curing duration
Grey Pro	$3.5mm$	30 minutes	60℃	60 minutes

Nylon samples 3D printed via fused deposition modeling (FDM): The base material for the second group of samples is flexible nylon. These samples are 3D printed using an FDM printer (Original Prusa i3 MK3s printer, Prusa Research) with the 3D printing settings shown in **Table 7-2**. Due to the relatively narrow width of the hexagonal and accordion-like architectural features, the struts are made up only by the outer walls. They contain no additional infill even when 100% infill is used for FDM 3D printing. As a result, the printing direction is always along the direction of the accordion-like (or honeycomb-like) struts for all the architectures presented in this investigation, independent of the orientation of the part on the print bed. Most parts are oriented at 45°, with respect to the principal axes of the print bed, and a brim is added since these selections reduce issues associated with detachment and warping of 3D printed parts.

Table 7-2- FDM 3D printing settings.

Filament	Sample thickness	Filament diameter	Extruding temperature	Bed temperature
Nylon	20 mm	1.75mm	280℃	90℃

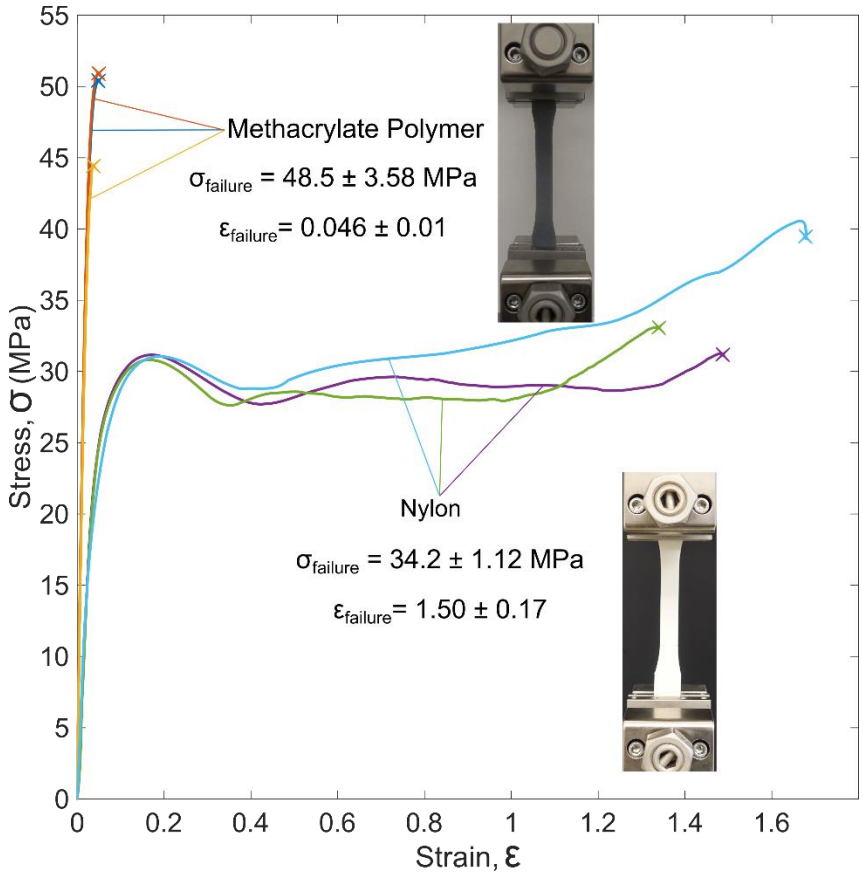

Figure 7-2- *Stress-strain curves for tension tests on 3D printed dogbone samples of methacrylate (brittle) photopolymer and nylon (flexible) thermoplastic polymer.*

The mechanical properties of both polymers are evaluated by performing tensile tests on 3D printed dogbone samples. **Figure 7-2** presents the results of tensile tests conducted according to the ASTM D638 standard. For each 3D printed polymer (brittle or flexible), three samples are

tested under tension by ADMET eXpert 8612 testing machine with a $20kN$ load cell. The strain is applied to the samples by a $5\,mm/sec$ rate. As observed in the stress-strain curve presented in **Fig. 7-2**, methacrylate polymer shows a brittle behavior under tension; stress increases proportionally with strain until an ultimate fracture at a relatively-low strain ($\varepsilon_{failure} \simeq 0.046$). On the contrary, the 3D printed nylon demonstrates a more resilient behavior, a linearly proportional stress-strain curved, followed by a plateau regime where stress remains almost constant with the increase of strain and ultimate fracture occurs after a rise in the stress.

7.4.2 Stretchability

Herein, *stretchability* (λ) is defined as the maximum change in the length of architecture when it fails, divided by distance between the grips when the material is undeformed, which is equivalent to the nominal failure strain (ε_f). Nominal stress, for cellular architectures, is also calculated by dividing the force exerted by the tensile test machine by the equivalent cross-section of a solid cell, i.e., $5 \times H \times W$ for a cellular solid comprising of 5×5 unit cells with an out-of-plane thickness of W (**Fig. 7-3**).

A tessellated cellular architecture, used for conducting experiments and detailed numerical simulation, is depicted in **Fig. 7-3a**. Each architected cellular material consists of 5 cells in both x and y directions; grip segments have been added to the top and bottom of tessellated cellular materials to facilitate fixing the 3D printed samples in the grips during the tensile test. The dimensions of the geometrical features of the cellular architecture introduced in **Fig. 7-3** are $H = 11.5mm, L = 5.75mm, r_1 = 80mm, r_2 = 23mm, r_3 = 35mm$.

The total size of the samples is designed to be large enough such that all of the geometrical features of the designed architecture can be 3D printed by the adopted FDM and SLA 3D printers in the

current study. The parameter t, correlated to the strut thickness of architected cellular solids, is also calculated based on the total relative density, which will be discussed in the next Subsection.

7.4.3 Accordion-like architectures with sinusoidal struts

Sharp corners in constitutive struts of the conventional cellular architectures cause stress concentration and structural failure, prior to allowing the other parts of constitutive building blocks to experience the applied stress. In order to enhance the stretching capability of cellular architectures, sharp corners in constitutive struts should be avoided. As a result, we replace the two straight struts of the arrowhead architecture with sinusoidal curves, as shown in **Fig. 7-3b**. The shape of the sinusoidal struts, which form the sinusoidal accordion-like cellular architectures, is defined by:

$$F_n(x) = \frac{L}{2}\cos\left(\frac{4\pi n}{H-2t}x\right), \tag{7.1}$$

where n determines the period of the trigonometric function. Different topologies associated with alternative values of n are presented in **Fig. 7-3c**. The relative density (i.e., $\rho_{relative} = \frac{Solid\ Volume}{Unit\ cell\ Volume}$) of the sinusoidal accordion-like cells can be determined as:

$$\rho_{relative} = 2HLt^2\left(\frac{1}{Ht} - \frac{1}{Lt} - \frac{2}{HL}\right) \tag{7.2}$$

In this study, the relative density of all samples is 0.5.

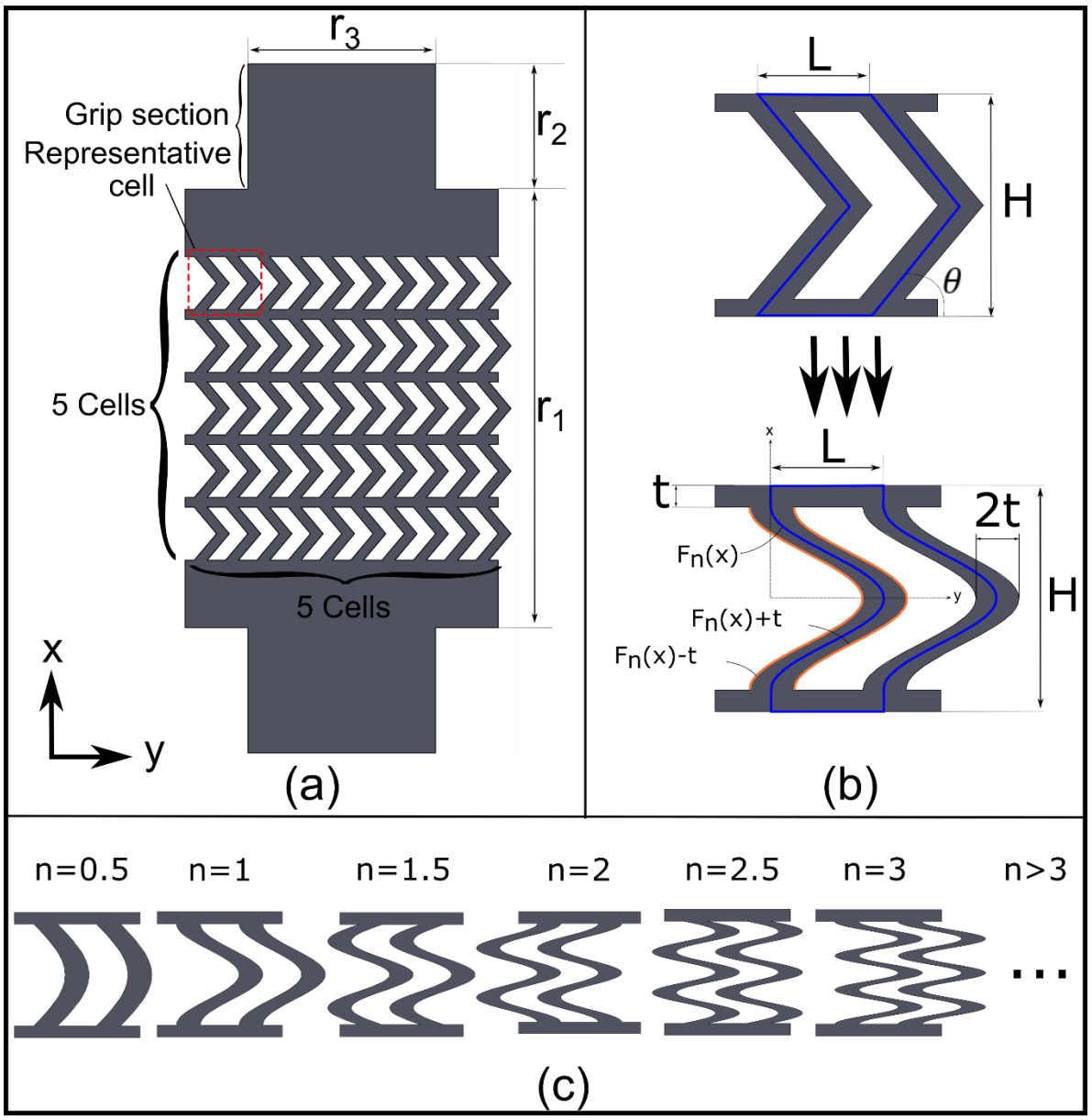

Figure 7-3- *Schematic view of architected cellular materials: (a) Tessellated cellular material, (b) Arrowhead and sinusoidal accordion-like unit cells, and (c) Sinusoidal accordion-like unit cells for alternative values of n.*

7.4.4 Finite element analysis

A nonlinear finite element analysis (FEA) is conducted using ANSYS Workbench (Version 19). Geometric nonlinearity is adopted for the numerical analysis to reflect the large deformation. Single point integration explicit elements are usually used for structural large deformation analyses; however, it can lead to inaccurate results when material nonlinearity and failure analysis are adopted. Adaptive meshing, which automatically re-meshes a discretized domain during FEA, is exploited to remediate this problem. Mesh size optimization is also performed, and each model is meshed with almost 10,000 adaptive quadrilateral shell elements. Multilinear isotropic hardening, with elastic and hardening parameters obtained from experimental data given in **Fig. 7-2**, is used as the material model for nonlinear FEA. The inputs for the multilinear isotropic hardening law were the true stress versus true plastic strain, instead of the total strain. Failure is also considered by deleting elements when the strain of an element reaches the failure strain of the base material.

7.5 Results and Discussion

7.5.1 Brittle methacrylate polymeric samples

Figure 7-4 demonstrates the stress-strain curves of conventional honeycombs, and arrowhead and sinusoidal accordion-like architectures obtained by uniaxial tensile tests on SLA 3D printed samples with $3.5mm$ out-of-plane thickness, fabricated from the brittle polymer. As shown in **Fig. 7-4a** the failure strain for honeycomb and re-entrant architectures is relatively low ($\varepsilon_f \sim 0.05$), which is close to the failure strain of the associated dog bone sample. Arrowhead design may increase the failure strain as θ decreases; a failure strain up to $\varepsilon_f \sim 0.23$ is obtained for arrowhead design with $\theta = 30^o$. The increase in the stretchability of arrowhead design with $\theta = 30^o$ is due

to the increase in bending moment applied to the struts. Nevertheless, the value of θ cannot be unboundedly decreased as it yields geometrically inadmissible unit cells. The presence of sharp corners in the constitutive struts of arrowhead design still causes stress concentration within the architecture and impedes achieving ultrahigh stretchability for these architected cellular solids.

Figure 7-4b shows that a substantial increase in the stretchability can be obtained by implementing sinusoidal accordion-like architectures. This figure presents two main trends in stiffness and stretchability. First, the overall stiffness of architected cellular solids can be controlled by changing the value of n, where a higher n leads to more flexible designs. Second, the stretchability increases by increasing n; hence, higher stretchability can be obtained for larger n values. **Table 7-3** presents pictures of the undeformed and deformed state (immediately before failure) for three selected 3D printed architectures under uniaxial tension. As evident in the pictures, the sinusoidal architecture made of a brittle polymer stretches significantly before ultimate fracture, which indicates design and 3D printing strategy for transforming brittle materials to ductile or elastomeric structural materials. While arrowhead design shows a brittle fracture behavior, the fracture response of sinusoidal architecture with high values of n is ductile/elastomeric.

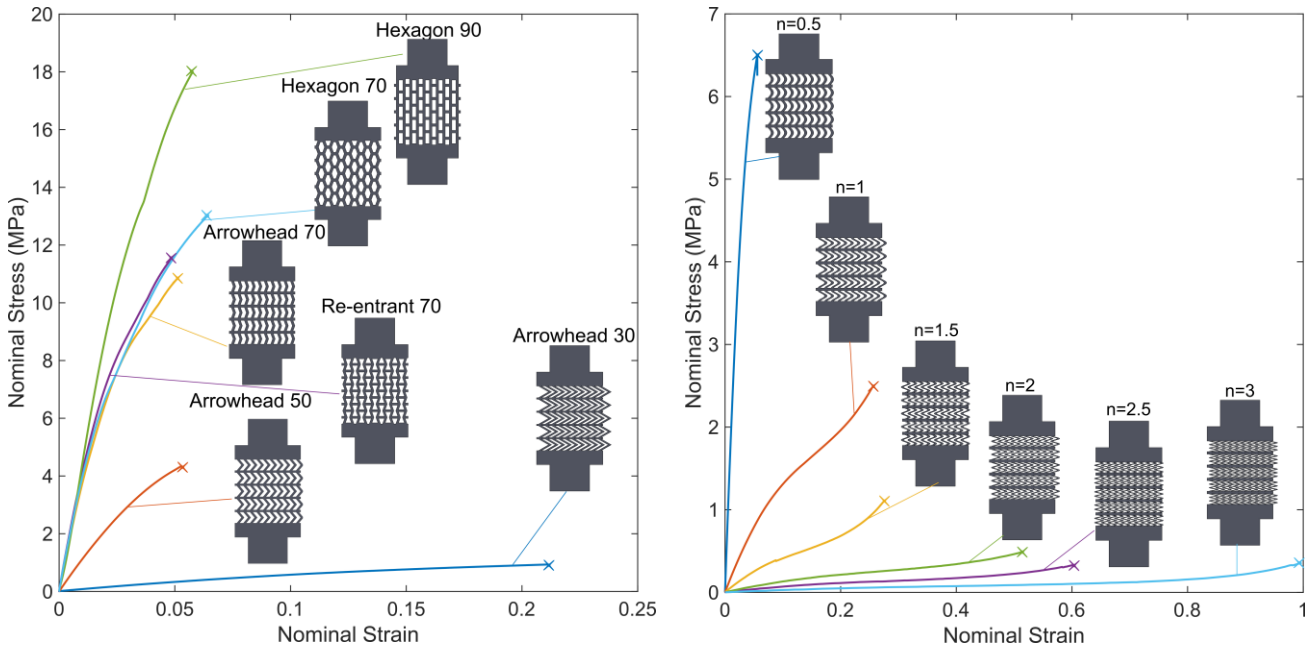

(a) *(b)*

Figure 7-4- *Stress-strain curves for 3D printed architected cellular architectures: (a) Honeycomb and arrowhead architectures and (b) Sinusoidal accordion-like architectures.*

Table 7-3- *Pictures of alternative SLA 3D printed cellular architectures under uniaxial tensile test in undeformed and deformed states.*

Architecture	**Arrowhead 70**	**Sinusoidal *n* = 1**	**Sinusoidal *n* = 3**
Undeformed state	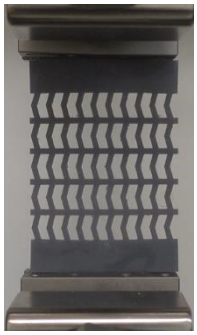		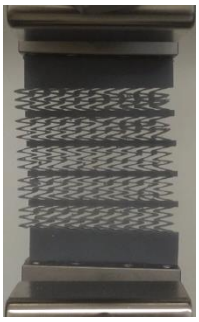
Deformed state *(Before failure)*		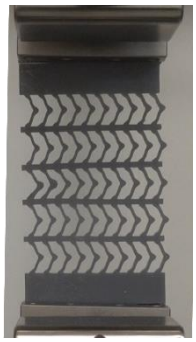	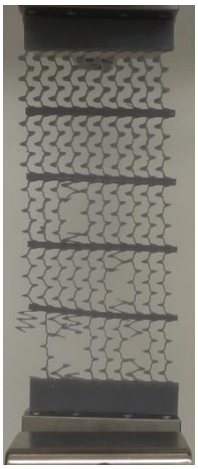
Strain at failure	$\varepsilon_f = 0.0513$	$\varepsilon_f = 0.2541$	$\varepsilon_f = 0.9277$

The experimental stress-strain curves are compared with the numerical results of FEA conducted by ANSYS finite element software. FEA helps to better understand the mechanisms that govern the deformation of the architected architectures experiencing a quasi-static uniaxial tension. **Figure 7-5** shows that the FEA results for stress-strain curves are in good agreement with experimental results; the results are almost coincident for small strain, while deviation slightly

increases for higher strains. The stress contours, obtained by FEA at a specific strain of $\varepsilon = 0.004$, are presented for each architecture in **Fig. 7-5**. It can be found that the maximum stress in honeycomb and arrowhead architectures mainly occurs at sharp corners connecting the constitutive struts. Consequently, eliminating the sharp edges by designing the sinusoidal struts can significantly reduce the maximum stress concentration; for example maximum stress concentration within a regular honeycomb with $\theta = 70^o$ is reduced from 31.7 MPa to 1.5 MPa by exploiting sinusoidal design with n = 3.

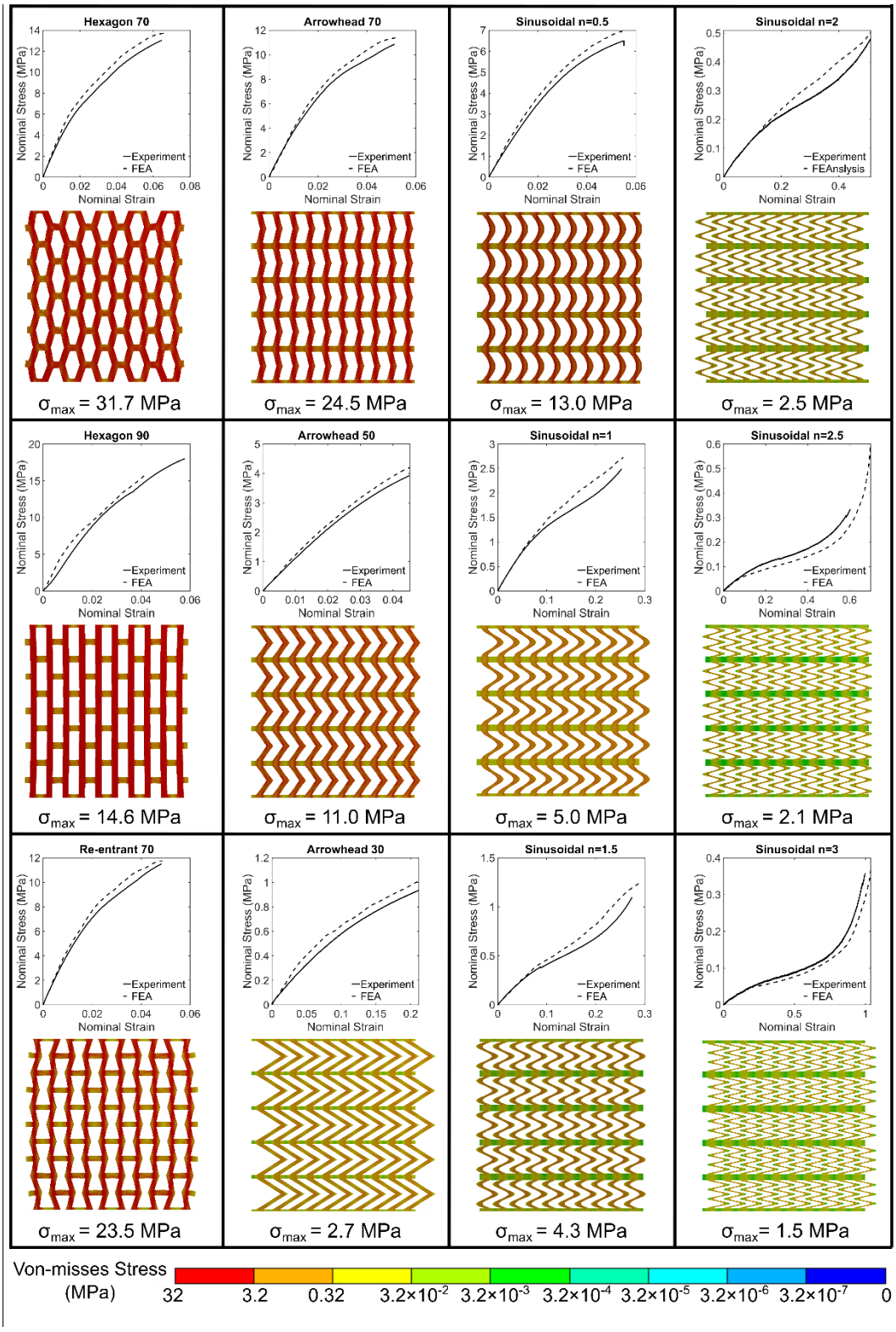

Figure 7-5- *Comparison of stress-strain curves obtained by experiment and FEA for samples made of the methacrylate polymer; stress contours are shown at strain* $\varepsilon = 0.004$.

In **Fig. 7-6a**, the energy absorption efficiency (η) of different cellular architectures is compared; η is defined as the ratio of actual absorbed energy by a material (area under stress-strain curve) normalized to the energy absorbed by an *ideal* absorber up to the same strain [49-51]:

$$\eta = \frac{\int_0^{\varepsilon_i} \sigma d\varepsilon}{\sigma_{max}\varepsilon_i} \tag{7.3}$$

where ε_i is a specific strain in which the efficiency is reported; σ_{max} is the stress at that strain. Energy absorption efficiency allows comparing the energy absorbed by architected cellular materials to the energy absorbed by an ideal absorber, i.e., an energy absorber whose stress-strain curve is a horizontal line at maximum stress. **Figure 7-6a** shows that the energy absorption efficiency remains roughly unchanged for different architectures and specific strains; consequently, these architectures are broadly similar in terms of efficiency for energy absorption. Nonetheless, as shown in **Fig. 7-6b**, stretchability is substantially increased by designing sinusoidal struts within architected accordion-like materials. Hence, sinusoidal struts can be introduced as a design strategy for magnifying the stretchability of cellular materials without sacrificing the energy absorption efficiency. For instance, experimental results on 3D printed brittle polymeric samples (which are repeated three times to assure the reliability of conclusions) show that using an architected accordion-like cell with $n = 3$ instead of a conventional honeycomb cell with $\theta = 70^o$ can significantly increase the stretchability from 0.051 to 1.02 (~ 20 times increase) while energy absorption efficiency remains constant ($\eta \sim 0.55$). In addition, **Fig. 7-6b** shows that FEA predictions for stretchability are in a close agreement with experimental data; the maximum difference is about 20% for Hexagon with $\theta = 90°$, while the mean value of this deviation is only 8%. The discrepancy between experimental data and detailed FEA results mainly emanates from the imperfections caused by 3D printing defects. The relation between the

stretchability and the value of n in sinusoidal architected materials can be approximated by a quadratic function with good accuracy both for experimental data and numerical simulation results. For the experimental data, the failure strain (stretchability) can be related to n through: $\varepsilon_f = 0.071n^2 + 0.086n + 0.027$ (R-square = 0.972). The correlation function for numerical data obtaining by finite element modeling is $\varepsilon_f = 0.093n^2 + 0.042n + 0.048$ (R-square = 0.985).

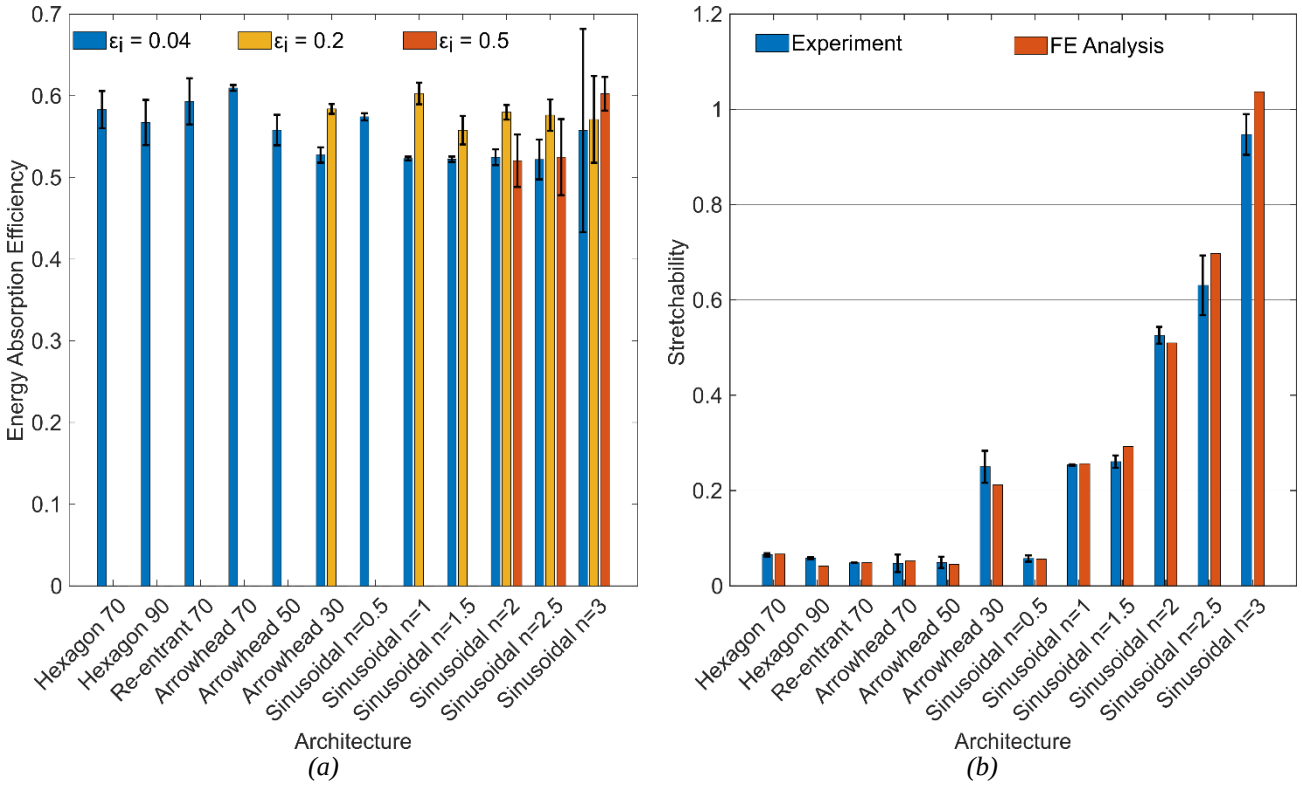

***Figure 7-6**- Comparison of the mechanical performance of honeycomb, arrowhead, and sinusoidal architectures in terms of (a) Energy absorption efficiency and (b) Stretchability.*

Material selection charts, often called Ashby charts [52], are presented in **Fig. 7-7** to compare the stretchability, Young's modulus, and density of proposed polymeric architected accordion-like materials with commonly-used materials. **Figure 7-7** illustrates that exploiting sinusoidal accordion-like materials enables the extension of material performance beyond the performance limitation of the base materials. Confirming the accuracy of our finite element simulation in **Figs.**

7-5 and 7-**6**, the stretchability and stiffness of architected accordion-like materials for higher values of n are determined by FEA and presented in **Fig. 7-7**. **Figure 7-7a** shows that the stretchability of architected cells with sinusoidal struts fabricated from a brittle polymer can be as high as elastomers. In other words, sinusoidal struts enable increased stretchability of the base materials by two orders of magnitude. This implies a design route to achieve ultrastretchable and lightweight advanced materials using brittle polymers. **Figure 7-7b** presents the elastic stiffness of accordion-like materials compared to conventional solid materials. We can notice that architected sinusoidal struts can lead to the development of materials that are lighter but as flexible as elastomers. As a result, stretchability and stiffness of polymeric cellular materials can be controlled for each relative density by tailoring the sinusoidal struts to satisfy the application requirements in flexible electronics, energy absorbers, and shape-morphing.

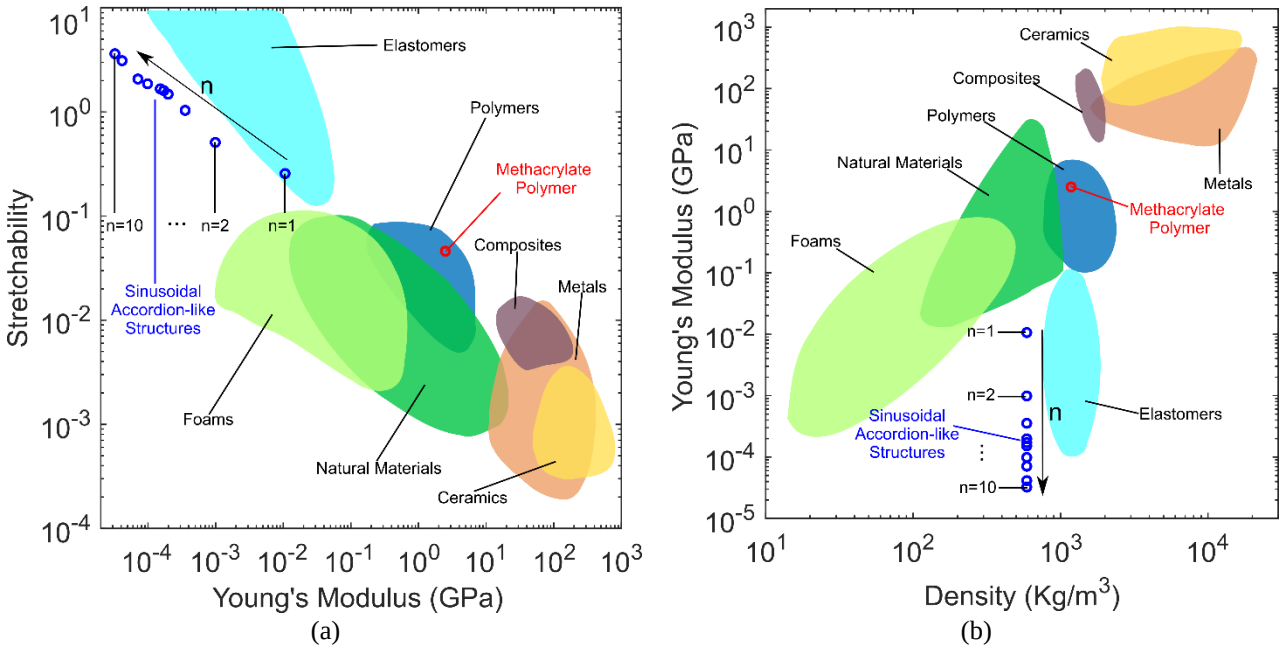

Figure 7-7- *Ashby charts for (a) Stretchability versus Young's modulus and (b) Young's modulus versus density for commonly used materials compared to architected accordion-like materials made of brittle methacrylate polymer.*

7.5.2 Flexible nylon samples

Similar architected cellular materials are 3D printed out of flexible nylon and tested under a sequence of tension and compression. **Figure 7-8** presents the experimental results for different honeycombs, arrowhead, and accordion-like architectures undergoing the equal tensile and compressive force of $1500N$, which is equivalent to the nominal stress of $\pm 1.3MPa$. Comparing the maximum strain under the same tensile and compressive stresses reveals that arrowhead design, as expected, can be more flexible than hexagonal and re-entrant architectures. Furthermore, the range of stretchability is efficiently increased by exploiting the sinusoidal architectures in accordion-like cells. Under compression, the constituent struts of architected cellular materials may experience self-contact, leading to a sharp increase in the stress that limits achieving ultrahigh compressive strain.

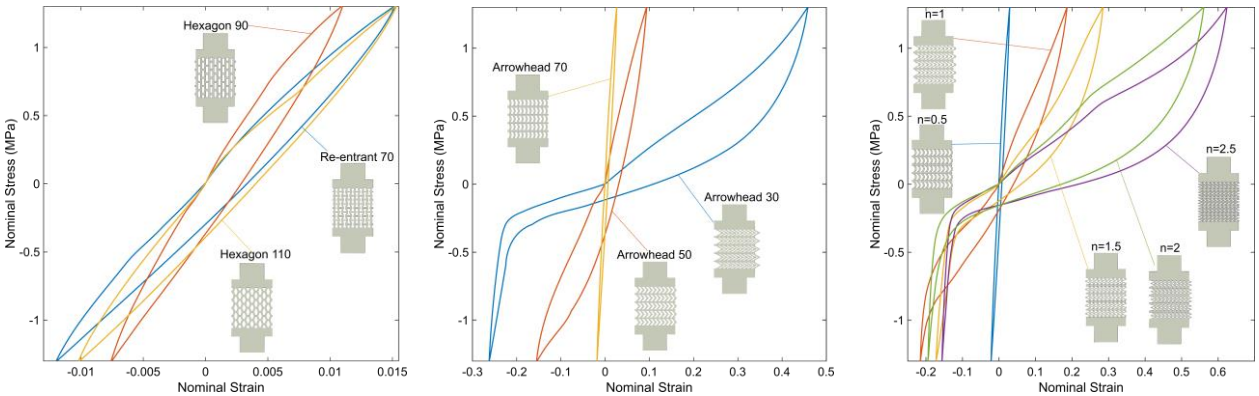

Figure 7-8- *Stress-strain curves for alternative cellular materials made of flexible nylon: (a) Honeycomb, (b) Arrowhead, and (c) Accordion-like architectures.*

Figure 7-9 shows the hysteresis energy, obtained from the area enclosed in the stress-strain curves presented in **Fig. 7-8**. The hysteresis energy in accordion-like materials with a sinusoidal

architecture is higher than those for conventional honeycomb design; the improvement in hysteresis energy is much more significant as *n* increases.

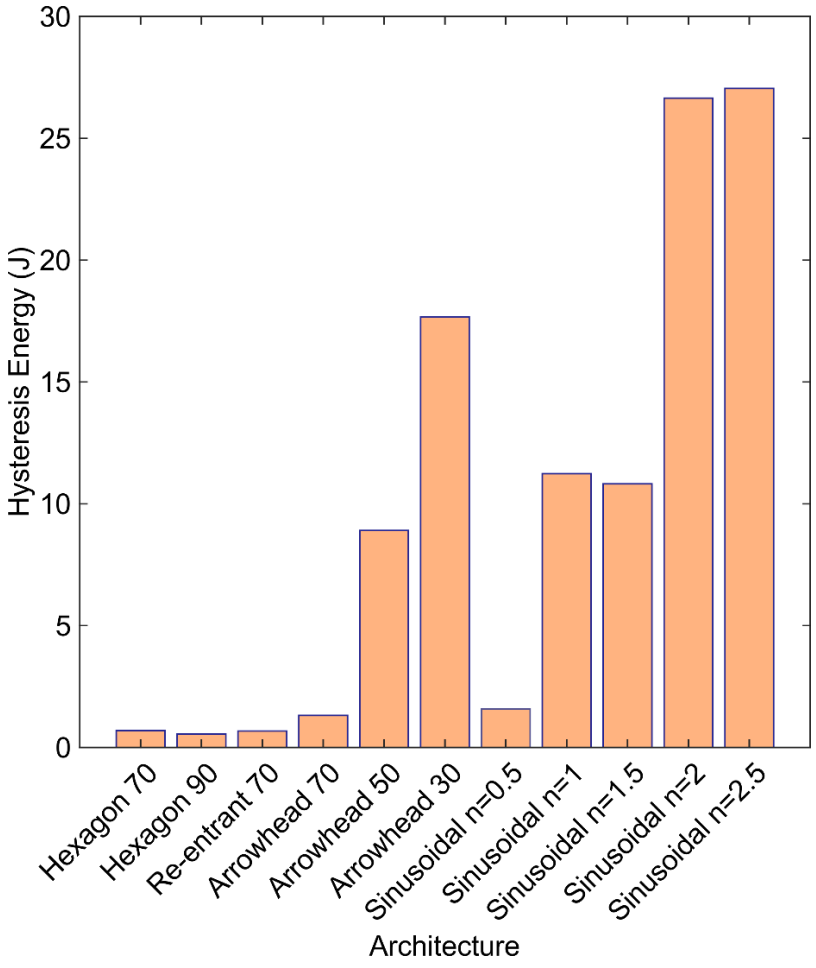

Figure 7-9- *Hysteresis energies for alternative 3D printed cellular architectures made of flexible nylon* 20 mm *thickness, when subjected to consecutive tensile and compressive stresses as* $\sigma = \pm 1.3\ MPa$.

7.6 Concluding Remarks

Architected cellular structures are designed to enhance the stretchability of brittle polymers. Multiple architected samples are fabricated with SLA and FDM 3D printing technologies to evaluate their stretchability, stiffness, and energy absorption experimentally. The stretchability of

different 3D printed cellular architectures is evaluated through conducting experimental testing and finite element analysis. The results reveal that architecting the cell topology enables designing cellular architectures with enhanced stretchability. Simulation results indicate that architecting the struts of cellular materials, in the form of sinusoidal shapes, can effectively decrease stress within the architecture to one-twentieth of the hexagonal honeycomb counterparts. Prototyping confirms that using the novel sinusoidal accordion-like design, materials fabricated from a brittle polymer can be stretched 20 times more than conventional honeycombs with the same weight. Through Ashby material selection charts, we observe that we can obtain stiffness and stretchability for densities that are not achievable by means of alternative natural and engineering base materials. The important advantage of such designs over elastomers or hydrogels is the possibility of tuning the stiffness and stretchability directionally. This means a material can sustain its stiffness and brittleness in one direction while it can be transformed to be significantly stretchable in other directions. Also, samples manufactured out of flexible nylon polymers can offer a significant increase in the hysteresis energy (almost 30 times higher) compared to hexagonal and re-entrant honeycombs for application where lightweight cellular materials are subjected to cyclic loadings. The manmade accordion-like cellular architectures, similar to helicoidal biological structural elements found in nature in the tendril stem/leaves of climbing plants, can open a new avenue for designing ultrastretchable advanced materials from both brittle and flexible base materials.

7.7 Acknowledgment

A.H. Akbarzadeh acknowledges the financial support by Natural Sciences and Engineering Research Council of Canada through NSERC Discovery Grant RGPIN-2016-0471, Canada Foundation for Innovation (CFI) through John R. Evans Leaders Fund, and McGill University. Quebec Research Fund - Nature and Technologies (FRQNT) post-doctoral (B3X) and doctoral

(B2X) awards support, respectively, H. Yazdani Sarvestani and H. Niknam. Support from Michael Barnes concerning 3D printed nylon is also gratefully acknowledged.

7.8 References

[1] T. Li, Y. Jiang, K. Yu, Q. Wang, Stretchable 3D lattice conductors, Soft Matter 13(42) (2017) 7731-7739.

[2] D.J. Lipomi, M. Vosgueritchian, B.C.K. Tee, S.L. Hellstrom, J.A. Lee, C.H. Fox, Z. Bao, Skin-like pressure and strain sensors based on transparent elastic films of carbon nanotubes, Nature Nanotechnology 6 (2011) 788.

[3] D.J. Lipomi, B.C.K. Tee, M. Vosgueritchian, Z. Bao, Stretchable Organic Solar Cells, Advanced Materials 23(15) (2011) 1771-1775.

[4] D.-H. Kim, N. Lu, R. Ma, Y.-S. Kim, R.-H. Kim, S. Wang, J. Wu, S.M. Won, H. Tao, A. Islam, K.J. Yu, T.-i. Kim, R. Chowdhury, M. Ying, L. Xu, M. Li, H.-J. Chung, H. Keum, M. McCormick, P. Liu, Y.-W. Zhang, F.G. Omenetto, Y. Huang, T. Coleman, J.A. Rogers, Epidermal Electronics, 333(6044) (2011) 838-843.

[5] D. Rus, M.T. Tolley, Design, fabrication and control of soft robots, Nature 521 (2015) 467.

[6] J.-Y. Sun, X. Zhao, W.R.K. Illeperuma, O. Chaudhuri, K.H. Oh, D.J. Mooney, J.J. Vlassak, Z. Suo, Highly stretchable and tough hydrogels, Nature 489 (2012) 133.

[7] E.A. Bubert, B.K.S. Woods, K. Lee, C.S. Kothera, N.M. Wereley, Design and Fabrication of a Passive 1D Morphing Aircraft Skin, Journal of Intelligent Material Systems and Structures 21(17) (2010) 1699-1717.

[8] M. Jakubinek, S. Roy, M. Palardy-Sim, B. Ashrafi, F. Shadmehri, G. Renaud, M. Barnes, Y. Martinez-Rubi, M. Rahmat, B. Simard, A. Yousefpour, F. Fortin, Stretchable Structure for a Benchtop-Scale Morphed Leading Edge Demonstration, AIAA Scitech 2019 Forum, American Institute of Aeronautics and Astronautics2019.

[9] M. Park, J. Im, M. Shin, Y. Min, J. Park, H. Cho, S. Park, M.-B. Shim, S. Jeon, D.-Y. Chung, J. Bae, J. Park, U. Jeong, K. Kim, Highly stretchable electric circuits from a composite material of silver nanoparticles and elastomeric fibres, Nature Nanotechnology 7 (2012) 803.

[10] J. Park, S. Wang, M. Li, C. Ahn, J.K. Hyun, D.S. Kim, D.K. Kim, J.A. Rogers, Y. Huang, S. Jeon, Three-dimensional nanonetworks for giant stretchability in dielectrics and conductors, Nature Communications 3 (2012) 916.

[11] J.-Y. Sun, X. Zhao, W.R.K. Illeperuma, O. Chaudhuri, K.H. Oh, D.J. Mooney, J.J. Vlassak, Z. Suo, Highly stretchable and tough hydrogels, Nature 489(7414) (2012) 133-136.

[12] K. Yu, A. Xin, H. Du, Y. Li, Q. Wang, Additive manufacturing of self-healing elastomers, NPG Asia Materials 11(1) (2019) 7.

[13] Y. Jiang, Q. Wang, Highly-stretchable 3D-architected Mechanical Metamaterials, Scientific Reports 6 (2016) 34147.

[14] N. Alcheikh, S.F. Shaikh, M.M. Hussain, Ultra-stretchable Archimedean interconnects for stretchable electronics, Extreme Mechanics Letters 24 (2018) 6-13.

[15] Y. Morikawa, S. Yamagiwa, H. Sawahata, M. Ishida, T. Kawano, An origami-inspired ultrastretchable bioprobe film device, 2016 IEEE 29th International Conference on Micro Electro Mechanical Systems (MEMS), 2016, pp. 149-152.

[16] T.C. Shyu, P.F. Damasceno, P.M. Dodd, A. Lamoureux, L. Xu, M. Shlian, M. Shtein, S.C. Glotzer, N.A. Kotov, A kirigami approach to engineering elasticity in nanocomposites through patterned defects, Nature Materials 14 (2015) 785.

[17] S. Ji, B.G. Hyun, K. Kim, S.Y. Lee, S.-H. Kim, J.-Y. Kim, M.H. Song, J.-U. Park, Photo-patternable and transparent films using cellulose nanofibers for stretchable origami electronics, Npg Asia Materials 8 (2016) e299.

[18] Z. Song, X. Wang, C. Lv, Y. An, M. Liang, T. Ma, D. He, Y.-J. Zheng, S.-Q. Huang, H. Yu, H. Jiang, Kirigami-based stretchable lithium-ion batteries, Scientific Reports 5 (2015) 10988.

[19] J.A. Rogers, T. Someya, Y. Huang, Materials and Mechanics for Stretchable Electronics, Science 327(5973) (2010) 1603.

[20] J. Nakajima, K. Fayazbakhsh, Y. Teshima, Experimental study on tensile properties of 3D printed flexible kirigami specimens, Additive Manufacturing 32 (2020) 101100.

[21] D.-Y. Khang, H. Jiang, Y. Huang, J.A. Rogers, A Stretchable Form of Single-Crystal Silicon for High-Performance Electronics on Rubber Substrates, Science 311(5758) (2006) 208.

[22] A. Bagal, E.C. Dandley, J. Zhao, X.A. Zhang, C.J. Oldham, G.N. Parsons, C.-H. Chang, Multifunctional nano-accordion structures for stretchable transparent conductors, Materials Horizons 2(5) (2015) 486-494.

[23] J. Mertens, R.W. Bowman, J.C.W. Willis, A. Robinson, D. Cotton, R. White, K.A. Seffen, J.J. Baumberg, Scalable Microaccordion Mesh for Deformable and Stretchable Metallic Films, Physical Review Applied 4(4) (2015) 044006.

[24] C.S. Ha, R.S. Lakes, M.E. Plesha, Design, fabrication, and analysis of lattice exhibiting energy absorption via snap-through behavior, Materials & Design 141 (2018) 426-437.

[25] J.X. Qiao, C.Q. Chen, Impact resistance of uniform and functionally graded auxetic double arrowhead honeycombs, International Journal of Impact Engineering 83 (2015) 47-58.

[26] Q.-T. Deng, Z.-C. Yang, Effect of poisson's ratio on functionally graded cellular structures, Materials Express 6(6) (2016) 461-472.

[27] S.J. Hollister, N. Kikuchi, A comparison of homogenization and standard mechanics analyses for periodic porous composites, Computational Mechanics 10(2) (1992) 73-95.

[28] A.H. Akbarzadeh, J.W. Fu, L. Liu, Z.T. Chen, D. Pasini, Electrically conducting sandwich cylinder with a planar lattice core under prescribed eigenstrain and magnetic field, Composite Structures 153(Supplement C) (2016) 632-644.

[29] H. Yazdani Sarvestani, A.H. Akbarzadeh, H. Niknam, K. Hermenean, 3D printed architected polymeric sandwich panels: Energy absorption and structural performance, Composite Structures 200 (2018) 886-909.

[30] W. Jiang, S.T. Tu, G.C. Li, J.M. Gong, Residual stress and plastic strain analysis in the brazed joint of bonded compliant seal design in planar solid oxide fuel cell, Journal of Power Sources 195(11) (2010) 3513-3522.

[31] A. Francavilla, C.V. Ramakrishnan, O.C. Zienkiewicz, Optimization of shape to minimize stress concentration, Journal of Strain Analysis 10(2) (1975) 63-70.

[32] P. Minetola, F. Calignano, M. Galati, Comparing geometric tolerance capabilities of additive manufacturing systems for polymers, Additive Manufacturing (2020) 101103.

[33] L. Rebaioli, I. Fassi, A review on benchmark artifacts for evaluating the geometrical performance of additive manufacturing processes, The International Journal of Advanced Manufacturing Technology 93(5) (2017) 2571-2598.

[34] N. Béraud, F. Vignat, F. Villeneuve, R. Dendievel, New Trajectories in Electron Beam Melting Manufacturing to Reduce Curling Effect, Procedia CIRP 17 (2014) 738-743.

[35] D. Melancon, Z.S. Bagheri, R.B. Johnston, L. Liu, M. Tanzer, D. Pasini, Mechanical characterization of structurally porous biomaterials built via additive manufacturing: experiments, predictive models, and design maps for load-bearing bone replacement implants, Acta Biomaterialia 63 (2017) 350-368.

[36] W. Zha, S. Anand, Geometric approaches to input file modification for part quality improvement in additive manufacturing, Journal of Manufacturing Processes 20 (2015) 465-477.

[37] S. Arabnejad, R. Burnett Johnston, J.A. Pura, B. Singh, M. Tanzer, D. Pasini, High-strength porous biomaterials for bone replacement: A strategy to assess the interplay between cell morphology, mechanical properties, bone ingrowth and manufacturing constraints, Acta Biomaterialia 30 (2016) 345-356.

[38] H. Gong, K. Rafi, H. Gu, T. Starr, B. Stucker, Analysis of defect generation in Ti–6Al–4V parts made using powder bed fusion additive manufacturing processes, Additive Manufacturing 1-4 (2014) 87-98.

[39] F. Mezzadri, V. Bouriakov, X. Qian, Topology optimization of self-supporting support structures for additive manufacturing, Additive Manufacturing 21 (2018) 666-682.

[40] I. Maskery, N.T. Aboulkhair, A.O. Aremu, C.J. Tuck, I.A. Ashcroft, Compressive failure modes and energy absorption in additively manufactured double gyroid lattices, Additive Manufacturing 16 (2017) 24-29.

[41] L. Zhang, S. Feih, S. Daynes, S. Chang, M.Y. Wang, J. Wei, W.F. Lu, Energy absorption characteristics of metallic triply periodic minimal surface sheet structures under compressive loading, Additive Manufacturing 23 (2018) 505-515.

[42] H. Yazdani Sarvestani, A.H. Akbarzadeh, A. Mirbolghasemi, K. Hermenean, 3D printed meta-sandwich structures: Failure mechanism, energy absorption and multi-hit capability, Materials & Design 160 (2018) 179-193.

[43] A. Gross, P. Pantidis, K. Bertoldi, S. Gerasimidis, Correlation between topology and elastic properties of imperfect truss-lattice materials, Journal of the Mechanics and Physics of Solids 124 (2019) 577-598.

[44] J.B. Berger, H.N.G. Wadley, R.M. McMeeking, Mechanical metamaterials at the theoretical limit of isotropic elastic stiffness, Nature 543 (2017) 533.

[45] M.-S. Pham, C. Liu, I. Todd, J. Lertthanasarn, Damage-tolerant architected materials inspired by crystal microstructure, Nature 565(7739) (2019) 305-311.

[46] Y. He, L. Zhou, J. Zhan, Q. Gao, J. Fu, C. Xie, H. Zhao, Y. Liu, Three-Dimensional Coprinting of Liquid Metals for Directly Fabricating Stretchable Electronics, 3D Printing and Additive Manufacturing 5(3) (2018) 195-203.

[47] S. Kee, M.A. Haque, D. Corzo, H.N. Alshareef, D. Baran, Self-Healing and Stretchable 3D-Printed Organic Thermoelectrics, Advanced Functional Materials 29(51) (2019) 1905426.

[48] X. Kuang, K. Chen, C.K. Dunn, J. Wu, V.C.F. Li, H.J. Qi, 3D Printing of Highly Stretchable, Shape-Memory, and Self-Healing Elastomer toward Novel 4D Printing, ACS Applied Materials & Interfaces 10(8) (2018) 7381-7388.

[49] P.H. Thornton, C.L. Magee, The Deformation of aluminum foams, Metallurgical Transactions A 6(6) (1975) 1253-1263.

[50] M. Mukherjee, U. Ramamurty, F. Garcia-Moreno, J. Banhart, The effect of cooling rate on the structure and properties of closed-cell aluminium foams, Acta Materialia 58(15) (2010) 5031-5042.

[51] A.C. Kaya, P. Zaslansky, M. Ipekoglu, C. Fleck, Strain hardening reduces energy absorption efficiency of austenitic stainless steel foams while porosity does not, Materials & Design 143 (2018) 297-308.

[52] L.J. Gibson, M.F. Ashby, Cellular Solids: Structure and Properties, Cambridge University Press1999.

8 Chapter Eight: General Conclusions

Cellular materials have already been developed for decades, and they have been employed in many applications. Still, their underlying architectures have been merely evolved and optimized until recent years, and by the emergence of advanced manufacturing technologies. Honeycombs and several other simple cubic topologies constituted a vast majority of lattice materials for various applications from sandwich structures to shock absorbers. Nonetheless, novel manufacturing technologies have created exciting opportunities for engineers and architects to propose innovative designs and to improve the functionality of the structural elements. Most of these novel designs are found based on complex and optimized geometries as an RVE of periodic lattice materials. However, in this dissertation, we not only study designing the underlying architecture of lattice materials but also, we propose the idea of the rational variation of the properties across the cellular structure to optimize the functionalities of lightweight structures further.

Three main approaches have been employed to study the behavior of cellular materials in this research; homogenized modeling, detailed finite element modeling, and experimentation. Various sources can be mentioned for the deviations between the results of these approaches. First, one of the assumptions of the homogenization theory is that the lattice material is periodic; however, in graded structures, this assumption is not always valid. Second, the boundary conditions modeled in the detailed finite element modeling and homogenized modeling is not perfectly similar to that of experiments. Third, the fabricated samples may consist of imperfections and defects that influence the experimental results. However, generally, the results of these methods are in an acceptable agreement and their differences are less than 15 percent in these three approaches.

Generally, our findings show that architecting the underlying structure of cellular materials is a powerful tool to engineer and to program the mechanical response of the whole structure. Through rational design, we can increase the stiffness, stretchability, flexural rigidity, buckling load, energy absorption, and strength of a cellular solid. The following statements can be used as a guideline for selecting the proper variation of relative density in graded cellular structures:

- A symmetric distribution of relative density along the length (and width) of the beam (or plate) with maximum relative density in the middle will increase the in-plane stiffness and flexural rigidity.
- A symmetric distribution of relative density across the thickness of the beam (or plate) with minimum relative density in the middle will increase the in-plane stiffness and flexural rigidity.
- The variation of the relative density across the thickness is more effective than in-plane direction for enhancing the flexural rigidity.
- Varying the relative density in the normal-to-force direction is more effective in increasing buckling load and energy absorption capability.
- The computational time of optimization algorithms that find the most desirable relative density distribution function for enhancing the flexural properties of lattice structures can be significantly reduced using a pre-defined bilinear function for relative density variation.
- Accordion-like architected lattice structures can replace the conventional design of lattices to significantly enhance the stretchability of lightweight materials and structures.

The abovementioned findings can help designers to choose the appropriate variation of relative density in lattice structures depending on the application where cellular solids are used. Below, we discuss examples of industries that can benefit from the graded cellular structures:

Automotive and Aircraft: The body of aircrafts and bumpers in automobiles consists of cellular materials whose functions are to maintain the structural integrity and damp the external loads and forces applied to these systems. If we replace these cellular materials with rationally designed graded cellular structures, we can enhance significantly reduce their weight while the functionality remains unchanged.

Construction: Beams and plates are the most fundamental elements in different construction structures; such as buildings and bridges. The strategy that we put forward can increase the efficiency of beams and plates used in these structures by increasing their stiffness and strength to weight ratio.

Energy: Energy industry can benefit from the proposed strategy in different ways. First, reducing the weight of vehicle leads to the reduction of fuel consumption. Also, the rational design of mechanical elements used in energy-generating turbomachines can increase the efficiency of energy-generating turbomachineries. For instance, tuning the deformation behavior of turbine parts subjected to thermal loading can effectively reduce their erosion and corrosion.

8.1 Future directions

Most of the early applications of cellular solids have begun with exploiting their mechanical properties. From a solid mechanics perspective, the design of cellular materials has been substantially advanced over the last few decades, and more efficient structures were proposed and

fabricated. In this dissertation, we also focused on the further development of cellular solids in the same aspect; however, the proposed strategy is yet to be explored from different aspects. Some suggestions for future research on graded cellular structures for improving mechanical and multiphysics properties are as followed:

8.1.1 Mechanical aspect

In addition to the studies conducted in this dissertation, further research can concentrate on the following subjects:

- Analytical modeling to predict the deformation sequence in cellular structures experiencing large deformation
- Architecting the deformed configuration of cellular structure to tune the stress-strain curve
- Effect of variation of cell topology across the structure on the quasi-static and dynamic responses of cellular structure
- Tuning the yield and fracture strength of cellular material by applying

8.1.2 Multiphysical aspect

Cellular solids have also shown potential in physics other than mechanical. As discussed in **Chapter 1**, they are being utilized for their thermal, electrical, and acoustic properties. Combining these functionalities can also lead cellular structures with unprecedented capabilities and potentials. We tried to draw the curtain on one of these functionalities by studying the thermo-mechanical bending of graded cellular beams in **Chapter 4**. However, a few other exciting topics are suggested for future works on this aspect of cellular solids:

- Architected graded lattice for tuning the thermal stresses and deformations
- Architected graded foam for the efficient insulation of thermal energy
- Architected lattice structures for minimizing thermal stress in the cellular sandwich panels subjected to thermal loads
- Designing a cellular membrane as an active piezoelectric filter that can be actuated and tuned by electric power

Bibliography

Ahmed, M., Meade, O., Medina, M.A., 2010. Reducing heat transfer across the insulated walls of refrigerated truck trailers by the application of phase change materials. Energy Conversion and Management 51, 383-392.

Ajdari, A., Canavan, P., Nayeb-Hashemi, H., Warner, G., 2009. Mechanical properties of functionally graded 2-D cellular structures: A finite element simulation. Materials Science and Engineering: A 499, 434-439.

Ajdari, A., Nayeb-Hashemi, H., Vaziri, A., 2011. Dynamic crushing and energy absorption of regular, irregular and functionally graded cellular structures. International Journal of Solids and Structures 48, 506-516.

Akbarzadeh, A., Abedini, A., Chen, Z., 2015a. Effect of micromechanical models on structural responses of functionally graded plates. Composite Structures 119, 598-609.

Akbarzadeh, A., Fu, J., Liu, L., Chen, Z., Pasini, D., 2016a. Electrically conducting sandwich cylinder with a planar lattice core under prescribed eigenstrain and magnetic field. Composite Structures 153, 632-644.

Akbarzadeh, A.H., Abedini, A., Chen, Z.T., 2015b. Effect of micromechanical models on structural responses of functionally graded plates. Composite Structures 119, 598-609.

Akbarzadeh, A.H., Arian Nik, M., Pasini, D., 2016b. Vibration responses and suppression of variable stiffness laminates with optimally steered fibers and magnetostrictive layers. Composites Part B: Engineering 91, 315-326.

Akbarzadeh, A.H., Fu, J.W., Chen, Z.T., Qian, L.F., 2014. Dynamic eigenstrain behavior of magnetoelastic functionally graded cellular cylinders. Composite Structures 116, 404-413.

Akbarzadeh, A.H., Fu, J.W., Liu, L., Chen, Z.T., Pasini, D., 2016c. Electrically conducting sandwich cylinder with a planar lattice core under prescribed eigenstrain and magnetic field. Composite Structures 153, 632-644.

Akbarzadeh, A.H., Fu, J.W., Liu, L., Chen, Z.T., Pasini, D., 2016d. Electrically conducting sandwich cylinder with a planar lattice core under prescribed eigenstrain and magnetic field. Composite Structures 153, 632-644.

Aktay, L., Johnson, A.F., Kröplin, B.-H., 2008. Numerical modelling of honeycomb core crush behaviour. Engineering Fracture Mechanics 75, 2616-2630.

Alcheikh, N., Shaikh, S.F., Hussain, M.M., 2018. Ultra-stretchable Archimedean interconnects for stretchable electronics. Extreme Mechanics Letters 24, 6-13.

Aldousari, S.M., 2017. Bending analysis of different material distributions of functionally graded beam. Applied Physics A 123, 296-296.

Allaire, G., Jouve, F., Toader, A.-M., 2004. Structural optimization using sensitivity analysis and a level-set method. Journal of Computational Physics 194, 363-393.

Allen, H.G., 1969. Chapter 4 - Analysis of sandwich beams and struts by strain energy methods, Analysis and Design of Structural Sandwich Panels. Pergamon, pp. 57-75.

Almutairi, M.M., Osman, M., Tlili, I., 2018. Thermal Behavior of Auxetic Honeycomb Structure: An Experimental and Modeling Investigation. Journal of Energy Resources Technology 140, 122904.

Aly, A.A., 2015. Heat treatment of polymers: a review. International Journal of Materials Chemistry and Physics 1, 132-140.

Aminanda, Y., Castanié, B., Barrau, J.J., Thevenet, P., 2005. Experimental analysis and modeling of the crushing of honeycomb cores. Applied Composite Materials 12, 213-227.

Andrea, V., Damiano, P., 2015. Analysis and design of lattice materials for large cord and curvature variations in skin panels of morphing wings. Smart Materials and Structures 24, 037006.

Andrew, J.J., Ubaid, J., Hafeez, F., Schiffer, A., Kumar, S., 2019. Impact performance enhancement of honeycombs through additive manufacturing-enabled geometrical tailoring. International Journal of Impact Engineering 134, 103360.

Arabnejad Khanoki, S., Pasini, D., 2012. Multiscale Design and Multiobjective Optimization of Orthopedic Hip Implants with Functionally Graded Cellular Material. Journal of Biomechanical Engineering 134, 031004-031004-031010.

Arabnejad, S., Burnett Johnston, R., Pura, J.A., Singh, B., Tanzer, M., Pasini, D., 2016. High-strength porous biomaterials for bone replacement: A strategy to assess the interplay between cell morphology, mechanical properties, bone ingrowth and manufacturing constraints. Acta Biomaterialia 30, 345-356.

Arabnejad, S., Pasini, D., 2013. Mechanical properties of lattice materials via asymptotic homogenization and comparison with alternative homogenization methods. International Journal of Mechanical Sciences 77, 249-262.

Araki, K., Halloran, J.W.J.J.o.t.A.C.S., 2005. Porous ceramic bodies with interconnected pore channels by a novel freeze casting technique. 88, 1108-1114.

Arias Herrera, A.M., 2014. Development of Natural Fiber Reinforced Polylactide-Based Biocomposites. 64.

Ashby, M.F., Evans, T., Fleck, N.A., Hutchinson, J., Wadley, H., Gibson, L., 2000. Metal foams: a design guide. Elsevier.

Avalle, M., Belingardi, G., Montanini, R., 2001. Characterization of polymeric structural foams under compressive impact loading by means of energy-absorption diagram. International Journal of Impact Engineering 25, 455-472.

Aydogdu, M., 2009. A new shear deformation theory for laminated composite plates. Composite Structures 89, 94-101.

Aydogdu, M., Taskin, V., 2007. Free vibration analysis of functionally graded beams with simply supported edges. Materials & Design 28, 1651-1656.

Babaee, S., Shim, J., Weaver, J.C., Chen, E.R., Patel, N., Bertoldi, K., 2013. 3D Soft Metamaterials with Negative Poisson's Ratio. Advanced Materials 25, 5044-5049.

Bagal, A., Dandley, E.C., Zhao, J., Zhang, X.A., Oldham, C.J., Parsons, G.N., Chang, C.-H., 2015. Multifunctional nano-accordion structures for stretchable transparent conductors. Materials Horizons 2, 486-494.

Bandaru, P., Vemuri, K., Canbazoglu, F., Kapadia, R., 2015. Layered thermal metamaterials for the directing and harvesting of conductive heat. AIP Advances 5, 053403.

Batra, R.C., 2007. Higher-order shear and normal deformable theory for functionally graded incompressible linear elastic plates. Thin-Walled Structures 45, 974-982.

Bendsøe, M.P., 1989. Optimal shape design as a material distribution problem. Structural Optimization 1 1, 193-202.

Bendsøe, M.P., Kikuchi, N., 1988. Generating optimal topologies in structural design using a homogenization method. Computer Methods in Applied Mechanics and Engineering 71, 197-224.

Bendsøe, M.P., Sigmund, O., 1999. Material interpolation schemes in topology optimization. Archive of Applied Mechanics (Ingenieur Archiv) 69, 635-654.

Béraud, N., Vignat, F., Villeneuve, F., Dendievel, R., 2014. New Trajectories in Electron Beam Melting Manufacturing to Reduce Curling Effect. Procedia CIRP 17, 738-743.

Berg, C.A., Tirosh, J., Israeli, M., 1972. Analysis of Short Beam Bending of Fiber Reinforced Composites, in: Corten, H.T. (Ed.). ASTM International, West Conshohocken, PA, pp. 206-218.

Berger, J.B., Wadley, H.N.G., McMeeking, R.M., 2017a. Mechanical metamaterials at the theoretical limit of isotropic elastic stiffness.

Bergman, T.L., Incropera, F.P., Lavine, A.S., Dewitt, D.P., 2011. Introduction to heat transfer. John Wiley & Sons.

Bertoldi, K., Boyce, M.C., 2008a. Mechanically triggered transformations of phononic band gaps in periodic elastomeric structures. Physical Review B 77, 052105-052105.

Bertoldi, K., Boyce, M.C., 2008b. Wave propagation and instabilities in monolithic and periodically structured elastomeric materials undergoing large deformations. Physical Review B 78, 184107.

Bertoldi, K., Boyce, M.C., Deschanel, S., Prange, S.M., Mullin, T., 2008. Mechanics of deformation-triggered pattern transformations and superelastic behavior in periodic elastomeric structures. Journal of the Mechanics and Physics of Solids 56, 2642-2668.

Bertoldi, K., Reis, P.M., Willshaw, S., Mullin, T., 2010. Negative Poisson's Ratio Behavior Induced by an Elastic Instability. Advanced Materials 22, 361-366.

Bezazi, A., Remillat, C., Innocenti, P., Scarpa, F., 2008. In-plane mechanical and thermal conductivity properties of a rectangular–hexagonal honeycomb structure. Composite Structures 84, 248-255.

Bi, S., Chen, E., Gaitanaros, S., 2020. Additive manufacturing and characterization of brittle foams. Mechanics of Materials 145, 103368.

Bikas, H., Stavropoulos, P., Chryssolouris, G., 2016. Additive manufacturing methods and modelling approaches: a critical review. The International Journal of Advanced Manufacturing Technology 83, 389-405.

Birtel, V., Mark, P., 2006. Parameterised finite element modelling of RC beam shear failure, ABAQUS users' conference, pp. 95-108.

Bitzer, T., 1997. Honeycomb core, in: Bitzer, T. (Ed.), Honeycomb Technology: Materials, Design, Manufacturing, Applications and Testing. Springer Netherlands, Dordrecht, pp. 10-42.

Boldrin, L., Hummel, S., Scarpa, F., Di Maio, D., Lira, C., Ruzzene, M., Remillat, C.D.L., Lim, T.C., Rajasekaran, R., Patsias, S., 2016. Dynamic behaviour of auxetic gradient composite hexagonal honeycombs. Composite Structures 149, 114-124.

Bonatti, C., Mohr, D., 2019a. Mechanical performance of additively-manufactured anisotropic and isotropic smooth shell-lattice materials: Simulations & experiments. Journal of the Mechanics and Physics of Solids 122, 1-26.

Bonatti, C., Mohr, D., 2019b. Smooth-shell metamaterials of cubic symmetry: Anisotropic elasticity, yield strength and specific energy absorption. Acta Materialia 164, 301-321.

Borovinšek, M., Vesenjak, M., Matela, J., Ren, Z., 2008. Computational reconstruction of scanned aluminum foams for virtual testing. Serbian Society of Computational Mechanics 2, 16-28.

Brischetto, S., Leetsch, R., Carrera, E., Wallmersperger, T., Kröplin, B., 2008. Thermo-Mechanical Bending of Functionally Graded Plates. Journal of Thermal Stresses 31, 286-308.

Buannic, N., Cartraud, P., 2001. Higher-order effective modeling of periodic heterogeneous beams. I. Asymptotic expansion method. International Journal of Solids and Structures 38, 7139-7161.

Bubert, E.A., Woods, B.K.S., Lee, K., Kothera, C.S., Wereley, N.M., 2010. Design and Fabrication of a Passive 1D Morphing Aircraft Skin. Journal of Intelligent Material Systems and Structures 21, 1699-1717.

Buitrago, B.L., Santiuste, C., Sánchez-Sáez, S., Barbero, E., Navarro, C., 2010. Modelling of composite sandwich structures with honeycomb core subjected to high-velocity impact. Composite Structures 92, 2090-2096.

Burton, H.E., Eisenstein, N.M., Lawless, B.M., Jamshidi, P., Segarra, M.A., Addison, O., Shepherd, D.E.T., Attallah, M.M., Grover, L.M., Cox, S.C., 2019. The design of additively manufactured lattices to increase the functionality of medical implants. Materials Science and Engineering: C 94, 901-908.

Burton, W., Noor, A., 1997. Assessment of continuum models for sandwich panel honeycomb cores. Computer methods in applied mechanics and engineering 145, 341-360.

Carbajal, G., Sobhan, C.B., Peterson, G.P., Queheillalt, D.T., Wadley, H.N.G., 2006. Thermal response of a flat heat pipe sandwich structure to a localized heat flux. International Journal of Heat and Mass Transfer 49, 4070-4081.

Carr, J.B., 2016. The Effect of Shear Flexibility and Rotatory Inertia on the Natural Frequencies of Uniform Beams. Aeronautical Quarterly 21, 79-90.

Carter, C.B., Norton, M.G., 2007. Ceramic materials: science and engineering. Springer.

Chen, D., Yang, J., Kitipornchai, S., 2015. Elastic buckling and static bending of shear deformable functionally graded porous beam. Composite Structures 133, 54-61.

Chen, F., Lei, D.Y., 2015. Experimental realization of extreme heat flux concentration with easy-to-make thermal metamaterials. Scientific reports 5, 11552.

Chen, K.L., Cao, Y.P., Zhang, M.G., Feng, X.Q., 2014. Indentation-triggered pattern transformation in hyperelastic soft cellular solids. Comptes Rendus - Mecanique 342, 292-298.

Cheng, L., Liu, J., Liang, X., To, A.C., 2018. Coupling lattice structure topology optimization with design-dependent feature evolution for additive manufactured heat conduction design. Computer Methods in Applied Mechanics and Engineering 332, 408-439.

Cheng, L., Zhang, P., Biyikli, E., Bai, J., Robbins, J., To, A., 2017. Efficient design optimization of variable-density cellular structures for additive manufacturing: theory and experimental validation. Rapid Prototyping Journal 23, 660-677.

Chung, J., Waas, A.M., 2002a. Compressive Response of Honeycombs Under In-Plane Uniaxial Static and Dynamic Loading, Part 1: Experiments. AIAA Journal 40, 966-973.

Chung, J., Waas, a.M., 2002b. Compressive response of honeycombs under in-plane uniaxial static and dynamic loading. II - Simulations. AIAA Journal 40, 974-980.

Compton, B.G., Lewis, J.A., 2014. 3D-Printing of Lightweight Cellular Composites. Advanced Materials 26, 5930-5935.

Coulais, C., Overvelde, J.T.B., Lubbers, L.A., Bertoldi, K., van Hecke, M., 2015. Discontinuous Buckling of Wide Beams and Metabeams. Physical Review Letters 115, 044301.

Cui, L., Kiernan, S., Gilchrist, M.D., 2009. Designing the energy absorption capacity of functionally graded foam materials. Materials Science and Engineering: A 507, 215-225.

Dabo, M., Roland, T., Dalongeville, G., Gauthier, C., Kékicheff, P., 2019. Ad-hoc modeling of closed-cell foam microstructures for structure-properties relationships. European Journal of Mechanics - A/Solids 75, 128-141.

Dai, G., Zhang, W., 2009. Cell size effects for vibration analysis and design of sandwich beams. Acta Mechanica Sinica 25, 353-365.

Dai, G.M., Zhang, W.H., 2008. Size effects of basic cell in static analysis of sandwich beams. International Journal of Solids and Structures 45, 2512-2533.

Daniel, I.M., Ishai, O., Daniel, I.M., Daniel, I., 1994. Engineering mechanics of composite materials. Oxford university press New York.

Dell'Isola, F., Giorgio, I., Pawlikowski, M., Rizzi, N.L., 2016, Large deformations of planar extensible beams and pantographic lattices: heuristic homogenization, experimental and numerical examples

Deng, Q.-T., Yang, Z.-C., 2016. Effect of poisson's ratio on functionally graded cellular structures. Materials Express 6, 461-472.

Deshpande, V.S., Fleck, N.A., 2001. Collapse of truss core sandwich beams in 3-point bending. International Journal of Solids and Structures 38, 6275-6305.

Deshpande, V.S., Fleck, N.A., Ashby, M.F., 2001. Effective properties of the octet-truss lattice material. Journal of the Mechanics and Physics of Solids 49, 1747-1769.

Dharmasena, K.P., Wadley, H.N.G., Xue, Z., Hutchinson, J.W., 2008. Mechanical response of metallic honeycomb sandwich panel structures to high-intensity dynamic loading. International Journal of Impact Engineering 35, 1063-1074.

Dizon, J.R.C., Espera, A.H., Chen, Q., Advincula, R.C., 2018. Mechanical characterization of 3D-printed polymers. Additive Manufacturing 20, 44-67.

Draiche, K., Bousahla, A.A., Tounsi, A., Alwabli, A.S., Tounsi, A., Mahmoud, S., 2019. Static analysis of laminated reinforced composite plates using a simple first-order shear deformation theory. Computers and Concrete 24, 369-378.

El Nady, K., Dos Reis, F., Ganghoffer, J.F., 2017, Computation of the homogenized nonlinear elastic response of 2D and 3D auxetic structures based on micropolar continuum models, Composite Structures 170 271-290.

Evans, A.G., He, M., Deshpande, V.S., Hutchinson, J.W., Jacobsen, A.J., Carter, W.B., 2010a. Concepts for enhanced energy absorption using hollow micro-lattices. International Journal of Impact Engineering 37, 947-959.

Evans, A.G., Hutchinson, J.W., Fleck, N.A., Ashby, M.F., Wadley, H.N.G., 2001. The topological design of multifunctional cellular metals. Progress in Materials Science 46, 309-327.

Evans, K.E., 1991. The design of doubly curved sandwich panels with honeycomb cores. Composite Structures 17, 95-111.

Evans, K.E., Alderson, A., 2000. Auxetic materials: functional materials and structures from lateral thinking! Advanced materials 12, 617-628.

Fan, H., Fang, D., Chen, L., Dai, Z., Yang, W., 2009. Manufacturing and testing of a CFRC sandwich cylinder with Kagome cores. Composites Science and Technology 69, 2695-2700.

Fan, H.L., Fang, D.N., Jing, F.N., 2008a. Yield surfaces and micro-failure mechanism of block lattice truss materials. Materials & Design 29, 2038-2042.

Fan, H.L., Fang, D.N., Jing, F.N., 2008b. Yield surfaces and micro-failure mechanism of block lattice truss materials. Materials and Design 29, 2038-2042.

Feng, J., Fu, J., Shang, C., Lin, Z., Li, B., 2019. Sandwich panel design and performance optimization based on triply periodic minimal surfaces. Computer-Aided Design 115, 307-322.

Fleck, N., Deshpande, V., Ashby, M., 2010a. Micro-architectured materials: past, present and future, Proceedings of the Royal Society of London A: Mathematical, Physical and Engineering Sciences. The Royal Society, pp. 2495-2516.

Fleck, N.A., Deshpande, V.S., Ashby, M.F., 2010b. Micro-architectured materials: past, present and future. Proceedings of the Royal Society A: Mathematical, Physical and Engineering Sciences 466, 2495-2516.

Florijn, B., Coulais, C., Van Hecke, M., 2014. Programmable mechanical metamaterials. Physical Review Letters 113, 1-5.

Florijn, B., Coulais, C., van Hecke, M., 2016. Programmable mechanical metamaterials: the role of geometry. Soft Matter 12, 8736-8743.

Francavilla, A., Ramakrishnan, C.V., Zienkiewicz, O.C., 1975. Optimization of shape to minimize stress concentration. Journal of Strain Analysis 10, 63-70.

Francesconi, L., Baldi, A., Liang, X., Aymerich, F., Taylor, M., 2019. Variable Poisson's ratio materials for globally stable static and dynamic compression resistance. Extreme Mechanics Letters 26, 1-7.

Friedl, O., Motz, C., Peterlik, H., Puchegger, S., Reger, N., Pippan, R.J.M., B, M.T., 2008. Experimental investigation of mechanical properties of metallic hollow sphere structures. 39, 135-146.

Gandhi, F., Kang, S.-G., 2007. Beams with controllable flexural stiffness. Smart Materials and Structures 16, 1179-1184.

Gauthier, M.M., 1995. Engineered materials handbook. ASM International.

Gent, A.N., 2012. Elasticity, Engineering with Rubber (Third Edition). Hanser, pp. 37-88.

Gere, J.M., Timoshenko, S., 2001. Mechanics of Materials, ; Brooks. Cole, Pacific Grove, CA, 815-839.

Ghugal, Y.M., Shimpi, R.P., 2001. A Review of Refined Shear Deformation Theories for Isotropic and Anisotropic Laminated Beams. Journal of Reinforced Plastics and Composites 20, 255-272.

Gibson, L.J., 2005. Biomechanics of cellular solids. Journal of Biomechanics 38, 377-399.

Gibson, L.J., Ashby, M.F., 1999. Cellular solids: structure and properties. Cambridge university press.

Gibson, L.J.A.M.F., Triantafillou, T.C., 1989. Failure surfaces for cellular materials under multixial loads - I. Modelling. Int. J. Mech. Sci. 31, 635-663.

Giunta, G., Biscani, F., Belouettar, S., Ferreira, A.J.M., Carrera, E., 2013. Free vibration analysis of composite beams via refined theories. Composites Part B: Engineering 44, 540-552.

Gong, H., Rafi, K., Gu, H., Starr, T., Stucker, B., 2014. Analysis of defect generation in Ti–6Al–4V parts made using powder bed fusion additive manufacturing processes. Additive Manufacturing 1-4, 87-98.

Grenestedt, J.L., 1999. Effective elastic behavior of some models for perfect cellular solids. International Journal of Solids and Structures 36, 1471-1501.

Gridgeman, N.T., 1970. Lamé ovals. The Mathematical Gazette, 31-37.

Grima, J.N., Farrugia, P.S., Gatt, R., Zammit, V., 2007. A system with adjustable positive or negative thermal expansion. Proceedings of the Royal Society A: Mathematical, Physical and Engineering Science 463, 1585.

Groen, J.P., Langelaar, M., Sigmund, O., Ruess, M., 2017. Higher-order multi-resolution topology optimization using the finite cell method. International Journal for Numerical Methods in Engineering 110, 903-920.

Gross, A., Pantidis, P., Bertoldi, K., Gerasimidis, S., 2019. Correlation between topology and elastic properties of imperfect truss-lattice materials. Journal of the Mechanics and Physics of Solids 124, 577-598.

Guo, S.-Z., Gosselin, F., Guerin, N., Lanouette, A.-M., Heuzey, M.-C., Therriault, D., 2013. 3D Printing: Solvent-Cast Three-Dimensional Printing of Multifunctional Microsystems (Small 24/2013). Small 9, 4090-4090.

Guo, X.E., Gibson, L.J., McMahon, T.A., Hayes, W.C., 1999. Post Yield Behaviour of Intact and Damaged Honeycombs: A Finite Element Study. 41, 85-105.

Ha, C.S., Lakes, R.S., Plesha, M.E., 2018. Design, fabrication, and analysis of lattice exhibiting energy absorption via snap-through behavior. Materials & Design 141, 426-437.

Habib, F.N., Iovenitti, P., Masood, S.H., Nikzad, M., 2018. Fabrication of polymeric lattice structures for optimum energy absorption using Multi Jet Fusion technology. Materials & Design 155, 86-98.

Haghpanah, B., Papadopoulos, J., Mousanezhad, D., Nayeb-Hashemi, H., Vaziri, A., 2014. Buckling of regular, chiral and hierarchical honeycombs under a general macroscopic stress state. Proceedings of the Royal Society A: Mathematical, Physical and Engineering Sciences 470, 20130856-20130856.

Han, S.C., Lee, J.W., Kang, K., 2015. A New Type of Low Density Material: Shellular. Advanced Materials 27, 5506-5511.

Hassan, M.R., Scarpa, F., Mohamed, N.A., 2009. In-plane Tensile Behavior of Shape Memory Alloy Honeycombs with Positive and Negative Poisson's Ratio. Journal of Intelligent Material Systems and Structures 20, 897-905.

Hassani, B., Hinton, E., 1998a. A review of homogenization and topology opimization II—analytical and numerical solution of homogenization equations. Computers & structures 69, 719-738.

Hassani, B., Hinton, E., 1998b. A review of homogenization and topology optimization I—homogenization theory for media with periodic structure. Computers & Structures 69, 707-717.

Hassani, B., Hinton, E., 1998c. A review of homogenization and topology optimization III—topology optimization using optimality criteria. Computers & Structures 69, 739-756.

He, Y., Guo, S., Liu, Z., Liew, K.M., 2015. Pattern transformation of thermo-responsive shape memory polymer periodic cellular structures. International Journal of Solids and Structures 71, 194-205.

He, Y., Zhou, L., Zhan, J., Gao, Q., Fu, J., Xie, C., Zhao, H., Liu, Y., 2018. Three-Dimensional Coprinting of Liquid Metals for Directly Fabricating Stretchable Electronics. 3D Printing and Additive Manufacturing 5, 195-203.

He, Y., Zhou, Y., Liu, Z., Liew, K.M., 2017. Pattern transformation of single-material and composite periodic cellular structures. Materials & Design 132, 375-384.

Hollister, S.J., Fyhrie, D.P., Jepsen, K.J., Goldstein, S.A., 1991. Application of homogenization theory to the study of trabecular bone mechanics. Journal of Biomechanics 24, 825-839.

Hollister, S.J., Kikuchi, N., 1992. A comparison of homogenization and standard mechanics analyses for periodic porous composites. Computational Mechanics 10, 73-95.

Hou, Y., Tai, Y.H., Lira, C., Scarpa, F., Yates, J.R., Gu, B., 2013. The bending and failure of sandwich structures with auxetic gradient cellular cores. Composites Part A: Applied Science and Manufacturing 49, 119-131.

Hu, J., He, Y., Lei, J., Liu, Z., 2013. Novel mechanical behavior of periodic structure with the pattern transformation. Theoretical and Applied Mechanics Letters 3, 054007-054007.

Hu, K., Lin, K., Gu, D., Yang, J., Wang, H., Yuan, L., 2019. Mechanical properties and deformation behavior under compressive loading of selective laser melting processed bio-inspired sandwich structures. Materials Science and Engineering: A 762, 138089.

Huang, J., Gong, X., Zhang, Q., Scarpa, F., Liu, Y., Leng, J., 2016. In-plane mechanics of a novel zero Poisson's ratio honeycomb core. Composites Part B: Engineering 89, 67-76.

Huang, J., Zhang, Q., Scarpa, F., Liu, Y., Leng, J., 2017. In-plane elasticity of a novel auxetic honeycomb design. Composites Part B: Engineering 110, 72-82.

Huang, M., Rahbar, N., Wang, R., Thompson, V., Rekow, D., Soboyejo, W.O., 2007. Bioinspired design of dental multilayers. Materials Science and Engineering: A 464, 315-320.

Hundley, J.M., Clough, E.C., Jacobsen, A.J., 2015. The low velocity impact response of sandwich panels with lattice core reinforcement. International Journal of Impact Engineering 84, 64-77.

Hutchinson, J., 2001. Shear coefficients for Timoshenko beam theory. Journal of Applied Mechanics 68, 87-92.

Ikeda, T., Nakajima, H., Aoki, T.J.M., A, M.T., 2005. Fabrication of lotus-type porous stainless steel by continuous zone melting technique and mechanical property. 36, 77-86.

Imbeni, V., Kruzic, J.J., Marshall, G.W., Marshall, S.J., Ritchie, R.O., 2005. The dentin-enamel junction and the fracture of human teeth. Nat Mater 4, 229-232.

Ingrole, A., Hao, A., Liang, R., 2017. Design and modeling of auxetic and hybrid honeycomb structures for in-plane property enhancement. Materials & Design 117, 72-83.

Innocenti, P., Scarpa, F., 2009. Thermal conductivity properties and heat transfer analysis of Multi-re-entrant auxetic honeycomb structures. Journal of Composite Materials 43, 2419-2439.

Jaeung Chung, A.M.W., 2001. In-plane biaxial crush response of polycarbonate honeycombs. 127, 180-193.

Jakubinek, M., Roy, S., Palardy-Sim, M., Ashrafi, B., Shadmehri, F., Renaud, G., Barnes, M., Martinez-Rubi, Y., Rahmat, M., Simard, B., Yousefpour, A., Fortin, F., 2019. Stretchable Structure for a Benchtop-Scale Morphed Leading Edge Demonstration, AIAA Scitech 2019 Forum. American Institute of Aeronautics and Astronautics.

Janbaz, S., Weinans, H., Zadpoor, A.A., 2016. Geometry-based control of instability patterns in cellular soft matter. RSC Advances 6, 20431-20436.

Jeon, N.J., Noh, J.H., Yang, W.S., Kim, Y.C., Ryu, S., Seo, J., Seok, S.I., 2015. Compositional engineering of perovskite materials for high-performance solar cells. Nature 517, 476.

Jha, D.K., Kant, T., Singh, R.K., 2013. A critical review of recent research on functionally graded plates. Composite Structures 96, 833-849.

Jhaver, R., Tippur, H., 2009. Processing, compression response and finite element modeling of syntactic foam based interpenetrating phase composite (IPC). Materials Science and Engineering: A 499, 507-517.

Ji, S., Hyun, B.G., Kim, K., Lee, S.Y., Kim, S.-H., Kim, J.-Y., Song, M.H., Park, J.-U., 2016. Photo-patternable and transparent films using cellulose nanofibers for stretchable origami electronics. Npg Asia Materials 8, e299.

Jia, Z., Wang, L., 2019. 3D printing of biomimetic composites with improved fracture toughness. Acta Materialia 173, 61-73.

Jia, Z., Yu, Y., Hou, S., Wang, L., 2019. Biomimetic architected materials with improved dynamic performance. Journal of the Mechanics and Physics of Solids 125, 178-197.

Jiang, W., Tu, S.T., Li, G.C., Gong, J.M., 2010. Residual stress and plastic strain analysis in the brazed joint of bonded compliant seal design in planar solid oxide fuel cell. Journal of Power Sources 195, 3513-3522.

Jiang, Y., Wang, Q., 2016. Highly-stretchable 3D-architected Mechanical Metamaterials. Scientific Reports 6, 34147.

Jopek, H., Strek, T., 2015. Thermal and structural dependence of auxetic properties of composite materials. physica status solidi (b) 252, 1551-1558.

Kader, M.A., Hazell, P.J., Brown, A.D., Tahtali, M., Ahmed, S., Escobedo, J.P., Saadatfar, M., 2020. Novel design of closed-cell foam structures for property enhancement. Additive Manufacturing 31, 100976.

Kapuria, S., Bhattacharyya, M., Kumar, A., 2008. Bending and free vibration response of layered functionally graded beams: a theoretical model and its experimental validation. Composite Structures 82, 390-402.

Karami, B., Janghorban, M., Tounsi, A., 2019. Galerkin's approach for buckling analysis of functionally graded anisotropic nanoplates/different boundary conditions. Engineering with Computers 35, 1297-1316.

Kaya, A.C., Zaslansky, P., Ipekoglu, M., Fleck, C., 2018. Strain hardening reduces energy absorption efficiency of austenitic stainless steel foams while porosity does not. Materials & Design 143, 297-308.

Kee, S., Haque, M.A., Corzo, D., Alshareef, H.N., Baran, D., 2019. Self-Healing and Stretchable 3D-Printed Organic Thermoelectrics. Advanced Functional Materials 29, 1905426.

Khang, D.-Y., Jiang, H., Huang, Y., Rogers, J.A., 2006. A Stretchable Form of Single-Crystal Silicon for High-Performance Electronics on Rubber Substrates. Science 311, 208.

Kim, B., Christensen, R.M., 2000. Basic two-dimensional core types for sandwich structures. International Journal of Mechanical Sciences 42, 657-676.

Kim, D.-H., Kim, H.-G., Kim, H.-S., 2015. Design optimization and manufacture of hybrid glass/carbon fiber reinforced composite bumper beam for automobile vehicle. Composite Structures 131, 742-752.

Kim, D.H., Lu, N., Ma, R., Kim, Y.-S., Kim, R.H., Wang, S., Wu, J., Won, S.M., Tao, H., Islam, A., Yu, K.J., Kim, T.-i., Chowdhury, R., Ying, M., Xu, L., Li, M., Chung, H.J., Keum, H., McCormick, M., Liu, P., Zhang, Y.-W., Omenetto, F.G., Huang, Y., Coleman, T., Rogers, J.A., 2011. Epidermal Electronics. 333, 838-843.

Koizumi, M., 1997. FGM activities in Japan. Composites Part B: Engineering 28, 1-4.

Kolpakov, A.G., 1991. Calculation of the characteristics of thin elastic rods with a periodic structure. Journal of Applied Mathematics and Mechanics 55, 358-365.

Kolpakov, A.G., 1998. Variational principles for stiffnesses of a non-homogeneous beam. 46, 1039-1053.

Komijani, M., Esfahani, S.E., Reddy, J.N., Liu, Y.P., Eslami, M.R., 2014. Nonlinear thermal stability and vibration of pre/post-buckled temperature- and microstructure-dependent functionally graded beams resting on elastic foundation. Composite Structures 112, 292-307.

Krishnadev, M., Larouche, M., Lakshmanan, V.I., Sridhar, R., 2008. Fracture of high carbon high strength anchor rods. 15, 1009-1018.

Kuang, X., Chen, K., Dunn, C.K., Wu, J., Li, V.C.F., Qi, H.J., 2018. 3D Printing of Highly Stretchable, Shape-Memory, and Self-Healing Elastomer toward Novel 4D Printing. ACS Applied Materials & Interfaces 10, 7381-7388.

Kuku, R., Raji, N., Bello, T., 2012. Development and performance evaluation of sound proof enclosure for portable generators. Research Journal of Applied Sciences 4, 2600-2603.

Kumar, R.S., McDowell, D.L., 2004a. Generalized continuum modeling of 2-D periodic cellular solids. International Journal of Solids and Structures 41, 7399-7422.

Kumar, R.S., McDowell, D.L., 2004b. Rapid Preliminary Design of Rectangular Linear Cellular Alloys for Maximum Heat Transfer. AIAA Journal 42, 1652-1661.

Landel, R.F., Nielsen, L.E., 1993. Mechanical properties of polymers and composites. CRC press.

Lawson, R.M., Lim, J., Hicks, S.J., Simms, W.I., 2006. Design of composite asymmetric cellular beams and beams with large web openings. Journal of Constructional Steel Research 62, 614-629.

Lee, D.-W., Khan, K.A., Abu Al-Rub, R.K., 2017. Stiffness and yield strength of architectured foams based on the Schwarz Primitive triply periodic minimal surface. International Journal of Plasticity 95, 1-20.

Lee, S.-J., Wang, J., Sankar, B.V., 2007. A micromechanical model for predicting the fracture toughness of functionally graded foams. International Journal of Solids and Structures 44, 4053-4067.

Li, T., Chen, Y., Hu, X., Li, Y., Wang, L., 2018. Exploiting negative Poisson's ratio to design 3D-printed composites with enhanced mechanical properties. Materials & Design 142, 247-258.

Li, T., Jiang, Y., Yu, K., Wang, Q., 2017. Stretchable 3D lattice conductors. Soft Matter 13, 7731-7739.

Librescu, L., Song, O., 2005. Thin-walled composite beams: theory and application. Springer Science & Business Media.

Lim, T.-C., 2008. Geometrical Correction to the Elastic Stiffness of Particulate Composites. Journal of Reinforced Plastics and Composites 29, 94-104.

Lim, T.-C., 2013. Negative thermal expansion in transversely isotropic space frame trusses. physica status solidi (b) 250, 2062-2069.

Lim, T.-C., 2015. Thermal stresses in auxetic plates and shells. Mechanics of Advanced Materials and Structures 22, 205-212.

Lim, T.C., 2002a. Functionally graded beam for attaining Poisson-curving. Journal of Materials Science Letters 21, 1899-1901.

Lim, T.C., 2002b. Unified practical bounds for the thermal conductivity of composite materials. Materials Letters 54, 152-157.

Lipomi, D.J., Tee, B.C.K., Vosgueritchian, M., Bao, Z., 2011a. Stretchable Organic Solar Cells. Advanced Materials 23, 1771-1775.

Lipomi, D.J., Vosgueritchian, M., Tee, B.C.K., Hellstrom, S.L., Lee, J.A., Fox, C.H., Bao, Z., 2011b. Skin-like pressure and strain sensors based on transparent elastic films of carbon nanotubes. Nature Nanotechnology 6, 788.

Lira, C., Scarpa, F., 2010. Transverse shear stiffness of thickness gradient honeycombs. Composites Science and Technology 70, 930-936.

Lira, C., Scarpa, F., Rajasekaran, R., 2011. A Gradient Cellular Core for Aeroengine Fan Blades Based on Auxetic Configurations. Journal of Intelligent Material Systems and Structures 22, 907-917.

Liu, D.-P., Chen, P.-J., Huang, H.-H., 2018. Realization of a thermal cloak–concentrator using a metamaterial transformer. Scientific Reports 8, 2493.

Liu, J.X., Deng, S.C., Zhang, J., Liang, N.G., 2007. Lattice type of fracture model for concrete. Theoretical and Applied Fracture Mechanics 48, 269-284.

Liu, Y., Zhang, X.-C., 2009. The influence of cell micro-topology on the in-plane dynamic crushing of honeycombs. International Journal of Impact Engineering 36, 98-109.

Liu, Y.P., Reddy, J.N., 2011. A nonlocal curved beam model based on a modified couple stress theory. International Journal of Structural Stability and Dynamics 11, 495-512.

Loiseau, A., Launois-Bernede, P., Petit, P., Roche, S., Salvetat, J.-P., 2006. Understanding Carbon Nanotubes: From Basics to Applications. Springer.

Lynch, M.E., Mordasky, M., Cheng, L., To, A., 2018. Design, testing, and mechanical behavior of additively manufactured casing with optimized lattice structure. Additive Manufacturing 22, 462-471.

Ma, L., Wang, T., 2003. Nonlinear bending and post-buckling of a functionally graded circular plate under mechanical and thermal loadings. International Journal of Solids and Structures 40, 3311-3330.

Mae, H., Omiya, M., Kishimoto, K., 2008. Effects of strain rate and density on tensile behavior of polypropylene syntactic foam with polymer microballoons. Materials Science and Engineering: A 477, 168-178.

Maldovan, M., Ullal, C.K., Jang, J.H., Thomas, E.L., 2007. Sub-Micrometer Scale Periodic Porous Cellular Structures: Microframes Prepared by Holographic Interference Lithography. Advanced Materials 19, 3809-3813.

Marur, S.R., Kant, T., 1996. Free vibration analysis of fiber reinforced composite beams using higher order theories and finite element modelling. Journal of Sound and Vibration 194, 337-351.

Maskery, I., Aboulkhair, N.T., Aremu, A.O., Tuck, C.J., Ashcroft, I.A., 2017. Compressive failure modes and energy absorption in additively manufactured double gyroid lattices. Additive Manufacturing 16, 24-29.

Maskery, I., Sturm, L., Aremu, A.O., Panesar, A., Williams, C.B., Tuck, C.J., Wildman, R.D., Ashcroft, I.A., Hague, R.J.M., 2018. Insights into the mechanical properties of several triply periodic minimal surface lattice structures made by polymer additive manufacturing. Polymer 152, 62-71.

Masters, I.G., Evans, K.E., 1996. Models for the elastic deformation of honeycombs. Composite Structures 35, 403-422.

Melancon, D., Bagheri, Z.S., Johnston, R.B., Liu, L., Tanzer, M., Pasini, D., 2017. Mechanical characterization of structurally porous biomaterials built via additive manufacturing: experiments, predictive models, and design maps for load-bearing bone replacement implants. Acta Biomaterialia 63, 350-368.

Melchels, F.P.W., Feijen, J., Grijpma, D.W., 2010. A review on stereolithography and its applications in biomedical engineering. Biomaterials 31, 6121-6130.

Mertens, J., Bowman, R.W., Willis, J.C.W., Robinson, A., Cotton, D., White, R., Seffen, K.A., Baumberg, J.J., 2015. Scalable Microaccordion Mesh for Deformable and Stretchable Metallic Films. Physical Review Applied 4, 044006.

Meseguer, J., Pérez-Grande, I., Sanz-Andrés, A., 2012. Spacecraft thermal control. Elsevier.

Meza, L.R., Zelhofer, A.J., Clarke, N., Mateos, A.J., Kochmann, D.M., Greer, J.R., 2015. Resilient 3D hierarchical architected metamaterials. 112, 11502-11507.

Mezzadri, F., Bouriakov, V., Qian, X., 2018. Topology optimization of self-supporting support structures for additive manufacturing. Additive Manufacturing 21, 666-682.

Mills, N.J., Stämpfli, R., Marone, F., Brühwiler, P.A., 2009. Finite element micromechanics model of impact compression of closed-cell polymer foams. International Journal of Solids and Structures 46, 677-697.

Mines, R.A.W., Alias, A., 2002. Numerical simulation of the progressive collapse of polymer composite sandwich beams under static loading. Composites Part A: Applied Science and Manufacturing 33, 11-26.

Mines, R.A.W., Tsopanos, S., Shen, Y., Hasan, R., McKown, S.T., 2013. Drop weight impact behaviour of sandwich panels with metallic micro lattice cores. International Journal of Impact Engineering 60, 120-132.

Minetola, P., Calignano, F., Galati, M., 2020. Comparing geometric tolerance capabilities of additive manufacturing systems for polymers. Additive Manufacturing, 101103.

Mirabolghasemi, A., Akbarzadeh, A.H., Rodrigue, D., Therriault, D., 2019. Thermal Conductivity of Architected Cellular Metamaterials. Acta Materialia.

Miserez, A., Schneberk, T., Sun, C., Zok, F.W., Waite, J.H., 2008. The Transition from Stiff to Compliant Materials in Squid Beaks. Science 319, 1816-1819.

Mohsenizadeh, M., Gasbarri, F., Munther, M., Beheshti, A., Davami, K., 2018. Additively-manufactured lightweight Metamaterials for energy absorption. Materials & Design 139, 521-530.

Morikawa, Y., Yamagiwa, S., Sawahata, H., Ishida, M., Kawano, T., 2016. An origami-inspired ultrastretchable bioprobe film device, 2016 IEEE 29th International Conference on Micro Electro Mechanical Systems (MEMS), pp. 149-152.

Morozov, E.V., Lopatin, A.V., Nesterov, V.A., 2011. Finite-element modelling and buckling analysis of anisogrid composite lattice cylindrical shells. Composite Structures 93, 308-323.

Mukherjee, M., Ramamurty, U., Garcia-Moreno, F., Banhart, J., 2010. The effect of cooling rate on the structure and properties of closed-cell aluminium foams. Acta Materialia 58, 5031-5042.

Mullin, T., Deschanel, S., Bertoldi, K., Boyce, M.C., 2007. Pattern transformation triggered by deformation. Physical Review Letters 99, 1-4.

Murr, L.E., Gaytan, S.M., Medina, F., Lopez, H., Martinez, E., Machado, B.I., Hernandez, D.H., Martinez, L., Lopez, M.I., Wicker, R.B., Bracke, J., 2010. Next-generation biomedical implants using additive manufacturing of complex, cellular and functional mesh arrays. Philosophical Transactions of the Royal Society A: Mathematical, Physical and Engineering Sciences 368, 1999.

Nakajima, J., Fayazbakhsh, K., Teshima, Y., 2020. Experimental study on tensile properties of 3D printed flexible kirigami specimens. Additive Manufacturing 32, 101100.

Naleway, S.E., Porter, M.M., McKittrick, J., Meyers, M.A., 2015. Structural Design Elements in Biological Materials: Application to Bioinspiration. Advanced Materials 27, 5455-5476.

Neff, C., Hopkinson, N., Crane, N.B., 2018. Experimental and analytical investigation of mechanical behavior of laser-sintered diamond-lattice structures. Additive Manufacturing 22, 807-816.

Nemat-Nasser, S., 2002 Experimentally-based Micromechanical Modeling of Metal Plasticity with Homogenization from Micro-to Macro-scale Properties, in: O.T. Bruhns, E. Stein (Eds.) IUTAM Symposium on Micro- and Macrostructural Aspects of Thermoplasticity, Springer Netherlands, Dordrecht, 101-113.

Ngo, T.D., Kashani, A., Imbalzano, G., Nguyen, K.T.Q., Hui, D., 2018. Additive manufacturing (3D printing): A review of materials, methods, applications and challenges. Composites Part B: Engineering 143, 172-196.

Niknam, H., Akbarzadeh, A.H., 2018. In-plane and out-of-plane buckling of architected cellular plates: Numerical and experimental study. Composite Structures 206, 739-749.

Niknam, H., Akbarzadeh, A.H., 2019. Thermo-mechanical bending of architected functionally graded cellular beams. Composites Part B: Engineering 174, 107060.

Niknam, H., Akbarzadeh, A.H., Rodrigue, D., Therriault, D., 2018. Architected multi-directional functionally graded cellular plates. Materials & Design 148, 188-202.

Niu, B., Yan, J., Cheng, G., 2008. Optimum structure with homogeneous optimum cellular material for maximum fundamental frequency. Structural and Multidisciplinary Optimization 39, 115.

Noda, N., Zhi-He, J., 1993. Thermal stress intensity factors for a crack in a strip of a functionally gradient material. International Journal of Solids and Structures 30, 1039-1056.

Ohno, N., Okumura, D., Noguchi, H., 2001. Microscopic Symmetric Bifurcation Analysis for Cellular Solids Based on a Homogenization Theory of Finite Deformation. 1st Report. Theory. Transactions of the Japan Society of Mechanical Engineers Series A 67, 618-624.

Overvelde, J.T.B., Shan, S., Bertoldi, K., 2012. Compaction Through Buckling in 2D Periodic, Soft and Porous Structures: Effect of Pore Shape. Advanced Materials 24, 2337-2342.

Padture, N.P., Gell, M., Jordan, E.H., 2002. Thermal barrier coatings for gas-turbine engine applications. Science 296, 280-284.

Panesar, A., Abdi, M., Hickman, D., Ashcroft, I., 2018. Strategies for functionally graded lattice structures derived using topology optimisation for Additive Manufacturing. Additive Manufacturing 19, 81-94.

Papka, S., Kyriakides, S., Structures, 1999. Biaxial crushing of honeycombs:—Part 1: Experiments. International Journal of Solids and Structures 36, 4367-4396.

Papka, S.D., Kyriakides, S., 1994a. In-plane compressive response and crushing of honeycomb. Journal of Mechanics and Physics of Solids 42, 1499-1532.

Papka, S.D., Kyriakides, S., 1998a. Biaxial crushing of honeycombs*Part I: Experiments. International Journal of Solids and Structures, 4367-4396.

Papka, S.D., Kyriakides, S., 1998b. Experiments and full-scale numerical simulations of in-plane crushing of a honeycomb. Acta Materialia 46, 2765-2776.

Papka, S.D., Kyriakides, S., 1998c. In-plane crushing of a polycarbonate honeycomb. International Journal of Solids and Structures 35, 239-267.

Papka, S.D., Kyriakides, S., 1999. Biaxial crushing of honeycombs. International Journal of Solids and Structures 36, 4367-4396.

Park, C., Nutt, S.J.M.S., A, E., 2000. PM synthesis and properties of steel foams. 288, 111-118.

Park, G., Kang, S., Lee, H., Choi, W., 2017a. Tunable Multifunctional Thermal Metamaterials: Manipulation of Local Heat Flux via Assembly of Unit-Cell Thermal Shifters. Scientific Reports 7, 41000.

Park, G., Kang, S., Lee, H., Choi, W., 2017b. Tunable multifunctional thermal metamaterials: Manipulation of local heat flux via assembly of unit-cell thermal shifters. Scientific Reports 7, 1-15.

Park, J., Wang, S., Li, M., Ahn, C., Hyun, J.K., Kim, D.S., Kim, D.K., Rogers, J.A., Huang, Y., Jeon, S., 2012a. Three-dimensional nanonetworks for giant stretchability in dielectrics and conductors. Nature Communications 3, 916.

Park, M., Im, J., Shin, M., Min, Y., Park, J., Cho, H., Park, S., Shim, M.-B., Jeon, S., Chung, D.-Y., Bae, J., Park, J., Jeong, U., Kim, K., 2012b. Highly stretchable electric circuits from a composite material of silver nanoparticles and elastomeric fibres. Nature Nanotechnology 7, 803.

Patel, V.M., Talukdar, P., 2018. Determination of radiative properties of representative and real open cell foam structures using the finite volume method. International Journal of Thermal Sciences 132, 117-128.

Pelleg, J., 2013. Fracture, Mechanical Properties of Materials. Springer Netherlands, Dordrecht, pp. 449-520.

Petras, A., Sutcliffe, M.P.F., 1999. Failure mode maps for honeycomb sandwich panels. Composite Structures 44, 237-252.

Pham, M.-S., Liu, C., Todd, I., Lertthanasarn, J., 2019. Damage-tolerant architected materials inspired by crystal microstructure. Nature 565, 305-311.

Pometcu, L., Méjean, C., Benzerga, R., Sharaiha, A., Pouliguen, P., Paven, C.L., 2017. On the choice of the dielectric characterization method for foam composite absorber material. Materials Research Bulletin 96, 107-114.

Portela, C.M., Vidyasagar, A., Krödel, S., Weissenbach, T., Yee, D.W., Greer, J.R., Kochmann, D.M., 2020. Extreme mechanical resilience of self-assembled nanolabyrinthine materials. 117, 5686-5693.

Praveen, G., Reddy, J., 1998a. Nonlinear transient thermoelastic analysis of functionally graded ceramic-metal plates. International journal of solids and structures 35, 4457-4476.

Praveen, G.N., Reddy, J.N., 1998b. Nonlinear transient thermoelastic analysis of functionally graded ceramic-metal plates. International Journal of Solids and Structures 35, 4457-4476.

Qiao, J.X., Chen, C.Q., 2015. Impact resistance of uniform and functionally graded auxetic double arrowhead honeycombs. International Journal of Impact Engineering 83, 47-58.

Qiu, X.M., Zhang, J., Yu, T.X., 2009. Collapse of periodic planar lattices under uniaxial compression, part II: Dynamic crushing based on finite element simulation. International Journal of Impact Engineering 36, 1231-1241.

Rackliffe, M.E., Jensen, D.W., Lucas, W.K., 2006. Local and global buckling of ultra-lightweight IsoTruss structures. Composites Science and Technology 66, 283-288.

Radman, A., Huang, X., Xie, Y.M., 2013. Topology optimization of functionally graded cellular materials. Journal of Materials Science 48, 1503-1510.

Rafsanjani, A., Akbarzadeh, A., Pasini, D., 2015. Snapping Mechanical Metamaterials under Tension. Advanced Materials 27, 5931-5935.

Rao, K.K., Rao, K.J., Sarwade, A., Varma, B.M.J.I.J.o.E., ISSN, A.T., 2012a. Bending Behavior of Aluminum Honey Comb Sandwich Panels. International Journal of Engineering and Advanced Technology 1, 2249-8958.

Rao, R.V., Savsani, V.J., Balic, J., 2012b. Teaching–learning-based optimization algorithm for unconstrained and constrained real-parameter optimization problems. Engineering Optimization 44, 1447-1462.

Rao, R.V., Savsani, V.J., Vakharia, D.P., 2011. Teaching–learning-based optimization: A novel method for constrained mechanical design optimization problems. Computer-Aided Design 43, 303-315.

Rao, R.V., Savsani, V.J., Vakharia, D.P., 2012c. Teaching–Learning-Based Optimization: An optimization method for continuous non-linear large scale problems. Information Sciences 183, 1-15.

Rathbun, H., Radford, D., Xue, Z., He, M., Yang, J., Deshpande, V., Fleck, N., Hutchinson, J., Zok, F., Evans, A., 2006. Performance of metallic honeycomb-core sandwich beams under shock loading. International journal of solids and structures 43, 1746-1763.

Rebaioli, L., Fassi, I., 2017. A review on benchmark artifacts for evaluating the geometrical performance of additive manufacturing processes. The International Journal of Advanced Manufacturing Technology 93, 2571-2598.

Reddy, J., 2000. Analysis of functionally graded plates. International Journal for Numerical Methods in Engineering 47, 663-684.

Reddy, J., Cheng, Z.-Q., 2001. Three-dimensional thermomechanical deformations of functionally graded rectangular plates. European Journal of Mechanics-A/Solids 20, 841-855.

Reddy, J.N., 1993. An introduction to the finite element method. McGraw-hill New York.

Reddy, J.N., 2004. Mechanics of laminated composite plates and shells: theory and analysis. CRC press.

Reddy, J.N., 2006. Theory and analysis of elastic plates and shells. CRC press.

Reddy, J.N., 2010. Nonlocal nonlinear formulations for bending of classical and shear deformation theories of beams and plates. International Journal of Engineering Science 48, 1507-1518.

Reed, R.C., 2008. The superalloys: fundamentals and applications. Cambridge university press.

Ricotti, L., Menciassi, A., 2015. Nanotechnology in biorobotics: opportunities and challenges. Nanoparticle Research 17, 84.

Robbins, D.H., Reddy, J.N., 1993. Modelling of thick composites using a layerwise laminate theory. International Journal for Numerical Methods in Engineering 36, 655-677.

Robert, F., 1985. An isotropic three-dimensional structure with Poisson's ratio--1. Journal of Elasticity 15, 427-430.

Rogers, J.A., Someya, T., Huang, Y., 2010. Materials and Mechanics for Stretchable Electronics. Science 327, 1603.

Romanoff, J., Varsta, P., 2007. Bending response of web-core sandwich plates. Composite Structures 81, 292-302.

Rosen, D.W., 2007. Computer-Aided Design for Additive Manufacturing of Cellular Structures. Computer-Aided Design and Applications 4, 585-594.

Ruan, D., Lu, G., Wang, B., Yu, T.X., 2003. In-plane dynamic crushing of honeycombs—a finite element study. International Journal of Impact Engineering 28, 161-182.

Rupani, S.V., Acharya, G., Jani, S.S., 2017. Design, Modelling and Manufacturing aspects of Honeycomb Sandwich Structures: A Review.

Rus, D., Tolley, M.T., 2015. Design, fabrication and control of soft robots. Nature 521, 467.

Russell, B., Deshpande, V., Wadley, H., 2008. Quasistatic deformation and failure modes of composite square honeycombs. Journal of mechanics of materials and structures 3, 1315-1340.

Ruzzene, M., Scarpa, F., 2005. Directional and band-gap behavior of periodic auxetic lattices. physica status solidi (b) 242, 665-680.

Ruzzene, M., Scarpa, F., Soranna, F., 2003. Wave beaming effects in two-dimensional cellular structures. Smart materials and structures 12, 363.

Sajadi, S.M., Owuor, P.S., Schara, S., Woellner, C.F., Rodrigues, V., Vajtai, R., Lou, J., Galvão, D.S., Tiwary, C.S., Ajayan, P.M., 2018. Multiscale Geometric Design Principles Applied to 3D Printed Schwarzites. Advanced Materials 30, 1704820.

Sasaki, M., Wang, Y., Hirano, T., Hirai, T., 1989. Design of SiC/C functionally gradient material and its preparation by chemical vapor deposition. Journal of the Ceramic Society of Japan 97, 539-543.

Sayir, M., Mitropoulos, C., 1980. On elementary theories of linear elastic beams, plates and shells. Zeitschrift für angewandte Mathematik und Physik ZAMP 31, 1-55.

Sayyad, A.S., Ghugal, Y.M., 2017. Bending, buckling and free vibration of laminated composite and sandwich beams: A critical review of literature. Composite Structures 171, 486-504.

Scarpa, F., Blain, S., Lew, T., Perrott, D., Ruzzene, M., Yates, J.R., 2007. Elastic buckling of hexagonal chiral cell honeycombs. Composites Part A: Applied Science and Manufacturing 38, 280-289.

Scarpa, F., Tomlinson, G., 2000. Theoretical characteristics of the vibration of sandwich plates with in-plane negative poisson's ratio values. Journal of Sound and Vibration 230, 45-67.

Schaedler, T.A., Carter, W.B., 2016. Architected Cellular Materials. Annual Review of Materials Research 46, 187-210.

Schenk, M., Guest, S.D., McShane, G.J., 2014. Novel stacked folded cores for blast-resistant sandwich beams. International Journal of Solids and Structures 51, 4196-4214.

Shan, S., Kang, S.H., Raney, J.R., Wang, P., Fang, L., Candido, F., Lewis, J.A., Bertoldi, K., 2015. Multistable Architected Materials for Trapping Elastic Strain Energy. Advanced Materials 27, 4296-4301.

Shen, H.-S., Wang, Z.-X., 2010. Nonlinear bending of FGM plates subjected to combined loading and resting on elastic foundations. Composite Structures 92, 2517-2524.

Shi, G., Lam, K.Y., 1999. Finite element vibration analysis of composite beams based on higher-order beam theory. Journal of Sound and Vibration 219, 707-721.

Shi, G., Tong, P., 1995. The derivation of equivalent constitutive equations of honeycomb structures by a two scale method. Computational Mechanics 15, 395-407.

Shi, J., Akbarzadeh, A.H., 2019. Architected cellular piezoelectric metamaterials: Thermo-electro-mechanical properties. Acta Materialia 163, 91-121.

Shyu, T.C., Damasceno, P.F., Dodd, P.M., Lamoureux, A., Xu, L., Shlian, M., Shtein, M., Glotzer, S.C., Kotov, N.A., 2015a. A kirigami approach to engineering elasticity in nanocomposites through patterned defects. Nature Materials 14, 785-789.

Shyu, T.C., Damasceno, P.F., Dodd, P.M., Lamoureux, A., Xu, L., Shlian, M., Shtein, M., Glotzer, S.C., Kotov, N.A., 2015b. A kirigami approach to engineering elasticity in nanocomposites through patterned defects. Nature Materials 14, 785.

Sideridis, E., Papadopoulos, G.A., 2004. Short-beam and three-point-bending tests for the study of shear and flexural properties in unidirectional-fiber-reinforced epoxy composites. Journal of Applied Polymer Science 93, 63-74.

Sigmund, O., 1997. On the Design of Compliant Mechanisms Using Topology Optimization. Mechanics of Structures and Machines 25, 493-524.

Sigmund, O., 2001. A 99 line topology optimization code written in Matlab. Structural and Multidisciplinary Optimization 21, 120-127.

Smith, B.H., Szyniszewski, S., Hajjar, J.F., Schafer, B.W., Arwade, S.R., 2012. Steel foam for structures: A review of applications, manufacturing and material properties. Journal of Constructional Steel Research 71, 1-10.

Smith, M., Guan, Z., Cantwell, W.J., 2013. Finite element modelling of the compressive response of lattice structures manufactured using the selective laser melting technique. International Journal of Mechanical Sciences 67, 28-41.

Soldatos, K.P., Timarci, T., 1993. A unified formulation of laminated composite, shear deformable, five-degrees-of-freedom cylindrical shell theories. Composite Structures 25, 165-171.

Song, Z., Wang, X., Lv, C., An, Y., Liang, M., Ma, T., He, D., Zheng, Y.-J., Huang, S.-Q., Yu, H., Jiang, H., 2015. Kirigami-based stretchable lithium-ion batteries. Scientific Reports 5, 10988.

Spinner, S., A comparison of experimental and theoretical relations between Young's modulus and the flexural and longitudinal resonance frequencies of uniform bars.

Stephen, N.G., Puchegger, S., 2006. On the valid frequency range of Timoshenko beam theory. Journal of Sound and Vibration 297, 1082-1087.

Stupp, S.I., Braun, P.V., 1997. Molecular manipulation of microstructures: biomaterials, ceramics, and semiconductors. Science 277, 1242-1248.

Sui, Q., Fan, H., Lai, C., 2015. Failure analysis of 1D lattice truss composite structure in uniaxial compression. Composites Science and Technology 118, 207-216.

Suleiman, A.S., Dukhan, N., 2014. Forced convection inside metal foam: Simulation over a long domain and analytical validation. International Journal of Thermal Sciences 86, 104-114.

Sun, G., Huo, X., Chen, D., Li, Q., 2017. Experimental and numerical study on honeycomb sandwich panels under bending and in-panel compression. Materials & Design 133, 154-168.

Sun, J.-Y., Zhao, X., Illeperuma, W.R.K., Chaudhuri, O., Oh, K.H., Mooney, D.J., Vlassak, J.J., Suo, Z., 2012a. Highly stretchable and tough hydrogels. Nature 489, 133-136.

Sun, J.-Y., Zhao, X., Illeperuma, W.R.K., Chaudhuri, O., Oh, K.H., Mooney, D.J., Vlassak, J.J., Suo, Z., 2012b. Highly stretchable and tough hydrogels. Nature 489, 133.

Takabatake, H., Yanagisawa, N., Kawano, T., 1996. A simplified analysis of rectangular cellular plates. International Journal of Solids and Structures 33, 2055-2074.

Takezawa, A., Zhang, X., Kato, M., Kitamura, M., 2019. Method to optimize an additively-manufactured functionally-graded lattice structure for effective liquid cooling. Additive Manufacturing 28, 285-298.

Tan, T., Rahbar, N., Allameh, S.M., Kwofie, S., Dissmore, D., Ghavami, K., Soboyejo, W.O., 2011. Mechanical properties of functionally graded hierarchical bamboo structures. Acta Biomaterialia 7, 3796-3803.

Tanaka, K., Tanaka, Y., Watanabe, H., Poterasu, V., Sugano, Y., 1993. An improved solution to thermoelastic material design in functionally gradient materials: Scheme to reduce thermal stresses. Computer Methods in Applied Mechanics and Engineering 109, 377-389.

Tancogne-Dejean, T., Diamantopoulou, M., Gorji, M.B., Bonatti, C., Mohr, D., 2018. 3D Plate-Lattices: An Emerging Class of Low-Density Metamaterial Exhibiting Optimal Isotropic Stiffness. Advanced Materials 30, 1803334.

Tancogne-Dejean, T., Mohr, D., 2018. Stiffness and specific energy absorption of additively-manufactured metallic BCC metamaterials composed of tapered beams. International Journal of Mechanical Sciences 141, 101-116.

Tang, G., Yan, Y., Chen, X., Zhang, J., Xu, B., Feng, Z., 2001. Dynamic damage and fracture mechanism of three-dimensional braided carbon fiber/epoxy resin composites. 22, 21-25.

Tang, Y., Dong, G., Zhou, Q., Zhao, Y.F., 2018. Lattice Structure Design and Optimization With Additive Manufacturing Constraints. IEEE Transactions on Automation Science and Engineering 15, 1546-1562.

Tarkhanyan, R.H., Niarchos, D.G., 2013. Reduction in lattice thermal conductivity of porous materials due to inhomogeneous porosity. International Journal of Thermal Sciences 67, 107-112.

Taylor, M., Francesconi, L., Gerendás, M., Shanian, A., Carson, C., Bertoldi, K., 2014. Low Porosity Metallic Periodic Structures with Negative Poisson's Ratio. Advanced Materials 26, 2365-2370.

Thai, H.-T., Kim, S.-E., 2015. A review of theories for the modeling and analysis of functionally graded plates and shells. Composite Structures 128, 70-86.

Thornton, P.H., Magee, C.L., 1975. The Deformation of aluminum foams. Metallurgical Transactions A 6, 1253-1263.

Tian, J., Lu, T.J., Hodson, H.P., Queheillalt, D.T., Wadley, H.N.G., 2007. Cross flow heat exchange of textile cellular metal core sandwich panels. International Journal of Heat and Mass Transfer 50, 2521-2536.

Timoshenko, S.P., 1921. LXVI. On the correction for shear of the differential equation for transverse vibrations of prismatic bars. The London, Edinburgh, and Dublin Philosophical Magazine and Journal of Science 41, 744-746.

Totaro, G., 2013a. Local buckling modelling of isogrid and anisogrid lattice cylindrical shells with hexagonal cells. Composite Structures 95, 403-410.

Totaro, G., 2013b. Local buckling modelling of isogrid and anisogrid lattice cylindrical shells with hexagonal cells. Composite Structures 95, 403-410.

Totaro, G., Nicola, F.D., Caramuta, P., 2013. Local buckling modelling of anisogrid lattice structures with hexagonal cells : An experimental verification. Composite Structures 106, 734-741.

Triantafyllidis, N., Schraad, M.W., 1998. Onset of failure in aluminum honeycombs under general in-plane loading. Journal of the Mechanics and Physics of Solids 46, 1089-1124.

Tsantilis, A.V., Triantafillou, T.C., 2018. Innovative seismic isolation of masonry infills using cellular materials at the interface with the surrounding RC frames. Engineering Structures 155, 279-297.

Tung, H.V., Duc, N.D., 2010. Nonlinear analysis of stability for functionally graded plates under mechanical and thermal loads. Composite Structures 92, 1184-1191.

Upadhya, K., Yang, J.M., Hoffman, W., 1997. Advanced Materials for Ultrahigh Temperature Structural Applications Above 2000 Deg C. American Ceramic Society Bulletin 76, 51-56.

Urgun-Demirtas, M., Benda, P.L., Gillenwater, P.S., Negri, M.C., Xiong, H., Snyder, S.W., 2012. Achieving very low mercury levels in refinery wastewater by membrane filtration. Journal of Hazardous Materials 215-216, 98-107.

Vasiliev, V., Razin, A., 2006. Anisogrid composite lattice structures for spacecraft and aircraft applications. Composite Structures 76, 182-189.

Vasiliev, V.V., Barynin, V.A., Razin, A.F., 2012. Anisogrid composite lattice structures – Development and aerospace applications. Composite Structures 94, 1117-1127.

Vemuri, K., Canbazoglu, F., Bandaru, P., 2014. Guiding conductive heat flux through thermal metamaterials. Applied Physics Letters 105, 193904.

Vemuri, K.P., Bandaru, P.R., 2013. Geometrical considerations in the control and manipulation of conductive heat flux in multilayered thermal metamaterials. Applied Physics Letters 103, 133111.

Vemuri, K.P., Bandaru, P.R., 2014. Anomalous refraction of heat flux in thermal metamaterials. Applied Physics Letters 104, 083901.

Vigliotti, A., Pasini, D., 2012. Stiffness and strength of tridimensional periodic lattices. Computer Methods in Applied Mechanics and Engineering 229, 27-43.

Vinson, J.R., 2005. Sandwich structures: past, present, and future, Sandwich structures 7: advancing with sandwich structures and materials. Springer, pp. 3-12.

Viskanta, R., 2009. Overview of radiative transfer in cellular porous materials, Proceedings of the ASME 2009 Heat Transfer Summer Conference, pp. 19-23.

Vodenitcharova, T., Zhang, L.C., 2006. Bending and local buckling of a nanocomposite beam reinforced by a single-walled carbon nanotube. International Journal of Solids and Structures 43, 3006-3024.

Wadley, H.J.C.M., Technology, M.F., 2001. Cellular metals and metal foaming technology. 381-386.

Wadley, H.N.G., 2002. Cellular Metals Manufacturing. Advanced Engineering Materials 4, 726-733.

Wadley, H.N.G., Fleck, N.A., Evans, A.G., 2003. Fabrication and structural performance of periodic cellular metal sandwich structures. Composites Science and Technology 63, 2331-2343.

Wang, A.J., McDowell, D.L., 2004. In-Plane Stiffness and Yield Strength of Periodic Metal Honeycombs. Journal of Engineering Materials and Technology 126, 137-156.

Wang, C., Ramakrishnan, K.R., Shankar, K., Morozov, E., Wang, H., Fien, A., 2020. Homogenized shell element-based modeling of low-velocity impact response of stainless-steel wire mesh. Mechanics of Advanced Materials and Structures, 1-16.

Wang, F., 2004. Precision extruding deposition and characterization of cellular poly-ε-caprolactone tissue scaffolds. Rapid Prototyping Journal 10, 42-49.

Wang, X., Jiang, M., Zhou, Z., Gou, J., Hui, D., 2017a. 3D printing of polymer matrix composites: A review and prospective. Composites Part B: Engineering 110, 442-458.

Wang, Y., Xu, H., Pasini, D., 2017b. Multiscale isogeometric topology optimization for lattice materials. Computer Methods in Applied Mechanics and Engineering 316, 568-585.

Wang, Y., Zhang, L., Daynes, S., Zhang, H., Feih, S., Wang, M.Y., 2018. Design of graded lattice structure with optimized mesostructures for additive manufacturing. Materials & Design 142, 114-123.

Warren, T.L., 1990. Negative Poisson's ratio in a transversely isotropic foam structure. Journal of Applied Physics 67, 7591-7594.

Willshaw, S., Mullin, T., 2012. Pattern switching in two and three-dimensional soft solids. Soft Matter 8, 1747-1750.

Wollmann, L., Nayak, A.K., Parkin, S.S.P., Felser, C., 2017. Heusler 4.0: Tunable Materials. Annual Review of Materials Research 47, 247-270.

Woo, J., Meguid, S., 2001. Nonlinear analysis of functionally graded plates and shallow shells. International Journal of Solids and structures 38, 7409-7421.

Xiao, D., Dong, Z., Li, Y., Wu, W., Fang, D., 2019. Compression behavior of the graded metallic auxetic reentrant honeycomb: Experiment and finite element analysis. Materials Science and Engineering: A 758, 163-171.

Xie, Y.M., Steven, G.P., 1993. A simple evolutionary procedure for structural optimization. Computers & Structures 49, 885-896.

Xiong, J., Ma, L., Stocchi, A., Yang, J., Wu, L., Pan, S., 2014. Bending response of carbon fiber composite sandwich beams with three dimensional honeycomb cores. Composite Structures 108, 234-242.

Xu, F., Zhang, X., Zhang, H., 2018. A review on functionally graded structures and materials for energy absorption. Engineering Structures 171, 309-325.

Xu, G., Zhang, H., Xie, M., Jin, Y., 2017a. Geometrical effects on the concentrated behavior of heat flux in metamaterials thermal harvesting devices. AIP Advances 7, 105322.

Xu, S., Chen, L., Gong, M., Hu, X., Zhang, X., Zhou, Z., 2017b. Characterization and engineering application of a novel ceramic composite insulation material. Composites Part B: Engineering 111, 143-147.

Yan, J., Yang, S., Yang, C., 2014. Multiscale Analysis of Thermal Stress of Lattice Materials and Its Size Effects. Journal of Thermal Stresses 37, 885-904.

Yang, D., Jin, L., Martinez, R.V., Bertoldi, K., Whitesides, G.M., Suo, Z., 2016. Phase-transforming and switchable metamaterials. Extreme Mechanics Letters 6, 1-9.

Yang, J., Shen, H.-S., 2003. Nonlinear bending analysis of shear deformable functionally graded plates subjected to thermo-mechanical loads under various boundary conditions. Composites Part B: Engineering 34, 103-115.

Yang, T., Vemuri, K.P., Bandaru, P.R., 2014. Experimental evidence for the bending of heat flux in a thermal metamaterial. Applied Physics Letters 105, 103-106.

Yang, X., Ma, J., Sun, Y., Yang, J., 2018. Ripplecomb: A novel triangular tube reinforced corrugated honeycomb for energy absorption. Composite Structures 202, 988-999.

Yazdani Sarvestani, H., Akbarzadeh, A.H., Mirabolghasemi, A., 2018a. Structural analysis of size-dependent functionally graded doubly-curved panels with engineered microarchitectures. Acta Mechanica 229, 2675-2701.

Yazdani Sarvestani, H., Akbarzadeh, A.H., Mirbolghasemi, A., Hermenean, K., 2018b. 3D printed meta-sandwich structures: Failure mechanism, energy absorption and multi-hit capability. Materials & Design 160, 179-193.

Yazdani Sarvestani, H., Akbarzadeh, A.H., Niknam, H., Hermenean, K., 2018c. 3D printed architected polymeric sandwich panels: Energy absorption and structural performance. Composite Structures 200, 886-909.

Yin, Z., Hannard, F., Barthelat, F., 2019. Impact-resistant nacre-like transparent materials. Science 364, 1260.

Yokozeki, T., Shimizu, Y., Ishii, M., Kimizuka, K., Suzuki, S., Yamasaki, Y., Terashima, K., Kamita, T., Aoki, T., 2017. Mechanical behavior in compression of skin-added X-lattice composite panel with corrugated ribs. Composite Structures 168, 863-871.

Youssef, S., Maire, E., Gaertner, R., 2005. Finite element modelling of the actual structure of cellular materials determined by X-ray tomography. Acta Materialia 53, 719-730.

Yu, K., Xin, A., Du, H., Li, Y., Wang, Q., 2019a. Additive manufacturing of self-healing elastomers. NPG Asia Materials 11, 7.

Yu, S., Sun, J., Bai, J., 2019b. Investigation of functionally graded TPMS structures fabricated by additive manufacturing. Materials & Design 182, 108021.

Zenkour, A.M., 2004. Analytical solution for bending of cross-ply laminated plates under thermo-mechanical loading. Composite Structures 65, 367-379.

Zha, W., Anand, S., 2015. Geometric approaches to input file modification for part quality improvement in additive manufacturing. Journal of Manufacturing Processes 20, 465-477.

Zhang, C., Akbarzadeh, A., Kang, W., Wang, J., Mirabolghasemi, A., 2018a. Nano-architected metamaterials: Carbon nanotube-based nanotrusses. Carbon 131, 38-46.

Zhang, D.-G., 2013. Nonlinear bending analysis of FGM beams based on physical neutral surface and high order shear deformation theory. Composite Structures 100, 121-126.

Zhang, D., Fei, Q., Zhang, P., 2017. In–plane dynamic crushing behavior and energy absorption of honeycombs with a novel type of multi-cells. Thin-Walled Structures 117, 199-210.

Zhang, J., Lu, G., Ruan, D., Wang, Z., 2018b. Tensile behavior of an auxetic structure: Analytical modeling and finite element analysis. International Journal of Mechanical Sciences 136, 143-154.

Zhang, J., Wang, Z., Zhao, L., 2016. Dynamic response of functionally graded cellular materials based on the Voronoi model. Composites Part B: Engineering 85, 176-187.

Zhang, L., Feih, S., Daynes, S., Chang, S., Wang, M.Y., Wei, J., Lu, W.F., 2018c. Energy absorption characteristics of metallic triply periodic minimal surface sheet structures under compressive loading. Additive Manufacturing 23, 505-515.

Zhang, X., Zhang, H., 2013. Theoretical and numerical investigation on the crush resistance of rhombic and kagome honeycombs. Composite Structures 96, 143-152.

Zhang, Z., Provis, J.L., Reid, A., Wang, H., 2015. Mechanical, thermal insulation, thermal resistance and acoustic absorption properties of geopolymer foam concrete. Cement and Concrete Composites 62, 97-105.

Zhao, C.Y., 2012. Review on thermal transport in high porosity cellular metal foams with open cells. International Journal of Heat and Mass Transfer 55, 3618-3632.

Zheng, Q., Jiang, D., Huang, C., Shang, X., Ju, S., 2015. Analysis of failure loads and optimal design of composite lattice cylinder under axial compression. Composite Structures 131, 885-894.

Zidi, M., Tounsi, A., Houari, M.S.A., Adda Bedia, E.A., Anwar Bég, O., 2014. Bending analysis of FGM plates under hygro-thermo-mechanical loading using a four variable refined plate theory. Aerospace Science and Technology 34, 24-34.